

UC Merced

UC Merced Electronic Theses and Dissertations

Title

Mechanistic Insights into Interband Transitions of Metallic Nanoparticles for Photocatalysis

Permalink

<https://escholarship.org/uc/item/9fv0w2t7>

Author

Lyu, Pin

Publication Date

2023

Peer reviewed|Thesis/dissertation

UNIVERSITY OF CALIFORNIA, MERCED

**Mechanistic Insights into Interband Transitions  
of Metallic Nanoparticles for Photocatalysis**

by  
Pin Lyu

A dissertation submitted in partial satisfaction of the requirements  
for the degree Doctor of Philosophy  
in  
Chemistry

Committee in charge:

Professor Erik Menke, Chair  
Professor Tao Ye  
Professor Sayantani Ghosh  
Professor Son C. Nguyen

Spring 2023

©2023 Pin Lyu

All rights reserved

Chapter 1 © 2023 The Authors and Royal Society of Chemistry

Chapter 2 Copyright ©2022 The Authors and Elsevier

Chapter 3 Copyright ©2021 American Chemical Society

Chapter 4 © The Authors and 2023 American Chemical Society

The Dissertation of Pin Lyu is approved, and it is acceptable  
in quality and form for publication on microfilm and electronically:

---

Erik Menke, Chair                      Date

---

Tao Ye                                      Date

---

Sayantani Ghosh                      Date

---

Son C. Nguyen                      Date

University of California, Merced

©2023 Pin Lyu

## ACKNOWLEDGEMENTS

*O ever youthful, O ever weeping.*

from *The Dharma Bums* by Jack Kerouac

Time flies so fast that I still remember the first day of entering the states and being picked up by my research advisor, Prof. Son Nguyen, from the SFO airport to Merced. We talked the way back all about Science and Society and I have been impressed with his passion and enthusiasm for scientific research. For the last four years, I have been keeping that spirit with constant, delicate, thoughtful, and valuable guidance from him, and intend to keep passing it in my future careers. None of my achievements including this dissertation could happen without his help. I would like to express my sincere gratitude to him and wish him the best!

I shall extend my acknowledgments to all the past and current group members in our research group for their patience and kindness: Dr. Ziliang Mao, Randy Espinoza, Duy Nguyen, William Spaller, and Daniel Valenzuela Cahua. Also, I was very fortunate to work with two talented undergraduate researchers and one high school student in our lab and learned a lot about mentoring and communicating research to a broader audience: Paulina Brambila, Riley Whitmer, and Siena Akira Murillo. Outside the Nguyen group, I would like to thank the 2019 cohorts of the Chemistry and Chemical Biology Program and other colleges that I had the opportunity to work with for their innumerable help with the course and daily operation of experiments.

Also, I would like to express my thanks to all my committee members for their continuous support along the way: Prof. Erik Menke, Prof. Tao Ye, and Prof. Sayantani Ghosh. And my extended gratitude to all the professors in our department that helped and guided me along the way: Prof. Hrant Hrachian, Prof. Christine Isborn, Prof. Liang Shi, Prof. Shahar Sukenik, and Prof. Henrik Larsson. Moreover, I would like to thank the instructors and lab supporting staff that have been helping me walk through the teaching smoothly and safely: Deborah Lair, Dr. Donna Jaramillo-Fellin, Dr. Melissa Russell, Dr. Jackie Shay, and Marcos García-Ojeda.

Last but not the least, I would like to thank the Chemistry and Biochemistry Department for summer fellowship support, Graduate Division for logistics and graduation paperwork, Office of International Affairs for visa and living resources, and other people or groups that have been helped me along the way.

As is said, *O ever youthful, O ever weeping, and O ever grateful!*

# TABLE OF CONTENT

ACKNOWLEDGEMENTS .....	iv
LIST OF FIGURES .....	ix
LIST OF TABLES .....	xii
ABSTRACT.....	xiii
<b>Chapter 1 Photocatalysis of Metallic Nanoparticles: Interband vs. Plasmon .....</b>	<b>1</b>
<b>1.1 Introduction.....</b>	<b>1</b>
1.1.1 Historical view of plasmon .....	1
1.1.2 Overview of metallic nanoparticles for catalysis.....	1
1.1.3 Metallic nanocrystal photocatalysts: Pros and Cons .....	3
1.1.4 Interband vs. Plasmon driven mechanisms: Concerns and opportunities.....	4
<b>1.2 Photoexcitation of metallic nanoparticles .....</b>	<b>4</b>
1.2.1 Physical picture of photoexcitation .....	4
1.2.2 Photo-generated hot carriers and their properties .....	5
1.2.3 Charge transfer for catalysis.....	7
<b>1.3 Photocatalyzed reactions driven by hot carriers.....</b>	<b>9</b>
1.3.1 Hot electron-mediated reactions.....	9
1.3.2 Hot hole-mediated reactions .....	11
1.3.3 Descriptors of photocatalysis efficiency .....	13
<b>1.4 Photocatalysis mechanism in metallic nanoparticles.....</b>	<b>15</b>
1.4.1 Plasmon Resonance.....	15
1.4.2 Interband Transitions.....	17
1.4.3 Other mechanisms .....	19
1.4.3.1 Near-field enhancement .....	19
1.4.3.2 Photo-charging effect .....	21
1.4.3.3 Photothermal effects.....	21
<b>1.5 Summary and future perspectives.....</b>	<b>22</b>
<b>1.6 References.....</b>	<b>23</b>
<b>Chapter 2 Mechanistic Insight into Deep Holes from Interband Transitions in Palladium Nanoparticle Photocatalysts.....</b>	<b>30</b>
<b>2.1 Introduction.....</b>	<b>30</b>
<b>2.2 Experimental section .....</b>	<b>32</b>

2.2.1 Synthesis of porous Pd nanoparticles .....	32
2.2.2 Characterizations .....	32
2.2.3 Typical photocatalyzed Suzuki–Miyaura reaction condition .....	32
2.2.4 Quantum yield calculation .....	33
2.3 Optical property of mesoporous Pd nanoparticles .....	34
2.4 Photocatalyzed condition of mesoporous Pd nanoparticles .....	39
2.5 Establishing the same reaction time and photon flux for comparing of quantum yields of photocatalyst under various excitation wavelengths .....	42
2.6 Wavelength dependence of photocatalytic activities.....	43
2.7 Proposed catalytic mechanism and related control experiments .....	47
2.8 Discussion on photocatalytic efficiency compared with other photocatalysts .....	50
2.9 Supporting notes .....	52
2.9.1 Note S1. Light scattering measurement .....	52
2.9.2 Note S2. Discussion on effect of local heating on the observed photocatalysis .....	54
2.9.3 Note S3. Design of control experiments to evaluate the catalysis contribution of leached Pd .....	55
2.9.4 Note S4. ICP-OES analysis for Pd in reaction supernatant .....	56
2.9.5 Note S5. XPS analysis of porous Pd nanoparticles.....	57
2.9.6 Note S6. Control experiments to confirm that hetero-coupling is the only product .....	59
2.9.7 Note S7. Exclusion of some other parallel processes besides the Suzuki-Miyaura reaction .....	62
2.9.8 Note S8. NMR spectra of standard compounds and typical reaction solutions, and product yield calculation .....	67
2.10 References.....	70
Chapter 3 Effect of Photocharging on Catalysis of Metallic Nanoparticles .....	75
3.1 Introduction.....	75
3.2 Experimental section .....	76
3.2.1 Chemicals and characterizations.....	76
3.2.2 Synthesis of porous Pd nanoparticles (denoted as Pd NPs).....	76
3.2.3 Photocharging procedures for Pd NPs before using as the catalysts for the reduction reaction .....	76
3.2.4 4-Nitrophenol reduction as a model reaction to evaluate the catalytic performance .....	77
3.2.5 Estimation of stored electrons on Pd NPs after the photocharging process .....	77

3.3 Experimental design for evaluating photo-charging effect on catalysis .....	78
3.4 Catalytic performance of photo-charged Pd NPs .....	79
3.5 Quantification of accumulated electrons from photo-charging process .....	83
3.6 Evaluation of photo-charging effect on catalytic performance of Pd NPs under different conditions .....	84
3.7 Conclusion and outlook .....	86
3.8 Supporting notes .....	89
3.8.1 Note S1. Estimation of number of electrons per nanoparticle and quantum yield of photocharging .....	89
3.9 References .....	91
<b>Chapter 4 From Noble to Non-noble Metallic Nanoparticle Photocatalyst: What Can Interband Transition Bring? .....</b>	<b>95</b>
4.1 Introduction.....	95
4.2 Experimental section .....	96
4.2.1 Chemicals and characterizations.....	96
4.2.2 Synthesis of Au nanoparticles (denoted as Au NPs) .....	97
4.2.3 Synthesis of porous Pd nanoparticles (denoted as Pd NPs).....	97
4.2.4 Synthesis of amorphous cobalt-boron nanoparticles (denoted as Co-B NPs).....	97
4.2.5 Nitrobenzene reduction with Co-B NPs as a model reaction for catalytic performance.....	98
4.2.6 Nitrobenzene reduction with photo-charged Co-B NPs for mechanistic study.....	98
4.2.7 Nitrobenzene reduction with Au NPs and Pd NPs for catalytic performance.....	98
4.3 Systematic comparison of Au, Pd and Co NPs.....	99
4.4 Experimental design and physicochemical properties of prepared NPs.....	100
4.4.1 Size and shape distributions of colloidal Au, Pd and Co-B NPs .....	100
4.4.2 Optical properties of colloidal Au, Pd and Co-B NPs.....	104
4.5 Evaluation of catalytic performance of Co-B NPs and mechanistic study .....	104
4.5.1 Catalytic performance of Co-B NPs under dark and photo-excitations .....	104
4.5.2 Photocatalytic performance of Co-B NPs under different wavelengths .....	110
4.5.3 Mechanistic study of photo-charging effect on Co-B NPs .....	112
4.6 Photocatalytic performance of Au, Pd and Co-B NPs.....	114
4.7 Conclusion .....	119
4.8 References .....	119
<b>Chapter 5 Summary and Future Perspectives .....</b>	<b>123</b>
5.1 Summary.....	123



<b>5.2 Future Perspectives</b> .....	124
<b>5.3 References</b> .....	126

## LIST OF FIGURES

<b>Figure 1.1</b> Milestones of plasmon research. ....	1
<b>Scheme 1.1</b> Overview of photocatalysis by metallic nanoparticles. ....	2
<b>Figure 1.2</b> Physical pictures and comparisons of plasmon resonance and interband transition. ....	5
<b>Figure 1.3</b> Hot carriers' generation and properties from interband transition and plasmon resonance.....	7
<b>Figure 1.4</b> Pathways and dynamics of charge transfer from metallic nanoparticles to adsorbates for photocatalysis. ....	8
<b>Figure 1.5</b> Hot electron-mediated photocatalytic reactions. ....	10
<b>Figure 1.6</b> Hot hole-mediated photocatalytic reactions. ....	12
<b>Figure 1.7</b> Quantifying the efficiency of photocatalysts.....	14
<b>Figure 1.8</b> Photocatalysis mechanisms from plasmon resonance.....	16
<b>Figure 1.9</b> Photocatalysis mechanisms from interband transitions.....	18
<b>Figure 1.10</b> Other photocatalysis mechanisms by metallic nanoparticles. ....	20
<b>Figure 2.1</b> Optical and morphological characterization of mesoporous Pd nanoparticles. ....	33
<b>Figure 2.2</b> FTIR spectra of mesoporous Pd nanoparticles and PS-b-PEO for comparison. ....	35
<b>Figure 2.3</b> TGA of porous Pd nanoparticles under argon atmosphere.....	35
<b>Figure 2.4</b> SEM images porous and non-porous Pd NPs.....	36
<b>Figure 2.5</b> Surface area and pore size analysis of porous Pd NPs. ....	36
<b>Figure 2.6</b> A series of tilt TEM images of a typical mesoporous Pd nanoparticle with various tilt angles of the sample holder. ....	37
<b>Figure 2.7</b> Normalized scattering cross section of porous Pd nanoparticles drop-casted on a glass slide and a plot of $y=1/\lambda^4$ function for comparison.....	38
<b>Figure 2.8</b> Extinction, total scattering (integrating over all scattering angles) and absorption spectra. ....	39
<b>Figure 2.9</b> Suzuki–Miyaura C-C coupling reaction for evaluating photocatalytic performance of porous Pd nanoparticles.....	39
<b>Figure 2.10</b> UV-Vis spectra of reaction solutions with and without porous Pd and of $[\text{PdCl}_4]^{2-}$ complex in the reaction solution and in water. ....	41
<b>Figure 2.11</b> UV-Vis spectra of the supernatants after 1 h reaction in of the leaching test in Experiment II under various excitation conditions. ....	44
<b>Figure 2.12</b> $\text{PdCl}_2$ was used as a pre-catalyst (the source of generating Pd(0) for the catalytic cycle) for the Suzuki–Miyaura reaction. ....	45
<b>Figure 2.13</b> Photocatalysis of porous Pd nanoparticles for Suzuki–Miyaura C-C coupling reaction.....	47
<b>Figure 2.14</b> Proposed mechanism. ....	48
<b>Scheme 3.1</b> A two-step experiment for evaluating photo-charging effect on catalysis. ...	78

<b>Figure 3.1</b> Catalytic performance of Pd NPs under non-photo-charging and photo-charging.....	79
<b>Figure 3.2</b> UV-vis spectra of porous Pd NP solutions. ....	80
<b>Figure 3.3</b> TEM images of Pd NPs. ....	80
<b>Figure 3.4</b> UV-vis spectra of 4-nitrophenol reduction with NaBH <sub>4</sub> catalyzed by Pd NPs without and with photocharging. ....	82
<b>Figure 3.5</b> Quantification of accumulated electrons from photo-charging process. ....	83
<b>Figure 3.6</b> Absorbance change of thionine (Th) when titrating with Pd NPs after photocharging. ....	84
<b>Figure 3.7</b> Evaluation of photo-charging effect on catalytic performance of Pd NPs under different conditions. ....	85
<b>Figure 3.8</b> XPS analysis of Pd NPs.....	88
<b>Scheme 4.1</b> Comparison of density of states (DOS), metal-adsorbate splitting states (bonding and antibonding), and interband transitions in three studied transition metals. .	99
<b>Figure 4.1</b> Digital images of colloidal solutions of metallic nanoparticles in 4-side cuvettes. ....	101
<b>Figure 4.2</b> TEM images of Au, Pd, and Co-B NPs.....	101
<b>Figure 4.3</b> Size distribution and zeta potential of Co-B NPs from DLS measurements.	102
<b>Figure 4.4</b> PXRD patterns of Au, Pd, and Co-B NPs. ....	103
<b>Figure 4.5</b> FTIR spectra of Au NPs, Pd NPs, and Co-B NPs in ATR (attenuated total reflection) mode. ....	104
<b>Figure 4.6</b> Optical properties of different metallic nanoparticles and catalytic performance of Co-B NPs under dark and photo-excitations. ....	105
<b>Figure 4.7</b> UV-vis spectra of standard solutions with either reactants or products from the nitrobenzene reduction.....	106
<b>Figure 4.8</b> UV-vis spectra of control reaction solutions in the dark.....	109
<b>Figure 4.9</b> UV-vis spectra of reaction solutions with Co-B NPs in the dark and under typical photocatalyzed conditions.....	107
<b>Figure 4.10</b> NMR spectra of standard solutions, scale-up dark reactions and scale-up photocatalyzed reactions. ....	108
<b>Figure 4.11</b> UV-vis time-dependent profiles of reaction solutions with Co-B NPs under typical photocatalyzed condition. ....	110
<b>Figure 4.12</b> Photocatalytic performance under different wavelength excitation and experimental evidence of photo-charging mechanism of Co-B NPs.....	110
<b>Figure 4.13</b> UV-vis time-dependent profiles of reaction solutions with Co-B NPs under typical photocatalyzed condition when using different wavelengths of LED but with the same incident power (150 mW).....	111
<b>Figure 4.14</b> Experimental evidence of photo-charging mechanism for Co-B NPs. ....	112
<b>Figure 4.15</b> UV-vis time-dependent profiles of reaction solutions with photo-charged Co-B NPs when using 405 nm LED (FWHM=12 nm) as the light source under different charging time. ....	113

<b>Figure 4.16</b> Photocatalytic performance of different metallic NPs. Reaction kinetics for nitrobenzene reduction in the dark or under typical photo-excitation conditions. ....	114
<b>Figure 4.17</b> UV-vis time-dependent profiles of reaction solutions with Au NPs and Pd NPs in the dark or typical photocatalyzed condition. ....	115
<b>Figure 4.18</b> UV-vis time-dependent profiles of reaction solutions with Pd NPs with doubled concentration. ....	116
<b>Figure 4.19</b> XPS analysis of Co-B NPs. ....	118
<b>Figure 5.1</b> Some benefits of moving from noble to affordable metal nanoparticles and utilizing their interband transitions for photocatalysis.....	124
<b>Figure 5.2</b> Using different oxidation power of hot holes for selective oxidation of toluene.....	125

## LIST OF TABLES

<b>Table 1.1</b> Compared photocatalytic properties of metallic nanoparticles to other common photocatalysts.....	3
<b>Table 2.1</b> Product yield (without catalyst) under different excitation wavelengths.....	41
<b>Table 2.2</b> Calculated quantum yield under 490 nm LED irradiation when changing reaction time.....	42
<b>Table 2.3</b> Calculated quantum yield under 470 nm LED irradiation when changing photon flux.....	43
<b>Table 2.4</b> Product yield from the control Experiment I, II and III in Note S3.....	44
<b>Table 2.5</b> Calculated quantum yield under various excitation wavelengths and same photon flux.....	46
<b>Table 2.6</b> Product yield of the reaction with and without isopropanol.....	49
<b>Table 2.7</b> Product yield of control reaction with only one reactant used.....	49
<b>Table 2.8</b> Comparison of photocatalytic efficiency of Suzuki-Miyaura reaction between previous works and the current work.....	51
<b>Table 3.1</b> Calculation of absorbed photon fluxes under various incident optical powers.....	80
<b>Table 3.2</b> Calculation of absorbed photon fluxes under various excitation wavelengths.....	86

## ABSTRACT

Metallic nanocrystals have gained growing interest in photocatalysis applications due to their robust nature for multicycle operation, strong light absorption, and relatively new catalytic mechanisms. Historically, photocatalysis induced by localized surface plasmon resonance (plasmon resonance for short) of these particles has been studied widely for more than a decade, but photocatalysis originating from interband transitions is still underexplored. In order to build a comprehensive map from photon utilization to hot-carrier harvesting, and related photocatalysis, the systematic comparison between plasmon resonance and interband transition needs to be conducted in light of hot carriers-mediated reaction. The energy levels, population, dynamics, and heating effect of those hot carriers, and as followed, the charge transfer, reaction pathway, and kinetics are all necessary to be discussed. In this dissertation, the physical picture and related properties of interband transition and plasmon resonance are reviewed, then some systematic approaches to evaluate these two excitations are demonstrated. As follows, the porous Palladium nanoparticles as the model catalysts with dominant spectra features corresponding to the interband transitions were employed for mechanistic insights. We have demonstrated that under shorter wavelengths, deeper holes in the *d*-band can catalyze the oxidative addition of aryl halide R-X onto Pd<sup>0</sup> at the nanoparticles' surface to form R-Pd<sup>II</sup>-X complex, thus accelerating the rate-determining step of the catalytic cycle, eventually increase the quantum yield of photocatalyzed Suzuki-Miyaura reactions. In the meantime, we have proved and quantified the effect of photocharging towards nanoparticle photocatalysis, as an underlying and often overlooked mechanism. We have built a proportional relation between accumulated charge and separate catalytic performance, which should deserve more attention in the future.

Furthermore, we have been exploring the possibility of using earth-abundant metals for sustainable photocatalysis and utilizing the intrinsic interband transitions in these metals to search for new catalytic properties. Combined with the electronic and band structure of Au, Pd, and Co metals, we have rationalized the interband transitions in the metal-adsorbate hybridized states of those three metals and confirmed the contribution of both interaction strength between metal and adsorbates and energy states of hot carriers from interband transitions to photocatalysis. And the cobalt-based metallic nanoparticle photocatalysts were proved to be a good candidate for designing better energy alignment between the *d*-band structure and interband transition than Au and Pd nanoparticles, which leads us to shift from noble to non-noble metallic nanoparticle photocatalyst and a sustainable future. Eventually, we have provided some future perspectives towards the design for non-noble-metal-based nanoparticle photocatalysts and related mechanistic insights of the hot-carrier behavior from interband transitions.

# Chapter 1 Photocatalysis of Metallic Nanoparticles: Interband vs. Plasmon

(This chapter covers similar materials as in a submitted manuscript to *Nanoscale* as an invited Review article. Reproduced with permission, copyright © 2023 Authors and Royal Society of Chemistry.)

## 1.1 Introduction

### 1.1.1 Historical view of plasmon

Light-matter interaction has been always a tremendously attractive and fascinating topic in lots of different areas, including modern spectroscopy, lasers, X-ray sources, light-emitting diodes, photodiodes, solar cells, high-energy particle detectors and advanced microscopy methods.<sup>1</sup> Tracing back to 1902, R.W. Wood discovered a pattern of unusual thin dark bands in the diffraction spectrum by an optical metallic diffraction grating and could not provide any interpretation at that time, so-called “singular anomalies”.<sup>2</sup> This led to the discovery of surface plasmon polariton and R.W. Wood was regarded as the initiator of plasmonics. After systematic study of plasma by Irving Langmuir in the 1920s,<sup>3</sup> the concept of plasmon, defined as the collective electron oscillations or plasma oscillation (the nature of charge density wave), was initially proposed in 1952 by David Pines and David Bohm.<sup>4</sup> Only a few years later, surface plasmon was first predicted by Rufus Ritchie in 1957,<sup>5</sup> and extensively developed theoretically and experimentally by many other scientists including T. Turbadar, E. N. Economou, Heinz Raether, E. Kretschmann, and A. Otto.<sup>6</sup> Surface plasmon, coherent non-propagating collective oscillations of electrons at the surfaces of bulk metals, was further studied under the framework of light-matter interaction, giving two new phenomena: surface plasmon polariton at the planar interface and localized surface plasmon at nanoparticle surface.<sup>7</sup> From the 1980s, the localized surface plasmon resonance, coherently oscillating of the driving electric field and conduction electrons in a sub-wavelength metallic nanoparticle, was brought to the stage and various kinds of areas were exploited including plasmonics, photonics and electronics.<sup>8</sup> The timeline of plasmon development was listed in Figure 1.1.

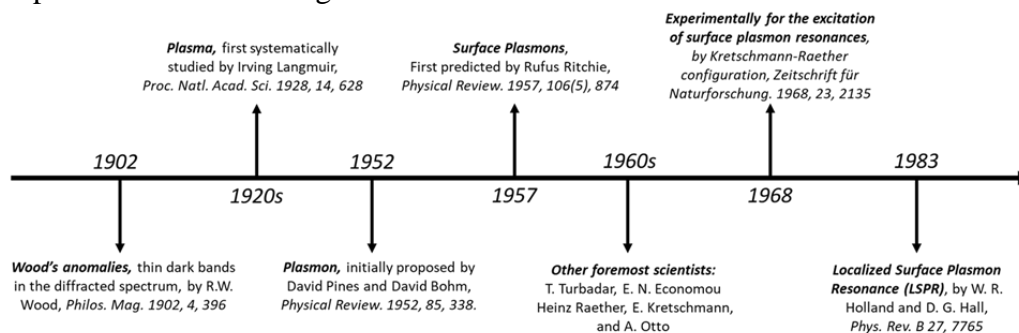
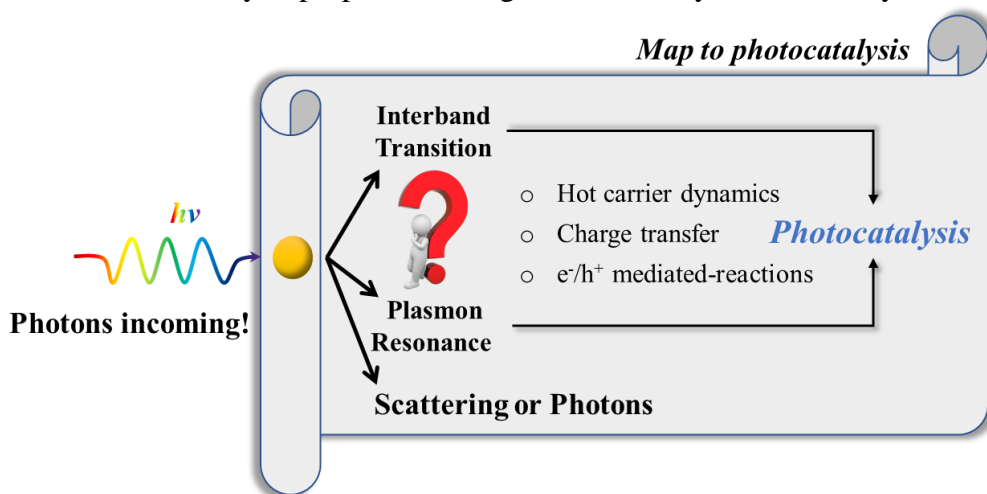


Figure 1.1 Milestones of plasmon research.

### 1.1.2 Overview of metallic nanoparticles for catalysis

Metals, as excellent electron reservoirs, are capable of donating or accepting electrons for facilitating chemical transformations. They have been used as heterogeneous catalysts

for decades, and their nanocrystals have recently gained more attention for improving the catalytic properties of the bulk or molecular versions.<sup>9, 10</sup> In general, metallic nanocrystals offer better catalytic activities and selectivities than the bulk versions due to their higher active sites per volume and more well-defined crystal facets. On the other hand, the nanocrystals are more robust than molecular catalysts and suitable for multicycle operation or integrating with other supporting substrates. Metallic nanocrystals were initially used in photocatalysis when they were loaded on TiO<sub>2</sub> as co-catalysts.<sup>11</sup> Since then, heterojunctions of metal and semiconductor nanocrystals have been used extensively for photocatalysis.<sup>12</sup> These heterojunctions have been mostly prepared by precipitation or impregnation of metal nanocrystals on supporting metal oxide nanocrystals. As a result, the metal nanocrystals have poor uniformities of size and shape, and consequently ill-defined catalytic sites. These factors create challenge on quantifying the relationship between the structure and the catalytic properties.<sup>13</sup> Recently, the development of colloidal synthesis has allowed us to create high quality metallic nanocrystals with high levels of controlling size, shape, crystal facet, uniformity, and surface functionalization.<sup>14-16</sup> This advancement in preparing nanocrystals now provides us an unprecedented opportunity to study and tune their catalytic properties with greater accuracy and reliability.



**Scheme 1.1** Overview of photocatalysis by metallic nanoparticles. From photon adsorption (interband transition or plasmon resonance) to hot-carrier-mediated photocatalytic reactions, different pathways may provide different physical pictures and mechanistic interpretations.

When studying photocatalytic mechanism of metallic nanocrystals, we have been relied on the well-known photo-physics of bulk metals and metal surfaces.<sup>17-19</sup> This is largely because we treat the nanocrystals as solids, and their electronic states are considered as continuous and metal-liked as long as their size is larger than few nanometers.<sup>20, 21</sup> As we will discuss in this review, the photo-physics of bulk metals cannot always be transferred to metallic nanocrystals due to many influenced factors evolving size, dimension, and shape of the nanocrystals. Among them, the most distinct properties of metallic nanocrystals form their bulk versions are the optical tunability and the corresponding photogenerated hot carriers. The two common optical regimes are localized surface



plasmon resonance (plasmon resonance for short) and interband transitions, and they generally can be selected by choosing suitable wavelengths of the absorbed photons. The application of the plasmon resonance for photocatalysis have been demonstrated for more than a decade and reviewed thoroughly in recent literature.<sup>22-27</sup> However, recent attention on utilizing interband transitions for photocatalyst has brought some promising results.<sup>28-32</sup> In fact, interband transitions has demonstrated better catalysis than plasmon resonance in many reactions.<sup>28-30, 32-34</sup> The purpose of this review is having a comprehensive understanding of fundamental steps in photocatalysis induced by these two optical regimes. The energy levels, populations, dynamics, and heating effect of the corresponding hot carriers, as well as the following charge transfer, catalytic pathway, and reaction kinetics will be discussed (see Scheme 1). We hope that these considerations will help to develop better metal-nanocrystal based photocatalysts.

### 1.1.3 Metallic nanocrystal photocatalysts: Pros and Cons

For decades, metallic nanocrystals have demonstrated their potential for photocatalyzing various chemical reactions.<sup>32, 35-37</sup> Regardless of the advantages and disadvantages as compared the well-known molecular<sup>38-43</sup> and semiconductor photocatalysts<sup>44-47</sup>, metallic nanocrystals have contributed significantly to the photocatalysis toolbox, and their photocatalytic properties are still relative new for further exploration. Their merits and demerits as compared to other common photocatalysts are presented in Table 1.1. It is important to note that each kind of photocatalysts has its own advantages and disadvantages. There is no champion among them. For example, the metallic nanocrystals have a higher recyclability than the molecular catalysts, but their most interior atoms do not participate in the photocatalysis, making the nanocrystals still less economical than the molecular catalysts in term of utilizing materials down to atomic levels. On the other note, metallic nanocrystals have no band gap, and the energy levels of photogenerated hot carriers can be tuned, eventually the catalytic activities can be tuned by light. The semiconductor photocatalysts, however, have band gaps. Thus, the energy levels of the electron and holes are confined to the conduction and valence bend and cannot be turned by light.

**Table 1.1** Compared photocatalytic properties of metallic nanoparticles to other common photocatalysts.

	Metallic NP	Molecule	Semiconductor NP
Pros	<ul style="list-style-type: none"> <li>• Tunable light absorption</li> <li>• Continuous electronic states</li> <li>• Hot carrier-induced catalysis</li> <li>• Nearfield-induced catalysis</li> <li>• High recyclability</li> </ul>	<ul style="list-style-type: none"> <li>• Better quantum yield</li> <li>• Metal-atom economy</li> <li>• Clear active site and catalytic mechanisms</li> <li>• Tunable selectivity</li> <li>• Longer lifetime for excited states</li> </ul>	<ul style="list-style-type: none"> <li>• Adjustable energy band alignment to reaction</li> <li>• Long lifetime excitons</li> <li>• Easy to recycle</li> </ul>

Cons	○ Low quantum yield	○ High recyclability ○ Poor stability	○ Band-gap limitation for photon absorption ○ Low quantum yield
	○ Capping ligands hinder catalytic activity		
	○ Interior atoms were not used efficiently		

---

#### 1.1.4 Interband vs. Plasmon driven mechanisms: Concerns and opportunities

Once the photon is adsorbed by the metallic nanoparticles, the first and most important step towards further catalysis is the photoexcitation pathway including plasmon resonance and interband transition. Currently, photocatalysis induced by plasmon resonance of metallic nanoparticles has proven to be able to catalyze a wide range of chemical transformations and the mechanisms involved have been profoundly studied.<sup>26, 48-52</sup> In contrast, much less has been reported for interband transition-based photocatalysis.<sup>32, 34, 53, 54</sup> This lack of attention should be addressed considering that many common noble metallic nanoparticles have spectral overlap between interband transitions and plasmon resonance. Since these two regimes of photoexcitation generate hot carriers with different energy and dynamics, it is important to take a careful investigation of these two processes in the corresponding photocatalysis.

In this review, we will systematically compare the plasmon resonance and interband transition of metallic nanoparticles in terms of photoexcitation, hot carrier-mediated reactions and mechanisms, with emphasis on the interband transitions that have less been reviewed in the photocatalysis community. We will start on the physical pictures of interband transition and plasmon resonance, focus on the properties of hot carriers generated from these two excitations and build a clear link of charge transfer in metallic nanoparticles for chemical reactions. Next, we will summarize the photocatalyzed reactions driven by hot electrons and hot holes separately, with a slight touch upon the descriptors for photocatalysis efficiency. Then, we will dig into different photocatalytic mechanisms involved in metallic nanoparticles' catalysis and build a comprehensive view of the interband transition and plasmon resonance. Finally, we will provide some future perspectives on how to utilize our understanding of those two excitations to improve the photocatalysis of metallic nanoparticles fundamentally and practically.

## 1.2 Photoexcitation of metallic nanoparticles

### 1.2.1 Physical picture of photoexcitation

In a nutshell, the plasmon resonance can be described by a classical picture as a collective oscillation of the nanoparticles' electrons in response to the electric field of exciting photons or a quantum mechanical picture as electron transitions from some *sp*-band states to other *sp*-band states (*i.e.* intraband transitions), while the interband transitions are given to electron transitions from the respective *d* to *sp* bands (Figures 1.2A and 1.2B).<sup>32</sup> Due to these origins, the plasmon resonance of metal nanoparticles offers strong optical absorption and tunable spectral shift depending on the particle morphology, but the interband transitions always provide a significant absorption within a defined spectral region. Moreover, plasmon resonance can promote the hot electrons to a higher energy state and leave the hot holes near the Fermi level ( $E_F$ ), while the interband transitions only promote the hot electrons near the  $E_F$  and leave the hot holes deep in the

*d*-band states. This fundamental difference plays a pivotal role in the following charge transfer and photocatalytic reactions.

Specifically, the interband transitions produce the non-equilibrium excited carriers with uniform angular distribution and the holes in the *d*-shell with large effective mass thus high potential energy but small kinetic energy and short mean free path (Figure 1.2C).<sup>19, 55</sup> In this case, the hot holes may afford a better chance of traveling and participating in the chemical reactions, compared to the hot electrons merge into the Fermi level. On the other hand, three different mechanisms are involved in the intraband excitation within the conduction *s*-band, such as phonon (or impurity)-assisted transition, EE Umklapp scattering-assisted transition, and Landau damping or surface collision-assisted “tilted” transition.<sup>19, 55</sup> The first and third ones are far more likely to generate sufficient high-energy electrons to overcome the surface (Schottky) barrier to be injected into adjacent absorbates or semiconductors. In this case, the hot electrons may take the lead for further reactions.

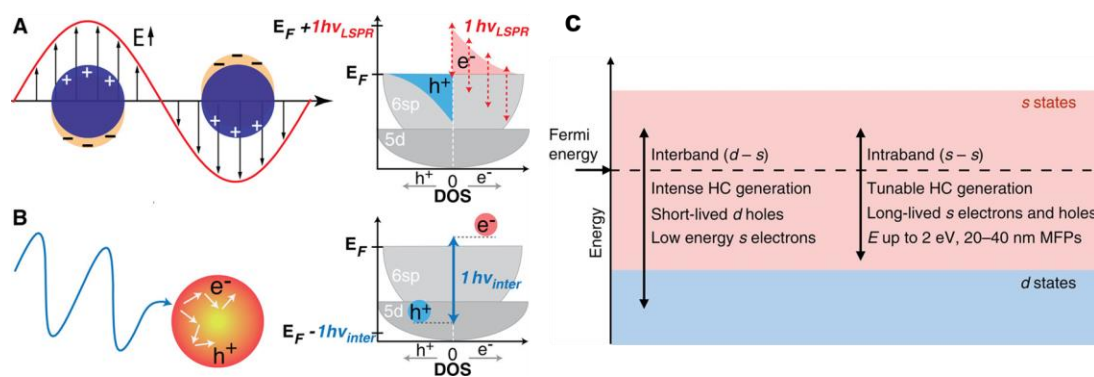


**Figure 1.2** Physical pictures and comparisons of plasmon resonance and interband transition. (A) A classical picture of collective electrons oscillation driven by plasmon resonance (represented as LSPR here). The plasmon decay into hot carriers follows a Fermi-Dirac distribution at different energies, in which the highest energy of hot electrons (red area) can reach one absorbed energy higher than the Fermi level ( $E_F$ ) but the hot holes (blue) reside near the  $E_F$  in *sp* band. A quantum mechanical picture describes the LSPR as a superposition of multiple isoenergetic, single-electron transitions when one photon is absorbed. This excitation is also regarded as the intraband transition since the hot electrons and holes are both in the *sp* bands. (B) Interband transition directly generates a pair of electron-hole ( $e^-$ - $h^+$ ) from adsorption of a higher energy photon, in which the hot electrons (red) are promoted to just above  $E_F$  and hot holes reside deep in the *d* band. (C) Comparison of interband transition and plasmon resonance (represented as intraband here) includes hot carrier (abbreviated as HC)’s generation intensity, lifetime, and energy states. A and B were adapted with permission from ref. 32, Open Access and Copyright © 2017 American Chemical Society and C from ref 55, Open Access and Copyright © 2015, The Author(s) and Springer Nature.

### 1.2.2 Photo-generated hot carriers and their properties

The optical excitations in the plasmon resonance or interband transition regime are expected to generate hot carriers with different energy states, populations, and dynamics,

in which different relaxation (or decay) processes are involved. Govorov and co-workers provided a theoretical perspective on the generation rates and the energy distributions of hot electrons in nanocrystals with various geometries in both quantum and classical mechanisms (Figures 1.3A and 1.3B).<sup>56</sup> In their theory, three main channels including classical Drude friction-like dissipation, interband transitions, and hot electrons' generation contribute to the plasmonic decay (Figure 1.3A). The rate of these processes along with scattering events of the hot electrons are well discussed numerically and analytically by Atwater,<sup>57</sup> Nordlander,<sup>58</sup> Khurgin<sup>59</sup>, and their co-workers. As for the energy distribution (Figure 1.3B), plasmon resonance would produce energetic hot carriers falling into the range between  $E_F + \hbar\omega$  (for hot electrons) and  $E_F - \hbar\omega$  (for hot holes), following the Fermi-Dirac distribution via electron-electron scattering.<sup>60</sup> In contrast, interband transition only produces hot electrons near the Fermi level (lower energy compared to the plasmon resonance) but energetic hot holes down to  $E_F - \hbar\omega$  (similar energy to the maximum from plasmon resonance but with larger distribution). The energy distribution of hot carriers from interband transitions depends on the intrinsic electronic and band structure of different metals, as predicted by Atwater and co-workers.<sup>61</sup> Those properties will play decisive roles in the following catalytic process and will be discussed in later sections.

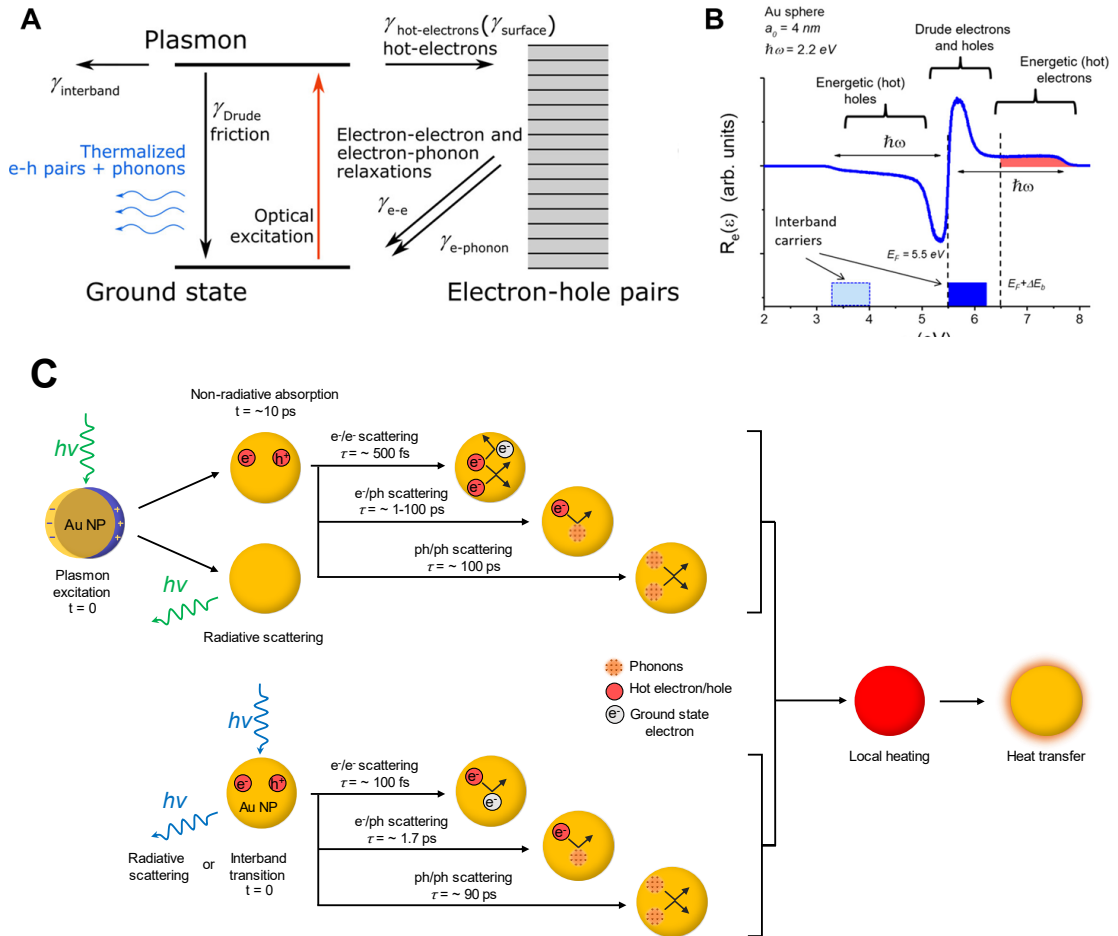


**Figure 1.3** Hot carriers' generation and properties from interband transition and plasmon resonance. (A) Plasmon decay into hot or thermalized electron-hole pairs or other scattering and relaxation processes. The symbol " $\gamma$ " represents the rate of each relaxation process. (B) Typical spectrum for the rate of carrier generation ( $R_e(\epsilon)$ ). Two different types of excited carriers including energetic (hot) and drude electron/holes are observed from plasmon resonance. One type of carrier is from the interband transition in blue regions. (C) Timescale demonstration of plasmon excitation, absorption or scattering, and relaxation for plasmon resonance and interband transition. A and B were adapted with permission from ref. 56, Copyright © 2017 American Chemical Society. Part of C was adapted with permission from ref. 50, Copyright © 2021, Springer Nature Limited.

After the generation of hot carriers, the dynamics of hot carriers including lifetime and mean free path are also critical before considering the utilization of these hot carriers. Once excited via plasmon resonance (Figure 1.3C), the metallic nanoparticles would undergo either non-radiative absorption to generate  $e^-h^+$  pairs or radiative scattering to re-emit the photons in the timescale of around 10 fs.<sup>50, 62</sup> The generation of hot carriers may last from 1-100 fs from different photon-electron interactions, in most case the Landau damping. This process is dependent on the size and shape of the nanoparticles as well as the wavelength of light (photon energy).<sup>63</sup> And the mean free path of these hot carriers varies from 10 to 20 nm for Au and 700 nm excitation depending on the relaxation pathways.<sup>19</sup> After that, the relaxation through  $e^-e^-$  scattering typically occurs around 500 fs and the  $e^-$ /phonon collisions lead to releasing thermal energy in a relatively long timescale up to a few hundreds of ps.<sup>62, 64</sup> On the other hand, for interband transition, the lifetime would be much shorter than the plasmon resonance since it is a direct momentum conserved transition and no other assistance needed.

For interband transitions, the mechanisms generating hot carriers and their initial energy states, and lifetimes vary to some degree from SPR intraband transitions. Excitation energies greater than the interband threshold of gold and copper ( $\sim 1.8$  eV) produce interband transitions dominated by  $d$  band hot holes with energies equal to or greater than the interband threshold.<sup>61, 65</sup> These transitions are instantaneous with far fewer hot carrier pairs from a single excitation. Therefore, the photon energy is distributed amongst fewer pairs of hot carriers, so the average energy per pair of hot carriers is greater energy than their SPR counterparts, most of it carried by the hole. The electron relaxation dynamics are similar to intraband transitions with hot carrier relaxations lifetimes of 1.7 ps for  $e^-$ -phonon,  $\sim 100$  fs for  $e^-e^-$ , and 90 ps for phonon-phonon scattering.<sup>65</sup> Keep in mind that these relaxation processes overlap, and these time constants vary depending on the excitation wavelength, where relaxation lifetimes are shorter when higher energy photons are used.<sup>66, 67</sup>

The time scale of these measurements, relying on the multiple-photon absorption under laser conditions rather than the single-photon event under photocatalytic reactions with continuous LED irradiation.

### 1.2.3 Charge transfer for catalysis

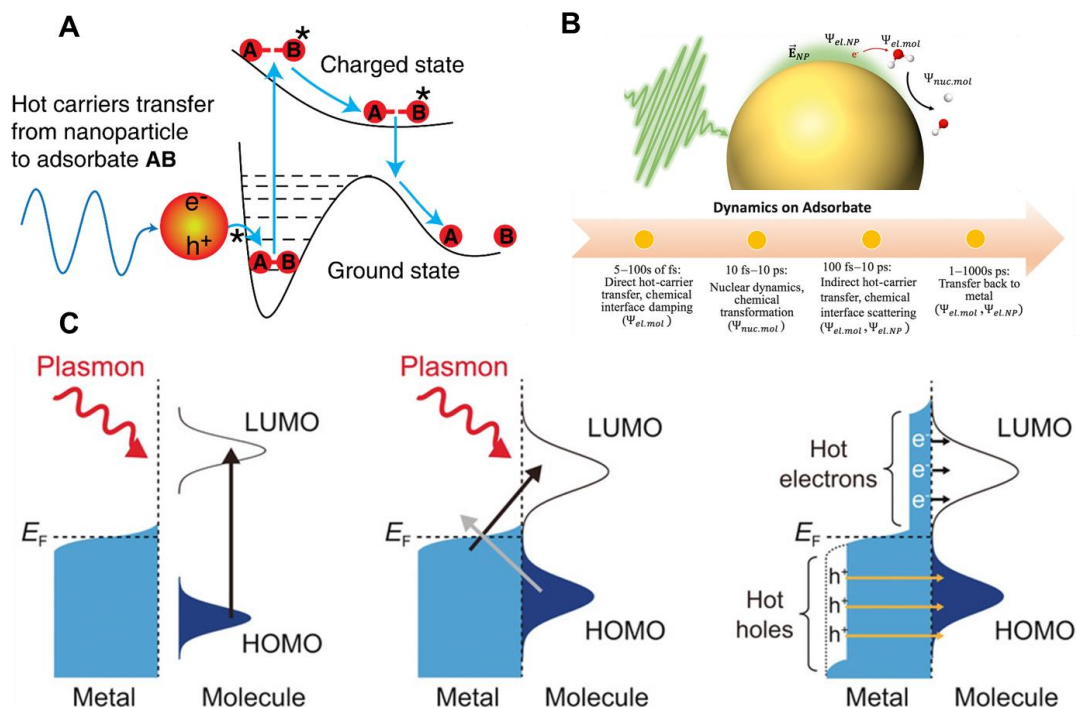


**Figure 1.4** Pathways and dynamics of charge transfer from metallic nanoparticles to adsorbates for photocatalysis. (A) Hot carriers transfer to the adsorbates and bring the adsorbates to charged or electronically excited potential energy surface (PES). The chemical bonds dissociate after the relaxation to a low-lying PES. (B) Hot carrier's dynamics for adsorbates on metallic nanoparticles including timescales and key quantities involved in each process.  $\Psi$  represents for wavefunction or degrees of freedom of nanoparticles (NP) or molecules (mol), el for electronic and nuc for nuclear. (C) Photoexcitation pathways to induce chemical reactions including direct intramolecular excitation, direct excitation of hybridized meta-adsorbate states, and charge transfer to corresponding molecular orbitals of adsorbates. B was adapted with permission from ref. 71, Copyright © 2020, The Materials Research Society and C from ref. 72, Copyright © 2020 Wiley-VCH Verlag GmbH & Co. KGaA, Weinheim.

Hot carriers generated from plasmon resonance or interband transitions may undergo different dynamics in a very short time scale inside metallic nanoparticles themselves, however when adsorbates are involved, an energy or charge transfer process may occur and drive chemical transformations at the surface. Several energy and charge transfer mechanisms have been proposed, for example, the hot carriers generated from optical excitations can transfer from nanoparticles to adsorbates (or reactants) and promote the adsorbates to charged or electronically excited potential energy surface (PES). The adsorbates then can relax to the low-lying potential energy surfaces in which chemical bonds can be dissociated later (Figure 1.4A). These energetic hot carriers may offer a new pathway to lower the activation energy barrier ( $E_a$ ) as described in the conventional thermally-driven reactions and the experimental features of these comparisons were well discussed.<sup>36</sup> Noting that this mechanism of desorption induced by electronic transitions

(DIET) for bond activation was initially stimulated by irradiating a solid surface<sup>68</sup> and expanded to the plasmon community.<sup>36, 69, 70</sup> However, it remains unclear whether the interband transitions would follow the exact same pathway, which requires more attention in this field to push it forward.

As for the comparison of hot carriers' dynamics on metallic nanoparticles or at the metal-adsorbate interface, a slightly longer timescale of the dynamic on adsorbate was observed through theoretical simulation and experimental characterizations (Figure 1.4B).<sup>71</sup> And those timescales are also closely related to specific photoexcitation pathways including direct intramolecular excitation, direct excitation of hybridized metal-adsorbate states, and charge transfer directly or indirectly to corresponding molecular orbitals of adsorbates (Figure 1.4C).<sup>72, 73</sup> Typically, direct excitation either intramolecularly or via hybridized metal-adsorbate states requires a suitable orbital overlap with strong interaction between metal and adsorbate, which may achieve higher energy efficiency but normally needs delicate systematic design of the interface.<sup>74</sup> On the other hand, the direct hot-carrier transfer via chemical interface damping (CID) or indirect hot-carrier transfer via chemical interface scattering (CIS) through an inelastic tunnelling process, are broadly demonstrated in various reaction conditions but suffer a significant energy loss due to scattering in the indirect pathway.<sup>75</sup> It is worth noting that most of these mechanisms start from the plasmon resonance and focus on the hot-electron transfer process, and multiple excitation pathways may occur in the same system, and some other effects including electromagnetic field enhancement and photo-thermal effect may complicate the system. Besides, few reports have mentioned the hot-hole transfer and the role of these holes in catalysis,<sup>76, 77</sup> which is essentially critical in interband transition related photocatalysis.

### **1.3 Photocatalyzed reactions driven by hot carriers**

Despite there being continuing debates about whether and how the hot carriers are involved in the catalytic process<sup>78-80</sup> and very little concrete experimental evidence can prove various mechanisms directly<sup>81</sup>, lots of practical chemical reactions have been demonstrated feasible by hot carriers generated from metallic nanoparticles. In this section, we will focus on presenting different types of photocatalytic reactions with metallic nanoparticles, mainly driven by hot electrons or hot holes.

#### **1.3.1 Hot electron-mediated reactions**

Hot electrons generated from plasmon resonance decay with higher energy above the Fermi level can be transferred to the unoccupied electronic states of the adsorbates to facilitate the bond activation before they are all dissipated with hot holes or phonons into heat. On the other hand, the hot electrons from interband transition remain near the Fermi level with lower energy, which still has the chance for electron transfer but with limited efficiency and under specific conditions. Thus, in this part, we will briefly summarize some of the hot-electron-mediated photocatalytic reactions mainly from plasmon resonance of metallic nanoparticles, since this topic has already been thoroughly reviewed by Wei's group,<sup>82</sup> Moores's group,<sup>26</sup> Moskovits' and Tian's group,<sup>83</sup> Xu' and Nam's group<sup>84</sup>.

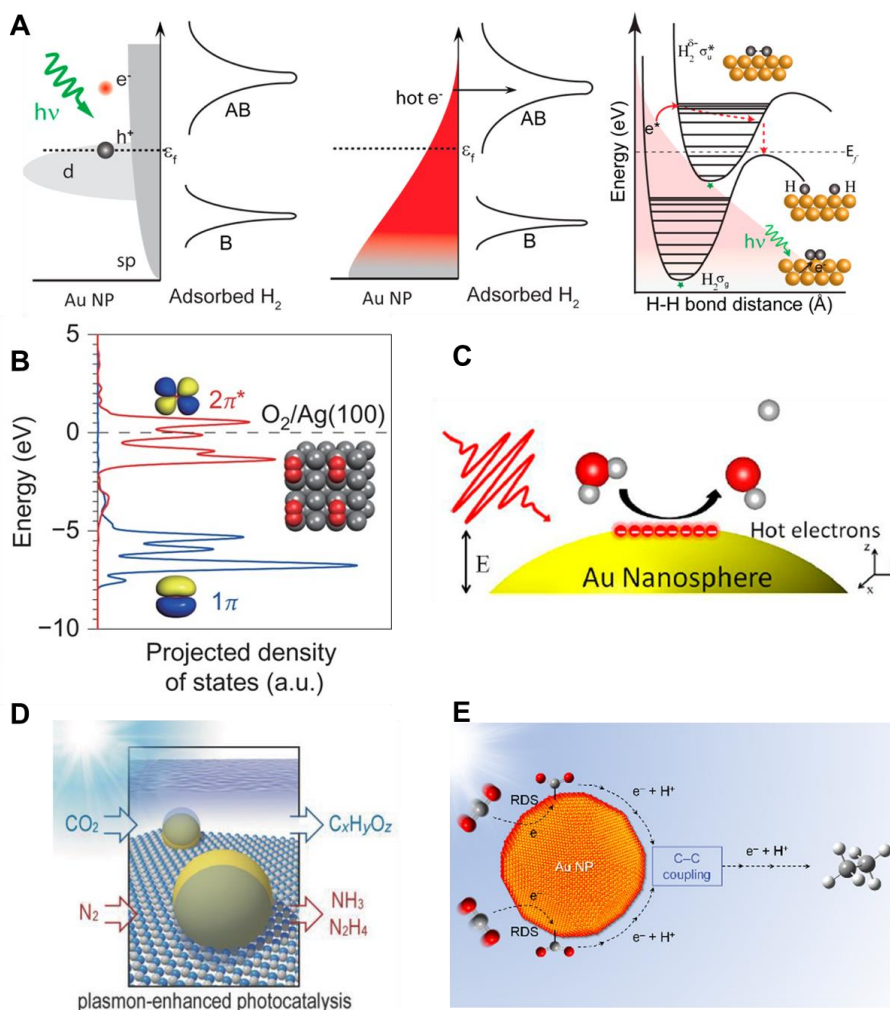


**Figure 1.5** Hot electron-mediated photocatalytic reactions. (A) H<sub>2</sub> dissociation on Au NP: d-band electron-hole pair generated after plasmon decay, Fermi-Dirac distribution of hot electrons transferring into the antibonding state of H<sub>2</sub>, and proposed mechanism. (B) O<sub>2</sub> dissociation on Ag(100): Molecular density of states projected on adsorbed O<sub>2</sub>. (C) H<sub>2</sub>O splitting on Au nanosphere. (D) CO<sub>2</sub> reduction and N<sub>2</sub> fixation by plasmon-enhanced photocatalysis. (E) CO<sub>2</sub> reduction to hydrocarbons by the multi-electron and multiphoton process. A was adapted with permission from ref. 85, Copyright © 2013, American Chemical Society, B from ref. 69, Copyright © 2011, Nature Publishing Group, C from ref. 86, Copyright © 2016, American Chemical Society, D from ref. 90, © 2018 WILEY-VCH Verlag GmbH & Co. KGaA, Weinheim and E from ref. 91, Copyright © 2018, American Chemical Society.

In early reports, proof-of-concept experiments about hot electron-mediated reactions were demonstrated by small-molecule activation on metallic nanoparticles, including H<sub>2</sub>/O<sub>2</sub> dissociation, H<sub>2</sub>O splitting, and CO<sub>2</sub>/CH<sub>4</sub>/N<sub>2</sub> activation. Nordlander's and Halas's groups reported the Room-temperature dissociation of H<sub>2</sub> on gold nanoparticles, which was triggered by hot electrons from plasmon resonance and detected by the formation of HD



molecules from H<sub>2</sub> and D<sub>2</sub> (Figure 1.5A).<sup>85</sup> Combined with DFT calculation, they proposed the mechanism that hot electron transferred from Au NP to the antibonding  $1\sigma_u^*$  state of an adsorbed H<sub>2</sub> molecule and then reduced the dissociation energy barrier (Figure 1.5A). Similarly, Linic's group demonstrated energetic hot electrons could transfer to antibonding orbitals of the O<sub>2</sub> molecule and then form a transient negative-ion state, followed by facilitating the rate-limiting O<sub>2</sub>-dissociation reaction (ethylene epoxidation) (Figure 1.5B).<sup>69</sup> Also, theoretical simulations suggested that with manipulation of the energy level of plasmon-induced hot carriers and adsorbates' unpopulated states, H<sub>2</sub>O splitting could be achieved on gold nanoparticles (Figure 1.5C).<sup>86</sup> This concept was then realized in different experimental setups<sup>87, 88</sup> and expanded to other plasmonic metallic nanoparticles or hybrid nanostructures<sup>89</sup>. Furthermore, the hot electron-mediated process was applied to more sophisticated reactions, including CO<sub>2</sub> reduction and N<sub>2</sub> fixation into high-value products, which was already discussed thoroughly by Jiang's and Wang's group (Figure 1.5D).<sup>90</sup> Due to the highly-stable nature of these molecules, much more effect needs to be done including designing better adsorption and active sites for those molecules, energy alignment of different metallic nanoparticles or hybrid structures, and selectivity toward specific products. Recently, Jain's group reported the plasmonic control of different hydrocarbon products (methane or ethane) by changing the light excitation characteristics such as interband transition or plasmon resonance pathways (Figure 1.5E).<sup>91</sup> And they further developed a rich catalog of different CO<sub>2</sub> photocatalytic reduction products with plasmonic Ag nanoparticles.<sup>92</sup> Another large portion of the reactions mediated by hot electrons are organic transformations on metallic nanoparticles, which is thoroughly reviewed by previous reports.<sup>26, 84</sup> The general idea is to integrate the hot electrons generated from metallic nanoparticles into the traditional catalytic cycle and find the critical role of these hot electrons, in which the specific mechanisms in different reactions may vary from each other. The ideal goal is to enhance the reaction rates or lower the reaction temperature from photon energy and improve the selectivity by controlling the reaction pathway with hot electrons.

Overall, the hot electrons generated from plasmon resonance in metallic nanoparticles are proved to be useful in various reduction reactions, however in different systems, specific designs or conditions may be needed to fulfill the best performance. It will cost much more effort to investigate the photocatalytic mechanism behind each reaction, which will be discussed in Section 4. Another issue here is that the underestimation or oversight of interband transitions (intrinsic and not dependent on size or shape) in these reactions may lead to an incomplete picture of the whole reaction process, which deserves more attention now.

### 1.3.2 Hot hole-mediated reactions

Hot carriers generated either from plasmon resonance or interband transition after decay are normally in a pair from including hot electrons and hot holes. While the hot electrons have been proved useful in those reduction reactions above, the hot hole-mediated reaction emerges into our sight just recently and deserves more attention.<sup>54, 76, 77</sup> Traditionally, hot holes generated from plasmon resonance can participate in the metal etching,<sup>33</sup> organic transformations,<sup>93-95</sup> polymerization,<sup>96</sup> and oxygen evolution reactions<sup>97</sup>. On the other hand, the deep holes generated from interband transitions should be better

candidates for oxidation reactions in theory, which has been overlooked and just been picked up and proved by our group.<sup>34, 53, 54</sup> In this part, we will focus on hot-hole mediated reactions, especially those deep holes from interband transitions, which will provide us with a different perspective and help us complete the whole picture of hot holes.

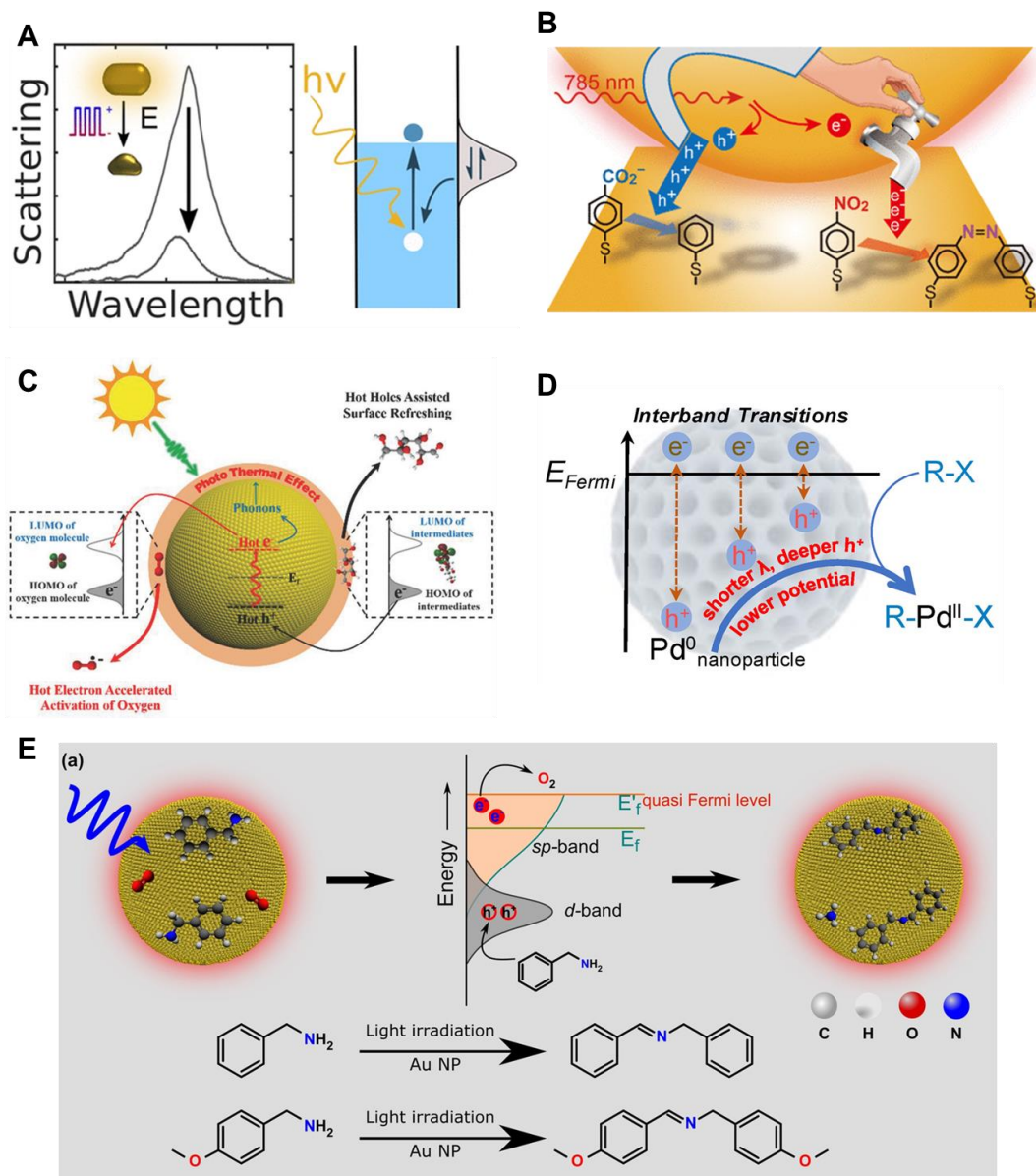


**Figure 1.6** Hot hole-mediated photocatalytic reactions. (A) Metal dissolution: enhance the rate of gold oxidation and subsequent electrodisolution. (B) Organic transformation: 4-mercaptobenzoic acid (MBA) decarboxylation to benzenethiol (BT) by plasmon-induced hole transfer. (C) Organic oxidation: benzylamine oxidation via a reactive iminium intermediate. (D) Organic coupling reaction: deeper holes from shorter-wavelength excitation in interband transitions producing a higher quantum yield of Suzuki-Miyaura reaction. (E) Organic oxidation: benzylamine oxidation to N-benzylidenebenzylamine (imine) by hot carriers. A was adapted with permission from ref. 33, Copyright © 2019,

American Chemical Society, B from ref. 93, Copyright © 2020, American Chemical Society, C from ref. 94, Copyright © 2018 WILEY-VCH Verlag GmbH & Co. KGaA, Weinheim, D from ref. 54, Copyright © 2022 The Authors (Open Access) and E from ref. 95, Copyright © 2021 Wiley-VCH GmbH.

Starting with the hot holes generated from plasmon resonance, Link's and Landes's groups demonstrated oxidative dissolution rate of individual Au nanorods was enhanced by plasmonic hot holes from photoexcitation and observed the process with millisecond resolution by snapshot hyperspectral imaging (Figure 1.6A).<sup>33</sup> Interestingly, they also compared the rate under plasmon resonance and interband transition and conclude that the d-band holes from interband transition were more efficiently than those holes from plasmon resonance for this dissolution,<sup>33</sup> which was consistent with previous reports by Alivisatos's and Somorjai's groups,<sup>32</sup> and Jain's group<sup>35</sup>. Later on, Yoon's group found out that both electron- and hole- transfer channels were critical for the reduction of 4-nitrobenzenethiol at the nanogaps between Au NPs and Au films, in which the hot hole promoted the decarboxylation of 4-mercaptobenzoic acid as the plasmonic switch (Figure 1.6B).<sup>93</sup> In the meantime, Zhang's and Li's groups revealed that during the glucose oxidation to glucose acid, the hot holes could assist the refreshing or reactivating the Au NPs' surface by favoring the oxidation and desorption of catalytic intermediates by DFT theoretical calculation and X-ray absorption spectrum analysis, while the hot electrons were responsible for the activation of oxygen molecules (Figure 1.6C).<sup>94</sup> Similar concept was also reported by Rao's group in the oxidative coupling of benzylamine into imine by photo-excited Au nanoparticles (Figure 1.6E).<sup>95</sup>

However, in above research, there are a few parameters that are missing (which are essential!) including the spectral overlap between plasmon resonance and interband transition, accurate evaluation of photocatalysis efficiency (see more in the next section), and quantitative analysis of the role of hot holes in reaction. For example, the spectra overlap would cause different energy distributions and temporal or spatial scales of hot carriers, which makes it hard to distinguish the contribution to catalysis between plasmon resonance and interband transitions. With those careful details in mind, our group has developed some rigorous model reactions to evaluate the size-dependent photocatalytic activity of gold nanoparticles<sup>34</sup> and tune the redox potential of these nanoparticles through photo-excitation<sup>53</sup>. Furthermore, we introduced the mesoporous structure into metallic nanoparticles to disentangle the spectral overlap and assigned interband transitions exclusively to the contribution of hot holes to photocatalytic activities (Figure 1.6D).<sup>54</sup> It was found that the deeper holes from shorter wavelength's excitation with stronger oxidation power could catalyze oxidation addition of aryl halide onto the Pd surface (the rate-determining step) of Suzuki-Miyaura reaction better, thus offering a higher quantum yield.<sup>54</sup> Indeed, this insight helps us complete the picture of hot hole-mediated reaction by either photo-excitations and guides us better design the catalytic reaction based on specific system. Still, the direct observation or evidence of hot holes-mediated reaction is not fully ripened out and further ultrafast and ultrafine techniques are needed to be utilized for this direction, especially in interband transition region.

### 1.3.3 Descriptors of photocatalysis efficiency

With the development of numerous photocatalyzed reactions mediated by hot carriers, there are still ongoing debates and an urgent need for the community to find a decent or standardized method to compare the efficiency of different photocatalysts. In traditional thermal catalysis, the TOF (turnover frequency) value has been well-recognized as a good descriptor for the catalytic activity, but still with a hard time finding the exact active sites, especially in heterogeneous catalysis.<sup>98</sup> When it comes to photocatalysis, it becomes even harder to define the specific active sites for the photo-excited process and the addition of photon adsorption for hot carriers is not only simply added on top of the traditional catalytic cycle. As discussed and recommended by the International Union of Pure and Applied Chemistry (IUPAC),<sup>99</sup> the quantum yield (QY), defined as the ratio of the number of product molecules to the number of absorbed photons, should be a better descriptor than the turnover frequency or apparent quantum efficiency (AQE) (Figure 1.7A). The AQE is a less accurate but still appropriate descriptor when the adsorbed photons are hard to quantify due to the unknown scattering-to-adsorption ratio of some solid catalysts, and the incident power can be accurately measured across different conditions.<sup>100</sup> Another perspective is to introduce the rate constants for the comparison, however, it only applies to some certain reaction systems with identical irradiation conditions, which is difficult to achieve.<sup>101</sup> Overall, the quantum yield has been demonstrated as a better descriptor for comparing photon utilization efficiency across different photocatalysts and systems, but still with lots of experimental details to be considered.

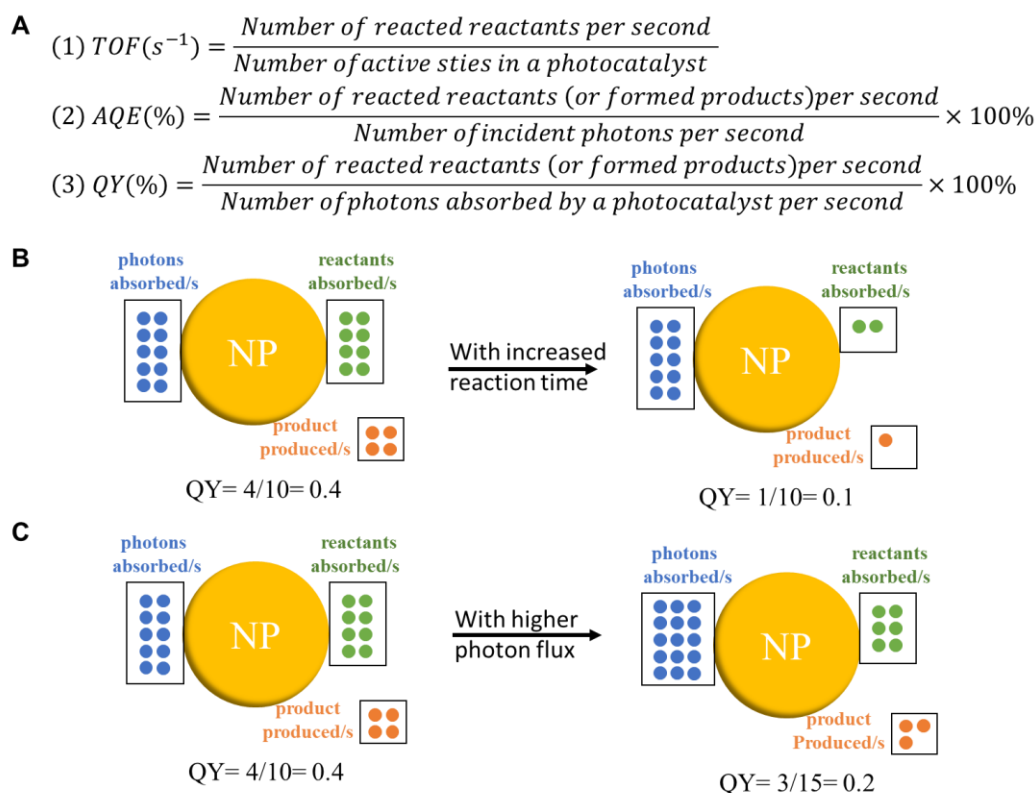


**Figure 1.7** Quantifying the efficiency of photocatalysts. (A) Descriptors for photocatalysis efficiency including turnover frequency (TOF), apparent quantum efficiency (AQE), and

quantum yield (QY). (B, C) Representative scheme for factors that would affect the quantum yield of the photocatalysts, including reaction time and photon flux.

Taking a closer look at the definition of quantum yield above, two critical parameters should be addressed including the reaction time and photon flux, which essentially affects how the photons are involved in the reaction in a timely manner.<sup>54</sup> An important note is that up to this point, the traditional factors that may affect the catalytic performance have already been controlled as the same when talking about those two effects, such as the size and shape of the catalysts, amount of catalysts in the system and so on. The simplified scheme of how reaction time and photon flux impact on the quantum yield is shown in Figures 1.7B and 1.7C respectively, which was demonstrated experimentally in our previous publication.<sup>54</sup> As the photon flux is fixed at the same level (meaning the adsorbed photons per second by the photocatalysts are the same), as the reaction time increases the reactants adsorbed on the nanoparticles' surface would be decreased, thus it makes the quantum yield decreases along with the reaction time (Figure 1.7B). The trend is indeed similar to the case of TOF under non-irradiation conditions.<sup>98, 102</sup> On the other hand, within the same reaction time, a higher photon flux could create more photo-excited nanoparticles thus more hot carriers involved in the reaction, then more reactants consumed and products formed and eventually the quantum yield decreased (Figure 1.7C). In short, keeping the same reaction time and photon flux is critical for evaluating the photocatalysis efficiency of metallic nanoparticles except for the same experimental conditions.

## **1.4 Photocatalysis mechanism in metallic nanoparticles**

As more and more photocatalytic reactions are being developed and various photocatalysts are involved in these reactions, it is of much importance and necessity to figure out the fundamental catalytic mechanism behind them, thus design better photocatalytic systems with higher photon utilization efficiency across the solar spectrum, especially in the visible range. In terms of metallic nanoparticles, plasmon resonance and interband transitions are the major optical responses in that range and related mechanisms will be discussed in this section, including some other mechanisms like field enhancement, photo-charging, and photo-thermal effects. We want to mention that in a real photocatalytic system, there may be more than one of these mechanisms or effects involved, and in this section, we will only try to clarify each effect in a specific model system and not distinguish or disentangle these in one system, and hopefully through these insights, we can achieve a comprehensive view of these mechanisms and use these to guide us understanding the complicated systems.

### **1.4.1 Plasmon Resonance**

As mentioned earlier, plasmon resonance can generate hot electrons much higher than the Fermi level and these energetic electrons can participate in the chemical reactions. When the metal surface and adsorbates interact with each other, the hybrid metal-adsorbate states are formed, and this process is very intuitive and helpful for our interpretation on a molecular level, however, is still without inconclusive experimental evidence to prove it. In a typical electron transfer process (Figures 1.8A and 1.8B), the hot electron can be either excited to empty states of metals and then transfer to the LUMO (lowest unoccupied molecular orbital) of metal-adsorbate hybrid states, which is called indirect electron

transfer. Or directly excited to the LUMO if the adsorbate has a strong interaction with the metal states via CID (chemical interface damping) named as direct electron transfer, which is reviewed by Christopher's group<sup>75</sup> and recently by Link's group<sup>103</sup>. Basically, these two electron transfer processes were well-studied both in the experimental and theoretical perspectives,<sup>82</sup> but in a specific system, the mismatch between the hot carriers' lifetime (up to nanosecond)<sup>48</sup> and the timescale of chemical reactions (in milliseconds)<sup>104</sup> indicates there may be other mechanism involved. Therefore, Christopher's group demonstrated the direct photoexcitation of targeted adsorbate-metal bonds of CO oxidation in a rich H<sub>2</sub> stream due to strong chemisorption hybridized bond formed between metal d-states and molecular adsorbate states (Figure 1.8C).<sup>105</sup> This concept was further developed in some other research,<sup>106,107</sup> however this process may need an exact match between photon energy and electronic transition energy of metal-adsorbate states which is hard to manipulate in different systems with different photocatalysts. Overall, since the plasmon resonance generates the energetic hot electrons, most catalytic mechanisms are involved in the electron transfer to some kind, which is in an approachable condition with current characterization techniques<sup>108</sup> and is within good interpretation with the experimental results.

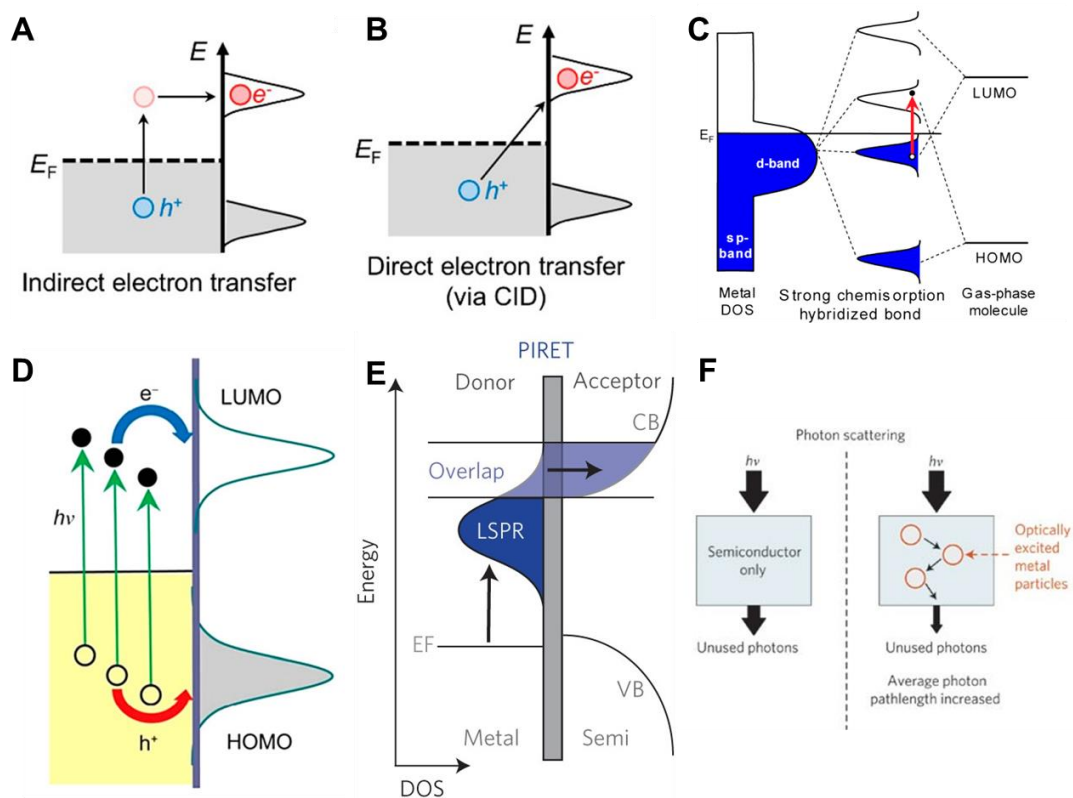


**Figure 1.8** Photocatalysis mechanisms from plasmon resonance. (A) Indirect electron transfer to the lowest unoccupied molecular orbitals (LUMOs) for adsorbates. (B) Direct electron transfer to LUMOs for adsorbates. (C) Direct photoexcitation of the hybridized substrate-adsorbate bond. (D) Hot hole transfer to highest occupied molecular orbitals (HOMOs) for adsorbates. (E) Plasmon-induced resonance energy transfer (PIRET) to adsorbates or semiconductors. (F) Photon scattering to increase the average photon

pathlength. A and B were adapted with permission from ref. 82, Copyright © 2017, American Chemical Society, C from ref. 105, Copyright © 2014, American Chemical Society, D from ref. 109, Copyright © 2015, Science China Press and Springer-Verlag Berlin Heidelberg and E from ref. 22, Copyright © 2011, Nature Publishing Group, a division of Macmillan Publishers Limited. All Rights Reserved.

Moreover, some other mechanisms in plasmon resonance are reported, which are still ongoing and will expand our knowledge of photocatalytic processes. For example, the hot holes left from the electron transfer process could also participate in the chemical reactions by transferring into the HOMO (highest occupied molecular orbital) of the metal-adsorbate states, thus promoting some oxidation reactions (Figure 1.8D).<sup>109, 110</sup> Recapping here that the hot holes generated from plasmon resonance reside near the Fermi level, which intrinsically are less energetic than the hot holes from interband transitions (see more in the next section) but still can catalyze the reactions. Another important category of plasmon resonance mechanism is the plasmon-induced resonance energy transfer (PIRET) from plasmonic metals to the adsorbates or mostly to semiconductors (Figure 1.8E).<sup>111</sup> This mechanism is similar to the Förster resonance energy transfer (FRET) in which the energy accumulated from localized surface plasmon resonance could transfer to the adsorbate, analogous to energy transfer between two chromophores via dipole-dipole coupling.<sup>112</sup> Noting that because this energy transfer mostly happens in the near field, thus there are very few reports covering the metal-adsorbate system and still in debates about how it contributes to the catalytic reactions.<sup>113, 114</sup> Last but not the least, with specific structure design, optically excited metallic nanoparticles by plasmon resonance can increase the average photon path length from the scattering multiple times of these adsorbed photons, eventually achieve higher photon utilization efficiency (Figure 1.8F).<sup>22</sup> This mechanism is critical when evaluating the quantum yield of the photocatalysts and provides a method for recycling or multiplying photons for better photocatalytic performance.

To be concluded, the plasmon resonance can generate energetic hot electrons through optical adsorption, thus the electron transfer mechanism dominates the photocatalytic mechanisms involved, eventually making it more suitable for the reduction reactions. Up to this point, we have made a comprehensive review of physical properties, mechanistic interpretation, and related photocatalytic reactions of plasmon resonance in metallic nanoparticles.

### **1.4.2 Interband Transitions**

In some other cases, the intrinsic interband transitions of metallic nanoparticles under photo-excitation are also involved in the catalytic reactions but are often overlooked in the mechanistic interpretation. As mentioned earlier, the physical pictures of plasmon resonance and interband transitions are completely different, and related hot carriers' behaviours play a decisive role in how the photocatalytic reaction proceeds. The most prominent one is that the plasmon resonance favors the reduction reaction driven by energetic hot electrons and interband transitions favor the oxidation reaction driven by deep holes with strong oxidizing power. One thing to mention here is that this preference is not absolutely contrary and for some specific reactions both hot electrons and hot holes are responsible for the catalysis cycle regardless of the photo-excitation mechanism. For

example, our previous report demonstrated that the deeper holes generated from shorter wavelengths with stronger oxidizing power could promote the rate-determining step of the Suzuki-Miyaura reaction thus offering a higher quantum yield, while the hot electron's contribution remained the same to that process due to the same energy level of these electrons from intrinsic interband transitions (Figure 1.9A).<sup>54</sup> Another case of utilizing hot electrons from interband transitions for the reaction was applying Au or Ag NPs as the plasmonic antennas to drive the reduction of Ni(II) complex for reductive cleavage of C–O bond and holes scavengers for quenching the holes and providing protons for the reaction from Zhu's group (Figure 1.9B).<sup>115</sup> In this case, the hot holes were sacrificed as many other researchers did, which is not economically efficient. On the other hand, the solely use of hot holes from interband transitions was also proved to be good electron “trappers” to catalyze oxidation reactions (Figure 1.9C) including citrate oxidation<sup>116</sup> and nanoelectrode dissolution,<sup>33</sup> which provided better catalytic performance than plasmon resonance. Overall, the photocatalysis mechanism by interband transitions is still under the way of exploring and many unsolved mysteries like hot carriers' dynamics and their contribution to the reaction kinetics are still awaiting.

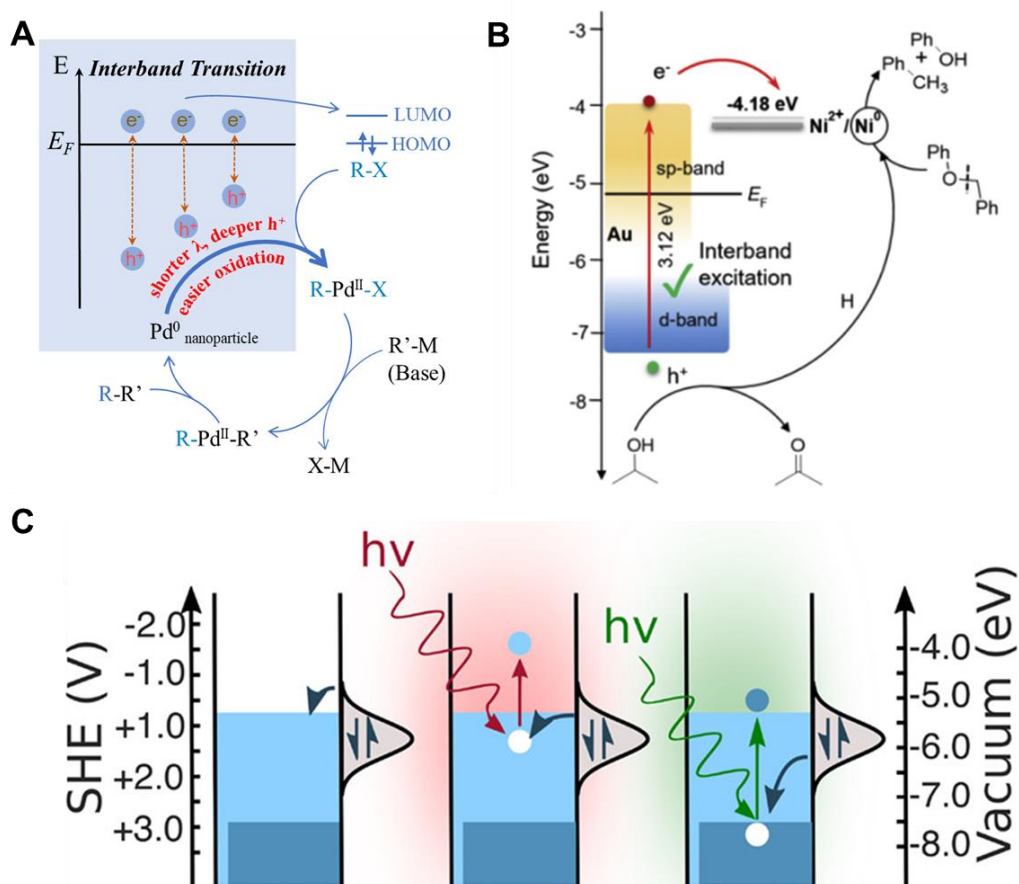


**Figure 1.9** Photocatalysis mechanisms from interband transitions. (A) Deeper holes from short-wavelength excitation offer a higher quantum yield of photocatalytic Suzuki–Miyaura reaction. (B) Hot electrons from interband excitations inducing Ni<sup>2+</sup> complex reduction for reductive cleavage of C–O bond. (C) Electrode dissolution of metals in the dark



or by photogenerated holes created by intraband transitions and interband transitions. A was adapted with permission from ref. 54, Copyright © 2022 The Authors (Open Access), B from ref. 115, Copyright © 2019 Elsevier Inc., and C from ref. 33, Copyright © 2019, American Chemical Society.

### **1.4.3 Other mechanisms**

Apart from the plasmon resonance and interband transitions as the major mechanisms for hot carriers' generation for photocatalysis, there are also some other processes involved during the photo-excitation responsible for the enhancement of photocatalysis. As mentioned earlier, in this section, we will briefly introduce a few of those processes and their effect on catalysis, and will not go through all the details since it's not our focus in this review, and those topics have been already reviewed thoroughly before.

#### **1.4.3.1 Near-field enhancement**

As a result of the collective oscillations of conduction electrons from plasmon resonance, the electric field near the nanoparticle's surface would be enhanced, thus causing strong optical adsorption and better photocatalytic activity. Since this enhancement is directly and highly dependent on the distance between the substance and the surface of the nanoparticles, only a few nanometers outside the particles could experience this enchantment and that's the reason why normally it's called near-field enhancement (Figure 1.10A).<sup>117</sup> This enhancement of electromagnetic field was reported about 10-100 times larger than the incident EM field intensity by simulation based on Maxwell's classic electromagnetism theory,<sup>118</sup> and the enhancement factor varies based on the geometry and arrangement of those nanoparticles.<sup>119</sup> Furthermore, this enhancement factor can be amplified at the "hot spots" between two adjacent nanoparticles, or sharp tips/corners of some specific shape (Figure 1.10A), which is commonly utilized for the surface-enhanced Raman spectroscopy (SERS) and up to around  $10^5$  enhancement of the Raman signal.<sup>120,</sup>  
121

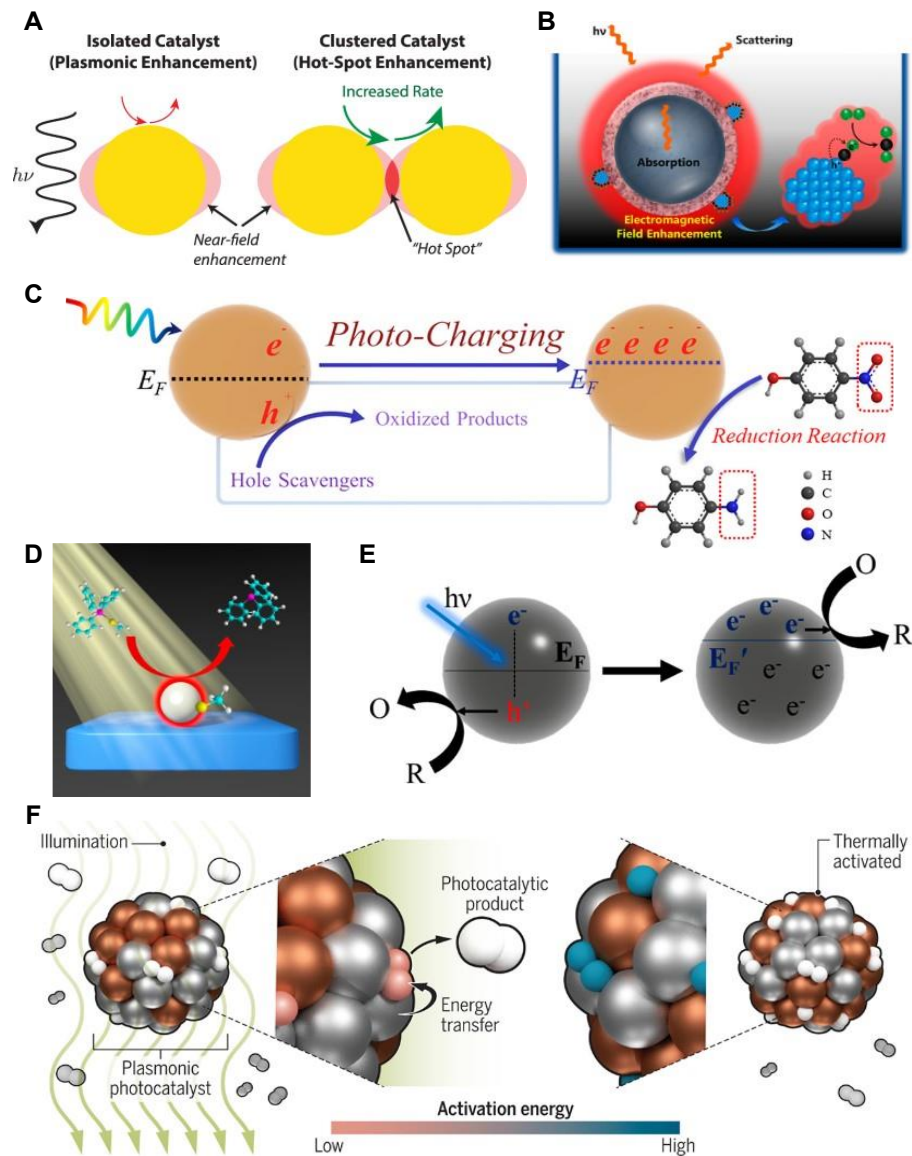


**Figure 1.10** Other photocatalysis mechanisms by metallic nanoparticles. (A) Near-field electromagnetic field enhancements at nanoparticle's surface or hot spots between nanoparticles. (B) Antenna–reactor system to maximize local field enhancements at the catalytically active Pt surface. (C) Photo-charging effect on the catalysis of metallic nanoparticles as a background contribution in photocatalysis. (D) The surface plasmon-mediated photothermal effect of local heating activates reactant molecules and boosts numerous types of chemical reactions. (E) Light-induced potentials lower the activation energy barrier or enhance reaction kinetics during photocatalytic reactions. (F) Quantifying hot carrier and thermal contributions in plasmonic photocatalysis. A was adapted with permission from ref. 117, Copyright © 2021, American Chemical Society, B from ref. 122, Copyright © 2017, American Chemical Society, C from ref. 127, Copyright © 2021, American Chemical Society, D from ref. 128, Copyright © 2014, American Chemical Society, E from ref. 126, Copyright © 2020, American Chemical Society and F from ref. 134, Copyright © 2018, The American Association for the Advancement of Science.

In terms of catalysis, within this near-field, the probability of electronic transitions of the adsorbates is significantly enhanced, thus improving the photocatalytic efficiency. Christopher's group reported that near-field enhancement has to be balanced with adsorption and scattering effects in the antenna–reactor system to achieve the optimal photocatalytic performance of Pt nanoparticles and Ag nanoparticle antenna (Figure 1.10B).<sup>122</sup> Another important topic when dealing with field enhancement is the plasmon coupling between nanoparticles that would induce the changes in optical absorption, carrier dynamics, and field enhancements, which has been reviewed by Nordlander's group.<sup>123</sup> Noting that most current claims about near-field enhancements come from plasmon resonance, and it remains an unsolved question whether interband transitions would induce the same effect or not.

#### 1.4.3.2 Photo-charging effect

The photo-charging effect on metallic nanoparticle photocatalysts is often overlooked in the mechanistic interpretation but critical in evaluating the actual catalytic performance of those nanoparticles, especially in those experiments with sacrificial reagents for quenching the hot electrons or hot holes. Typically, if one of the hot carriers was scavenged during the photo-excitation process, the other part of the hot carrier could accumulate inside the nanoparticles and thus change the Fermi level of the nanoparticles, proved by our previous report.<sup>53</sup> This change in the Fermi level also brings the distinct difference in the redox potential of these nanoparticles, which could potentially change the reactivity of those nanoparticles.

The photo-charging effect was initially proposed by Brus's group as a photovoltage mechanism for explaining the photo-induced nanoparticle growth.<sup>124</sup> Furthermore, Kamat's group and Jain's group demonstrated this voltage mechanism as electron charging effect of metallic nanoparticles in dye-sensitized solar cells,<sup>125</sup> and light-induced potential lowering the activation barrier under photoexcitation of metallic nanoparticles (Figure 1.10E).<sup>126</sup> However, none of these experiments separated the charging process and catalytic step, which made it harder to evaluate the contribution of the photo-charging effect to the catalytic activity. Until recently, our group proposed a two-step experiment to photo-charge the nanoparticle first with hole scavengers and evaluate the catalytic performance right after, thus building a quantitative relationship between the accumulated charge and reaction rate constant (Figure 1.10C).<sup>127</sup> As following up, the *in-situ* evaluation of the photo-charging effect during the photocatalysis still remains an unsolved problem, but we believe with delicate design, it should be address in the near future.

#### 1.4.3.3 Photothermal effects

The photothermal effect is a result of the final nonradiative events that occur after photoexcitation of the metal nanoparticle. During this process, the vibrational coupling between the hot carriers and low-frequency phonons causes a rise in the temperature of the metal nanoparticles. Under the right optical conditions, the temperature of the metal nanoparticle can be elevated, enough to initiate chemical transformations on the metal nanoparticle (Figure 1.10D).<sup>128</sup> The temperature arising from the local heating effect may go up from a few to hundreds of K depending on the experimental setup and illumination

conditions. Some experimental procedures were already proposed and reviewed by Baffou's group to examine the photothermal effect on hot-carrier photocatalysis including reaction condition survey, activation barrier calculation, reaction rate comparison, accurate temperature measurements on single or collective heating and so on.<sup>129</sup> Still, no conclusive arguments haven been achieved, and the take-home-message here is that the photothermal effect is an unavoidable component whenever dealing with photocatalysis by metallic nanoparticles and worth some considerations in the future research.

On the other hand, there is still a constantly ongoing debate about quantifying the hot carrier and thermal effects in plasmonic photocatalysts in the plasmonic community (Figure 1.10F),<sup>130-134</sup> and our point of view of this is that depending on the specific reaction system, the photothermal effects may play different roles in the catalysis. Typically, in the colloidal system with careful experimental design including the concentration of nanoparticles, continuous light source, or temperature control setup, the photothermal effect can be minimized to the point that it will not be a dominant contribution to the photocatalysis.

### **1.5 Summary and future perspectives**

Throughout this review, a comprehensive understanding of photocatalysis by metallic nanoparticles with detailed physical and chemical pictures about how the light-induced hot carriers involved in the catalysis is expected to be built. Two major photo-excitation mechanisms of plasmon resonance and interband transitions are thoroughly discussed, with regard to their difference in the hot-carriers generation, charge transfer, and related photocatalyzed reactions. As it turns out, the plasmon resonance favors the reduction reaction with hot electrons and the interband transition favors the oxidation reaction with hot holes, but it is not contradictory and sometimes can be mutually exchanged for specific reactions. Noteworthy that interband transition is an intrinsic transition across all the metallic nanoparticles not restricted to the size and shape effect, while the plasmon resonance is the collective oscillation of conduction electrons highly dependent on the geometry and composite of these nanoparticles. In an experimental catalytic system, this consideration and other mechanisms like photo-charging and photothermal effects should be addressed before jumping to the final conclusion.

As the field of photocatalysis of metallic nanoparticles moves forward, the shift from noble metallic nanoparticles such as Au and Ag to non-noble metallic nanoparticles like Al and Co is emerging very recently, as reviewed by Yu's, Liu's, and Jaroniec's groups.<sup>135</sup> As we can anticipate, this shift may cause a very critical impact on plasmon resonance due to the change in the filling state of conduction electrons and Fermi level, however, it should not deteriorate the influence of interband transitions of metallic nanoparticles. Then the future perspective about this direction will be developing more and more non-noble metallic nanoparticles for photocatalysis in terms of interband transition and expanding the territory into more catalytic systems. On the other side, an integrated system between different metallic nanoparticles or emerging into heterojunctions has always been a hot topic in the community to achieve high efficiency in harvesting the hot carriers. And those hybrid structures are very promising in terms of overall catalysis efficiency and re-considering the interband transitions in this structure is another important factor for improvement. Even further, the plasmonic coupling with interband transitions to generate

hot electrons and hot holes simultaneously, and utilizing those hot carriers to catalyze redox reactions separately or together could be another approach to improve the photocatalysis by metallic nanoparticles.

## 1.6 References

- (1) Rivera, N.; Kaminer, I. Light–matter interactions with photonic quasiparticles. *Nat. Rev. Phys.* **2020**, *2*, 538-561.
- (2) Wood, R. W. XLII. On a remarkable case of uneven distribution of light in a diffraction grating spectrum. *The London, Edinburgh, and Dublin Philosophical Magazine and Journal of Science* **1902**, *4*, 396-402.
- (3) Langmuir, I. Oscillations in ionized gases. *Proc. Natl. Acad. Sci. U. S. A.* **1928**, *14*, 627.
- (4) Pines, D.; Bohm, D. A collective description of electron interactions: II. Collective vs individual particle aspects of the interactions. *Phys. Rev.* **1952**, *85*, 338.
- (5) Ritchie, R. H. Plasma losses by fast electrons in thin films. *Phys. Rev.* **1957**, *106*, 874.
- (6) Kretschmann, E.; Raether, H. Radiative decay of non-radiative surface plasmons excited by light. *Z. Naturforsch. a* **1968**, *23*, 2135-2136.
- (7) Maier, S. A. *Plasmonics: fundamentals and applications*. Springer Science & Business Media: 2007.
- (8) Zia, R.; Schuller, J. A.; Chandran, A.; Brongersma, M. L. Plasmonics: the next chip-scale technology. *Mater. Today* **2006**, *9*, 20-27.
- (9) Liu, L.; Corma, A. Metal Catalysts for Heterogeneous Catalysis: From Single Atoms to Nanoclusters and Nanoparticles. *Chem. Rev.* **2018**, *118*, 4981-5079.
- (10) Zaera, F. Nanostructured materials for applications in heterogeneous catalysis. *Chem. Soc. Rev.* **2013**, *42*, 2746-2762.
- (11) Fujishima, A.; Zhang, X.; Tryk, D. A. TiO<sub>2</sub> photocatalysis and related surface phenomena. *Surf. Sci. Rep.* **2008**, *63*, 515-582.
- (12) Zhao, J.; Wang, J.; Brock, A. J.; Zhu, H. Plasmonic heterogeneous catalysis for organic transformations. *J. Photochem. Photobiol. C: Photochem. Rev.* **2022**, *52*, 100539.
- (13) Munnik, P.; de Jongh, P. E.; de Jong, K. P. Recent Developments in the Synthesis of Supported Catalysts. *Chem. Rev.* **2015**, *115*, 6687-6718.
- (14) Grzelczak, M.; Pérez-Juste, J.; Mulvaney, P.; Liz-Marzán, L. M. Shape control in gold nanoparticle synthesis. *Chem. Soc. Rev.* **2008**, *37*, 1783-1791.
- (15) Shi, Y.; Lyu, Z.; Zhao, M.; Chen, R.; Nguyen, Q. N.; Xia, Y. Noble-Metal Nanocrystals with Controlled Shapes for Catalytic and Electrocatalytic Applications. *Chem. Rev.* **2021**, *121*, 649-735.
- (16) Burrows, N. D.; Vartanian, A. M.; Abadeer, N. S.; Grzincic, E. M.; Jacob, L. M.; Lin, W.; Li, J.; Dennison, J. M.; Hinman, J. G.; Murphy, C. J. Anisotropic Nanoparticles and Anisotropic Surface Chemistry. *The Journal of Physical Chemistry Letters* **2016**, *7*, 632-641.
- (17) Zhu, X. Surface Photochemistry. *Annu. Rev. Phys. Chem.* **1994**, *45*, 113-144.
- (18) Frischkorn, C.; Wolf, M. Femtochemistry at Metal Surfaces: Nonadiabatic Reaction Dynamics. *Chem. Rev.* **2006**, *106*, 4207-4233.
- (19) Khurgin, J. B. Fundamental limits of hot carrier injection from metal in nanoplasmonics. *Nanophotonics* **2020**, *9*, 453-471.
- (20) Li, L.; Larsen, A. H.; Romero, N. A.; Morozov, V. A.; Glinsvad, C.; Abild-Pedersen, F.; Greeley, J.; Jacobsen, K. W.; Nørskov, J. K. Investigation of Catalytic Finite-Size-Effects of Platinum Metal Clusters. *The Journal of Physical Chemistry Letters* **2013**, *4*, 222-226.
- (21) Jens K. Nørskov, F. S., Frank Abild-Pedersen, Thomas Bligaard. The Electronic Factor in Heterogeneous Catalysis. In *Fundamental Concepts in Heterogeneous Catalysis*, John Wiley & Sons, Inc.: 2014; pp 114-137.

- (22) Linic, S.; Christopher, P.; Ingram, D. B. Plasmonic-Metal Nanostructures for Efficient Conversion of Solar to Chemical Energy. *Nat. Mater.* **2011**, *10*, 911-921.
- (23) Hou, W.; Cronin, S. B. A Review of Surface Plasmon Resonance-Enhanced Photocatalysis. *Adv. Funct. Mater.* **2013**, *23*, 1612-1619.
- (24) Xin, H.; Namgung, B.; Lee, L. P. Nanoplasmonic Optical Antennas for Life sciences and Medicine. *Nat. Rev. Mater.* **2018**, *3*, 228-243.
- (25) Brus, L. Noble Metal Nanocrystals: Plasmon Electron Transfer Photochemistry and Single-Molecule Raman Spectroscopy. *Acc. Chem. Res.* **2008**, *41*, 1742-1749.
- (26) Gellé, A.; Jin, T.; de la Garza, L.; Price, G. D.; Besteiro, L. V.; Moores, A. Applications of Plasmon-Enhanced Nanocatalysis to Organic Transformations. *Chem. Rev.* **2020**, *120*, 986-1041.
- (27) Yu, Y.; Wijesekara, K. D.; Xi, X.; Willets, K. A. Quantifying Wavelength-Dependent Plasmonic Hot Carrier Energy Distributions at Metal/Semiconductor Interfaces. *ACS Nano* **2019**, *13*, 3629-3637.
- (28) Kim, Y.; Dumett Torres, D.; Jain, P. K. Activation Energies of Plasmonic Catalysts. *Nano Lett.* **2016**, *16*, 3399-3407.
- (29) Hou, W.; Hung, W. H.; Pavaskar, P.; Goepfert, A.; Aykol, M.; Cronin, S. B. Photocatalytic Conversion of CO<sub>2</sub> to Hydrocarbon Fuels via Plasmon-Enhanced Absorption and Metallic Interband Transitions. *ACS. Catal.* **2011**, *1*, 929-936.
- (30) Liu, L.; Li, P.; Adisak, B.; Ouyang, S.; Umezawa, N.; Ye, J.; Kodiyath, R.; Tanabe, T.; Ramesh, G. V.; Ueda, S.; Abe, H. Gold Photosensitized SrTiO<sub>3</sub> for Visible-Light Water Oxidation Induced by Au Interband Transitions. *J. Mater. Chem. A* **2014**, *2*, 9875-9882.
- (31) Huang, Y. M.; Liu, Z.; Gao, G. P.; Xiao, Q.; Martens, W.; Du, A. J.; Sarina, S.; Guo, C.; Zhu, H. Y. Visible Light-Driven Selective Hydrogenation of Unsaturated Aromatics in an Aqueous Solution by Direct Photocatalysis of Au Nanoparticles. *Catal. Sci. Technol.* **2018**, *8*, 726-734.
- (32) Zhao, J.; Nguyen, S. C.; Ye, R.; Ye, B. H.; Weller, H.; Somorjai, G. A.; Alivisatos, A. P.; Toste, F. D. A Comparison of Photocatalytic Activities of Gold Nanoparticles Following Plasmonic and Interband Excitation and a Strategy for Harnessing Interband Hot Carriers for Solution Phase Photocatalysis. *ACS Cent. Sci.* **2017**, *3*, 482-488.
- (33) Al-Zubeidi, A.; Hoener, B. S.; Collins, S. S. E.; Wang, W.; Kirchner, S. R.; Hosseini Jebeli, S. A.; Joplin, A.; Chang, W.-S.; Link, S.; Landes, C. F. Hot Holes Assist Plasmonic Nanoelectrode Dissolution. *Nano Lett.* **2019**, *19*, 1301-1306.
- (34) Mao, Z.; Vang, H.; Garcia, A.; Tohti, A.; Stokes, B. J.; Nguyen, S. C. Carrier Diffusion—The Main Contribution to Size-Dependent Photocatalytic Activity of Colloidal Gold Nanoparticles. *ACS. Catal.* **2019**, *9*, 4211-4217.
- (35) Kim, Y.; Smith, J. G.; Jain, P. K. Harvesting Multiple Electron-hole Pairs Generated through Plasmonic Excitation of Au Nanoparticles. *Nat. Chem.* **2018**, *10*, 763-769.
- (36) Aslam, U.; Rao, V. G.; Chavez, S.; Linic, S. Catalytic Conversion of Solar to Chemical Energy on Plasmonic Metal Nanostructures. *Nat. Catal.* **2018**, *1*, 656-665.
- (37) Zhou, L.; Martirez, J. M. P.; Finzel, J.; Zhang, C.; Swearer, D. F.; Tian, S.; Robotjazi, H.; Lou, M.; Dong, L.; Henderson, L.; Christopher, P.; Carter, E. A.; Nordlander, P.; Halas, N. J. Light-driven methane dry reforming with single atomic site antenna-reactor plasmonic photocatalysts. *Nature Energy* **2020**, *5*, 61-70.
- (38) Zhang, B.; Sun, L. Artificial photosynthesis: opportunities and challenges of molecular catalysts. *Chem. Soc. Rev.* **2019**, *48*, 2216-2264.
- (39) McAtee, R. C.; McClain, E. J.; Stephenson, C. R. J. Illuminating Photoredox Catalysis. *Trends in Chemistry* **2019**, *1*, 111-125.
- (40) Twilton, J.; Le, C.; Zhang, P.; Shaw, M. H.; Evans, R. W.; MacMillan, D. W. C. The merger of transition metal and photocatalysis. *Nat. Rev. Chem.* **2017**, *1*, 0052.

- (41) Arias-Rotondo, D. M.; McCusker, J. K. The photophysics of photoredox catalysis: a roadmap for catalyst design. *Chem. Soc. Rev.* **2016**, *45*, 5803-5820.
- (42) Juris, A.; Balzani, V.; Barigelletti, F.; Campagna, S.; Belser, P.; von Zelewsky, A. Ru(II) polypyridine complexes: photophysics, photochemistry, electrochemistry, and chemiluminescence. *Coord. Chem. Rev.* **1988**, *84*, 85-277.
- (43) Romero, N. A.; Nicewicz, D. A. Organic Photoredox Catalysis. *Chem. Rev.* **2016**, *116*, 10075-10166.
- (44) Li, X.-B.; Xin, Z.-K.; Xia, S.-G.; Gao, X.-Y.; Tung, C.-H.; Wu, L.-Z. Semiconductor nanocrystals for small molecule activation via artificial photosynthesis. *Chem. Soc. Rev.* **2020**, *49*, 9028-9056.
- (45) Xu, C.; Ravi Anusuyadevi, P.; Aymonier, C.; Luque, R.; Marre, S. Nanostructured materials for photocatalysis. *Chem. Soc. Rev.* **2019**, *48*, 3868-3902.
- (46) Weiss, E. A. Designing the Surfaces of Semiconductor Quantum Dots for Colloidal Photocatalysis. *ACS Energy Lett.* **2017**, *2*, 1005-1013.
- (47) DuBose, J. T.; Kamat, P. V. Efficacy of Perovskite Photocatalysis: Challenges to Overcome. *ACS Energy Lett.* **2022**, *7*, 1994-2011.
- (48) Brongersma, M. L.; Halas, N. J.; Nordlander, P. Plasmon-induced hot carrier science and technology. *Nature Nanotechnology* **2015**, *10*, 25-34.
- (49) Clavero, C. Plasmon-induced hot-electron generation at nanoparticle/metal-oxide interfaces for photovoltaic and photocatalytic devices. *Nat. Photon.* **2014**, *8*, 95-103.
- (50) Linic, S.; Chavez, S.; Elias, R. Flow and extraction of energy and charge carriers in hybrid plasmonic nanostructures. *Nat. Mater.* **2021**, *20*, 916-924.
- (51) Devasia, D.; Das, A.; Mohan, V.; Jain, P. K. Control of Chemical Reaction Pathways by Light-Matter Coupling. *Annu. Rev. Phys. Chem.* **2021**, *72*, 423-443.
- (52) Cortés, E.; Camargo, P. H. *Plasmonic Catalysis: From Fundamentals to Applications*. John Wiley & Sons: 2021.
- (53) Mao, Z.; Espinoza, R.; Garcia, A.; Enwright, A.; Vang, H.; Nguyen, S. C. Tuning Redox Potential of Gold Nanoparticle Photocatalysts by Light. *ACS Nano* **2020**, *14*, 7038-7045.
- (54) Lyu, P.; Espinoza, R.; Khan, M. I.; Spaller, W. C.; Ghosh, S.; Nguyen, S. C. Mechanistic insight into deep holes from interband transitions in Palladium nanoparticle photocatalysts. *iScience* **2022**, *25*, 103737.
- (55) Bernardi, M.; Mustafa, J.; Neaton, J. B.; Louie, S. G. Theory and computation of hot carriers generated by surface plasmon polaritons in noble metals. *Nat. Commun.* **2015**, *6*, 7044.
- (56) Besteiro, L. V.; Kong, X.-T.; Wang, Z.; Hartland, G.; Govorov, A. O. Understanding Hot-Electron Generation and Plasmon Relaxation in Metal Nanocrystals: Quantum and Classical Mechanisms. *ACS Photonics* **2017**, *4*, 2759-2781.
- (57) Sundararaman, R.; Narang, P.; Jermyn, A. S.; Goddard III, W. A.; Atwater, H. A. Theoretical predictions for hot-carrier generation from surface plasmon decay. *Nat. Commun.* **2014**, *5*, 5788.
- (58) Manjavacas, A.; Liu, J. G.; Kulkarni, V.; Nordlander, P. Plasmon-Induced Hot Carriers in Metallic Nanoparticles. *ACS Nano* **2014**, *8*, 7630-7638.
- (59) Khurgin, J. B. How to deal with the loss in plasmonics and metamaterials. *Nature Nanotechnology* **2015**, *10*, 2-6.
- (60) Hartland, G. V.; Besteiro, L. V.; Johns, P.; Govorov, A. O. What's so Hot about Electrons in Metal Nanoparticles? *ACS Energy Lett.* **2017**, *2*, 1641-1653.
- (61) Narang, P.; Sundararaman, R.; Atwater, H. A. Plasmonic hot carrier dynamics in solid-state and chemical systems for energy conversion. *Nanophotonics* **2016**, *5*, 96-111.
- (62) Zhan, C.; Chen, X.-J.; Yi, J.; Li, J.-F.; Wu, D.-Y.; Tian, Z.-Q. From plasmon-enhanced molecular spectroscopy to plasmon-mediated chemical reactions. *Nat. Rev. Chem.* **2018**, *2*, 216-230.

- (63) Bonatti, L.; Gil, G.; Giovannini, T.; Corni, S.; Cappelli, C. Plasmonic Resonances of Metal Nanoparticles: Atomistic vs. Continuum Approaches. *Front. Chem.* **2020**, *8*.
- (64) Saavedra, J. R. M.; Asenjo-Garcia, A.; García de Abajo, F. J. Hot-Electron Dynamics and Thermalization in Small Metallic Nanoparticles. *ACS Photonics* **2016**, *3*, 1637-1646.
- (65) Tagliabue, G.; DuChene, J. S.; Abdellah, M.; Habib, A.; Gosztola, D. J.; Hattori, Y.; Cheng, W.-H.; Zheng, K.; Canton, S. E.; Sundararaman, R.; Sá, J.; Atwater, H. A. Ultrafast Hot-hole Injection Modifies Hot-electron Dynamics in Au/p-GaN Heterostructures. *Nat. Mater.* **2020**, *19*, 1312-1318.
- (66) Burda, C.; Chen, X.; Narayanan, R.; El-Sayed, M. A. Chemistry and Properties of Nanocrystals of Different Shapes. *Chem. Rev.* **2005**, *105*, 1025-1102.
- (67) Link, S.; Burda, C.; Wang, Z. L.; El-Sayed, M. A. Electron dynamics in gold and gold–silver alloy nanoparticles: The influence of a nonequilibrium electron distribution and the size dependence of the electron–phonon relaxation. *The Journal of Chemical Physics* **1999**, *111*, 1255-1264.
- (68) Ageev, V. N. Desorption induced by electronic transitions. *Prog. Surf. Sci.* **1994**, *47*, 55-203.
- (69) Christopher, P.; Xin, H.; Linic, S. Visible-light-enhanced catalytic oxidation reactions on plasmonic silver nanostructures. *Nat. Chem.* **2011**, *3*, 467-472.
- (70) Zhou, L.; Lou, M.; Bao, J. L.; Zhang, C.; Liu, J. G.; Martirez, J. M. P.; Tian, S.; Yuan, L.; Swearer, D. F.; Robotjazi, H.; Carter, E. A.; Nordlander, P.; Halas, N. J. Hot carrier multiplication in plasmonic photocatalysis. *Proc. Natl. Acad. Sci.* **2021**, *118*, e2022109118.
- (71) Harutyunyan, H.; Suchanek, F.; Lemasters, R.; Foley, J. J. Hot-carrier dynamics in catalysis. *MRS Bull.* **2020**, *45*, 32-36.
- (72) Kazuma, E.; Lee, M.; Jung, J.; Trenary, M.; Kim, Y. Single-Molecule Study of a Plasmon-Induced Reaction for a Strongly Chemisorbed Molecule. *Angew. Chem. Int. Ed.* **2020**, *59*, 7960-7966.
- (73) Kazuma, E.; Jung, J.; Ueba, H.; Trenary, M.; Kim, Y. Real-space and real-time observation of a plasmon-induced chemical reaction of a single molecule. *Science* **2018**, *360*, 521-526.
- (74) Ahmed, I.; Shi, L.; Pasanen, H.; Vivo, P.; Maity, P.; Hatamvand, M.; Zhan, Y. There is plenty of room at the top: generation of hot charge carriers and their applications in perovskite and other semiconductor-based optoelectronic devices. *Light: Science & Applications* **2021**, *10*, 174.
- (75) Kale, M. J.; Avanesian, T.; Christopher, P. Direct Photocatalysis by Plasmonic Nanostructures. *ACS. Catal.* **2014**, *4*, 116-128.
- (76) Ahlawat, M.; Mittal, D.; Govind Rao, V. Plasmon-induced hot-hole generation and extraction at nano-heterointerfaces for photocatalysis. *Communications Materials* **2021**, *2*, 114.
- (77) Zhang, C.; Jia, F.; Li, Z.; Huang, X.; Lu, G. Plasmon-generated hot holes for chemical reactions. *Nano Res.* **2020**, *13*, 3183-3197.
- (78) Dubi, Y.; Sivan, Y. “Hot” electrons in metallic nanostructures—non-thermal carriers or heating? *Light: Science & Applications* **2019**, *8*, 89.
- (79) Halas, N. J. Spiers Memorial Lecture Introductory lecture: Hot-electron science and microscopic processes in plasmonics and catalysis. *Faraday Discuss.* **2019**, *214*, 13-33.
- (80) Baumberg, J. J. Hot electron science in plasmonics and catalysis: what we argue about. *Faraday Discuss.* **2019**, *214*, 501-511.
- (81) Simoncelli, S.; Pensa, E. L.; Brick, T.; Gargiulo, J.; Lauri, A.; Cambiasso, J.; Li, Y.; Maier, S. A.; Cortés, E. Monitoring plasmonic hot-carrier chemical reactions at the single particle level. *Faraday Discuss.* **2019**, *214*, 73-87.
- (82) Zhang, Y.; He, S.; Guo, W.; Hu, Y.; Huang, J.; Mulcahy, J. R.; Wei, W. D. Surface-Plasmon-Driven Hot Electron Photochemistry. *Chem. Rev.* **2018**, *118*, 2927-2954.
- (83) Zhan, C.; Moskovits, M.; Tian, Z.-Q. Recent Progress and Prospects in Plasmon-Mediated Chemical Reaction. *Matter* **2020**, *3*, 42-56.



- (84) Kim, M.; Lin, M.; Son, J.; Xu, H.; Nam, J.-M. Hot-Electron-Mediated Photochemical Reactions: Principles, Recent Advances, and Challenges. *Adv. Opt. Mater.* **2017**, *5*, 1700004.
- (85) Mukherjee, S.; Libisch, F.; Large, N.; Neumann, O.; Brown, L. V.; Cheng, J.; Lassiter, J. B.; Carter, E. A.; Nordlander, P.; Halas, N. J. Hot Electrons Do the Impossible: Plasmon-Induced Dissociation of H<sub>2</sub> on Au. *Nano Lett.* **2013**, *13*, 240-247.
- (86) Yan, L.; Wang, F.; Meng, S. Quantum Mode Selectivity of Plasmon-Induced Water Splitting on Gold Nanoparticles. *ACS Nano* **2016**, *10*, 5452-5458.
- (87) Cai, X.; Zhu, M.; Elbanna, O. A.; Fujitsuka, M.; Kim, S.; Mao, L.; Zhang, J.; Majima, T. Au Nanorod Photosensitized La<sub>2</sub>Ti<sub>2</sub>O<sub>7</sub> Nanosteps: Successive Surface Heterojunctions Boosting Visible to Near-Infrared Photocatalytic H<sub>2</sub> Evolution. *ACS. Catal.* **2018**, *8*, 122-131.
- (88) Shi, X.; Ueno, K.; Oshikiri, T.; Sun, Q.; Sasaki, K.; Misawa, H. Enhanced water splitting under modal strong coupling conditions. *Nature Nanotechnology* **2018**, *13*, 953-958.
- (89) Lee, J. B.; Choi, S.; Kim, J.; Nam, Y. S. Plasmonically-assisted nanoarchitectures for solar water splitting: Obstacles and breakthroughs. *Nano Today* **2017**, *16*, 61-81.
- (90) Yang, J.; Guo, Y.; Lu, W.; Jiang, R.; Wang, J. Emerging Applications of Plasmons in Driving CO<sub>2</sub> Reduction and N<sub>2</sub> Fixation. *Adv. Mater.* **2018**, *30*, 1802227.
- (91) Yu, S.; Wilson, A. J.; Heo, J.; Jain, P. K. Plasmonic Control of Multi-Electron Transfer and C–C Coupling in Visible-Light-Driven CO<sub>2</sub> Reduction on Au Nanoparticles. *Nano Lett.* **2018**, *18*, 2189-2194.
- (92) Devasia, D.; Wilson, A. J.; Heo, J.; Mohan, V.; Jain, P. K. A rich catalog of C–C bonded species formed in CO<sub>2</sub> reduction on a plasmonic photocatalyst. *Nat. Commun.* **2021**, *12*, 2612.
- (93) Lee, D.; Yoon, S. Plasmonic Switching: Hole Transfer Opens an Electron-Transfer Channel in Plasmon-Driven Reactions. *The Journal of Physical Chemistry C* **2020**, *124*, 15879-15885.
- (94) Peng, T.; Miao, J.; Gao, Z.; Zhang, L.; Gao, Y.; Fan, C.; Li, D. Reactivating Catalytic Surface: Insights into the Role of Hot Holes in Plasmonic Catalysis. *Small* **2018**, *14*, 1703510.
- (95) Swaminathan, S.; Rao, V. G.; Bera, J. K.; Chandra, M. The Pivotal Role of Hot Carriers in Plasmonic Catalysis of C–N Bond Forming Reaction of Amines. *Angew. Chem. Int. Ed.* **2021**, *60*, 12532-12538.
- (96) Pensa, E.; Gargiulo, J.; Lauri, A.; Schlücker, S.; Cortés, E.; Maier, S. A. Spectral Screening of the Energy of Hot Holes over a Particle Plasmon Resonance. *Nano Lett.* **2019**, *19*, 1867-1874.
- (97) Suzuki, K.; Li, X.; Wang, Y.; Nagasawa, F.; Murakoshi, K. Active Intermediates in Plasmon-Induced Water Oxidation at Au Nanodimer Structures on a Single Crystal of TiO<sub>2</sub>. *ACS Energy Lett.* **2020**, *5*, 1252-1259.
- (98) Kozuch, S.; Martin, J. M. L. “Turning Over” Definitions in Catalytic Cycles. *ACS. Catal.* **2012**, *2*, 2787-2794.
- (99) Braslavsky, S. E.; Braun, A. M.; Cassano, A. E.; Emeline, A. V.; Litter, M. I.; Palmisano, L.; Parmon, V. N.; Serpone, N. Glossary of terms used in photocatalysis and radiation catalysis (IUPAC Recommendations 2011). *Pure Appl. Chem.* **2011**, *83*, 931-1014.
- (100) Melchionna, M.; Fornasiero, P. Updates on the Roadmap for Photocatalysis. *ACS. Catal.* **2020**, *10*, 5493-5501.
- (101) Kisch, H.; Bahnemann, D. Best Practice in Photocatalysis: Comparing Rates or Apparent Quantum Yields? *The Journal of Physical Chemistry Letters* **2015**, *6*, 1907-1910.
- (102) Lente, G. Comment on “‘Turning Over’ Definitions in Catalytic Cycles”. *ACS. Catal.* **2013**, *3*, 381-382.
- (103) Lee, S. A.; Link, S. Chemical Interface Damping of Surface Plasmon Resonances. *Acc. Chem. Res.* **2021**, *54*, 1950-1960.
- (104) Boerigter, C.; Campana, R.; Morabito, M.; Linic, S. Evidence and implications of direct charge excitation as the dominant mechanism in plasmon-mediated photocatalysis. *Nat. Commun.* **2016**, *7*, 10545.

- (105) Kale, M. J.; Avanesian, T.; Xin, H.; Yan, J.; Christopher, P. Controlling Catalytic Selectivity on Metal Nanoparticles by Direct Photoexcitation of Adsorbate–Metal Bonds. *Nano Lett.* **2014**, *14*, 5405-5412.
- (106) Kazuma, E.; Jung, J.; Ueba, H.; Trenary, M.; Kim, Y. Direct Pathway to Molecular Photodissociation on Metal Surfaces Using Visible Light. *J. Am. Chem. Soc.* **2017**, *139*, 3115-3121.
- (107) Xiao, Q.; Sarina, S.; Waclawik, E. R.; Zhu, H. Direct visible photoexcitation on palladium nanocatalysts by chemisorption with distinct size dependence. *Catal. Sci. Technol.* **2021**, *11*, 2073-2080.
- (108) Cortés, E.; Grzeschik, R.; Maier, S. A.; Schlücker, S. Experimental characterization techniques for plasmon-assisted chemistry. *Nat. Rev. Chem.* **2022**, *6*, 259-274.
- (109) Wu, D.-Y.; Zhang, M.; Zhao, L.-B.; Huang, Y.-F.; Ren, B.; Tian, Z.-Q. Surface plasmon-enhanced photochemical reactions on noble metal nanostructures. *Science China Chemistry* **2015**, *58*, 574-585.
- (110) Zhan, C.; Chen, X.-J.; Huang, Y.-F.; Wu, D.-Y.; Tian, Z.-Q. Plasmon-Mediated Chemical Reactions on Nanostructures Unveiled by Surface-Enhanced Raman Spectroscopy. *Acc. Chem. Res.* **2019**, *52*, 2784-2792.
- (111) Li, J.; Cushing, S. K.; Meng, F.; Senty, T. R.; Bristow, A. D.; Wu, N. Plasmon-induced resonance energy transfer for solar energy conversion. *Nat. Photon.* **2015**, *9*, 601-607.
- (112) Cushing, S. K.; Li, J.; Meng, F.; Senty, T. R.; Suri, S.; Zhi, M.; Li, M.; Bristow, A. D.; Wu, N. Photocatalytic Activity Enhanced by Plasmonic Resonant Energy Transfer from Metal to Semiconductor. *J. Am. Chem. Soc.* **2012**, *134*, 15033-15041.
- (113) Zhang, B.; Zhao, Y.; Liang, W. Collaborative effect of plasmon-induced resonance energy and electron transfer on the interfacial electron injection dynamics of dye-sensitized solar cell. *The Journal of Chemical Physics* **2019**, *151*, 044702.
- (114) Yu, Z.; Frontiera, R. R. Intermolecular Forces Dictate Vibrational Energy Transfer in Plasmonic–Molecule Systems. *ACS Nano* **2022**, *16*, 847-854.
- (115) Han, P.; Tana, T.; Xiao, Q.; Sarina, S.; Waclawik, E. R.; Gómez, D. E.; Zhu, H. Promoting Ni(II) Catalysis with Plasmonic Antennas. *Chem* **2019**, *5*, 2879-2899.
- (116) Schlather, A. E.; Manjavacas, A.; Lauchner, A.; Marangoni, V. S.; DeSantis, C. J.; Nordlander, P.; Halas, N. J. Hot Hole Photoelectrochemistry on Au@SiO<sub>2</sub>@Au Nanoparticles. *The Journal of Physical Chemistry Letters* **2017**, *8*, 2060-2067.
- (117) Agrawal, S.; Mysko, R. A.; Nigra, M. M.; Mohanty, S. K.; Hoepfner, M. P. Plasmonic Photocatalytic Enhancement of L-Cysteine Self-Assembled Gold Nanoparticle Clusters for Fenton Reaction Catalysis. *Langmuir* **2021**, *37*, 3281-3287.
- (118) Oubre, C.; Nordlander, P. Optical Properties of Metallodielectric Nanostructures Calculated Using the Finite Difference Time Domain Method. *The Journal of Physical Chemistry B* **2004**, *108*, 17740-17747.
- (119) Wang, L.; Hasanzadeh Kafshgari, M.; Meunier, M. Optical Properties and Applications of Plasmonic-Metal Nanoparticles. *Adv. Funct. Mater.* **2020**, *30*, 2005400.
- (120) Ueno, K.; Misawa, H. Surface plasmon-enhanced photochemical reactions. *J. Photochem. Photobiol. C: Photochem. Rev.* **2013**, *15*, 31-52.
- (121) Hao, E.; Schatz, G. C. Electromagnetic fields around silver nanoparticles and dimers. *The Journal of Chemical Physics* **2004**, *120*, 357-366.
- (122) Li, K.; Hogan, N. J.; Kale, M. J.; Halas, N. J.; Nordlander, P.; Christopher, P. Balancing Near-Field Enhancement, Absorption, and Scattering for Effective Antenna–Reactor Plasmonic Photocatalysis. *Nano Lett.* **2017**, *17*, 3710-3717.
- (123) Halas, N. J.; Lal, S.; Chang, W.-S.; Link, S.; Nordlander, P. Plasmons in Strongly Coupled Metallic Nanostructures. *Chem. Rev.* **2011**, *111*, 3913-3961.

- (124) Wu, X.; Redmond, P. L.; Liu, H.; Chen, Y.; Steigerwald, M.; Brus, L. Photovoltage Mechanism for Room Light Conversion of Citrate Stabilized Silver Nanocrystal Seeds to Large Nanoprisms. *J. Am. Chem. Soc.* **2008**, *130*, 9500-9506.
- (125) Choi, H.; Chen, W. T.; Kamat, P. V. Know Thy Nano Neighbor. Plasmonic versus Electron Charging Effects of Metal Nanoparticles in Dye-Sensitized Solar Cells. *ACS Nano* **2012**, *6*, 4418-4427.
- (126) Wilson, A. J.; Jain, P. K. Light-Induced Voltages in Catalysis by Plasmonic Nanostructures. *Acc. Chem. Res.* **2020**, *53*, 1773-1781.
- (127) Lyu, P.; Nguyen, S. C. Effect of Photocharging on Catalysis of Metallic Nanoparticles. *The Journal of Physical Chemistry Letters* **2021**, *12*, 12173-12179.
- (128) Qiu, J.; Wei, W. D. Surface Plasmon-Mediated Photothermal Chemistry. *The Journal of Physical Chemistry C* **2014**, *118*, 20735-20749.
- (129) Baffou, G.; Bordacchini, I.; Baldi, A.; Quidant, R. Simple experimental procedures to distinguish photothermal from hot-carrier processes in plasmonics. *Light: Science & Applications* **2020**, *9*, 108.
- (130) Zhou, L.; Swearer, D. F.; Zhang, C.; Robotjazi, H.; Zhao, H.; Henderson, L.; Dong, L.; Christopher, P.; Carter, E. A.; Nordlander, P.; Halas, N. J. Quantifying hot carrier and thermal contributions in plasmonic photocatalysis. *Science* **2018**, *362*, 69-72.
- (131) Sivan, Y.; Baraban, J.; Un, I. W.; Dubi, Y. Comment on "Quantifying hot carrier and thermal contributions in plasmonic photocatalysis". *Science* **2019**, *364*, eaaw9367.
- (132) Zhou, L.; Swearer, D. F.; Robotjazi, H.; Alabastri, A.; Christopher, P.; Carter, E. A.; Nordlander, P.; Halas, N. J. Response to Comment on "Quantifying hot carrier and thermal contributions in plasmonic photocatalysis". *Science* **2019**, *364*, eaaw9545.
- (133) Aizpurua, J.; Baletto, F.; Baumberg, J.; Christopher, P.; Nijs, B. d.; Deshpande, P.; Diaz Fernandez, Y.; Fabris, L.; Freakley, S.; Gawinkowski, S.; Govorov, A.; Halas, N.; Hernandez, R.; Jankiewicz, B.; Khurgin, J.; Kuisma, M.; Kumar, P. V.; Lischner, J.; Liu, J.; Marini, A.; Maurer, R. J.; Mueller, N. S.; Parente, M.; Park, J. Y.; Reich, S.; Sivan, Y.; Tagliabue, G.; Torrente-Murciano, L.; Thangamuthu, M.; Xiao, X.; Zayats, A. Theory of hot electrons: general discussion. *Faraday Discuss.* **2019**, *214*, 245-281.
- (134) Cortés, E. Activating plasmonic chemistry. *Science* **2018**, *362*, 28-29.
- (135) Sayed, M.; Yu, J.; Liu, G.; Jaroniec, M. Non-Noble Plasmonic Metal-Based Photocatalysts. *Chem. Rev.* **2022**.

## Chapter 2 Mechanistic Insight into Deep Holes from Interband Transitions in Palladium Nanoparticle Photocatalysts

(This chapter covers similar materials as in Pin Lyu, Randy Espinoza, Md. Imran Khan, William C. Spaller, Sayantani Ghosh, Son C. Nguyen\*., **Mechanistic insight into deep holes from interband transitions in Palladium nanoparticle photocatalysts**. *iScience*, 2022, 25, 2, 103737.

Reproduced with permission, copyright 2022 Authors and Elsevier. This article is available under the Creative Commons CC-BY-NC-ND license and permits non-commercial use of the work as published, without adaptation or alteration provided the work is fully attributed.)

### Abstract

Utilizing hot electrons generated from localized surface plasmon resonance is of widespread interest in the photocatalysis of metallic nanoparticles. However, hot holes, especially generated from interband transitions, have not been fully explored for photocatalysis yet. In this study, a photocatalyzed Suzuki-Miyaura reaction using mesoporous Pd nanoparticle photocatalyst served as a model to study the role of hot holes. Quantum yields of the photocatalyst increase under shorter wavelength excitations and correlate to “deeper” energy of the holes from the Fermi level. This work suggests that deeper holes in the *d*-band catalyze the oxidative addition of aryl halide R-X onto Pd<sup>0</sup> at the nanoparticles’ surface to form R-Pd<sup>II</sup>-X complex, thus accelerate the rate-determining step of the catalytic cycle. The hot electrons do not play a decisive role. In the future, catalytic mechanism induced by deep holes should deserve as much attention as the well-known hot electron transfer mechanism.

### 2.1 Introduction

Metallic nanoparticles have gained a growing interest for applications in photocatalysis.<sup>1-17</sup> The strong light absorption, high surface-area-to-volume ratio, and robust nature of these nanoparticles make them great potential candidates for exploring better photocatalytic activities and high recyclability. Historically, photocatalysis induced by localized surface plasmon resonance (plasmon resonance for short) of these particles has been studied widely for more than a decade,<sup>15, 16, 18-21</sup> but photocatalysis originating from interband excitations is still underexplored.<sup>7, 10, 12, 22, 23</sup> In short, the plasmon resonance can be described by a classical picture as a collective oscillation of the nanoparticles’ electrons in response to electric field of exciting photons or a quantum mechanical picture as electron transitions from some *sp*-band states to other *sp*-band states (*i.e.* intraband transitions), while the interband transitions are given to electron transitions from the respective *d* to *sp* bands. Due to these origins, the plasmon resonance of metal nanoparticles offers strong optical absorption and tunable spectral shift depending on the particle morphology, but the interband transitions always provide a significant absorption within a defined spectral region. The optical excitations in these two regimes are expected to exhibit different catalytic outcomes because the generated hot carriers have different energy states, population and dynamics for each regime.<sup>24-26</sup> With the generation of hot electrons above

the Fermi level ( $E_F$ ) and hot holes near  $E_F$  by the plasmon resonance, the extraction of the hot electrons is more favorable than that of the hot holes, and electron transfer from the nanoparticle photocatalysts to reactants (reductive pathway) is generally preferred. This catalytic mechanism has been demonstrated in many reductive reactions, such as reduction of  $\text{CO}_2$  or nitro compounds.<sup>15, 17</sup> Recently, the hot holes could also be utilized for some oxidative reactions, such as alcohol oxidation.<sup>27-30</sup> On the other hand, interband transitions, generating “deeper” holes below  $E_F$  and electrons near  $E_F$ , are more suitable for the oxidative pathway where the nanoparticle photocatalysts are better used for hole-mediated oxidation reactions. This suggested mechanism will provide a new perspective in understanding the photocatalysis of metal nanoparticles and designing better photocatalyzed reactions.

In order to shed light on the catalytic mechanisms in previous experiments, many research groups have compared the catalytic efficiencies under these two excitations, but it has been difficult to disentangle the origin of the observed efficiencies due to the strong spectral overlap of these two excitations.<sup>10, 16, 31-33</sup> For example, the plasmon resonance of spherical gold nanoparticle catalysts in the region around 480 to 650 nm is spectrally overlapped with the intrinsic *d-to-sp* interband transitions. These interband transitions have strong absorption in the ultraviolet region and extend to the visible region with an absorption tailed up to about 600 nm.<sup>34</sup> Thus it is desirable to tune the plasmon resonance absorption away from the interband absorption to resolve the catalytic mechanism. This approach is demonstrated in this paper by using mesoporous structure.

In this study, mesoporous Pd nanoparticles were employed due to their spectral shift of plasmon resonance from visible to near-infrared regions and the dominant contribution of interband transitions in the optical region that we surveyed (*i.e.*, 400-600 nm). Usually, the non-porous Pd nanoparticles have a plasmon resonance associated with a very broad spectral feature in the ultraviolet-visible region, and this plasmonic peak appears on top of the entire spectral region of the interband transitions (Figure 2.1A).<sup>35, 36</sup> In contrast, the porous version shows a featureless absorption with no peak of plasmon resonance in the 400-600 nm region (Figure 2.1A), therefore the observed photocatalytic activities could be attributed mainly to interband transitions. Another advantage of the mesoporous structure is the shorter travel distance for hot carriers diffusing to particles' surface, thus the efficiency of harvesting them is expected to be improved.<sup>11</sup>

The Suzuki-Miyaura reaction between bromobenzene and phenylboronic acid in water was used as a prototype reaction to evaluate the catalytic activities induced by interband transitions of porous Pd nanoparticles. Generally, the rate-determining step of this reaction is the oxidative addition of the aryl halide, which was proposed to be accelerated by hot electrons generated from the photocatalysts.<sup>15, 37, 38</sup> The performance of these photocatalysts was evaluated by their quantum yields; monitoring the quantum yields under photoirradiation at different wavelengths provided more mechanistic insight. As demonstrated in this work, keeping the same photon flux and reaction time (besides of preparing the same chemical concentration and temperature) was a critical experimental condition to make a fair comparison of the quantum yields across different excitation wavelengths. It was found that leaching of Pd from the mesoporous Pd nanoparticles was not a major contribution to the observed catalytic activities. Eventually, the observed wavelength dependence of quantum yields was correlated with the wavelength dependence

of the energy state of hot carriers, and a possible mechanism was proposed. This mechanism was overlooked in some previous studies<sup>38-41</sup>, and it deserves more attention in utilizing hot carriers for catalysis.

## 2.2 Experimental section

### 2.2.1 Synthesis of porous Pd nanoparticles

Mesoporous Pd nanoparticles were synthesized by following the method from the Yamauchi's group. In a 7-mL glass vial, 200  $\mu$ L THF (containing 8 mg PS<sub>(5000)</sub>-b-PEO<sub>(2200)</sub>, Polymer Source Co.), 160  $\mu$ L HCl (2 M), 500  $\mu$ L H<sub>2</sub>PdCl<sub>4</sub> (76.8 mM), 1140  $\mu$ L H<sub>2</sub>O and 2000  $\mu$ L ascorbic acid (0.1 M) were added and under stirring. The glass vial was then put in a water bath set at 50 °C for 10 h reduction reaction to form a dark grey solution, followed by centrifuging at 14,100 g-force and washing with THF and water (3:1 volume ratio) for three times. Eventually, the final product was calcinated in a muffle furnace at 200 °C for one hour to remove the solvent and most of the polymer.

### 2.2.2 Characterizations

The mesoporous Pd nanoparticle photocatalyst was characterized by UV-Vis spectroscopy (USB4000, Ocean Optics), DLS (Zetasizer Pro, Malvern Panalytical), SEM (Quanta 200, 5.0 kV, FEI), TEM (Talos F200C G2, 200 kV, Thermo Fisher Scientific), FTIR spectroscopy (Nicolet iS50R, Thermo Fisher Scientific) and TGA (TA Q2000, argon flow at 100 mL/min, heating rate of 10 °C/min, TA Instruments). The biphenyl product was extracted from the reaction solution by dichloromethane, then the solvent was evaporated, and the product was dissolved in deuterated chloroform (CDCl<sub>3</sub>) and quantified by <sup>1</sup>H-NMR (Varian-INOVA 400 MHz, Agilent Technologies) with mesitylene used as the internal standard. There was no signal of any other side products. The amount of leached Pd was determined by ICP-OES (Optima 5300 DV Inductively Coupled Plasma Optical Emission Spectrometer, PerkinElmer). The analyzed samples were prepared by collecting the supernatants after centrifuging the reaction solutions, followed by 800 °C calcination to remove all the organics, digestion with aqua regia, dilution to a final 1-5 % HNO<sub>3</sub> v/v concentration solution, and filtration with 0.2  $\mu$ m filter. Standard solutions were prepared with trace-metal-free nitric acid from a commercial standard solution (ICP Precious Metal Std, Inorganic Ventures Co.) The surface oxidation state of porous Pd nanoparticles before and after reactions was detected by x-ray photoelectron spectrometer (Nexsa, Thermo Fisher Scientific) with monochromated, micro-focused, low power Al K $\alpha$  X-ray source. The possible by-products generated from parallel processes were determined by GC-MS (7890A GC system and 5975C inert MSD, Agilent Technologies).

### 2.2.3 Typical photocatalyzed Suzuki–Miyaura reaction condition

In a 1x1 cm quartz cuvette (R-3010-T, Spectrocell), 21  $\mu$ L bromobenzene (0.2 mmol, 1 equiv.), 36 mg phenylboronic acid (1.5 equiv.), 495  $\mu$ L CTAC (cetyltrimethylammonium chloride, 400 mM), 600  $\mu$ L NaOH (sodium hydroxide, 1 M) and 884  $\mu$ L porous Pd nanoparticles stock solution were added under stirring. The stock porous Pd nanoparticle solution was prepared by dispersing the dry particles in water to have the final ratio of 0.78 % of [Pd<sub>atom</sub>] to [bromobenzene] (0.0078 equiv.) in the reaction solution. Then, the cuvette was sealed by a screw cap with rubber septa, then stirred under 1000 rpm and purged with

N<sub>2</sub> for 20 minutes to get rid of oxygen before being irradiated under different LEDs (Mounted type, Thorlabs). The photocatalyzed reactions were under constant stirring at 1000 rpm and controlled at room temperature by using cooling fans. The optical powers before and after the cuvette were recorded by power meters (PM100D console with S170C sensor, Thorlabs) for following calculation of absorbed photon flux. After a certain reaction time, the biphenyl product was extracted from the reaction solution by dichloromethane, then the solvent was evaporated at 50 °C in a vacuum oven for 20 minutes, and the product was dissolved in CDCl<sub>3</sub> and quantified by <sup>1</sup>H-NMR with mesitylene used as the internal standard. The NMR spectra and product yield calculation were listed in Note S8.

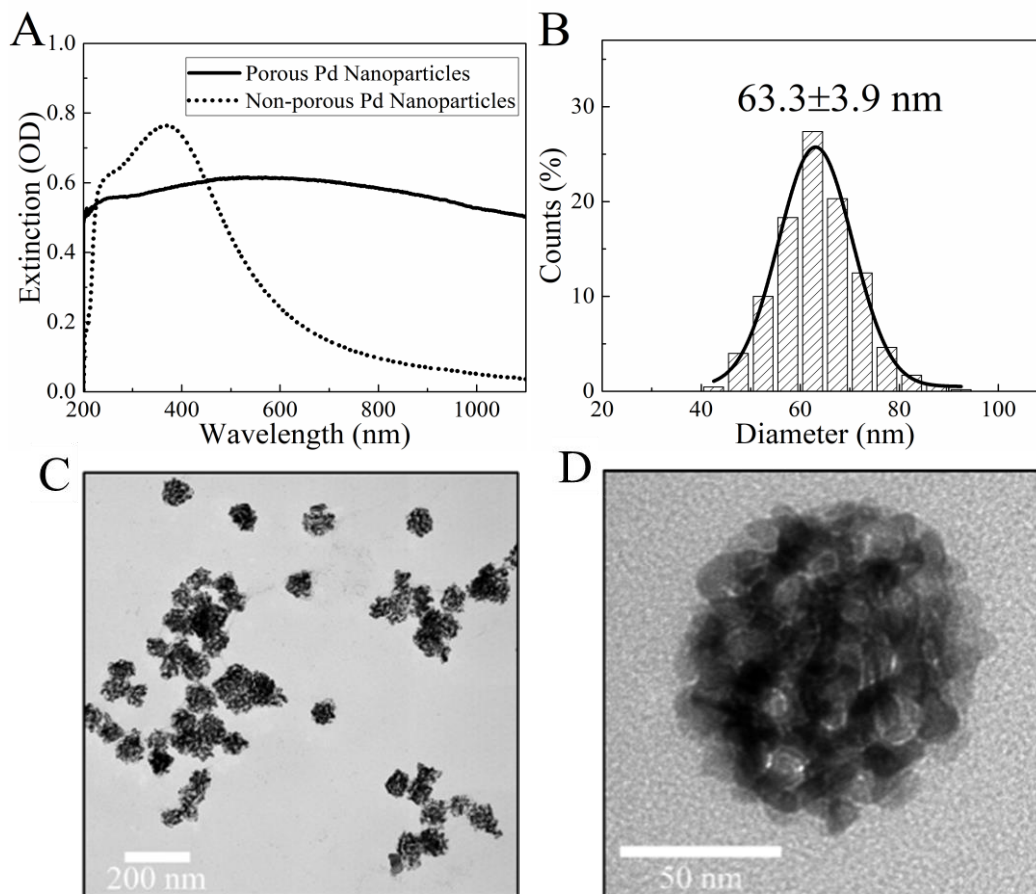


**Figure 2.1 Optical and morphological characterization of mesoporous Pd nanoparticles.**

(A) UV-Vis spectra of colloidal mesoporous Pd nanoparticles (solid line) in water and non-porous 50 nm Pd nanoparticles solution (dotted line) for comparison.

(B) Size distribution based on analyzing 500 nanoparticles from SEM image in Figure 2.4.

(C, D) Representative TEM images of mesoporous Pd nanoparticles.

#### 2.2.4 Quantum yield calculation

Using the same calculation in our previous work<sup>11</sup>, the quantum yield is defined as the ratio of the number of biphenyl molecules produced per second ( $\Delta N_{biphenyl}/\Delta t$ ) to number of photons absorbed per second ( $N_{abs}/s$ ).

$$Quantum\ Yield\ (\%) = \frac{\#(biphenyl\ produced/s)}{\#(photons\ absorbed/s)} \times 100\ \% = \frac{\frac{\Delta N_{biphenyl}}{\Delta t}}{\frac{N_{abs}}{s}} \times 100\ \%$$

In which:

$$\Delta N_{biphenyl} = 0.2\ mmol \times Product\ Yield \times 6.022 \times 10^{23}\ mol^{-1}\ (*)$$

$\Delta t$ : reaction time in second

$$\frac{N_{abs}}{s} = \frac{P_{absorbed}}{\frac{hc}{\lambda}}\ (**)$$

(\*) The product yield of the photocatalyzed reaction was determined by <sup>1</sup>H-NMR spectroscopy and further corrected by subtracting the background product yield of the non-irradiated reaction within the same reaction time.

(\*\*) ( $N_{abs}/s$ ) were quantified by measuring the optical power at positions before and after the cuvette having the reaction solution during the photoreactions.

$$Photon\ Flux\ (photons \cdot s^{-1} \cdot cm^{-2}) = \frac{N_{abs}}{s \times A} = \frac{P_{absorbed}}{\frac{hc}{\lambda} \times \pi(\frac{\varphi}{2})^2}$$

In which:  $\varphi$  is the beam size of the LED light that passes through the cuvette having the reaction solution. The beam size was 0.95 cm, which is smaller than the 1cm width of the cuvette.

### 2.3 Optical property of mesoporous Pd nanoparticles

Mesoporous Pd nanoparticles were prepared by a typical hard-template wet-chemical method, in which polystyrene-block-poly(ethylene oxide) and ascorbic acid acted as the template and the reductant, respectively.<sup>42</sup> The as-synthesized particles were cleaned by tetrahydrofuran (THF) and calcinated at 200 °C for one hour to remove the solvent and most of the polymer, and the porous structure was still preserved.<sup>42</sup> The dry particles were further characterized and used as the catalyst. Fourier-transform infrared spectroscopy (FTIR) did not detect any vibrational signal of organic compounds on the dry particles, indicating that the catalyst does not have much polymer left (Figure 2.2). Thermogravimetric analysis (TGA) confirmed that 22 % of the dry particles' weight is the leftover polymer (Figure 2.3).



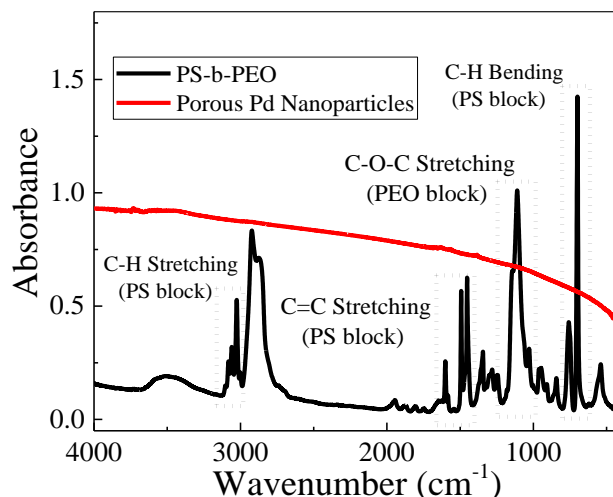


**Figure 2.2** FTIR spectra of mesoporous Pd nanoparticles and PS-b-PEO for comparison. Mesoporous Pd nanoparticle powder (0.9 % w/w to KBr) and PS-b-PEO polymer (3.3 % w/w to KBr) samples were prepared in KBr matrix for FTIR measurements. The high background of the Pd nanoparticle sample is due to the light scattering of the aggregated microstructure of the nanoparticles. Considering a large amount of Pd nanoparticles in the beam path, the undetected vibration signal of any organic compound indicates that the catalyst does not have much polymer left.

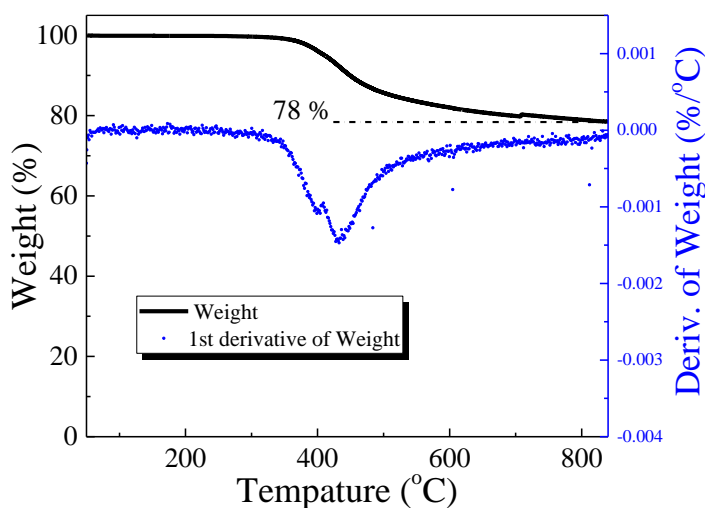


**Figure 2.3** TGA of porous Pd nanoparticles under argon atmosphere. The remained polymer in the porous Pd nanoparticles is about 22 % of the overall weight. The assignment of the weight lost was based on the TGA of similar polymers.<sup>43, 44</sup>

The particles have an average hydrodynamic diameter of  $79.9 \pm 5.9$  nm and a zeta potential of 0.6 mV when dispersed in water and measured by dynamic light scattering (DLS), a narrow size distribution of  $63.3 \pm 3.9$  nm as determined by scanning electron microscopy (SEM) (Figure 2.1B and Figure 2.4A), and an average pore size of  $11.3 \pm 3.3$

nm (analyzed 100 pores in Figure 2.1C). The porous Pd nanoparticles had a large specific Brunauer, Emmett and Teller (BET) surface area of  $57.1 \text{ m}^2/\text{g}$  and average pore size of 5.6 nm, determined by  $\text{N}_2$  adsorption-desorption isotherms (See details in Figure 2.5). The particles have polycrystalline structures with grain sizes that are larger than the pore wall thickness<sup>42</sup>, and the pores form open channels throughout the particles as shown in a series of tilt transmission electron microscopy (TEM) images (Figure 2.6).

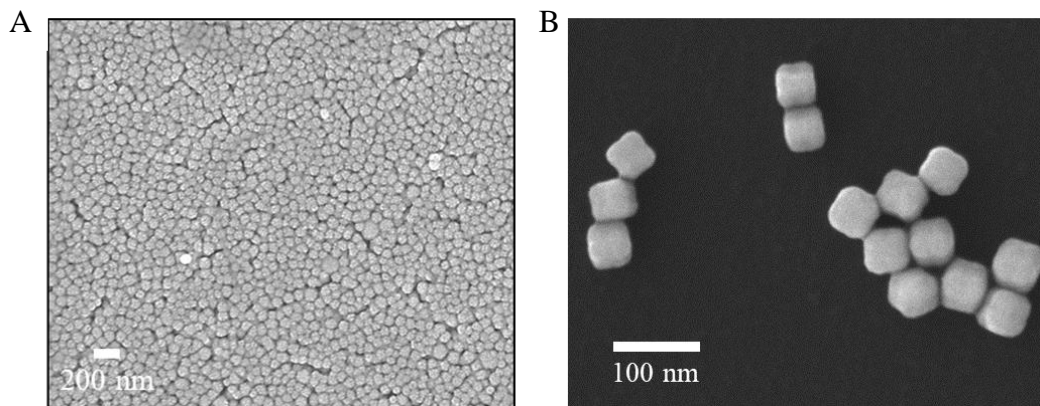


**Figure 2.4** SEM images porous and non-porous Pd NPs. (A) Porous Pd nanoparticles prepared by following the method developed by Yamauchi and coworkers<sup>42</sup> and (B) Non-porous Pd nanoparticles synthesized by following the method published by Wenxin Nie *et al.*<sup>36</sup>

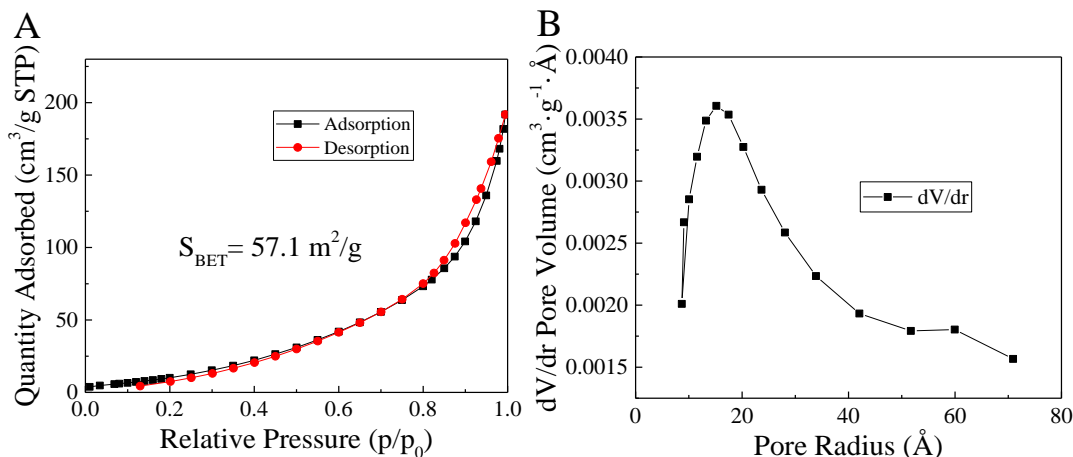


**Figure 2.5** Surface area and pore size analysis of porous Pd NPs. (A)  $\text{N}_2$  adsorption-desorption isotherms and (B) pore radius distribution of porous Pd nanoparticles.

The specific Brunauer, Emmett and Teller (BET) surface area of the porous Pd nanoparticles was  $57.1 \text{ m}^2/\text{g}$ , which was around 7 times larger than that of the non-porous Pd nanoparticles with a similar diameter (see calculations below). The pore volume of the porous Pd nanoparticles was  $0.30 \text{ cm}^3/\text{g}$  from the above measurement. The pore radius distribution acquired from Barrett, Joyner, and Halenda (BJH) desorption showed an average pore radius of 2.8 nm, or a pore size of 5.6 nm. The difference of pore size from BJH (5.6 nm) and TEM (11.3 nm) data came from different perspectives of the two measurements and non-uniformity of pore structures.

Estimated surface area of 1 g spherical nonporous Pd nanoparticles with an average size of 60 nm :

Mass of one nanoparticle ( $m_1$ ):

$$m_1 = \rho \cdot V = \rho \cdot \left(\frac{4}{3}\pi r^3\right)$$

$$\rho: \text{density of Pd, } 12.023 \times 10^3 \frac{\text{kg}}{\text{m}^3}$$

$V$ : volume of one nanoparticle

$r$ : radius of one nanoparticle,  $30 \times 10^{-9} \text{ m}$

$$\text{So, } m_1 = 1.360 \times 10^{-18} \text{ kg} = 1.360 \times 10^{-15} \text{ g}$$

Then, the number of nanoparticles in 1 g Pd (#):

$$\# = \frac{1 \text{ g}}{1.360 \times 10^{-15} \text{ g}} = 7.354 \times 10^{14}$$

Surface area for one nanoparticle ( $S_1$ ):

$$S_1 = 4\pi r^2 = 1.131 \times 10^{-14} \text{ m}^2$$

Thus, the estimated total surface area of the nonporous Pd nanoparticles ( $S_E$ ) will be

$$S_E = \# \cdot S_1 = 8.32 \text{ m}^2/\text{g}$$

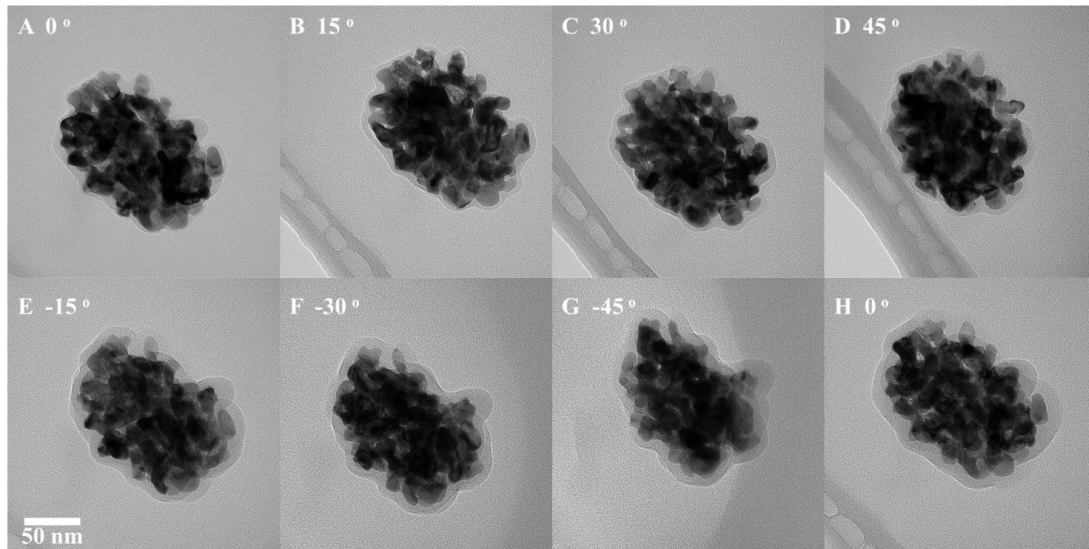


**Figure 2.6** A series of tilt TEM images of a typical mesoporous Pd nanoparticle with various tilt angles of the sample holder. The grey area around the nanoparticle is the carbon deposition induced by the long exposure of the sample to the electron beam. The fact that the particle still preserves its 3D structure perfectly under a long exposure time (see insets **A** and **H**) indicates that the porous structure is constructed by the inter-connections of small parts of the particles rather than the aggregation (induced by Van der Waals force) of small individual nanoparticles.

The mesoporous Pd nanoparticle solution has a broad UV-Vis spectrum as compared to that of non-porous forms (Figure 2.1A).<sup>35, 36</sup> For example, the non-porous 50 nm Pd nanoparticles (see a SEM image in Figure 2.4B) with a comparable mass to our catalyst

have a broad absorption peak at 370 nm due to both plasmon resonance and interband transitions, but the absorption drops significantly in the red-photon and longer wavelength regions.<sup>36, 45</sup> In contrast, the porous particles' plasmon resonance absorption shifted significantly to these low energy regions, but the interband transitions stayed in the UV-Vis region due to the unchanged electronic structure of Pd (Figure 2.1A). Similarly, the mesoporous form of gold or platinum nanoparticles also shows significant red-shifts of plasmon resonances to the near IR regions.<sup>46, 47</sup> The plasmonic coupling between adjacent crystal domains or pore walls within proximity may be responsible for these red-shifts.<sup>42, 48</sup> Thus, the optical absorbance of porous Pd nanoparticles in the 400-600 nm region focused in this study can only be assigned to interband transitions. On a drop-cast sample, the scattering intensity measured by an integrating sphere and a tunable laser follows approximately a  $1/\lambda^4$  dependence, resembling Rayleigh scattering (Figure 2.7).

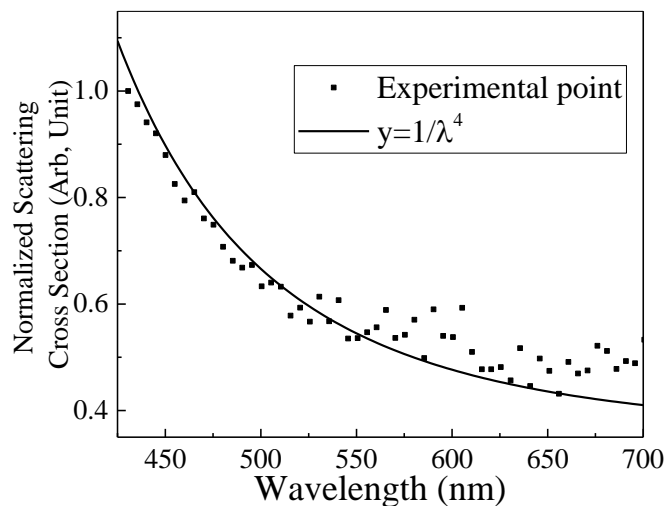


**Figure 2.7** Normalized scattering cross section of porous Pd nanoparticles drop-casted on a glass slide and a plot of  $y=1/\lambda^4$  function for comparison. See experimental details in Note S1.

Further measurement by a home-built setup for determining optical scattering and extinction on the colloidal solution in a 1x1cm quartz cuvette showed that the total light scattering in the range of 400 to 800 nm of the colloidal solution was almost neglectable. Less than 3 % of the incident photons were scattered from the photocatalyst and more than 97 % were absorbed (Figure 2.8 and Note S1). From these results, it was concluded that the porous Pd nanoparticles had strong absorbance in the 400-600 nm region, and the dominant contribution to this absorbance is the interband transitions but not the plasmon resonance.

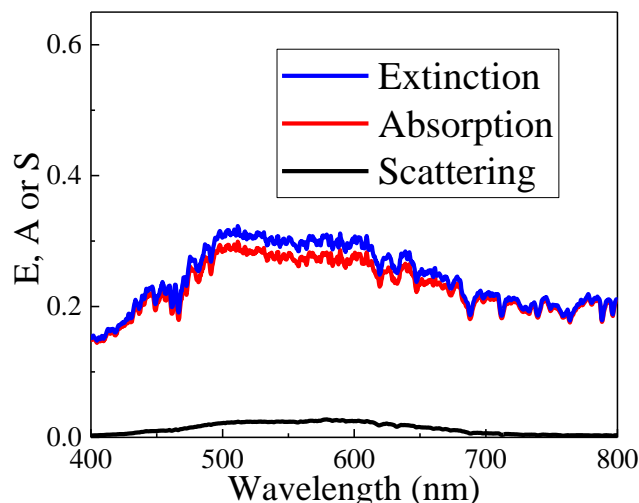


**Figure 2.8** Extinction, total scattering (integrating over all scattering angles) and absorption spectra. The ratio of total scattering to extinction was less than 3 %, thus the scattered photons can be neglected in quantum yield calculation. Note that the extinction curve does not look flat as compared to the spectrum in Figure 2.7 due to the low quality of our neutral density filters. See experimental details in Note S1.

#### 2.4 Photocatalyzed condition of mesoporous Pd nanoparticles

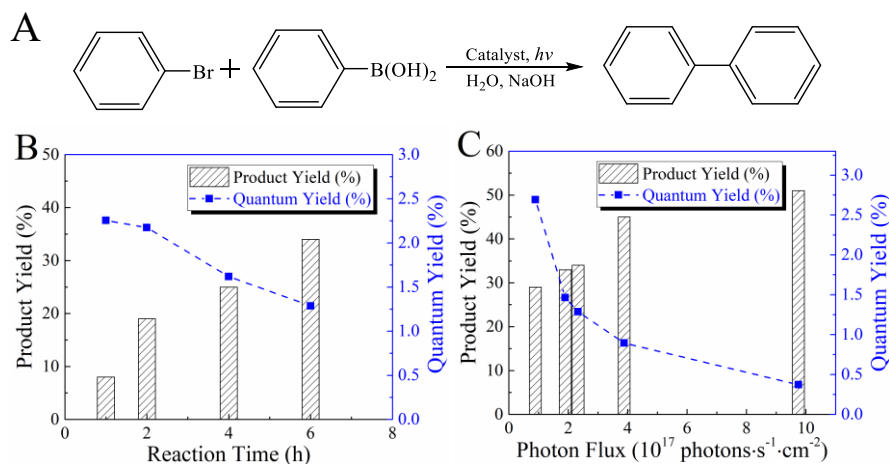


**Figure 2.9** Suzuki–Miyaura C–C coupling reaction for evaluating photocatalytic performance of porous Pd nanoparticles. (A) Typical reaction process. (B and C) Measured product yields (left axis) and quantum yields of the catalyst (right axis) under 405 nm LED irradiation with: (B) different reaction times under the same photon flux (around  $2.4 \times 10^{17}$  photons·s<sup>-1</sup>·cm<sup>-2</sup>), and (C) different photon fluxes under the same 6-hour reaction. Small background product yields of the non-irradiated reactions with the catalyst were subtracted from the observed product yields when calculating the quantum yields.

Suzuki–Miyaura reactions have been employed to evaluate the photocatalytic performance of Au–Pd alloy nanoparticles or Pd nanoparticles loaded on metal oxides or

WS<sub>2</sub>.<sup>38, 49-51</sup> Besides the versatile applications of this reaction in creating C-C bonds and the transparent solutions of reactants and products for convenient photocatalysis study, the oxidative addition of aryl halides (*i.e.*, the rate-determining step of the catalytic cycle)<sup>52</sup> could be catalyzed by hot electrons generated from photo-exciting the Pd nanoparticle catalyst. In our typical reaction condition at room temperature with different light-emitting diode (LED) light sources, bromobenzene and phenylboronic acid served as the coupling partners, sodium hydroxide as a base, and cetyltrimethylammonium chloride (CTAC) as a solubilizer to facilitate the dissolution of organic reactant and product into the aqueous solution (Figure 2.9A).<sup>49, 50</sup> The zeta potential of the porous Pd nanoparticle photocatalyst is around 60 mV in the reaction solution, which suggests some degree of adsorption of CTAC on the particles and explains for their high stability during the reaction. This DLS analysis also confirmed that the particles did not aggregate in the solution, and they maintained in colloidal form during the reaction. The biphenyl product was extracted from the reaction solution by dichloromethane and analyzed by proton nuclear magnetic resonance (<sup>1</sup>H-NMR). The reaction time was purposely kept short enough to get a reasonable conversion range for reliable kinetic comparison<sup>53</sup>, though a higher conversion was achieved with a longer reaction time.

The photothermal effect on the catalysis is neglectable in our experiment as local heating is minimal under continuous-wave irradiation and stirring (see detailed explanation in Note S2).<sup>54, 55</sup> When considering the following processes after a colloidal metal nanoparticle in a stirring solution absorbs a single photon: i) electron thermalization due to electron-electron and electron-phonon couplings (within few picoseconds<sup>56, 57</sup>), ii) heat transfer from the particle to the local solvent (within 3 nanoseconds<sup>54</sup>), iii) time gap for absorbing the second photon (about hundreds of nanoseconds, see Note S2), then it is obvious that the nanoparticle dissipates all the heat to the surrounding environment long before it absorbs the second photon. Since the hot carriers are well thermalized before the nanoparticle can transfer heat to the environment, it is reasonable to estimate the average temperature rise of the particle based on the energy of an absorbed photon, specific heat of Pd and the particle's mass. This temperature rise is about 0.001°C under our experimental condition (Note S2), which should have no photothermal effect on our studied reaction. Under the constant stirring at high speed of the reaction solution, the transient heat in the LED beam path should be distributed evenly in the entire solution.<sup>58</sup> The macroscopic temperature of reaction solutions rose only 1-2 °C as cooling fans were used.

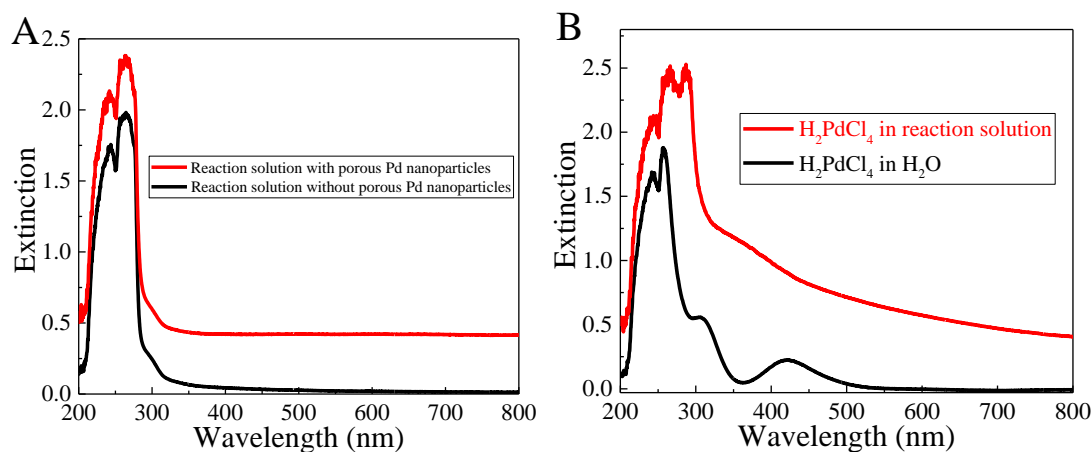


**Figure 2.10** (A) UV-Vis spectra of reaction solutions with and without porous Pd nanoparticles. (B) UV-Vis spectra of  $[\text{PdCl}_4]^{2-}$  complex in the reaction solution and in water.

A UV-Vis spectrum of reaction solution without the catalyst showed no obvious absorption at any wavelengths longer than 400 nm (Figure 2.10A). Blank tests on the reaction without the catalyst under different excitation wavelengths did not show any detectable product yield (Table 2.1). These control experiments confirmed that the light absorption of reactants could be ignored in our experiments, and the reaction under irradiation almost does not happen without the photocatalyst. It is worth noting that the reaction with the catalyst under the dark condition in 6 hours gave a background product yield of 5 %. This background yield was subtracted from the product yields that were used to calculate quantum yields for the photocatalyzed reactions with 6-hour irradiation. For photocatalyzed reactions with shorter irradiation times, the corresponding background yields were extrapolated from the ratios between the actual reaction times and 6 hours. This extrapolation is reasonable for a very low conversion range where the reaction rate is assumed to be unchanged.<sup>59</sup>

**Table 2.1** Product yield (without catalyst) under different excitation wavelengths.

Entry	Catalyst	Wavelength (nm)	Incident Light (mW)	Absorbed Light (mW)	Product Yield (%)
1	none	405	201	14	Not detected
2	none	450	143	2	Not detected
3	none	470	210	11	Not detected
4	none	490	124	12	Not detected
5	none	530	105	5	Not detected
6	none	595	213	4	Not detected

Reaction conditions: See typical condition details in experimental section. There was no catalyst used and the reaction time was 6 hours.

## 2.5 Establishing the same reaction time and photon flux for comparing of quantum yields of photocatalyst under various excitation wavelengths

Quantifying the efficiency of photocatalysts is an important criterion for practical application. This efficiency, here defined as the quantum yield of the catalyst, is calculated as the ratio of the number of product molecules to the number of absorbed photons. This quantity has two important benefits: it helps us understand the photocatalysis mechanism, and it establishes the effective cost of using photons for catalyzed chemical reactions. In practice, when monitoring a photocatalyzed reaction, the quantum yield of the photocatalyst is calculated as the number of product molecules produced per a specific time divided by the number of photons absorbed during that time. These two quantities can be extracted from the measured reaction rate and optical power absorbed by the photocatalyst. It is obvious that the reaction rate decreases as the reaction proceeds. Since the photon absorption rate is unchanged at any given time, the measured quantum yield, as defined above, is expected to be lower when the reaction happens for a longer time.

**Table 2.2** Calculated quantum yield under 490 nm LED irradiation when changing reaction time.

Entry	Catalyst	Wavelength (nm)	Absorbed Light (mW)	Absorbed Photon Flux ( $10^{17}$ photons $\cdot$ s $^{-1}\cdot$ cm $^{-2}$ )	Reaction Time (h)	Product Yield (%)	Quantum Yield (%)
1	Porous Pd NPs	Dark	NA	NA	6	5	NA
3	Porous Pd NPs	490	67	2.3	1	7	1.6
4	Porous Pd NPs	490	65	2.3	2	13	1.1
5	Porous Pd NPs	490	67	2.3	4	17	0.94
6	Porous Pd NPs	490	70	2.4	6	29	0.86

Reaction conditions: See typical condition details in experimental section. The incident light was kept at around 123 mW and all the absorbed photon fluxes were kept as close together as possible.

NPs for nanoparticles, NA for not applicable.

To demonstrate this reasoning, the interval reaction rates were measured (*i.e.*, total product molecules formed/total reaction time in seconds) when the reaction times were varied from 1 to 6 hours under the same absorbed photon flux of a 405 nm LED. The quantum yields reduced from 2.3 % to 1.3 % (Figure 2.9B). The same trend was also observed under 490 nm LED irradiation (Table 2.2). This time-dependent behavior is similar to the case of using turn over frequency (TOF) to quantify the efficiency of catalysts under non-irradiated conditions. The measured TOF value always reduces as the catalyzed reaction proceeds, regardless of using homogeneous or heterogeneous catalysts.<sup>59, 60</sup> The



TOF does not entirely reflect the kinetics of a catalyzed reaction, and the rate law should be the better description.<sup>60</sup> In our study, since we wanted to compare quantum yields of the photocatalyst under various excitation wavelengths, we did not need to derive a rate law of our photocatalyzed reaction under each excitation wavelength. However, we did need to have the photocatalyzed reactions run for the same time interval when comparing quantum yields of the catalyst under different excitations.

**Table 2.3** Calculated quantum yield under 470 nm LED irradiation when changing photon flux.

Entry	Catalyst	Wavelength (nm)	Incident Light (mW)	Absorbed Light (mW)	Absorbed Photon Flux ( $10^{17}$ photons· $s^{-1}$ · $cm^{-2}$ )	Product Yield (%)	Quantum Yield (%)
1	Porous Pd NPs	Dark	NA	NA	NA	5	NA
2	Porous Pd NPs	470	100	70	2.3	37	1.1
3	Porous Pd NPs	470	207	143	4.7	40	0.66
4	Porous Pd NPs	470	502	282	9.4	42	0.31

Reaction conditions: See typical condition details in experimental section and the reaction time was 6 hours.

Using a similar argument based on chemical kinetics as mentioned above, a higher photon flux condition creates more photo-excited nanoparticles, and effectively causes higher product yield and lower reactant concentration. As the reaction proceeds, each nanoparticle catalyst encounters a decreasing concentration of reactants, and the efficiency of extracting hot carriers is reduced, hence the quantum yield will be effectively reduced. Using the same reaction condition with 405 nm LED irradiation and 6 hour reaction time for comparison, when the photon flux increases from  $0.9 \times 10^{17}$  to  $9.8 \times 10^{17}$  photons· $s^{-1}$ · $cm^{-2}$ , the measured quantum yield decreases from 2.7 % to 0.4 % (Figure 2.9C). A similar trend was observed with 470 nm LED irradiation (Table 2.3).

To recap, when comparing the quantum yields of the photocatalyst under different irradiation condition, we should keep not only the same starting experimental condition but also the exact same reaction time and photon flux. This prerequisite is critical for revealing the photocatalytic mechanism in the next section.

## 2.6 Wavelength dependence of photocatalytic activities

**Table 2.4** Product yield from the control Experiment I, II and III in Note S3.

Entry	Catalyst	Wavelength (nm)	Product Yield from Experiment I (%)	Product Yield from Experiment II (%)	Product Yield from Experiment III (%)
1	Porous Pd NPs	405	34	9	7
2	Porous Pd NPs	450	35	11	6
3	Porous Pd NPs	470	37	9	4
4	Porous Pd NPs	490	29	6	3
5	Porous Pd NPs	530	17	9	3
6	Porous Pd NPs	595	11	7	3

Reaction conditions: See typical condition details in experimental section and the reaction design in Note S3. The absorbed optical power was the same in all experiments.

Before moving into the comparison of quantum yields at different excitation wavelengths, we want to examine any catalytic mechanism other than the hot carriers induced photocatalysis mechanism. It is known that leaching of Pd atoms from nanostructures into the reaction solution may complicate the catalytic mechanism<sup>38, 53, 61, 62</sup>. In our hot filtration tests (see details in Note S3), the photocatalyzed reactions were allowed to proceed for one hour followed by the removal of nanoparticles from the reaction solution via centrifugation, then the reactions were allowed to continue for another 5 hours before determining the product yields. These product yields were much lower than those of full reactions with 6-hour irradiation (Table 2.4) but were higher than the yields of control experiments in which the photocatalyzed reactions were only let to react for one hour and the product yield was determined immediately.

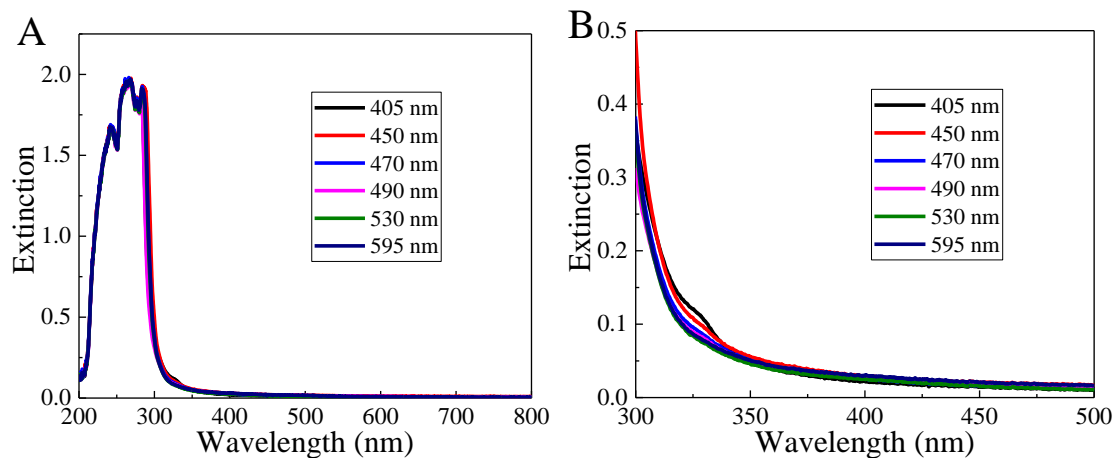


**Figure 2.11** (A) UV-Vis spectra of the supernatants after 1 h reaction in of the leaching test in Experiment II under various excitation conditions. (B) Enlarged part from 300-500 nm of a. See Experiment II details in Note S3.

UV-Vis spectra of the supernatants after 1 h reaction (Figure 2.11) did not exhibit any noticeable features of  $[\text{PdCl}_4]^{2-}$  complex (Figure 2.10B) or the mesoporous Pd nanoparticles. These results indicate that the supernatants from hot filtration have little leached Pd that can also catalyze the reaction, and the contribution of leached Pd to the observed catalysis is small. Also, the above result is also consistent with other studies under similar reaction conditions using Au–Pd alloy nanoparticle photocatalyst loaded on  $\text{ZrO}_2$ .<sup>38, 63</sup> More importantly, this contribution did not exhibit a clear wavelength dependence in our experiments (2.4).

Furthermore, inductively coupled plasma optical emission spectroscopic (ICP-OES) analysis for Pd in the supernatants of the 6-hour reactions under either dark or irradiation conditions showed that the amount of Pd was under detection limit, thus the utmost Pd leached based on the detection limit was estimated to be about 1.2 % of the total Pd in the nanoparticle photocatalyst (See details in Note S4).

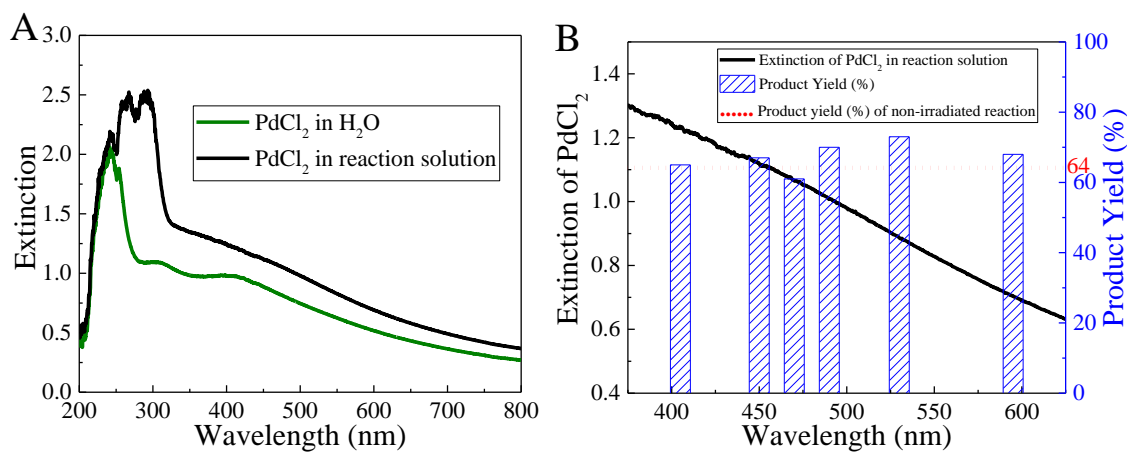


**Figure 2.12** PdCl<sub>2</sub> was used as a pre-catalyst (the source of generating Pd(0) for the catalytic cycle) for the Suzuki–Miyaura reaction. (A) UV-Vis spectra of PdCl<sub>2</sub> in H<sub>2</sub>O and reaction solution. (B) Product yield (right axis) under different excitation wavelengths and a UV-Vis spectrum of PdCl<sub>2</sub> in reaction solution (left axis) for reference. The red-dot line represents the product yield of a non-irradiated reaction. The reaction conditions were similar to a typical procedure in experimental section, but the reaction time was reduced to 0.5 h due to the high activities of the homogeneous Pd<sup>2+</sup> pre-catalyst. The amount of PdCl<sub>2</sub> was used with a ratio of 1 % of  $[\text{Pd}_{\text{atom}}]$  to [bromobenzene].

While the chemical structure or formula of this leached Pd species is still unknown and not the focus of this study, another control reaction using PdCl<sub>2</sub> as the pre-catalyst (the source of generating Pd(0) for the catalytic cycle) showed no wavelength dependence of the product yields (Figure 2.12). This test indicates that the complete catalytic cycle of the molecular Pd catalyst does not depend on any tested wavelengths. Lastly, X-ray

photoelectron spectroscopy (XPS) showed no distinct changes of the oxidation state of Pd(0) in porous Pd nanoparticles before and after reactions in the dark and photocatalyzed conditions (Note S5).

Overall, it is clear that the photo-excited Pd nanoparticles, hence the hot electrons and holes generated in the particles, are the key catalysts of the studied reaction, and the wavelength dependence of quantum yields must be attributed to the different states of hot carriers generated by different excitation wavelengths.

In experiments determining the wavelength dependence of quantum yields of the catalyst, the same absorbed photon flux (around  $2.4 \times 10^{17}$  photons $\cdot$ s $^{-1}$  $\cdot$ cm $^{-2}$ ) and reaction time (6 hours) were maintained for each excitation wavelength. Interestingly, the quantum yields do not track the extinction spectrum of porous Pd nanoparticles (Table 2.5 and Figure 2.13). Indeed, the quantum yields are much higher in the shorter wavelength region.

**Table 2.5** Calculated quantum yield under various excitation wavelengths and same photon flux.

En-try	Catalyst	Wave-length (nm)	Incident Light (mW)	Absorbed Light (mW)	Absorbed Photon Flux ( $10^{17}$ photons $\cdot$ s $^{-1}$ $\cdot$ cm $^{-2}$ )	Product Yield (%)	Quantum Yield (%)
1	Porous Pd NPs	Dark	NA	NA	NA	5	NA
2	Porous Pd NPs	405	150	81	2.3	34	1.3
3	Porous Pd NPs	450	190	74	2.4	35	1.2
4	Porous Pd NPs	470	100	70	2.3	37	1.1
5	Porous Pd NPs	490	123	70	2.4	29	0.86
6	Porous Pd NPs	530	100	61	2.4	17	0.26
7	Porous Pd NPs	595	100	55	2.4	11	0.18

Reaction conditions: See typical condition details in experimental section and the reaction time was 6 hours. All the absorbed photon fluxes were kept as close together as possible. The data is plotted in Figure 2.13 below.

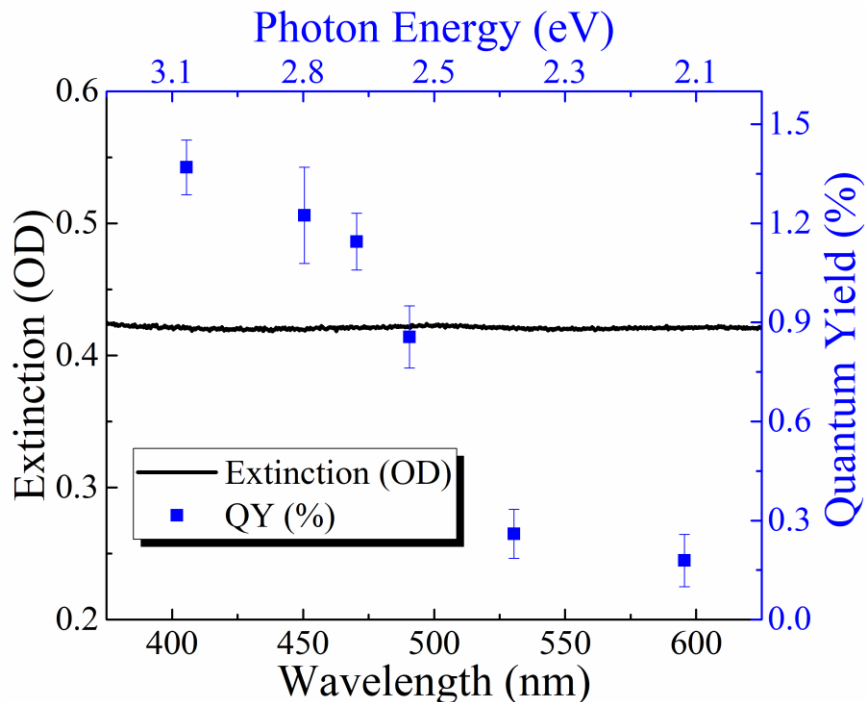


**Figure 2.13** Photocatalysis of porous Pd nanoparticles for Suzuki–Miyaura C-C coupling reaction. Wavelength dependence of quantum yields (right axis) and the optical spectrum of reaction solution with porous Pd nanoparticles (left axis) for comparison. Each error bar is one standard deviation of the mean.

## 2.7 Proposed catalytic mechanism and related control experiments

In order to explain this observation, it is important to correlate this wavelength-dependent trend with the state of hot holes and electrons generated in the porous Pd nanoparticles at different excitation wavelengths. It is known that each interband transition in *d*-block metals generates a pair of hot electron and hole, in which the hot electron resides near the Fermi level, and the hot hole resides in the *d*-band. When shorter wavelength photons are absorbed, the holes reside at much lower energy states or “deeper” in the *d*-band, but the electrons remain almost the same energy just above the Fermi level.<sup>14, 26, 64</sup> Thus, a possible photocatalytic mechanism was proposed in Figure 2.14, emphasizing on the role of deeper hot holes with stronger oxidizing power for accelerating the oxidative addition step of aryl halide, a rate determining step in the C-C coupling catalytic cycle.<sup>52</sup>

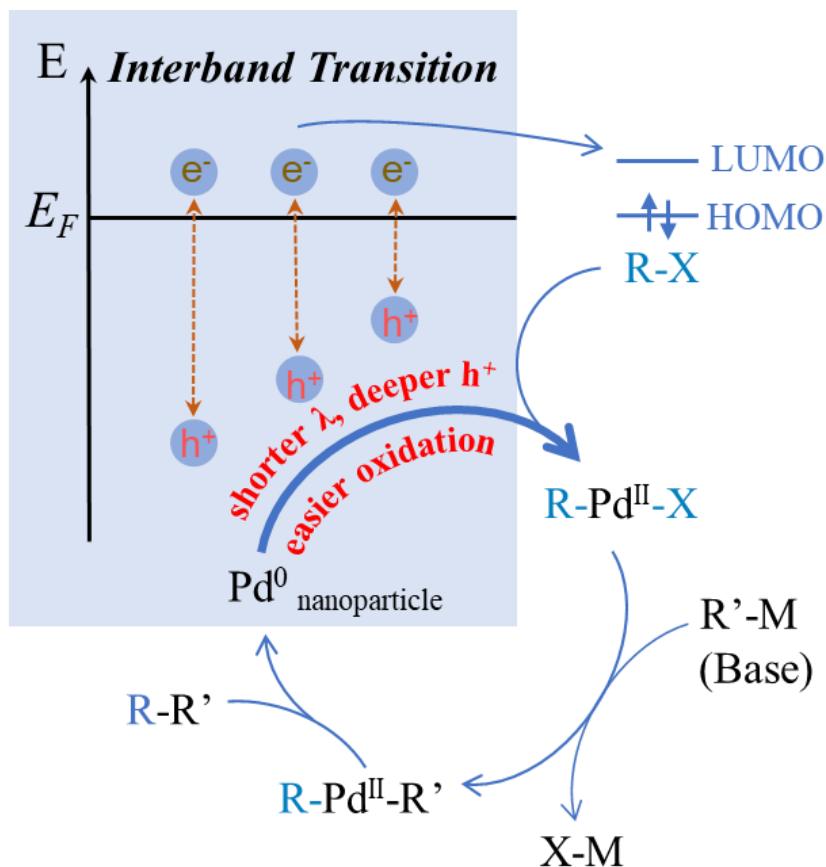


**Figure 2.14** Proposed mechanism. Proposed photocatalytic mechanism of hot holes in accelerating the oxidative addition, a rate-determining step of the catalytic cycle.

In other words, deeper holes have much lower energy than Fermi level, and the lowest possible energy (as compared to vacuum level) is  $E_{hole}^{NP} (eV) = E_F^{NP} - h\nu$ . The reduction potential of Pd(II)/Pd(0) for the nanoparticle photocatalyst under the influence of these holes,  $E_{Pd(II)/Pd(0)}^{NP-hole} (V \text{ vs SHE})$ , can be determined by this relationship:  $E_{hole}^{NP} = -4.44 eV + eE_{Pd(II)/Pd(0)}^{NP-hole}$ .<sup>55, 65</sup> Thus, deeper holes lower the reduction potential of Pd(II)/Pd(0) and favor the oxidation of Pd on the nanoparticle catalyst. Thus, more R-Pd<sup>II</sup>-X intermediates are produced, and eventually the reaction yields and the quantum yields increase. Direct detection of R-Pd<sup>II</sup>-X intermediates is still a challenge,<sup>66</sup> however, the deeper hot holes have been observed to catalyze the oxidation of metal nanoparticles better.<sup>10, 13, 67</sup> Thus, the oxidative addition step in this study must be catalyzed by the hot holes.

Figure 2.13 shows that the quantum yield starts to pick up at around 530 nm region and increases drastically around 490 nm region, resembling a step-function-like dependence of the quantum yields to the excitation wavelengths. This behavior suggests a threshold of photon energy is needed to overcome the barrier of the oxidative addition reaction.

**Table 2.6** Product yield of the reaction with and without isopropanol.

Entry	Catalyst	Wavelength (nm)	Product Yield without isopropanol (%)	Product Yield with isopropanol (%)
1	Porous Pd NPs	Dark	5	5
2	Porous Pd NPs	405	34	4
3	Porous Pd NPs	490	29	4
4	Porous Pd NPs	595	11	7

Reaction conditions: See typical condition details in experimental section and the reaction time was 6 hours. The absorbed optical power was the same in all experiments. Isopropanol (0.3 mmol, 1.5 equiv.) was used as a hole scavenger.

The crucial role of hot holes involved in the oxidative addition step was further confirmed by adding a hole scavenger, isopropanol, to the reaction. Under different excitation wavelengths, the product yields were quite close to that of a non-irradiated reaction (Table 2.6). This result can be explained by the fact that isopropanol is a stronger reducing agent ( $E^\circ$  of acetone/isopropanol is around 0.76 V vs SHE)<sup>68</sup> than Pd ( $E^\circ$  of Pd(II)/Pd(0) is around 0.92 V vs SHE)<sup>69</sup> and that the holes are quenched by isopropanol before they can catalyze the formation of R-Pd<sup>II</sup>-X intermediate.

**Table 2.7** Product yield of control reaction with only one reactant used.

Entry	Catalyst	Reactant	Wavelength (nm)	Product Yield (%)
1	Porous Pd NPs	Phenylboronic acid	Dark	Not detected
2	Porous Pd NPs	Phenylboronic acid	405	Not detected
3	Porous Pd NPs	Phenylboronic acid	490	Not detected
4	Porous Pd NPs	Phenylboronic acid	595	Not detected
5	Porous Pd NPs	Bromobenzene	Dark	Not detected
6	Porous Pd NPs	Bromobenzene	405	Not detected
7	Porous Pd NPs	Bromobenzene	490	Not detected
8	Porous Pd NPs	Bromobenzene	595	Not detected

Reaction conditions: See typical condition details in experimental section and the reaction time was 6 hours. The absorbed optical power was the same in all experiments.

To address the concern of homocoupling of phenylboronic acid<sup>70</sup> that could be catalyzed by the hot holes<sup>15</sup> or bromobenzene to the biphenyl, a series of control experiments using only either reactant showed non-detected product under various irradiation conditions (Table 2.7). Other control experiments with 4-bromoanisole and phenylboronic acid under the dark and 405 nm irradiation conditions confirmed that hetero-coupled 4-methoxy-1,1'-biphenyl was the only product (see details in Note S6).

In addition, some other possible side reactions including deborylation, debromination or, substitution by hydroxyl group of the reactants were neglectable as compared to the formation of the biphenyl product as confirmed by gas chromatography–mass spectrometry (GC-MS, see details in Note S7).

Moreover, as we mentioned in our hot filtration tests, the leaching of Pd atoms (in the form of molecular Pd species) has a very small contribution to the observed product yield, thus the R-Pd<sup>II</sup>-X intermediate catalyzed by hot holes is likely to stay on the nanoparticle surface, and the consequent catalytic steps (*e.g.*, transmetallation, reductive elimination) may happen on this surface, as suggested by other studies.<sup>52, 71</sup>

Our proposed mechanism provides another insight into the role of deep holes in the photocatalysis of Pd nanoparticles. A previous work using non-porous Pd nanoparticles on ZrO<sub>2</sub> powder concluded that hot electrons played a decisive role in the oxidation addition step. It was proposed that the shorter excitation wavelengths generated higher energy electrons due to interband transitions, and the hotter electrons catalyzed the oxidative addition step better.<sup>50</sup> In fact, as we discussed above, the general physical picture of shorter wavelength excitation in the interband transition regime is the hot electrons reside near the Fermi level, and hot holes reside deeper in the *d*-band.<sup>14, 26, 64</sup> Thus, the observed wavelength dependence of the quantum yields in that experiment could be explained by the stronger oxidizing power of the hot holes in the deeper *d*-band, as suggested in Figure 2.14. The hot electrons near the Fermi level may activate the aryl halide by promoting electron transfer from the metal to the LUMO of the aryl halide, but this step should not show a strong wavelength dependence in the interband transition regime.

## 2.8 Discussion on photocatalytic efficiency compared with other photocatalysts

The wavelength dependence of quantum yield or reaction yield of similar C-C coupling reactions was also observed in other photocatalysts,<sup>15</sup> such as Au-Pd alloy nanoparticles supported on ZrO<sub>2</sub><sup>38</sup> or Pd nanoparticles decorated on gold nanorods<sup>49</sup>. However, the role of hot holes generated from interband transitions was not fully explored yet. It is important to mention that our porous Pd nanoparticle photocatalyst has several advantages of revealing the photocatalytic mechanism, such as the suppression of plasmon resonance and the dominant contribution of interband transitions in the optical region studied, a very low light scattering for determining quantum yield with high accuracy, and no interference of supporting materials to the photocatalytic interpretation. Furthermore, our catalyst does show a higher photocatalytic efficiency as compared to the non-porous Pd nanoparticles and some other catalysts under similar experimental conditions (see comparison in Table 2.8), probably because the porous structure increases the probability of hot carrier diffusion to the catalyst's surface.<sup>11, 72, 73</sup> It is known that the hot holes have smaller kinetic energy



and shorter mean free path than electrons do,<sup>26</sup> thus the porous structure may overcome these obstacles.

**Table 2.8** Comparison of photocatalytic efficiency of Suzuki-Miyaura reaction between previous works and the current work.

Photocatalyst	Reactant	Reaction Condition	Light source, wavelength and intensity	Photocatalytic efficiency	Reference
Au-Pd/ZrO <sub>2</sub>	3-Iodo-toluene	30 °C, 6 h, Ar	Halogen lamp, 400 nm, 0.5 W/cm <sup>2</sup>	AQY, 0.3 %	38
Pd/ZrO <sub>2</sub>	3-Iodo-toluene	30 °C, 6 h, Ar	Halogen lamp, visible, 400-750 nm, 0.5 W/cm <sup>2</sup>	AQY, 1.2 %	38
TiO <sub>2</sub> -AA-Pd (Ascorbic Acid)	Iodo-benzene	70 °C, 1 h,	CFL lamp (40W), 400 nm, 1.1 W/cm <sup>2</sup>	AQY, 0.1 %	39
Pd(II)-Dendrimer @TiO <sub>2</sub>	Iodo-benzene	27-30 °C, 0.5 h	Sunlight (18 W), 400 nm, N/A	AQY, 0.4 %	39
Porous Pd nanoparticle	Bromo-benzene	RT, 6 h, N <sub>2</sub>	LED, 405 nm, 0.11 W/cm <sup>2</sup>	QY, 1.3 %	This work
Non-porous Pd nanoparticle	Bromo-benzene	RT, 6 h, N <sub>2</sub>	LED, 405 nm, 0.11 W/cm <sup>2</sup>	QY, 0.1 %	This work*

Note: AQY: Apparent Quantum Yield, QY: Quantum Yield.

\*: The nanoparticle photocatalyst with a diameter of 50 nm was prepared according to the literature<sup>36</sup> and the catalysis experiments were conducted in our lab with typical reaction conditions in experimental section. The product yield of dark reaction was less than 1 % and 405 nm LED photocatalytic reaction was around 7 %.

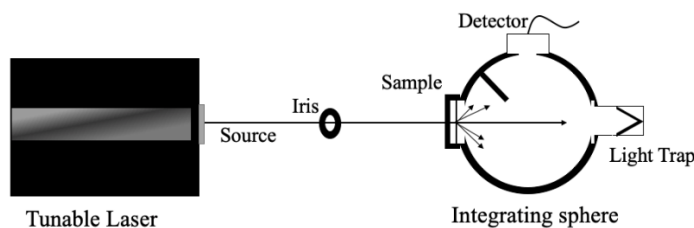
In summary, the interband transitions of porous Pd nanoparticles were examined to reveal the wavelength-dependent quantum yields of a prototype C-C coupling reaction. With shorter excitation wavelengths, the deeper holes in the *d*-band with stronger oxidizing power can catalyze the oxidative addition of aryl halide R-X onto Pd<sup>0</sup> better to form more R-Pd<sup>II</sup>-X intermediates in the catalytic cycle, thus the quantum yield of the catalyst increases. It is known that the oxidative addition process can be catalyzed by hot electrons, especially electrons with high kinetic energy generated from plasmon resonance.<sup>38, 49, 50</sup> However, we showed here that interband transitions could also catalyze the oxidation reaction by another process: the strong oxidizing holes can also promote the oxidation of Pd<sup>0</sup> to Pd<sup>II</sup>. We hope this work will prompt more interest in utilizing deep holes from interband transitions for higher photocatalytic efficiency, which has recently picked up some attention.<sup>13, 16, 74, 75</sup>

## 2.9 Supporting notes

### 2.9.1 Note S1. Light scattering measurement

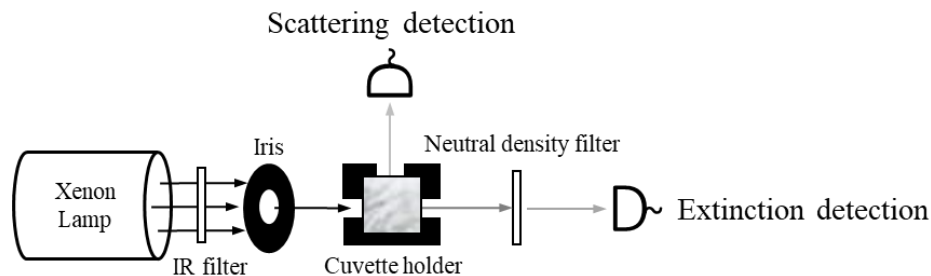
#### (1) Drop-cast sample

A thin film of the sample was prepared by spin coating (1000 rpm, 45 sec, KW-4A Spin Coater, Chemat Technologies.) on a transparent circular quartz substrate with a diameter of one inch. An integrating sphere (Barium sulfate coated, Newport Corp.) was used for measuring scattering cross sections by collecting diffusely transmitted and reflected light. A tunable laser system (430 nm -700 nm, 400 mW, SuperK Extreme Supercontinuum, NKT photonics) was used as a light source. The scattered light was collected at the 90° port of the integrating sphere for both diffused transmission and diffused reflection by a spectrometer (Acton SP2300, Princeton Instruments). The schematic of the experimental setup is shown below:



#### (2) Colloidal sample

The purpose of this experiment is to ensure that the scattered light from the photocatalyzed reaction is negligible as compared to the absorbed light during the photoreaction. Briefly, the Xe lamp (300 W Research Arc Lamp Source, Newport Corp.) was set at 60 W, a 1.5 inch liquid water filter was used to remove the unwanted IR light, and the UV-Vis light was collimated and sent the colloidal sample. Two neutral density filters (OD ~1.1 for each) were inserted into the transmitted path to lower the light intensity at the detector. An optical fiber (300  $\mu\text{m}$  Premium, Ocean Optics) coupled to a collimating lens (74-UV, Ocean Optics) was set to detect scattered and transmitted light from the sample (see the below scheme). The other end of the fiber was connected to an UV-Vis spectrometer (USB4000, Ocean Optics). The colloidal sample was prepared by dispersing 0.4 mg of mesoporous Pd nanoparticle powder in 2 ml of H<sub>2</sub>O and transferred to a 1x1cm quartz cuvette for the measurement. A similar setup for scattering and extinction measurement can be found in literature.<sup>76, 77</sup> The scheme of experimental setup is shown below:



As seen from the above scheme, the transmitted light intensity after the light source passes through the colloidal nanoparticles should be corrected by the scattering background of water and the used cuvette. This transmitted light intensity at each wavelength,  $I_T(\text{Sample})$ , is defined as:

$$I_T(\text{Sample}) = \frac{I_T(H_2O) - I_T(\text{Sample in } H_2O)}{10^{-2OD}}$$

Where:

$I_T(H_2O)$ : the measured transmitted intensity of pure water.

$I_T(\text{Sample in } H_2O)$ : the measured transmitted intensity of colloidal nanoparticles in water.

Note that a factor of  $10^{-2OD}$  was used to account for the attenuation of the transmitted beam by the two neutral density filters.

Besides, the intensity of the incident light before the cuvette, ( $I_0$ ), is calculated based on the transmitted light intensity of the pure water sample:

$$I_0 = \frac{I_T(H_2O)}{10^{-2OD}}$$

Similarly, the scattering intensity at a scattering angle of  $90^\circ$ ,  $I_{s,90}(\text{Sample})$ , is defined as:

$$I_{s,90}(\text{Sample}) = I_{s,90}(\text{Sample in } H_2O) - I_{s,90}(H_2O)$$

Where:

$I_{s,90}(H_2O)$ : the measured scattering intensity of pure water.

$I_{s,90}(\text{Sample in } H_2O)$ : the measured scattering intensity of colloidal nanoparticles in water.

To account for the total scattered photons at all scattering angles, a geometric scaling factor of 7.84 was used. This factor was calculated based on the ratio of the collecting area of the used collimating lens to the estimated surface area of a sphere having a radius from the center of the cuvette to the collimating lens. This estimation is reasonable since our mesoporous particles follow Rayleigh scattering (see Figure 2.7), hence the scattering intensity is even at any angles.<sup>78</sup> Thus, the total scattering intensity is determined as:  $I_s(\text{Sample}) = 7.84 \times I_{s,90}(\text{Sample})$ .

From the above experimental data, the scattering-over-extinction ratio was calculated based on a similar method reported by Ren's group.<sup>76</sup> The extinction intensity ( $I_E$ ) of the sample is the sum of the absorption ( $I_A$ ) and scattering intensities ( $I_S$ ):

$$I_E = I_A + I_S$$

The incident light intensity is the sum of the extinction and transmitted light intensities:

$$I_0 = I_E + I_T = I_A + I_S + I_T$$

Then, the extinction (E), scattering (S) and absorption (A) are calculated as:

$$E = -\log_{10} \frac{I_T(\text{Sample})}{I_0} = -\log_{10} \frac{I_T(H_2O) - I_T(\text{Sample in } H_2O)}{I_0 \cdot (10^{-2OD})}$$

$$A = -\log_{10} \frac{I_T(\text{Sample}) + I_s(\text{Sample})}{I_0}$$

$$S = E - A = -\log_{10} \frac{I_T(\text{Sample})}{I_T(\text{Sample}) + I_s(\text{Sample})}$$

### 2.9.2 Note S2. Discussion on effect of local heating on the observed photocatalysis

The photothermal effect on the observed photocatalysis has been alerted recently in some previous experiments.<sup>79, 80</sup> Note that our “continuous-wave irradiation and stirring” condition is very different from other experimental conditions in which pulse laser was used and heat dissipation was poor. Local heating, the temperature rise in the vicinity of individual nanoparticles in our experiment, should be neglectable after considering the three timescales of the three below processes after a nanoparticle absorbs a photon.

The first timescale is the relaxation time of the hot carriers, which eventually converts the energy of an absorbed photon into heat in the nanoparticle. The longest observed time for this relaxation is about few picoseconds for gold nanoparticles.<sup>56</sup> The hot carriers are well thermalized within these few picoseconds due to the ultrafast electron-electron and electron-phonon couplings,<sup>57</sup> and the nanoparticles should have even temperature distribution within this timescale. Thus, it is reasonable to estimate the temperate rise of the particle based on the energy of a single photon absorbed, the specific heat of the metal and the mass of a single nanoparticle. This temperature rise was estimated well below 1 °C in a previous study.<sup>81</sup> In our experiment, the temperature rise for each mesoporous Pd particle are about 0.00131 or 0.00113 °C for a 405 or 470 nm photon absorbed, respectively (see the calculation in the below table).

The second timescale is the time for the heat transfers from the nanoparticle to the surrounding environment. This timescale for colloidal gold nanoparticles in water is about two to three nanoseconds.<sup>54</sup> Although this time scale was measured for gold nanoparticles, it is reasonable to assume that the heat dissipation from our mesoporous Pd nanoparticles to water is completed within 3 nanoseconds.

The third timescale is the period between the two photons can be absorbed by the same nanoparticle. Since we know the number of photons absorbed in the colloidal solution and the amount of nanoparticles in the beam path, we can estimate the average number of photons absorbed by individual nanoparticle under each second of irradiation. The below table shows that the third timescale is roughly 293 nanoseconds under a typical experimental condition in our study. In an extreme case, a 470 nm LED with incident power of 502 mW causes an absorption of 282 mW in the reaction solution, the corresponding third timescale is about 73 nanoseconds. It is obvious that some nanoparticles may diffuse in and out of the LED beam area during this third timescale, but we can ignore this effect since the beam size is quite big. Besides, on the timescale of hundreds of nanoseconds, the percentage of nanoparticles diffusing in and out of the LED beam is quite small. Note that the absorption is not uniformed across the entire area of the LED beam. However, the absorbance of the reaction solution is quite low, about 0.42 OD for all wavelengths, thus there is no huge change in the absorption profile. Overall, the approximated third timescales are very large as compared to the above second timescale, thus the nanoparticle dissipated all the heat long before the time it absorbs another photon.<sup>26</sup> Under our stirring condition, the accumulated heat in the beam path is effective transferred to the entire cuvette.<sup>58</sup> With a cooling fan, the reaction solution in the cuvette only has a temperate rise within 1-2 °C.

Center wavelength of the LED (nm)	405	470
-----------------------------------	-----	-----

Amount of light absorbed by mesoporous Pd nanoparticle catalyst in the reaction solution (mW)	81	282
Number of photons absorbed by the nanoparticle per second (photon/second)	$1.65 \times 10^{17}$	$6.67 \times 10^{17}$
Volume of the LED beam passed through the reaction solution <sup>a</sup> (ml)	0.708	0.708
Total mesoporous Pd nanoparticles in the reaction solution (particle)	$1.37 \times 10^{11}$	$1.37 \times 10^{11}$
Total of mesoporous Pd nanoparticles in the LED beam path (particle)	$4.84 \times 10^{10}$	$4.84 \times 10^{10}$
Average number of photons absorbed by each nanoparticle per second (photon/(particle·second))	$3.41 \times 10^6$	$1.38 \times 10^7$
Average time gap between two absorbed photons for each nanoparticle (nanosecond)	293	73
Average temperature rise of each nanoparticle <sup>b</sup> (°C)	$1.31 \times 10^{-3}$	$1.13 \times 10^{-3}$

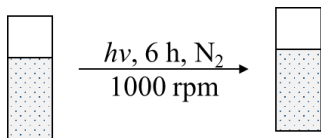
<sup>(a)</sup> Volume =  $\pi(\frac{\varphi}{2})^2 l$ , where:  $\varphi = 0.95$  cm is the LED beam size, and  $l = 1$  cm is the beam path length in the reaction solution.

<sup>(b)</sup> Average temperature rise = energy of a photon/(specific heat  $\times$  mass of a single particle)

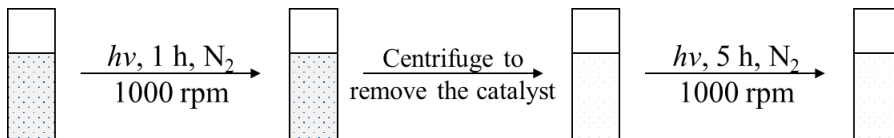
Where: the mass of a nanoparticle was calculated based on the particle diameter and an assumption that the porous particle has a density close to that of Pd metal.

### 2.9.3 Note S3. Design of control experiments to evaluate the catalysis contribution of leached Pd

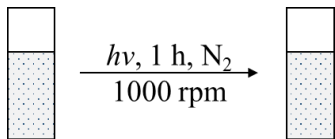
Experiment I: Typical reaction with mesoporous Pd nanoparticle photocatalyst under 6 hour irradiation



Experiment II: In this hot filtration test, the catalyst was removed after 1 hour irradiation, and the reaction was allowed to proceed for another 5 hours.



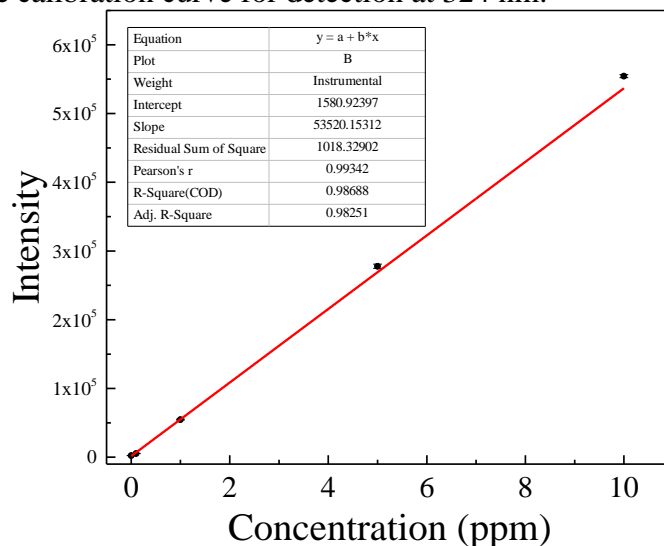
Experiment III: Control reaction with the catalyst under 1 hour irradiation.



### 2.9.4 Note S4. ICP-OES analysis for Pd in reaction supernatant

#### (1) Establishing the standard curve

The concentration of standard solutions was varied from 0.1 to 1, 5 and 10 ppm. All samples were measured at three different wavelengths (324, 340 and 363 nm) for three times. Below is the calibration curve for detection at 324 nm.



#### (2) Analysis of possibly leached Pd from reaction supernatant

All samples were measured with three different wavelengths (324, 340 and 363 nm) for three times. The Pd concentration was below the detection limit of the instrument. The analysis result was shown below:

Entry	Catalysts	Wavelength (nm)	Amount of leached Pd from ICP-OES
1	Porous Pd NPs	Dark	Non-detectable
2	Porous Pd NPs	405	Non-detectable
3	Porous Pd NPs	450	Non-detectable
4	Porous Pd NPs	470	Non-detectable
5	Porous Pd NPs	490	Non-detectable
6	Porous Pd NPs	530	Non-detectable
7	Porous Pd NPs	595	Non-detectable

Reaction conditions: See typical condition details in experimental section and the corresponding conditions were the same as shown in Figure 2.13 and Table 2.5. The supernatant was obtained by centrifuging the reaction solution after 6-hour reaction and the total volume of each supernatant was 2 mL.

#### (3) Estimation of the utmost amount of leached Pd

An amount of 1 mL of the supernatant (total reaction volume = 2 mL) was used in the ICP-OES analysis. The sample digestion and preparation processes were shown in experimental section. The final volume of analyzed samples was 10 mL. The amount of Pd used in each reaction was 0.00156 mmol (0.1660 mg). Considering the lowest

concentration of the standard curve (0.1 ppm) which approaches the detection limit of the instrument, it is reasonable to use 0.1 ppm as the upper-limit of the leached Pd amount in the analyzed samples. Thus, the utmost amount of leached Pd in the supernatant was 0.2 ppm, which is about 1.2 % of the total Pd in the nanoparticle photocatalyst.

### 2.9.5 Note S5. XPS analysis of porous Pd nanoparticles

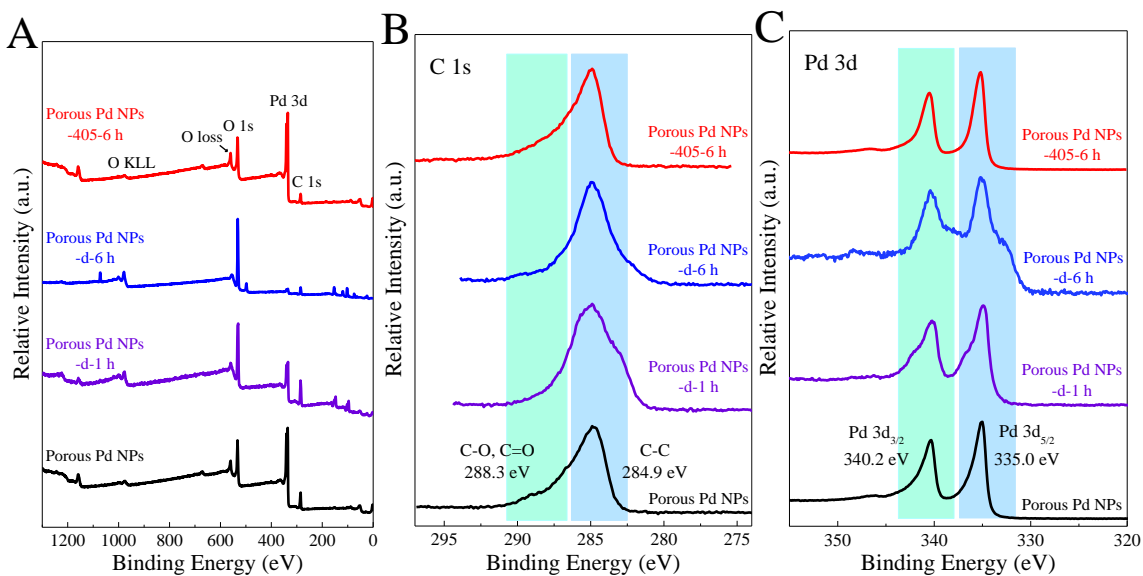
#### (1) Sample design

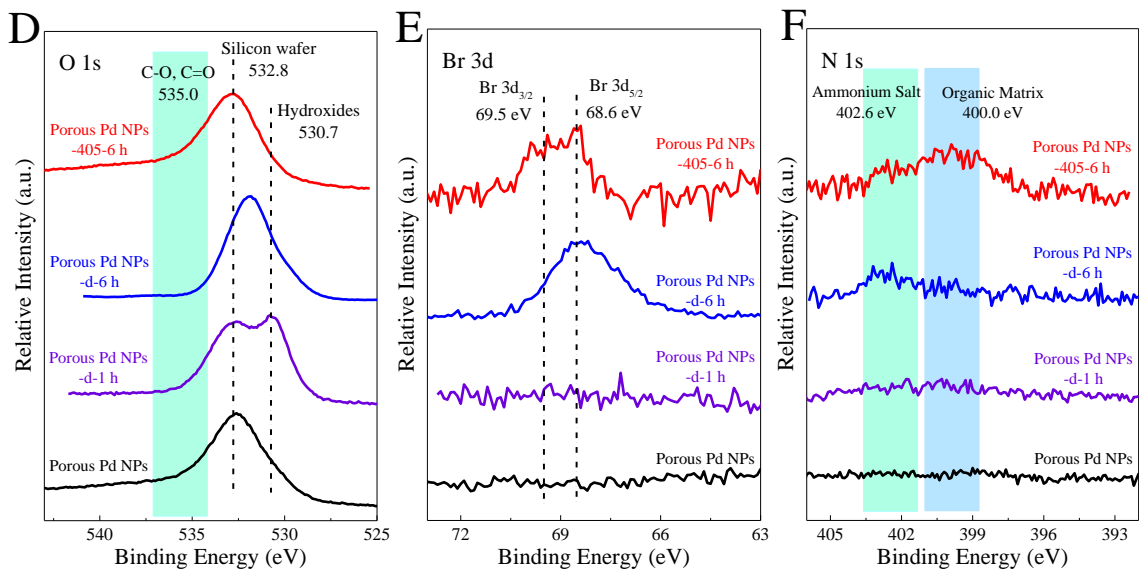
In order to compare the oxidation state of Pd on the surfaces of the photocatalysts before and after Suzuki reaction, some contrast samples were designed as listed below.

Entry	Treatment	Notation
1	None	Porous Pd NPs
2	In reaction mixture in the dark for 1 h	Porous Pd NPs-d-1 h
3	Dark reaction for 6 h	Porous Pd NPs-d-6 h
4	Photocatalytic reaction (405 nm LED) for 6 h	Porous Pd NPs-405-6 h

Note: After treatment with different conditions, the sample was washed with water and ethanol and centrifuged for 3 times for further XPS analysis. Entry 3 and 4 were under the same typical reaction conditions as shown in Entry 1 and 2 in Table 2.5. The reaction mixture was prepared under the same typical reaction conditions.

#### (2) XPS analysis





XPS spectra of four contrast samples were shown above. (A) XPS survey and (B-F) high-resolution XPS spectra of C 1s, Pd 3d, O 1s, Br 3d, and N 1s. The charge calibration was based on the contamination carbon (284.9 eV for C-C). The assignment of respective peaks was based on the handbook of XPS<sup>82</sup> and chemicals used for the reaction, as discussed below.

The presence of Pd, O, and C elements was observed across all samples in the survey spectrum (A). For the as-prepared porous Pd nanoparticles, there was no bromine or nitrogen occurred in the sample, indicating a relatively clean surface of the initial catalysts. Also, the narrow and distinct peak in Pd 3d at 335.0 eV and 340.2 eV matched with the Pd 3d<sub>5/2</sub> and Pd 3d<sub>3/2</sub>, which meant the oxidation state of Pd in the as-prepared sample was mostly zero on the surface. The result was consistent with the previous report from Yamauchi's group.<sup>83</sup> The occurrence of carbonates in the C 1s and O 1s spectra was due to the atmospheric carboxylic acids absorbed on the surface.<sup>84</sup> The peak at 532.8 eV in O 1s was assigned to the oxidation layer of the silicon wafer used as a substrate for XPS measurement or adventitious contamination from the atmosphere.

After one-hour equilibrium with reaction mixture, the Pd 3d peaks became broader and demonstrated a tiny shoulder peak at higher binding energy but the positions did not shift from the Pd(0) state, probably resulting from the adsorption and activation of bromobenzene on porous Pd surface.<sup>85</sup> Also, the occurrence of hydroxides in the O 1s spectrum was due to the phenylboronic acid and sodium hydroxides used for the Suzuki reaction.

After 6-hour dark reaction, the Pd 3d peaks were still broad compared to the as-prepared sample but still within the range of the Pd(0) state. The noisy background was possibly from multiple kinds of organic absorbates remaining on the surface. Besides, the occurrence of bromine was distinct in Br 3d spectrum compared to the as-prepared sample and Porous Pd NPs-d-1 h, which could be coming from the residual bromide ion absorbed strongly on the Pd surface after certain amounts of Suzuki reaction catalytic cycles.<sup>86</sup> Also, the O 1s peak position located between the substrate and hydroxides, indicating the proceeding of the reaction.



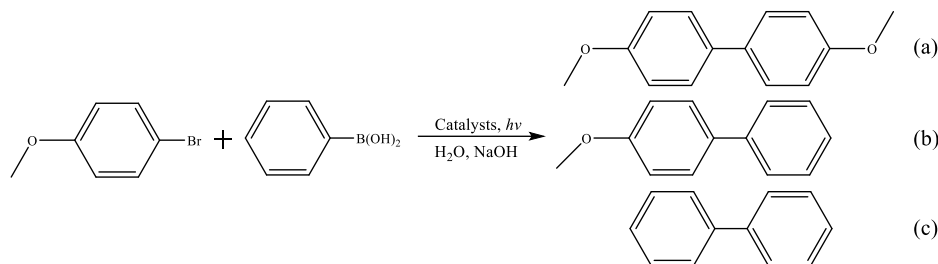
In terms of the photocatalytic reaction under 405 nm LED for 6 hours, the narrow Pd 3d peaks were almost identical with that in the as-prepared porous Pd nanoparticles, revealing the similar oxidation state of Pd(0) before and after the photocatalytic reaction. This identity also applied into the C 1s and O 1s peaks, revealing a relatively clean surface of porous Pd nanoparticles after the photocatalytic reaction. It may be due to the surface self-cleaning effect by holes generated during photocatalysis, similar to the widely-studied case of titanium oxide photocatalysts.<sup>87</sup> Moreover, the leftover bromide ion from the reaction and ammonium salt or organic matrix from the solubilizer CTAC were observed in Br 3d and N 1s spectra.

In general, there were no distinct shifts of Pd 3d peaks across the four samples and the analysis of all potential elements on porous Pd nanoparticles' surface illustrated that the oxidation state of Pd did not change before and after the reaction, either in the dark or photocatalytic conditions.

## 2.9.6 Note S6. Control experiments to confirm that hetero-coupling is the only product

### (1) Experimental design

Under our standard reaction between bromobenzene and phenylboronic acid, the hetero- and homo-coupling product, biphenyl, is indistinguishable. As shown in control experiments reported in Table 2.7, there was no biphenyl product when either bromobenzene or phenylboronic acid was used. Still, other control reactions with an expected unsymmetric product are necessary to confirm the presumed hetero-coupling process under our reaction conditions. The reaction between 4-bromoanisole and phenylboronic acids was conducted to validate the hetero-coupling as shown below:



The homo-coupling product would be 4,4'-dimethoxy-1,1'-biphenyl (a) or biphenyl (c), while the hetero-coupling product would be 4-methoxy-1,1'-biphenyl (b). All reaction conditions were conducted as the same as the typical condition in experimental section except for the replacement of bromobenzene by 4-bromoanisole.

### (2) Analysis method and experimental results

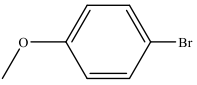
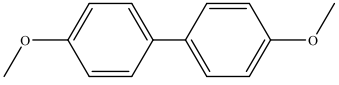
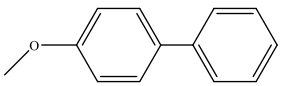
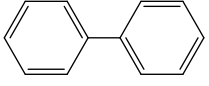
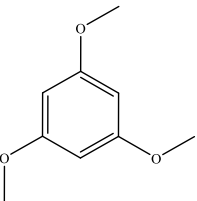
Entry	Wavelength (nm)	Absorbed Light (mW)	Product Yield		
			(a)	(b)	(c)
1	Dark	NA	Not detected	7	Not detected

2	405	81	Not detected	13	Not detected
3*	Dark	NA	Not observed	37	Not observed
4*	405	81	Not observed	63	Not observed

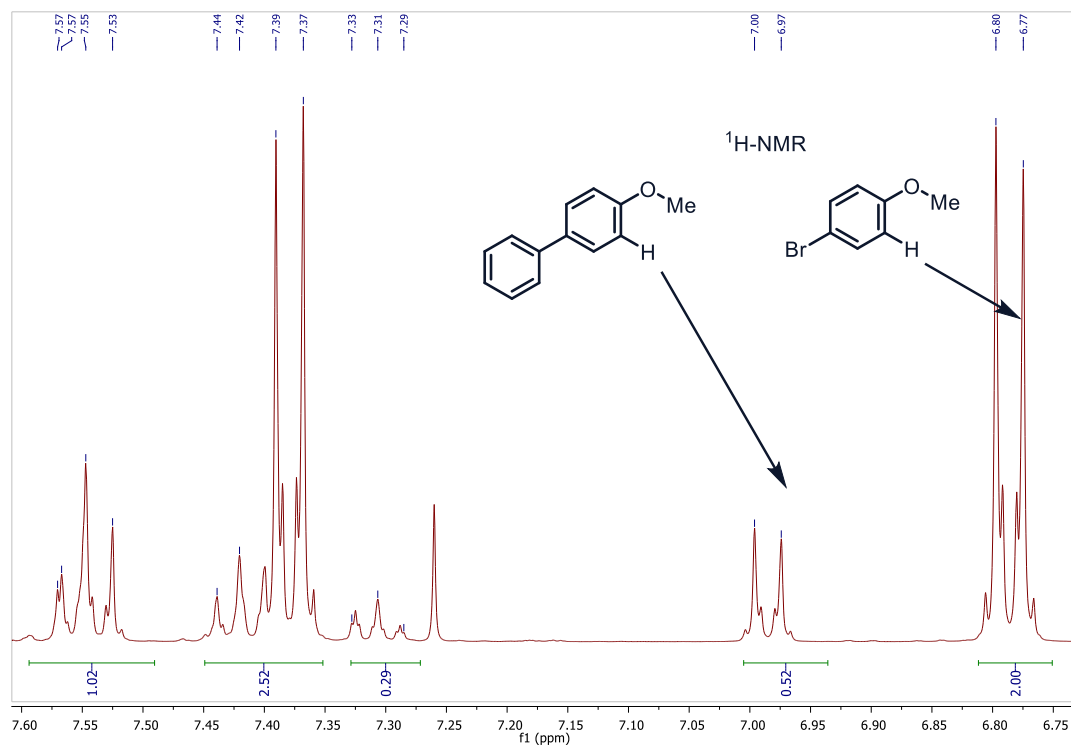
Reaction conditions: See typical condition details in the Methods section in experimental section and the reaction time was 6 hours unless specified. The photon flux was kept as around  $2.3 \times 10^{17}$  photons  $\cdot$  s<sup>-1</sup>  $\cdot$  cm<sup>-2</sup> and the amount of reactant (4-bromoanisole) were kept as 0.2 mmol. 1,3,5-trimethoxybenzene was used as the internal standard for product yield analysis by <sup>1</sup>H-NMR spectroscopy unless specified.

\* Reaction time was 24 hours, and the product yields were determined from the mass of isolated 4-methoxy-1,1'-biphenyl product collected from extracting of the crude reaction solution with dichloromethane and running column chromatography with 1:9 EtOAc(ethyl acetate)-hexane to 1:1 EtOAc-hexane. There were no observable homo-coupling products occurred during column chromatography.

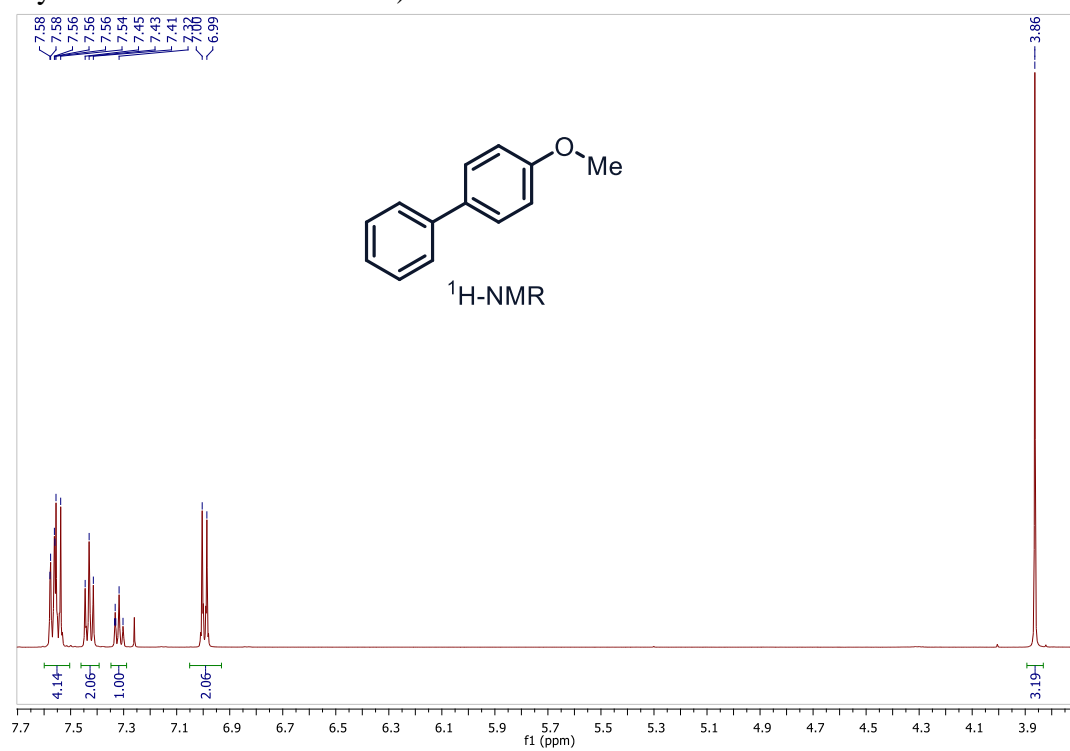
### (3) NMR data of reaction solution with 4-bromoanisole

Compound	Structure	Chemical shift (ppm)
4-bromoanisole		<sup>1</sup> H NMR (400 MHz, CDCl <sub>3</sub> ) δ 7.38 (d, <i>J</i> = 7.5 Hz, 2H), 6.78 (d, <i>J</i> = 7.5 Hz, 2H), 3.78 (s, 3H).
4,4'-dimethoxy-1,1'-biphenyl (a)		<sup>1</sup> H NMR (400 MHz, CDCl <sub>3</sub> ) δ 7.43 (d, <i>J</i> = 7.5 Hz, 4H), 7.05 (d, <i>J</i> = 7.5 Hz, 4H), 3.83 (s, 6H).
4-methoxy-1,1'-biphenyl (b)		<sup>1</sup> H NMR (300 MHz, CDCl <sub>3</sub> ) δ 7.59 – 7.54 (m, 4H), 7.44(t, <i>J</i> =7.3 Hz, 2H), 7.32 (t, <i>J</i> =7.2 Hz, 1H), 7.00 (d, <i>J</i> =8.8 Hz, 2H), 3.87 (s, 3H). <sup>88</sup>
Biphenyl (c)		<sup>1</sup> H NMR (400 MHz, CDCl <sub>3</sub> ) δ 7.65 (dd, <i>J</i> = 7.5, 1.3 Hz, 4H), 7.49 (t, <i>J</i> = 7.4 Hz, 4H), 7.39 (t, <i>J</i> = 7.4 Hz, 2H).
1,3,5-trimethoxybenzene		<sup>1</sup> H NMR (500 MHz, CDCl <sub>3</sub> ) δ 6.20 (s, 3H), 3.85 (s, 9H).

NMR spectrum of 405 nm LED irradiated reaction solution with internal standards (Entry 2 in above reaction results)



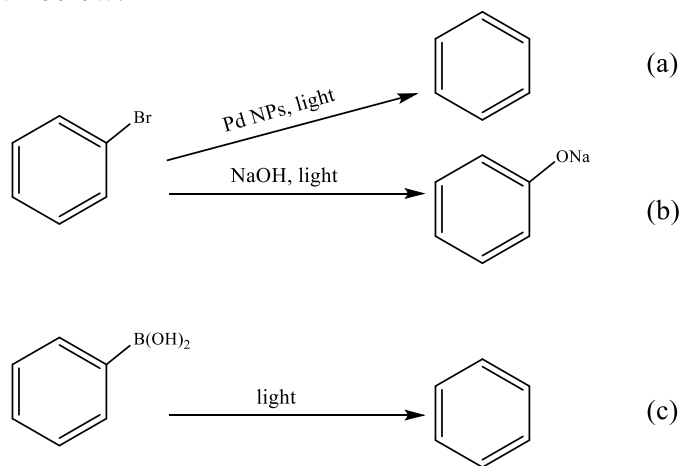
NMR spectrum of isolated pure product from 405 nm LED irradiated reaction solution (Entry 4 in above reaction results)



### 2.9.7 Note S7. Exclusion of some other parallel processes besides the Suzuki-Miyaura reaction

(1) Considering some other possible processes that could happen in parallel to the Suzuki-Miyaura reaction

Under photocatalytic reaction conditions, there may be some parallel processes that may be concurrent to the proposed photocatalyzed reaction. For example, the debromination (a), substitution by a hydroxyl group of the reactant (b), or deborylation (c) may occur as shown below:



(2) Experimental design to exclude the above possible processes

The reagents that involved in above processes were abbreviated as listed for convenience. Ph-Br for bromobenzene, Ph for benzene, Ph-B(OH)<sub>2</sub> for phenylboronic acid, Ph-Ph for biphenyl, Ph-ONa for sodium phenolate, Ph-OH for Phenol, and DCM for dichloromethane. GC-MS for gas chromatography–mass spectrometry.

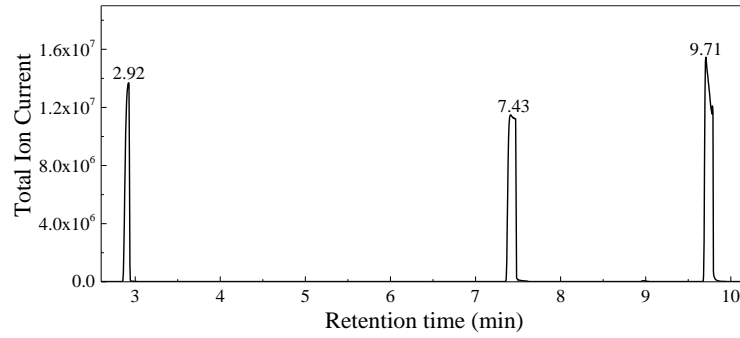
In general, our strategy here was to extract any side products from crude reaction mixture by DCM (both from organic or aqueous phase) and directly send the solution for GC-MS analysis. Two standard sample vials, noted as A and B here, were prepared: (i) Vial A for detecting processes a and c; (ii) Vial B for process b. Vial A contained Ph-Br, Ph, and Ph-Ph (0.2 mmol for each) in 1 mL DCM. Vial B contained Ph-Br, Ph-OH, and Ph-Ph (0.2 mmol for each) in 1 mL DCM.

Secondly, the procedure of reaction mixture post-processing was optimized a little bit to test above processes. After photocatalytic reaction (in this note, 405 nm LED chosen as an example, referred to the typical reaction condition in entry 2 of Table 2.5), the crude reaction mixture was extracted by 1 mL DCM to retrieve the organic compounds from the aqueous solution, which was labeled as 405-O. And the leftover aqueous solution from the previous step was extracted by 1 mL DCM after adding 600  $\mu$ L hydrochloric acid (HCl, 1M, to neutralize the basic solution and convert Ph-ONa to Ph-OH), which was labeled as 405-H. Those samples were directly sent for the GC-MS analysis.

(3) GC-MS spectra and analysis

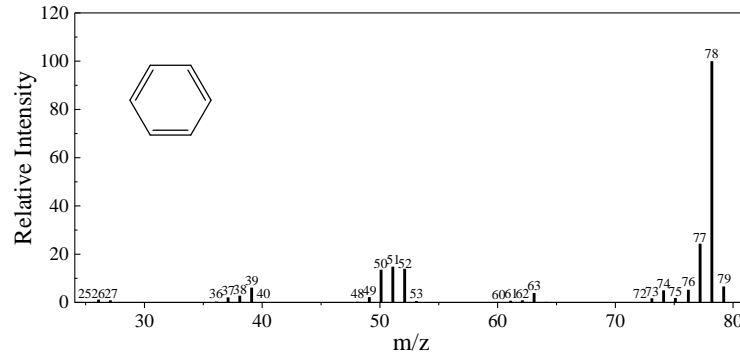
Vial A:

GC TIC spectrum (TIC for total ion current)

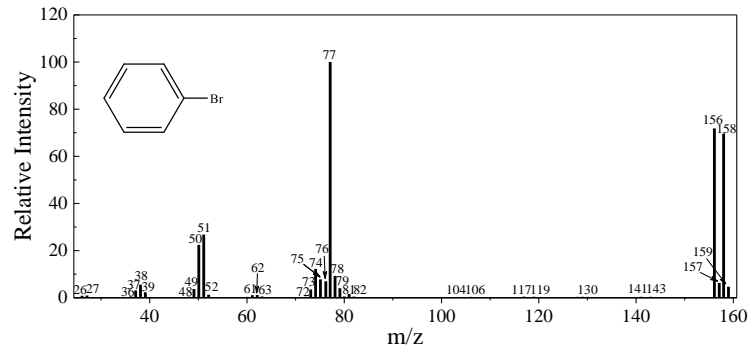


MS spectra

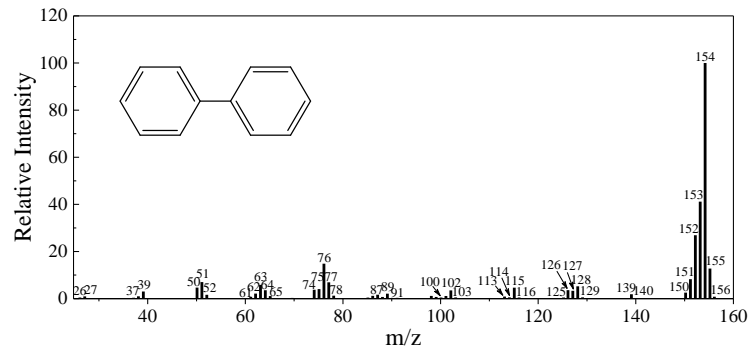
RT=2.92 min (RT for retention time)



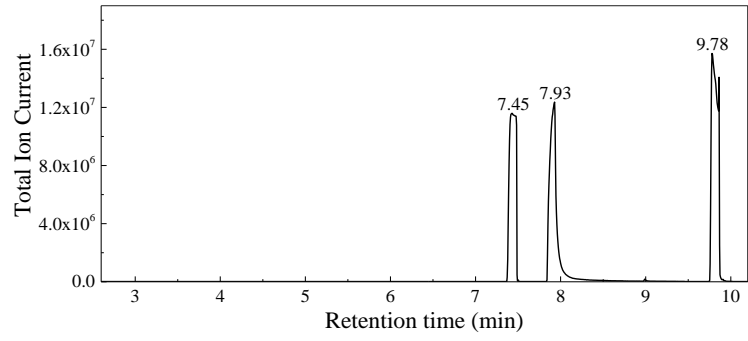
RT=7.43 min



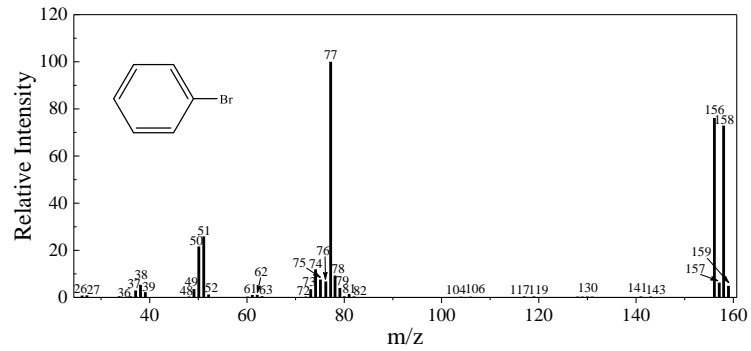
RT=9.71 min



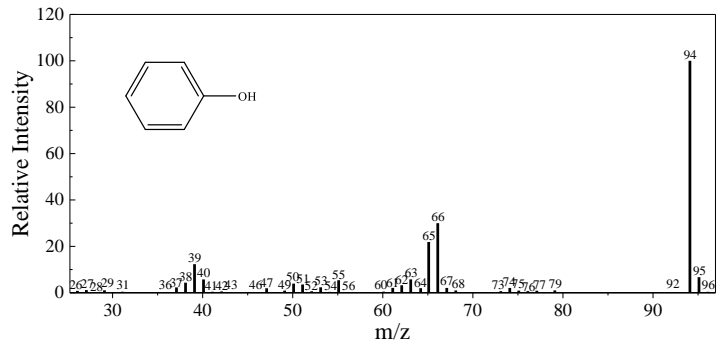
Vial B  
GC TIC spectrum



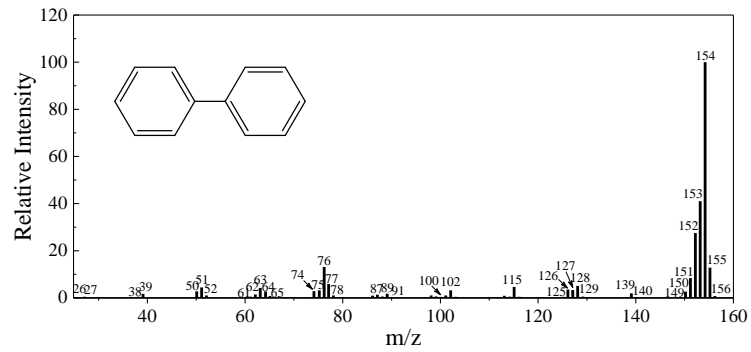
MS spectra  
RT=7.45 min



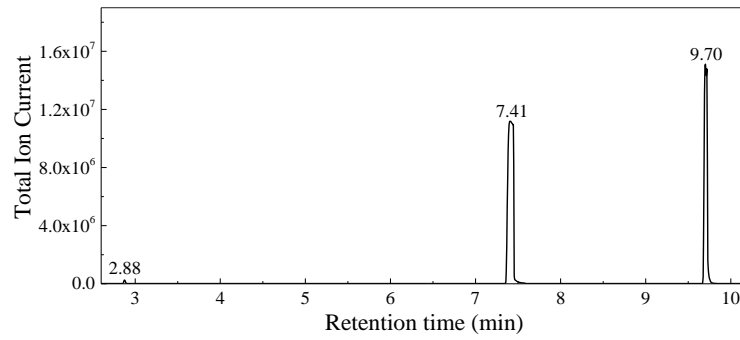
RT=7.93 min



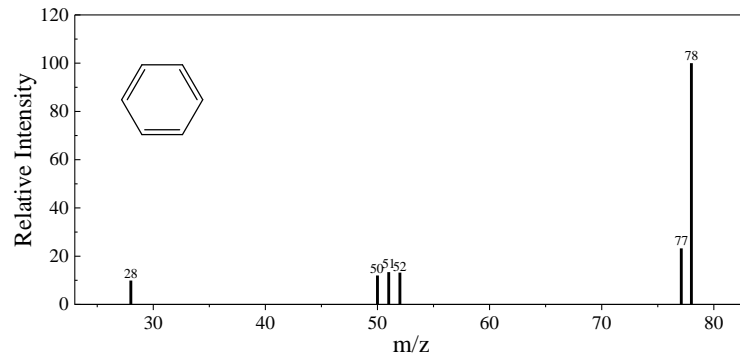
RT=9.78 min



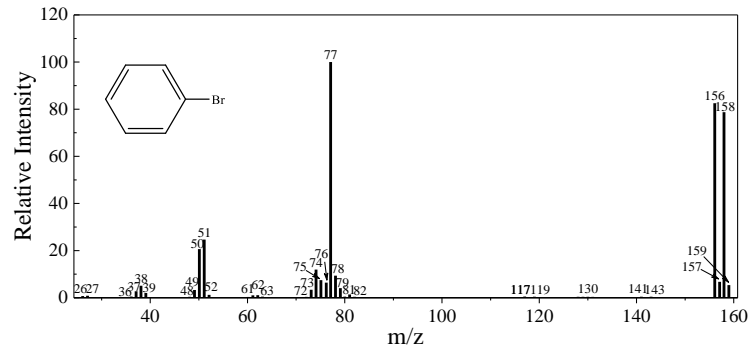
405-O  
GC TIC spectrum



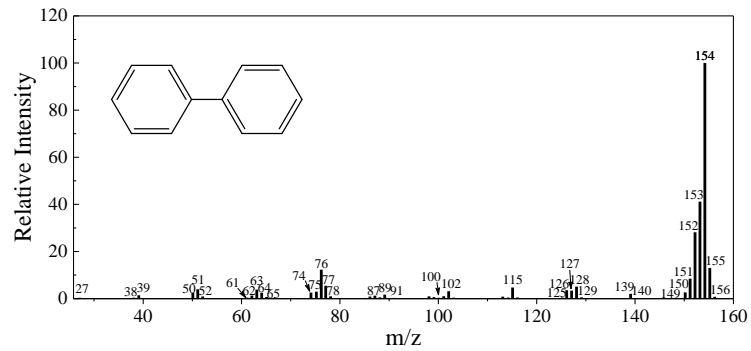
MS spectra  
RT=2.88 min



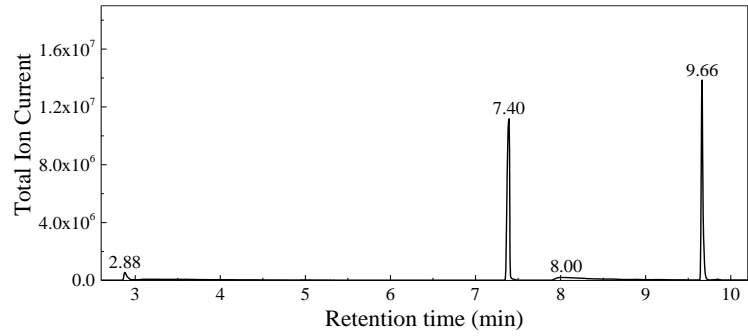
RT=7.41 min



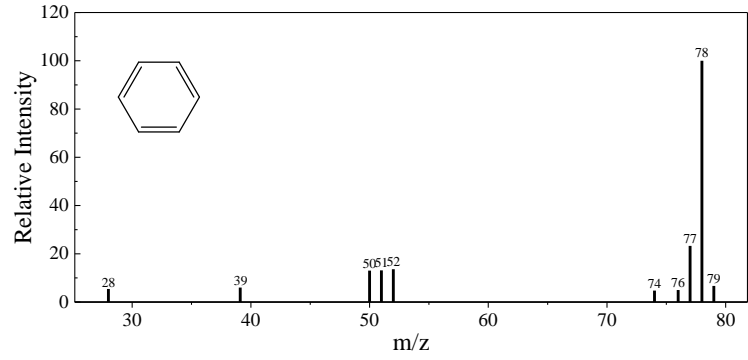
RT=9.70 min



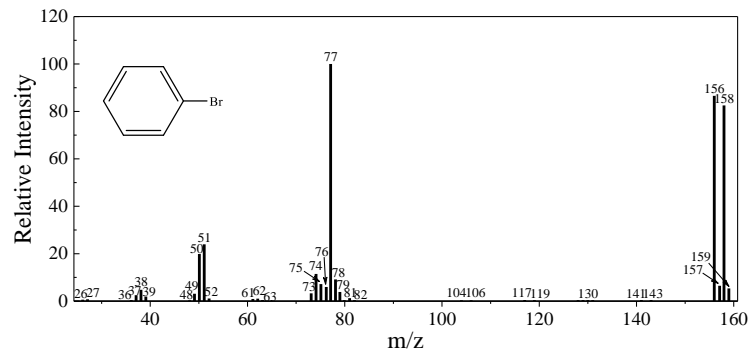
405-H  
GC TIC spectrum



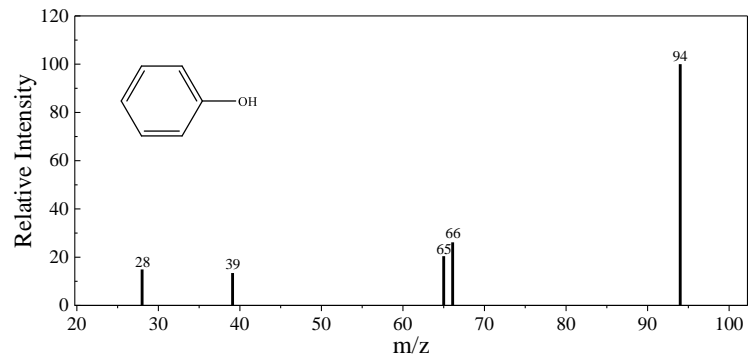
RT=2.88 min



RT=7.40 min

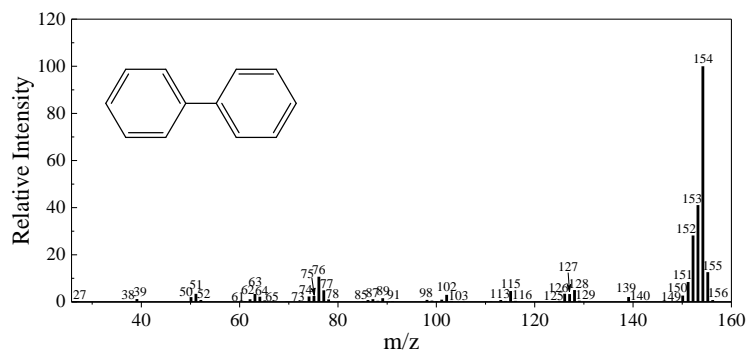


RT=8.00 min



RT=9.66 min





Analysis results:

In the GC-MS spectra of vials A and B, the retention time of Ph, Ph-Br, Ph-OH, and Ph-Ph were well separated in the total ion chromatogram and the MS spectra of those chemicals were well aligned to their mass fragments. Thus, any potential by-products could be detected and distinguished from the reactants in the photocatalytic reaction.

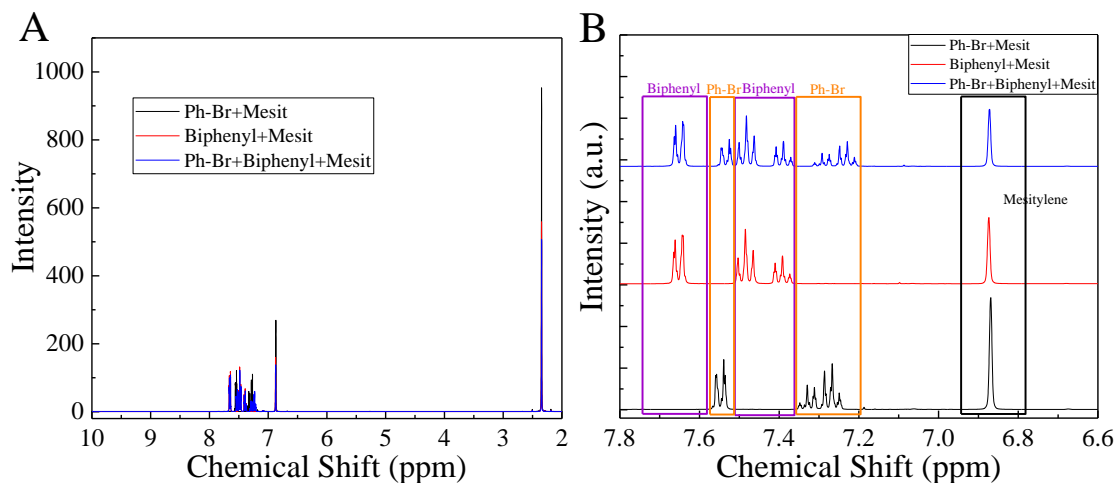
As for the sample 405-O (directly extracted from reaction mixture), the GC spectrum demonstrated a tiny amount of Ph generated compared to the Ph-Ph formed, suggesting that the processes (a) and (c) in part (1) may occur during photocatalytic reaction. However, considering its relatively low amount, those processes should not be considered as major side-reactions to the Suzuki reaction process. Similarly, for the sample 405-H, the process (b) may happen but not contribute a lot to the Suzuki reaction. One thing to mention here, the product occurred in the sample 405-H due to the solubilizer CTAC used in the reaction which would bring a certain amount of organic compounds into the aqueous phase (which was shown to be less than 10 % amount of the total organics in the aqueous solution in a separate experiment, not shown here).

Overall, the deborylation/debromination or, probably, substitution by hydroxyl group of the reactants may occur during the photocatalytic reactions by porous Pd nanoparticles but proved to be negligible compared to the formation of desired biphenyl product.

### 2.9.8 Note S8. NMR spectra of standard compounds and typical reaction solutions, and product yield calculation

(1) NMR spectra of standard samples

The NMR spectra of bromobenzene (Ph-Br), biphenyl and their mixture in CDCl<sub>3</sub> with mesitylene (Mesit) as internal standard were listed below. (A) NMR spectrum with chemical shift from 2 to 10 ppm, and (B) The enlarged part from 6.6 to 7.8 ppm of (A).



Chemical shift for the above compounds:

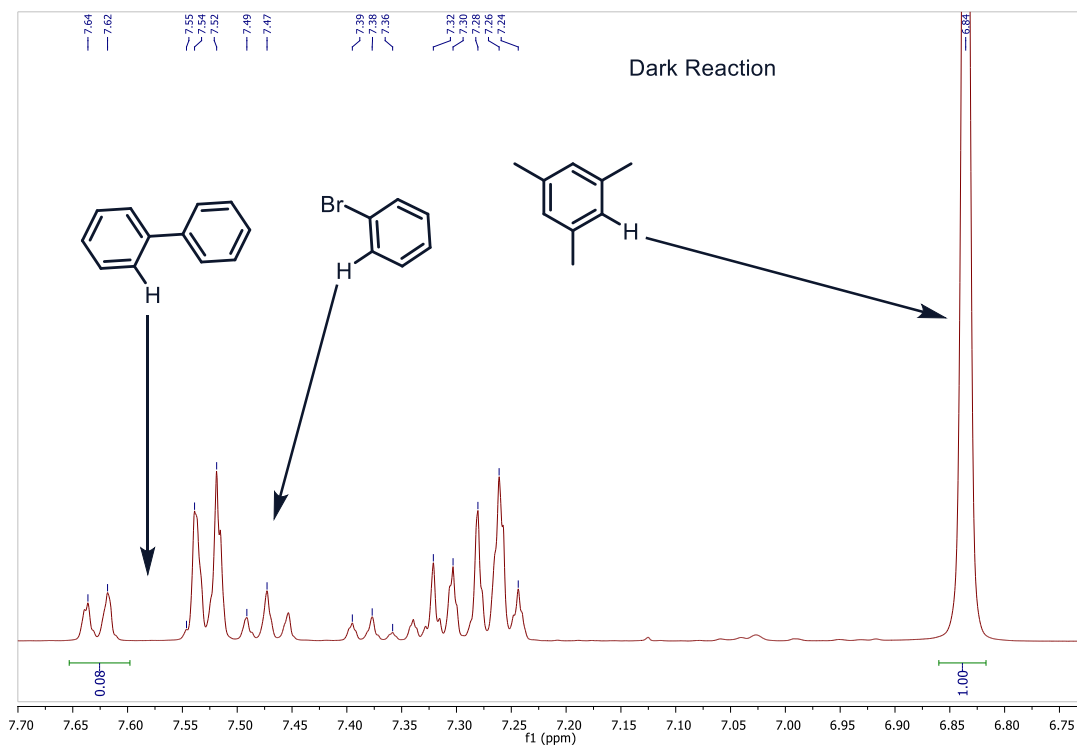
Compound	Structure	Chemical shift (ppm)
Bromobenzene		$^1\text{H NMR}$ (400 MHz, $\text{CDCl}_3$ ) $\delta$ 7.55 (d, $J = 5.9$ Hz, 2H), 7.36–7.24 (m, 3H).
Biphenyl		$^1\text{H NMR}$ (400 MHz, $\text{CDCl}_3$ ) $\delta$ 7.65 (dd, $J = 7.5, 1.3$ Hz, 4H), 7.49 (t, $J = 7.4$ Hz, 4H), 7.39 (t, $J = 7.4$ Hz, 2H).
Mesitylene		$^1\text{H NMR}$ (400 MHz, $\text{CDCl}_3$ ) $\delta$ 6.87 (s, 3H), 2.35 (s, 9H).

## (2) Product yield calculation

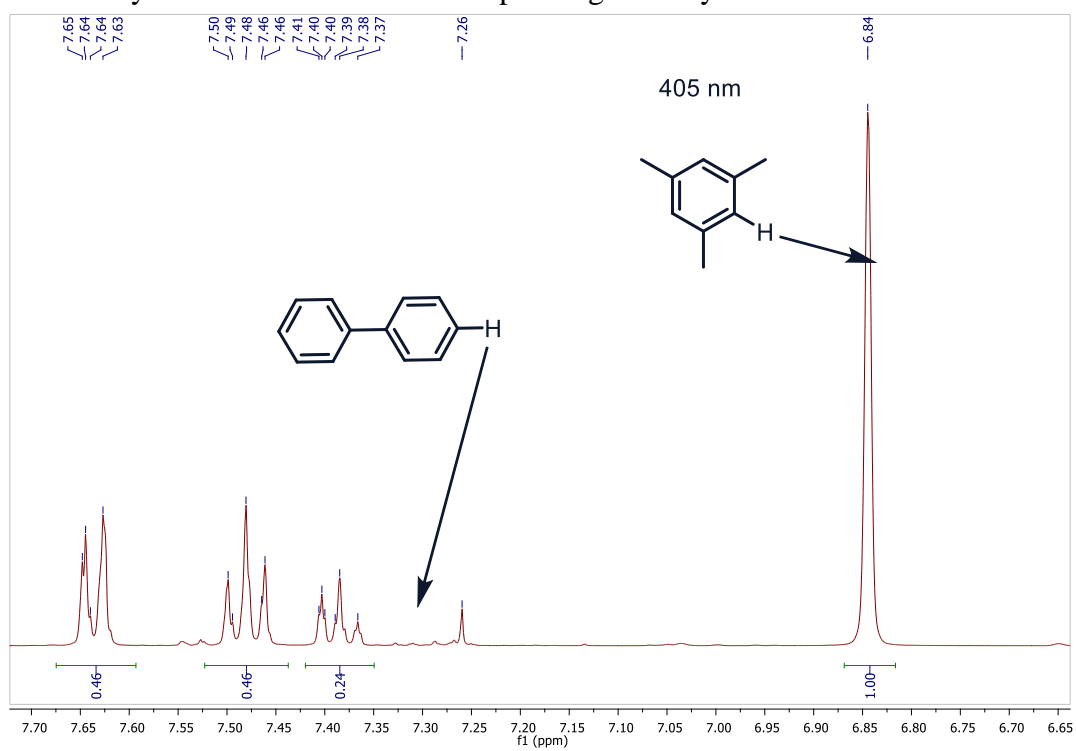
The targeted product biphenyl yield was calculated from integration of the peak area at  $\delta$  7.58–7.52 (m, 2H) with the known amount of internal standard mesitylene at  $\delta$  6.87 (s, 3H).

## (3) NMR spectra of typical Suzuki reaction solutions

a. Dark reaction solution corresponding to Entry 1 in Table 2.5. Peaks observed in the  $^1\text{H-NMR}$  spectra are correlated with arrows to the corresponding hydrogens.



b. Photocatalyzed reaction solution corresponding to Entry 2 in Table 2.5



## 2.10 References

- (1) Aslam, U.; Rao, V. G.; Chavez, S.; Linic, S. Catalytic Conversion of Solar to Chemical Energy on Plasmonic Metal Nanostructures. *Nat. Catal.* **2018**, *1*, 656-665.
- (2) Zhou, L. A.; Swearer, D. F.; Zhang, C.; Robotjazi, H.; Zhao, H. Q.; Henderson, L.; Dong, L. L.; Christopher, P.; Carter, E. A.; Nordlander, P.; Halas, N. J. Quantifying Hot Carrier and Thermal Contributions in Plasmonic Photocatalysis. *Science* **2018**, *362*, 69-72.
- (3) Seemala, B.; Therrien, A. J.; Lou, M. H.; Li, K.; Finzel, J. P.; Qi, J.; Nordlander, P.; Christopher, P. Plasmon-Mediated Catalytic O<sub>2</sub> Dissociation on Ag Nanostructures: Hot Electrons or Near Fields? *ACS Energy Lett.* **2019**, *4*, 1803-1809.
- (4) Chang, L.; Besteiro, L. V.; Sun, J. C.; Santiago, E. Y.; Gray, S. K.; Wang, Z. M.; Govorov, A. O. Electronic Structure of the Plasmons in Metal Nanocrystals: Fundamental Limitations for the Energy Efficiency of Hot Electron Generation. *ACS Energy Lett.* **2019**, *4*, 2552-2568.
- (5) DuChene, J. S.; Tagliabue, G.; Welch, A. J.; Cheng, W. H.; Atwater, H. A. Hot Hole Collection and Photoelectrochemical CO<sub>2</sub> Reduction with Plasmonic Au/p-GaN Photocathodes. *Nano Lett.* **2018**, *18*, 2545-2550.
- (6) Kim, Y.; Smith, J. G.; Jain, P. K. Harvesting Multiple Electron-Hole Pairs Generated through Plasmonic Excitation of Au Nanoparticles. *Nat. Chem.* **2018**, *10*, 763-769.
- (7) Huang, Y. M.; Liu, Z.; Gao, G. P.; Xiao, Q.; Martens, W.; Du, A. J.; Sarina, S.; Guo, C.; Zhu, H. Y. Visible Light-Driven Selective Hydrogenation of Unsaturated Aromatics in an Aqueous Solution by Direct Photocatalysis of Au Nanoparticles. *Catal. Sci. Technol.* **2018**, *8*, 726-734.
- (8) Kazuma, E.; Kim, Y. Mechanistic Studies of Plasmon Chemistry on Metal Catalysts. *Angew. Chem. Int. Ed.* **2019**, *58*, 4800-4808.
- (9) Zhang, Z. L.; Zhang, C. Y.; Zheng, H. R.; Xu, H. X. Plasmon-Driven Catalysis on Molecules and Nanomaterials. *Acc. Chem. Res.* **2019**, *52*, 2506-2515.
- (10) Zhao, J.; Nguyen, S. C.; Ye, R.; Ye, B. H.; Weller, H.; Somorjai, G. A.; Alivisatos, A. P.; Toste, F. D. A Comparison of Photocatalytic Activities of Gold Nanoparticles Following Plasmonic and Interband Excitation and a Strategy for Harnessing Interband Hot Carriers for Solution Phase Photocatalysis. *ACS Cent. Sci.* **2017**, *3*, 482-488.
- (11) Mao, Z.; Vang, H.; Garcia, A.; Tohti, A.; Stokes, B. J.; Nguyen, S. C. Carrier Diffusion—The Main Contribution to Size-Dependent Photocatalytic Activity of Colloidal Gold Nanoparticles. *ACS. Catal.* **2019**, *9*, 4211-4217.
- (12) Kim, Y.; Dumett Torres, D.; Jain, P. K. Activation Energies of Plasmonic Catalysts. *Nano Lett.* **2016**, *16*, 3399-3407.
- (13) Al-Zubeidi, A.; Hoener, B. S.; Collins, S. S. E.; Wang, W.; Kirchner, S. R.; Hosseini Jebeli, S. A.; Joplin, A.; Chang, W.-S.; Link, S.; Landes, C. F. Hot Holes Assist Plasmonic Nanoelectrode Dissolution. *Nano Lett.* **2019**, *19*, 1301-1306.
- (14) Christopher, P.; Moskovits, M. Hot Charge Carrier Transmission from Plasmonic Nanostructures. *Annu. Rev. Phys. Chem.* **2017**, *68*, 379-398.
- (15) Gellé, A.; Jin, T.; de la Garza, L.; Price, G. D.; Besteiro, L. V.; Moores, A. Applications of Plasmon-Enhanced Nanocatalysis to Organic Transformations. *Chem. Rev.* **2020**, *120*, 986-1041.
- (16) Yu, Y.; Wijesekara, K. D.; Xi, X.; Willets, K. A. Quantifying Wavelength-Dependent Plasmonic Hot Carrier Energy Distributions at Metal/Semiconductor Interfaces. *ACS Nano* **2019**, *13*, 3629-3637.
- (17) Zhang, Y.; He, S.; Guo, W.; Hu, Y.; Huang, J.; Mulcahy, J. R.; Wei, W. D. Surface-Plasmon-Driven Hot Electron Photochemistry. *Chem. Rev.* **2018**, *118*, 2927-2954.
- (18) Linic, S.; Christopher, P.; Ingram, D. B. Plasmonic-Metal Nanostructures for Efficient Conversion of Solar to Chemical Energy. *Nat. Mater.* **2011**, *10*, 911-921.
- (19) Hou, W.; Cronin, S. B. A Review of Surface Plasmon Resonance-Enhanced Photocatalysis. *Adv. Funct. Mater.* **2013**, *23*, 1612-1619.

- (20) Xin, H.; Namgung, B.; Lee, L. P. Nanoplasmonic Optical Antennas for Life sciences and Medicine. *Nat. Rev. Mater.* **2018**, *3*, 228-243.
- (21) Brus, L. Noble Metal Nanocrystals: Plasmon Electron Transfer Photochemistry and Single-Molecule Raman Spectroscopy. *Acc. Chem. Res.* **2008**, *41*, 1742-1749.
- (22) Hou, W.; Hung, W. H.; Pavaskar, P.; Goepfert, A.; Aykol, M.; Cronin, S. B. Photocatalytic Conversion of CO<sub>2</sub> to Hydrocarbon Fuels via Plasmon-Enhanced Absorption and Metallic Interband Transitions. *ACS. Catal.* **2011**, *1*, 929-936.
- (23) Liu, L.; Li, P.; Adisak, B.; Ouyang, S.; Umezawa, N.; Ye, J.; Kodiyath, R.; Tanabe, T.; Ramesh, G. V.; Ueda, S.; Abe, H. Gold Photosensitized SrTiO<sub>3</sub> for Visible-Light Water Oxidation Induced by Au Interband Transitions. *J. Mater. Chem. A* **2014**, *2*, 9875-9882.
- (24) Sundararaman, R.; Narang, P.; Jermyn, A. S.; Goddard Iii, W. A.; Atwater, H. A. Theoretical Predictions for Hot-Carrier Generation from Surface Plasmon Decay. *Nat. Commun.* **2014**, *5*, 5788.
- (25) Bernardi, M.; Mustafa, J.; Neaton, J. B.; Louie, S. G. Theory and Computation of Hot Carriers Generated by Surface Plasmon Polaritons in Noble Metals. *Nat. Commun.* **2015**, *6*, 7044.
- (26) Khurgin, J. B. Fundamental Limits of Hot Carrier Injection from Metal in Nanoplasmonics. *Nanophotonics* **2020**, *9*, 453-471.
- (27) Kontoleta, E.; Tsoukala, A.; Askes, S. H. C.; Zoethout, E.; Oksenberg, E.; Agrawal, H.; Garnett, E. C. Using Hot Electrons and Hot Holes for Simultaneous Cocatalyst Deposition on Plasmonic Nanostructures. *ACS. Appl. Mater. Inter.* **2020**, *12*, 35986-35994.
- (28) Boltersdorf, J.; Forcherio, G. T.; McClure, J. P.; Baker, D. R.; Leff, A. C.; Lundgren, C. Visible Light-Promoted Plasmon Resonance to Induce “Hot” Hole Transfer and Photothermal Conversion for Catalytic Oxidation. *J. Phys. Chem. C* **2018**, *122*, 28934-28948.
- (29) Zhang, C.; Jia, F.; Li, Z.; Huang, X.; Lu, G. Plasmon-generated Hot Holes for Chemical Reactions. *Nano Res.* **2020**, *13*, 3183-3197.
- (30) Zhu, H.; Chen, X.; Zheng, Z.; Ke, X.; Jaatinen, E.; Zhao, J.; Guo, C.; Xie, T.; Wang, D. Mechanism of Supported Gold Nanoparticles as Photocatalysts under Ultraviolet and Visible Light Irradiation. *Chem. Commun.* **2009**, 7524-7526.
- (31) Christopher, P.; Xin, H.; Linic, S. Visible-Light-Enhanced Catalytic Oxidation Reactions on Plasmonic Silver Nanostructures. *Nat. Chem.* **2011**, *3*, 467-472.
- (32) Mukherjee, S.; Libisch, F.; Large, N.; Neumann, O.; Brown, L. V.; Cheng, J.; Lassiter, J. B.; Carter, E. A.; Nordlander, P.; Halas, N. J. Hot Electrons Do the Impossible: Plasmon-Induced Dissociation of H<sub>2</sub> on Au. *Nano Lett.* **2013**, *13*, 240-247.
- (33) Sakamoto, H.; Ohara, T.; Yasumoto, N.; Shiraishi, Y.; Ichikawa, S.; Tanaka, S.; Hirai, T. Hot-Electron-Induced Highly Efficient O<sub>2</sub> Activation by Pt Nanoparticles Supported on Ta<sub>2</sub>O<sub>5</sub> Driven by Visible Light. *J. Am. Chem. Soc.* **2015**, *137*, 9324-9332.
- (34) Guerrisi, M.; Rosei, R.; Winsemius, P. Splitting of the Interband Absorption Edge in Au. *Phys. Rev. B* **1975**, *12*, 557-563.
- (35) Langhammer, C.; Yuan, Z.; Zorić, I.; Kasemo, B. Plasmonic Properties of Supported Pt and Pd Nanostructures. *Nano Lett.* **2006**, *6*, 833-838.
- (36) Niu, W.; Li, Z.-Y.; Shi, L.; Liu, X.; Li, H.; Han, S.; Chen, J.; Xu, G. Seed-Mediated Growth of Nearly Monodisperse Palladium Nanocubes with Controllable Sizes. *Cryst. Growth Des.* **2008**, *8*, 4440-4444.
- (37) Molnár, Á. Efficient, Selective, and Recyclable Palladium Catalysts in Carbon–Carbon Coupling Reactions. *Chem. Rev.* **2011**, *111*, 2251-2320.
- (38) Xiao, Q.; Sarina, S.; Jaatinen, E.; Jia, J.; Arnold, D. P.; Liu, H.; Zhu, H. Efficient Photocatalytic Suzuki Cross-Coupling Reactions on Au–Pd Alloy Nanoparticles under Visible Light Irradiation. *Green Chem.* **2014**, *16*, 4272-4285.

- (39) Zhang, S.; Chang, C.; Huang, Z.; Ma, Y.; Gao, W.; Li, J.; Qu, Y. Visible-Light-Activated Suzuki–Miyaura Coupling Reactions of Aryl Chlorides over the Multifunctional Pd/Au/Porous Nanorods of CeO<sub>2</sub> Catalysts. *ACS Catal.* **2015**, *5*, 6481–6488.
- (40) Trinh, T. T.; Sato, R.; Sakamoto, M.; Fujiyoshi, Y.; Haruta, M.; Kurata, H.; Teranishi, T. Visible to Near-infrared Plasmon-enhanced Catalytic Activity of Pd Hexagonal Nanoplates for the Suzuki Coupling Reaction. *Nanoscale* **2015**, *7*, 12435–12444.
- (41) Han, D.; Bao, Z.; Xing, H.; Yang, Y.; Ren, Q.; Zhang, Z. Fabrication of Plasmonic Au–Pd Alloy Nanoparticles for Photocatalytic Suzuki–Miyaura Reactions under Ambient Conditions. *Nanoscale* **2017**, *9*, 6026–6032.
- (42) Li, C.; Iqbal, M.; Jiang, B.; Wang, Z.; Kim, J.; Nanjundan, A. K.; Whitten, A. E.; Wood, K.; Yamauchi, Y. Pore-Tuning to Boost the Electrocatalytic Activity of Polymeric Micelle-Templated Mesoporous Pd Nanoparticles. *Chem. Sci.* **2019**, *10*, 4054–4061.
- (43) Iatridi, Z.; Evangelatou, K.; Theodorakis, N.; Angelopoulou, A.; Avgoustakis, K.; Tsitsilianis, C. Multicompartmental Mesoporous Silica/Polymer Nanostructured Hybrids: Design Capabilities by Integrating Linear and Star-Shaped Block Copolymers. *Polymers* **2020**, *12*, 51.
- (44) Deng, Y.; Yu, T.; Wan, Y.; Shi, Y.; Meng, Y.; Gu, D.; Zhang, L.; Huang, Y.; Liu, C.; Wu, X. Ordered Mesoporous Silicas and Carbons with Large Accessible Pores Templated from Amphiphilic Diblock Copolymer Poly(ethylene oxide)-b-polystyrene. *J. Am. Chem. Soc.* **2007**, *129*, 1690–1697.
- (45) Creighton, J. A.; Eadon, D. G. Ultraviolet–Visible Absorption Spectra of the Colloidal Metallic Elements. *J. Chem. Soc., Faraday Trans.* **1991**, *87*, 3881–3891.
- (46) Lv, H.; Xu, D.; Henzie, J.; Feng, J.; Lopes, A.; Yamauchi, Y.; Liu, B. Mesoporous Gold Nanospheres via Thiolate–Au(i) Intermediates. *Chem. Sci.* **2019**, *10*, 6423–6430.
- (47) Lu, Z.; Gao, J.; Fang, C.; Zhou, Y.; Li, X.; Han, G. Porous Pt Nanospheres Incorporated with GO<sub>x</sub> to Enable Synergistic Oxygen-Inductive Starvation/Electrodynamic Tumor Therapy. *Adv. Sci.* **2020**, *7*, 2001223.
- (48) Liu, K.; Bai, Y.; Zhang, L.; Yang, Z.; Fan, Q.; Zheng, H.; Yin, Y.; Gao, C. Porous Au–Ag Nanospheres with High-Density and Highly Accessible Hotspots for SERS Analysis. *Nano Lett.* **2016**, *16*, 3675–3681.
- (49) Wang, F.; Li, C.; Chen, H.; Jiang, R.; Sun, L.-D.; Li, Q.; Wang, J.; Yu, J. C.; Yan, C.-H. Plasmonic Harvesting of Light Energy for Suzuki Coupling Reactions. *J. Am. Chem. Soc.* **2013**, *135*, 5588–5601.
- (50) Sarina, S.; Zhu, H.-Y.; Xiao, Q.; Jaatinen, E.; Jia, J.; Huang, Y.; Zheng, Z.; Wu, H. Viable Photocatalysts under Solar-Spectrum Irradiation: Nonplasmonic Metal Nanoparticles. *Angew. Chem. Int. Ed.* **2014**, *53*, 2935–2940.
- (51) Raza, F.; Yim, D.; Park, J. H.; Kim, H.-I.; Jeon, S.-J.; Kim, J.-H. Structuring Pd Nanoparticles on 2H-WS<sub>2</sub> Nanosheets Induces Excellent Photocatalytic Activity for Cross-Coupling Reactions under Visible Light. *J. Am. Chem. Soc.* **2017**, *139*, 14767–14774.
- (52) Biffis, A.; Centomo, P.; Del Zotto, A.; Zecca, M. Pd Metal Catalysts for Cross-Couplings and Related Reactions in the 21st Century: A Critical Review. *Chem. Rev.* **2018**, *118*, 2249–2295.
- (53) Sun, B.; Ning, L.; Zeng, H. C. Confirmation of Suzuki–Miyaura Cross-Coupling Reaction Mechanism through Synthetic Architecture of Nanocatalysts. *J. Am. Chem. Soc.* **2020**, *142*, 13823–13832.
- (54) Nguyen, S. C.; Zhang, Q.; Manthiram, K.; Ye, X.; Lomont, J. P.; Harris, C. B.; Weller, H.; Alivisatos, A. P. Study of Heat Transfer Dynamics from Gold Nanorods to the Environment via Time-Resolved Infrared Spectroscopy. *ACS Nano* **2016**, *10*, 2144–2151.
- (55) Mao, Z.; Espinoza, R.; Garcia, A.; Enwright, A.; Vang, H.; Nguyen, S. C. Tuning Redox Potential of Gold Nanoparticle Photocatalysts by Light. *ACS Nano* **2020**, *14*, 7038–7045.

- (56) Minutella, E.; Schulz, F.; Lange, H. Excitation-Dependence of Plasmon-Induced Hot Electrons in Gold Nanoparticles. *J. Phys. Chem. Lett.* **2017**, *8*, 4925-4929.
- (57) Link, S.; El-Sayed, M. A. Shape and Size Dependence of Radiative, Non-radiative and Photothermal Properties of Gold Nanocrystals. *Int. Rev. Phys. Chem.* **2000**, *19*, 409-453.
- (58) Un, I.-W.; Sivan, Y. The Role of Heat Generation and Fluid Flow in Plasmon-Enhanced Reduction–Oxidation Reactions. *ACS Photonics* **2021**.
- (59) Kozuch, S.; Martin, J. M. L. “Turning Over” Definitions in Catalytic Cycles. *ACS. Catal.* **2012**, *2*, 2787-2794.
- (60) Lente, G. Comment on “‘Turning Over’ Definitions in Catalytic Cycles”. *ACS. Catal.* **2013**, *3*, 381-382.
- (61) Costa, P.; Sandrin, D.; Scaiano, J. C. Real-Time Fluorescence Imaging of a Heterogeneously Catalysed Suzuki–Miyaura Reaction. *Nat. Catal.* **2020**, *3*, 427-437.
- (62) Phan, N. T. S.; Van Der Sluys, M.; Jones, C. W. On the Nature of the Active Species in Palladium Catalyzed Mizoroki–Heck and Suzuki–Miyaura Couplings–Homogeneous or Heterogeneous Catalysis, A Critical Review. *Adv. Synth. Catal.* **2006**, *348*, 609-679.
- (63) Cong, H.; Porco, J. A. Chemical Synthesis of Complex Molecules Using Nanoparticle Catalysis. *ACS. Catal.* **2012**, *2*, 65-70.
- (64) Weaver, J. H.; Benbow, R. L. Low-energy Interband Absorption in Pd. *Phys. Rev. B* **1975**, *12*, 3509-3510.
- (65) Reiss, H. The Fermi Level and the Redox Potential. *J. Phys. Chem.* **1985**, *89*, 3783-3791.
- (66) Chen, Z.; Vorobyeva, E.; Mitchell, S.; Fako, E.; Ortuño, M. A.; López, N.; Collins, S. M.; Midgley, P. A.; Richard, S.; Vilé, G.; Pérez-Ramírez, J. A heterogeneous single-atom palladium catalyst surpassing homogeneous systems for Suzuki coupling. *Nature Nanotechnology* **2018**, *13*, 702-707.
- (67) Saito, K.; Tanabe, I.; Tatsuma, T. Site-Selective Plasmonic Etching of Silver Nanocubes. *J. Phys. Chem. Lett.* **2016**, *7*, 4363-4368.
- (68) Waidhas, F.; Haschke, S.; Khanipour, P.; Fromm, L.; Görling, A.; Bachmann, J.; Katsounaros, I.; Mayrhofer, K. J. J.; Brummel, O.; Libuda, J. Secondary Alcohols as Rechargeable Electrofuels: Electrooxidation of Isopropyl Alcohol at Pt Electrodes. *ACS. Catal.* **2020**, *10*, 6831-6842.
- (69) Bratsch, S. G. Standard Electrode Potentials and Temperature Coefficients in Water at 298.15 K. *J. Phys. Chem. Ref. Data* **1989**, *18*, 1-21.
- (70) Adamo, C.; Amatore, C.; Ciofini, I.; Jutand, A.; Lakmini, H. Mechanism of the Palladium-Catalyzed Homocoupling of Arylboronic Acids: Key Involvement of a Palladium Peroxo Complex. *J. Am. Chem. Soc.* **2006**, *128*, 6829-6836.
- (71) Pérez-Lorenzo, M. Palladium Nanoparticles as Efficient Catalysts for Suzuki Cross-Coupling Reactions. *J. Phys. Chem. Lett.* **2012**, *3*, 167-174.
- (72) Wang, F.; Li, C.; Sun, L.-D.; Xu, C.-H.; Wang, J.; Yu, J. C.; Yan, C.-H. Porous Single-Crystalline Palladium Nanoparticles with High Catalytic Activities. *Angew. Chem. Int. Ed.* **2012**, *51*, 4872-4876.
- (73) Huang, S.-C.; Wang, X.; Zhao, Q.-Q.; Zhu, J.-F.; Li, C.-W.; He, Y.-H.; Hu, S.; Sartin, M. M.; Yan, S.; Ren, B. Probing Nanoscale Spatial Distribution of Plasmonically Excited Hot Carriers. *Nat. Commun.* **2020**, *11*, 4211.
- (74) Tagliabue, G.; DuChene, J. S.; Abdellah, M.; Habib, A.; Gosztola, D. J.; Hattori, Y.; Cheng, W.-H.; Zheng, K.; Canton, S. E.; Sundararaman, R.; Sá, J.; Atwater, H. A. Ultrafast Hot-hole Injection Modifies Hot-electron Dynamics in Au/p-GaN Heterostructures. *Nat. Mater.* **2020**, *19*, 1312-1318.
- (75) Tagliabue, G.; Jermyn, A. S.; Sundararaman, R.; Welch, A. J.; DuChene, J. S.; Pala, R.; Davoyan, A. R.; Narang, P.; Atwater, H. A. Quantifying the Role of Surface Plasmon Excitation and Hot Carrier Transport in Plasmonic Devices. *Nat. Commun.* **2018**, *9*, 3394.

- (76) Liu, B.-J.; Lin, K.-Q.; Hu, S.; Wang, X.; Lei, Z.-C.; Lin, H.-X.; Ren, B. Extraction of Absorption and Scattering Contribution of Metallic Nanoparticles Toward Rational Synthesis and Application. *Anal. Chem.* **2015**, *87*, 1058-1065.
- (77) Wang, J.; Xu, C.; Nilsson, A. M.; Fernandes, D. L. A.; Strömberg, M.; Wang, J.; Niklasson, G. A. General Method for Determining Light Scattering and Absorption of Nanoparticle Composites. *Adv. Opt. Mater.* **2019**, *7*, 1801315.
- (78) He, G. S.; Qin, H.-Y.; Zheng, Q. Rayleigh, Mie, and Tyndall Scatterings of Polystyrene Microspheres in Water: Wavelength, Size, and Angle Dependences. *J. Appl. Phys.* **2009**, *105*, 023110.
- (79) Jain, P. K. Taking the Heat Off of Plasmonic Chemistry. *J. Phys. Chem. C* **2019**, *123*, 24347-24351.
- (80) Dubi, Y.; Un, I. W.; Sivan, Y. Thermal Effects – an Alternative Mechanism for Plasmon-assisted Photocatalysis. *Chem. Sci.* **2020**, *11*, 5017-5027.
- (81) Zhao, J.; Nguyen, S. C.; Ye, R.; Ye, B.; Weller, H.; Somorjai, G. A.; Alivisatos, A. P.; Toste, F. D. A Comparison of Photocatalytic Activities of Gold Nanoparticles Following Plasmonic and Interband Excitation and a Strategy for Harnessing Interband Hot Carriers for Solution Phase Photocatalysis. *ACS Cent. Sci.* **2017**, *3*, 482-488.
- (82) Chastain, J.; King Jr, R. C. Handbook of X-ray Photoelectron Spectroscopy. *Perkin-Elmer Corporation* **1992**, *40*, 221.
- (83) Iqbal, M.; Li, C.; Jiang, B.; Hossain, M. S. A.; Islam, M. T.; Henzie, J.; Yamauchi, Y. Tethering Mesoporous Pd Nanoparticles to Reduced Graphene Oxide Sheets Forms Highly Efficient Electrooxidation Catalysts. *J. Mater. Chem. A* **2017**, *5*, 21249-21256.
- (84) Balajka, J.; Hines, M. A.; DeBenedetti, W. J. I.; Komora, M.; Pavelec, J.; Schmid, M.; Diebold, U. High-affinity Adsorption Leads to Molecularly Ordered Interfaces on TiO<sub>2</sub> in Air and Solution. *Science* **2018**, *361*, 786.
- (85) Gniewek, A.; Trzeciak, A. M.; Ziółkowski, J. J.; Kępiński, L.; Wrzyszczyk, J.; Tylus, W. Pd-PVP Colloid as Catalyst for Heck and Carbonylation Reactions: TEM and XPS Studies. *J. Catal.* **2005**, *229*, 332-343.
- (86) Fu, Z.; Li, T.; He, X.; Liu, J.; Wu, Y. The Recyclable Cyclopalladated Ferrocenylimine Self-assembly Catalytic Film and Investigation of its Role in the Mechanism of Heterogeneous Catalysis. *RSC Adv.* **2014**, *4*, 26413-26420.
- (87) Fujishima, A.; Zhang, X.; Tryk, D. A. TiO<sub>2</sub> Photocatalysis and Related Surface Phenomena. *Surf. Sci. Rep.* **2008**, *63*, 515-582.
- (88) Ghosh, R.; Sarkar, A. Bidentate P, N-P Ligand for Nickel-Catalyzed Cross-Coupling of Aryl or Benzyl Chlorides with ArMgX. *J. Org. Chem.* **2010**, *75*, 8283-8286.



## Chapter 3 Effect of Photocharging on Catalysis of Metallic Nanoparticles

(This chapter covers similar materials as in Pin Lyu and Son C. Nguyen\*, **Effect of Photocharging on Catalysis of Metallic Nanoparticles**. *J. Phys. Chem. Lett.*, **2021**, 12, 51, 12173–12179. Reprinted (adapted) with permission from *J. Phys. Chem. Lett.*, **2021**, 12, 51, 12173–12179. Copyright © 2021 American Chemical Society.)

### Abstract

The photocharging effect is widely known across different research fields, has rarely been quantified as a background contribution in photocatalysis, and has often been overlooked in mechanistic interpretation of nanoparticle photocatalysts. To address these issues, this work presents a two-step experiment: charging colloidal Pd nanoparticles with light and hole scavengers and using the charged particles to catalyze the reduction of 4-nitrophenol by NaBH<sub>4</sub> under non-irradiation conditions. Experimental kinetics demonstrated a proportional correlation between accumulated electrons and catalytic improvement of Pd nanoparticles. This work reminds us that photocharged nanoparticles may still catalyze chemical reactions as a background phenomenon even when they are not undergoing photoexcitation.

### 3.1 Introduction

Photo-charging, a photostationary state of accumulating ground-state electrons or holes, has been used in many research fields, such as environmental remediation,<sup>1, 2</sup> photo-rechargeable battery,<sup>3, 4</sup> photoelectrochemistry,<sup>5, 6</sup> photocatalysis,<sup>7-9</sup> and so on. In some previous studies, photo-charging effect was demonstrated via composite systems such as Ag-TiO<sub>2</sub>,<sup>2</sup> Au-TiO<sub>2</sub>,<sup>10</sup> or WO<sub>3</sub>-TiO<sub>2</sub>,<sup>11</sup> where one material absorbs light and generates hot carriers while the other creates a barrier for charge separation and stores the charge for further reactions. In these composites, interfacial effects such as electrostatic potential<sup>12</sup> and atomic structure change<sup>13</sup> could complicate the photo-charging effect on catalysis. Thus, colloidal metallic nanoparticles were used to avoid any side effects from conjunction to the catalytic mechanism.<sup>7, 8, 14</sup>

Photo-charging effect on metallic nanoparticles was initially reported by Brus and co-workers as a photovoltage mechanism to explain the growth of silver nanoprisms.<sup>7, 15</sup> Recent studies have a similar approach to create light-induced voltages for lowering the activation energy barriers of chemical reactions,<sup>8, 16</sup> catalyze anisotropic growth of gold nanoprisms,<sup>17</sup> control multi-electron transfer for better catalytic selectivities,<sup>18, 19</sup> enhance photochemical potential for redox reactions,<sup>20, 21</sup> improve catalytic activities under different excitation wavelengths<sup>14, 22, 23</sup> or tune reduction potential of nanoparticle photocatalysts<sup>9</sup>. However, the relationship between accumulated charge from photo-charging process and catalytic performance of photo-charged nanoparticles is still underexplored. Moreover, previous studies have explored the photocatalysis of photo-charged metallic nanoparticles under continuous irradiation. It is important to see if the photo-charged metallic nanoparticles can still catalyze chemical reactions after stopping irradiation.

In principle, metallic nanoparticles can undergo photo-charging when the photogenerated hot electrons (or hot holes) are quenched by sacrificial agents, leaving ground-state holes (or electrons) on the particles.<sup>16, 18, 19, 24, 25</sup> The charging and discharging processes were observed by many analytical methods, such as electrochemistry<sup>26, 27</sup> or chemical titration<sup>28, 29</sup>, and sometimes used to explain some typical photocatalytic mechanisms.<sup>30, 31</sup> In fact, metallic nanoparticles have high susceptibility for increasing electron density, making them good candidates for storing electrons.<sup>32</sup> It was demonstrated that interband transitions by shorter wavelength excitations could accumulate more electrons and lower reduction potential (raise Fermi level) of gold nanoparticles.<sup>9</sup> During a photocatalyzed reaction, when there is an imbalance in consuming either electrons or holes on metallic nanoparticle catalysts,<sup>8</sup> the consequent photo-charging may create an extra catalytic process besides the well-known hot-carrier or plasmon mediated catalysis. This extra process acts as a hidden background, which is often overlooked and hard to be directly quantified. In order to reveal this background, it is crucial to photo-charge the nanoparticles first and then separately evaluate how accumulated charge influences the catalysis under non-irradiation.

## **3.2 Experimental section**

### **3.2.1 Chemicals and characterizations**

All chemicals and reagents were used without any purification. Absorption spectra were measured by a UV-vis spectrophotometer (USB4000 Ocean Optics). Morphology of porous Pd nanoparticles were examined by transmission electron microscopy (Talos F200C G2, 200 kV, Thermo Fisher Scientific). Oxidation states of surface species on the nanoparticles was measured by an x-ray photoelectron spectrometer (Nexsa, Al K $\alpha$  X-ray source, Thermo Fisher Scientific).

### **3.2.2 Synthesis of porous Pd nanoparticles (denoted as Pd NPs)**

The synthesis protocol was modified according to the hard-template method developed by the Yamauchi's group.<sup>33</sup> Briefly, 8 mg PS<sub>5000</sub>-b-PEO<sub>2200</sub> (Polymer Source Co.) was added into a mixture of 200  $\mu$ L tetrahydrofuran, 160  $\mu$ L of 2 M HCl, 500  $\mu$ L of 76.8 mM H<sub>2</sub>PdCl<sub>4</sub>, and 1140  $\mu$ L of ultrapure H<sub>2</sub>O. The solution was stirred and added 2 mL of 0.1 M ascorbic acid to initiate the reduction process. The solution was then incubated at 50 °C for 10 h. The final products were washed with THF and calcinated at 200 °C for 1 h to remove the excess polymers.

### **3.2.3 Photocharging procedures for Pd NPs before using as the catalysts for the reduction reaction**

The photocharging process was conducted in a quartz cuvette (1x1 cm, R-3010-T, Spectrocell) sealed by a screw cap with a rubber septum. Firstly, 200  $\mu$ L of porous Pd NP stocked solution, 1300  $\mu$ L of H<sub>2</sub>O, and 0.26 mmol of hole scavengers (20  $\mu$ L for isopropyl alcohol) were added and purged with N<sub>2</sub> for 20 minutes under vigorous stirring to remove the oxygen. Then, the cuvette was stirred by a magnetic bar, irradiated by an LED, and cooled by a fan to maintain its temperature close to room temperature. The optical power before and behind the cuvette was recorded by a power meter (PM100D console with S170C sensor, Thorlabs) and calculated for the absorbed photon fluxes. The LED beam

size passing through the cuvette was maintained as about 0.95 cm for all experiments. Specifically, for different excitation wavelengths, the absorbed photon fluxes were maintained the same for a fair comparison.<sup>23</sup> The 405, 470, and 530 nm LEDs (M405L4, M470L4, M530L4, Thorlabs) have the center emissions at 405, 470, and 530 nm and FWHMs of 12.5, 26, and 35 nm, respectively. Typical photocharged nanoparticles were denoted as Pd NPs-405nm-450mW-IPA, which means that the porous Pd nanoparticles were charged by a 405 nm LED with an incident power of 450 mW and IPA was the hole scavenger. The photocharging time was 6 hours unless specified. After the photocharging process, the cuvette with the colloidal catalysts was immediately used as a reactor for further reactions.

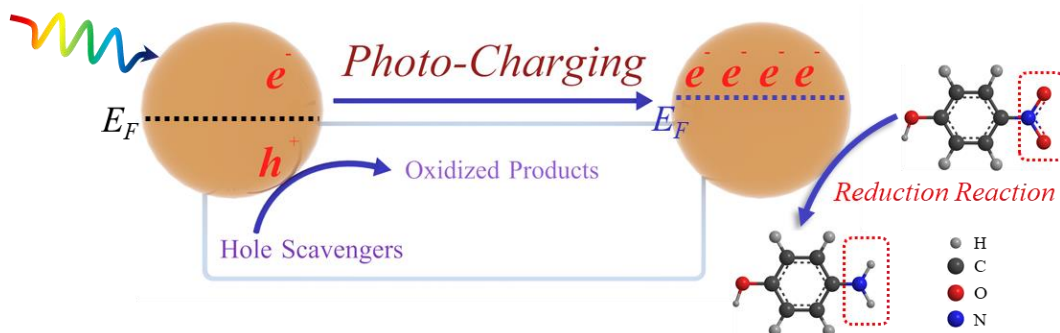
### **3.2.4 4-Nitrophenol reduction as a model reaction to evaluate the catalytic performance**

4-Nitrophenol reduction to 4-aminophenol was utilized as a model reaction. Typically, a mixture of 0.75 mL of 0.2 mM 4-nitrophenol and 0.75 mL of 60 mM freshly made sodium borohydride was added into the cuvette with the photocharges particles described in the previous section. The reaction solution was stirred and monitored by the UV-vis spectrometer. The control sample without applying the photocharging process was prepared with similar procedures except for placing the cuvette in the dark rather than under LED irradiations. The concentration change of 4-nitrophenol was monitored from its absorbance at 400 nm. This absorbance was corrected by subtracting the absorbance at 800 nm due to the relatively flat baseline absorbance of Pd NPs. This absorbance was further used for kinetic analysis and rate constant calculation. The linear fit for the initial 30 s was applied for the  $\ln(C_t/C_0)$  vs. time plot to get the apparent rate constant.

### **3.2.5 Estimation of stored electrons on Pd NPs after the photocharging process**

The electron transfer from nanoparticles to dye molecules with a large extinction coefficient and low reduction potential was considered as a useful method to quantify the charges accumulated in the nanoparticles.<sup>28, 34</sup> In our system, thionine (Th) was utilized to determine the stored electrons on Pd NPs by monitoring its absorbance at 600 nm. The electrons consumed by the Th were calculated from the following equation:  $Th (color) + 2e^- \rightarrow Th^{2-} (colorless)$ . Experimentally, after the photocharging process for Pd NPs with hole scavengers, the cuvette was placed under the dark and injected with 10  $\mu$ L of 1 mM Th solution under stirring. The time-dependent absorption spectra of the solution were recorded and those spectra have baseline correction by subtracting the absorbance at 800 nm due to the relatively flat absorbance of the Pd NPs (see Figure 3.2). The spectra were used to calculate the concentration change of Th.

### 3.3 Experimental design for evaluating photo-charging effect on catalysis



**Scheme 3.1** A two-step experiment for evaluating photo-charging effect on catalysis: i) photo-charging Pd nanoparticles for accumulating extra electrons. ii) using photo-charged particles for catalyzing 4-nitrophenol reduction by NaBH<sub>4</sub> under non-irradiation condition. (NaBH<sub>4</sub> is not shown).

Herein, we design a two-step experiment including a photo-charging process and a subsequent reduction reaction to evaluate the catalytic performance of photo-charged nanoparticles (Scheme 3.1). In brief, porous palladium nanoparticles (Pd NPs) were photo-charged by hole scavengers under light-emitting diode (LED) irradiation for a certain amount of time and then immediately used as the catalysts for the reduction of 4-nitrophenol to 4-aminophenol by NaBH<sub>4</sub>. The reaction kinetics were then compared to kinetics of control reactions in which photo-charging was not executed. The number of accumulated electrons from the photo-charging process was quantified through a sensitive and fast electron transfer reaction with thionine dye. Eventually, a proportional correlation was built between the accumulated charge and apparent reaction rate constants.

Starting with photo-charging step, 63 nm porous Pd NPs were employed as model catalysts due to their flat absorption and low scattering in the common visible region (400–600 nm) for photocatalysis studies. Due to the porous structure, the plasmon resonance is shifted to the near IR region and interband transitions are the main spectral feature in the visible region. These optical properties were studied and proved to be convenient for mechanistic interpretation, and the related hot-carrier mediated catalysis was discussed thoroughly in a recent work.<sup>23</sup> The typical photo-charging condition included isopropyl alcohol (IPA) as a hole scavenger and 6-hour LED (centred at 405 nm) irradiation under N<sub>2</sub> atmosphere unless specified when altering the condition (see details in the Experimental Section 3.2.3).

For the catalysis step, the reduction of 4-nitrophenol by NaBH<sub>4</sub> was chosen as a model because it happens reasonably fast on the surface of metallic nanoparticles, and kinetic analysis could be performed by UV-Vis spectroscopy.<sup>35</sup> The reaction happened extremely slow when metallic nanoparticle catalysts were not used. Despite many studies on the reduction of nitroaromatic compounds using nanocrystal photocatalysts and hole scavengers,<sup>36, 37</sup> photo-charging effect on the catalysis has not been studied yet. Based on the well-accepted Langmuir–Hinshelwood mechanism of this surface-catalyzed reaction, the rate-determining step is generally considered as the reduction of 4-hydroxylaminophenol intermediate to 4-aminophenol by surface hydrogen species

provided from  $\text{NaBH}_4$ ,<sup>38, 39</sup> and a pseudo-first-order analysis on 4-nitrophenol is sufficient for evaluating the catalytic activity of metallic nanoparticles.<sup>40, 41</sup> A typical reaction started by mixing aqueous 4-nitrophenol and freshly-prepared  $\text{NaBH}_4$  solutions first, and then adding the mixture into the Pd NPs' solution that was just finished photo-charging. The overall temperature of photo-charged solutions rose only 1-2 °C, which had almost no influence on the catalyzed reactions. As the same amount of nanoparticles and reactants were used in this second step, the extracted apparent reaction rate constants only depended on the photo-charging process in the first step.

### 3.4 Catalytic performance of photo-charged Pd NPs

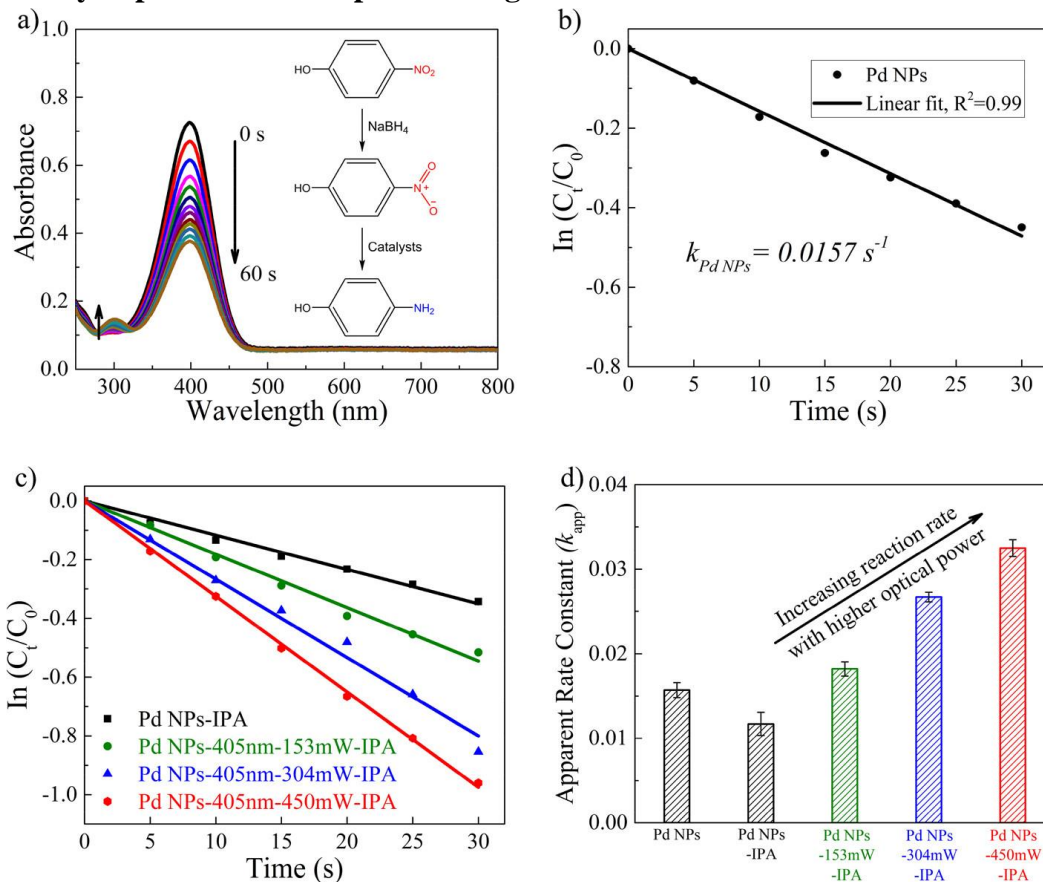


**Figure 3.1** Catalytic performance of Pd NPs under non-photo-charging and photo-charging. (a) UV-Vis spectra of reaction solution of 4-nitrophenol reduction by  $\text{NaBH}_4$  on Pd NPs. Reaction steps are inserted. (b) Kinetic analysis for the reaction in (a) following pseudo-first-order for 4-nitrophenol. (c) Reaction kinetics when using Pd NPs without and with 6-hour photo-charging. Incident optical power of 405 nm LED was varied. Solid lines are linear fits for extracting apparent rate constants. (d) Comparison of rate constants extracted from (b) and (c). Error bars represent one standard deviation of the means.

Kinetic traces of 4-nitrophenol at 400 nm absorption (in form of nitrophenolate ion) were plotted following pseudo-first-order to extract the apparent reaction rate constants (Figure 3.1). The first chemical kinetics was performed for the experiment without a photo-

charging step (no irradiation and no scavenger), and  $k_{\text{Pd NPs}}$  was obtained as  $0.0157 \text{ s}^{-1}$ . This first reference was used to compare to the rate constants of reactions using photo-charged catalysts.

**Table 3.1** Calculation of absorbed photon fluxes under various incident optical powers.

Entry	Sample label	Wavelength (nm)	Incident light (mW)	Absorbed light (mW)	Absorbed photon flux ( $10^{17} \text{ photons} \cdot \text{s}^{-1} \cdot \text{cm}^{-2}$ )
1	Pd NPs-IPA	N/A	N/A	N/A	N/A
2	Pd NPs-405nm-153mW-IPA	405	153	54	1.5
3	Pd NPs-405nm-304mW-IPA	405	304	61	1.8
4	Pd NPs-405nm-450mW-IPA	405	450	76	2.2

Notes: See photocharging conditions in the Experimental section. The charging time was 6 hours. These conditions were corresponded to data shown in Figure 3.1c.

To validate the photo-charging effect on catalysis, the amount of charge per catalyst particle was tuned by adjusting the incident optical power of the 405 nm LED (Table 3.1). As the power increased, each nanoparticle had an averaged increase in absorbed photons and generated carriers. As an excess amount of IPA was used (molar ratio to Pd > 575), the hot carriers were expected to be the limiting component, thus the scavenging was sufficient to create more photo-charged electrons for higher optical power (*vide infra*). After charging, UV-Vis spectroscopic and electron microscopic analyses on the catalysts did not detect any noticeable change, implying that they remained the same structure and colloidal form in the solution (Figures 3.2 and 3.3). Hence, the significant change for the catalysts after photo-charging is the number of accumulated electrons.

To account for the large amount of IPA that may affect the reduction reaction in the second step, the reaction rate constant for a reduction reaction using both the particles and IPA under uncharged condition,  $k_{\text{Pd NPs-IPA}}$ , was used as the second reference. It is important to note that the porous Pd nanoparticles have poor homogeneity (Figure 3.3). To account for consequent effect on the observed reaction rate constants, only two batches of synthesized nanoparticles were used. We then established the ratio of  $k_{\text{Pd NPs-IPA}}$  when using the second batch to that standard value when using the first batch. This ratio was 1.08 and used to calibrate all the rate constants whenever using the second batch.

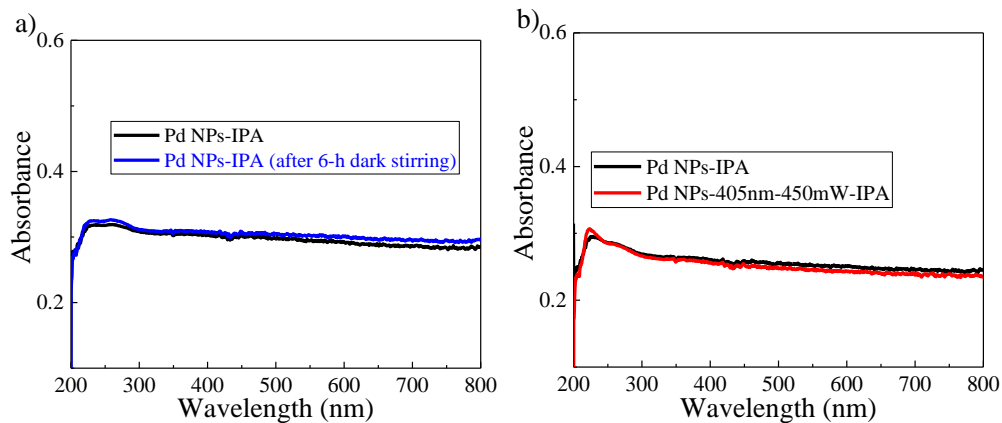


**Figure 3.2** UV-vis spectra of porous Pd NP solutions: (a) in the dark without photocharging, (b) before and after photocharging.

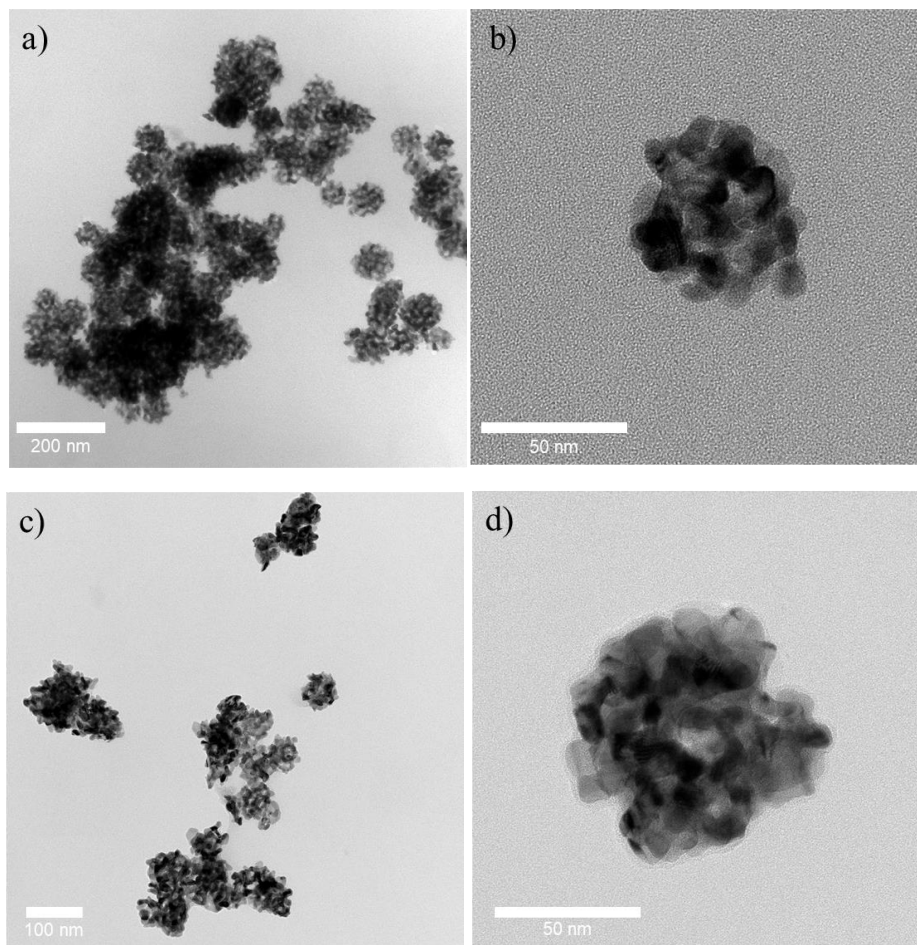


**Figure 3.3** TEM images of Pd NPs: (a, b) before and (c, d) after a typical photocharging process (450 mW irradiation of 405 nm LED for 6 hours and IPA as a hole scavenger). The average diameter of Pd NPs before and after photocharging were  $63.0 \pm 8.6$  nm and  $64.2 \pm 9.7$  nm, respectively.

As the optical power increased, the catalytic performance of photo-charged Pd NPs was improved as shown in the proportional increase of the rate constant (Figures 3.1c and 3.1d). For example, when the 405 nm LED was set at 450 mW, the  $k_{\text{Pd NPs-405nm-450mW-IPA}} = 0.0325 \text{ s}^{-1}$  was about 3 times larger than  $k_{\text{Pd NPs-IPA}} = 0.0117 \text{ s}^{-1}$  for the non-charging control sample. The detailed UV-Vis spectra for those reactions with time-dependent profiles were further provided in Figure 3.4 for a direct comparison. It was noted that  $k_{\text{Pd NPs-IPA}}$  was slightly smaller than  $k_{\text{Pd NPs}}$  (Figure 3.1d), which could be ascribed to the fact that adsorption of IPA on the catalysts may block some active sites for the following reduction reaction.<sup>42</sup> Jain and coworkers reported an increase in reduction rate of ferricyanide catalyzed by gold nanoparticle photocatalysts after increasing photon flux.<sup>16, 19</sup> Despite the different experimental conditions, mainly due to our separation of photo-charging and catalyzing reaction, our results show a similar trend. While multi-electron transfer reactions were possible under continuous irradiation in previous studies,<sup>14, 17, 19</sup> the observation of 4-aminophenol product (a rising peak at 300 nm in Figure 3.1) in this study indicates a six-electron reduction was achieved under our photo-charging, then stopping irradiation and evaluating catalysis.

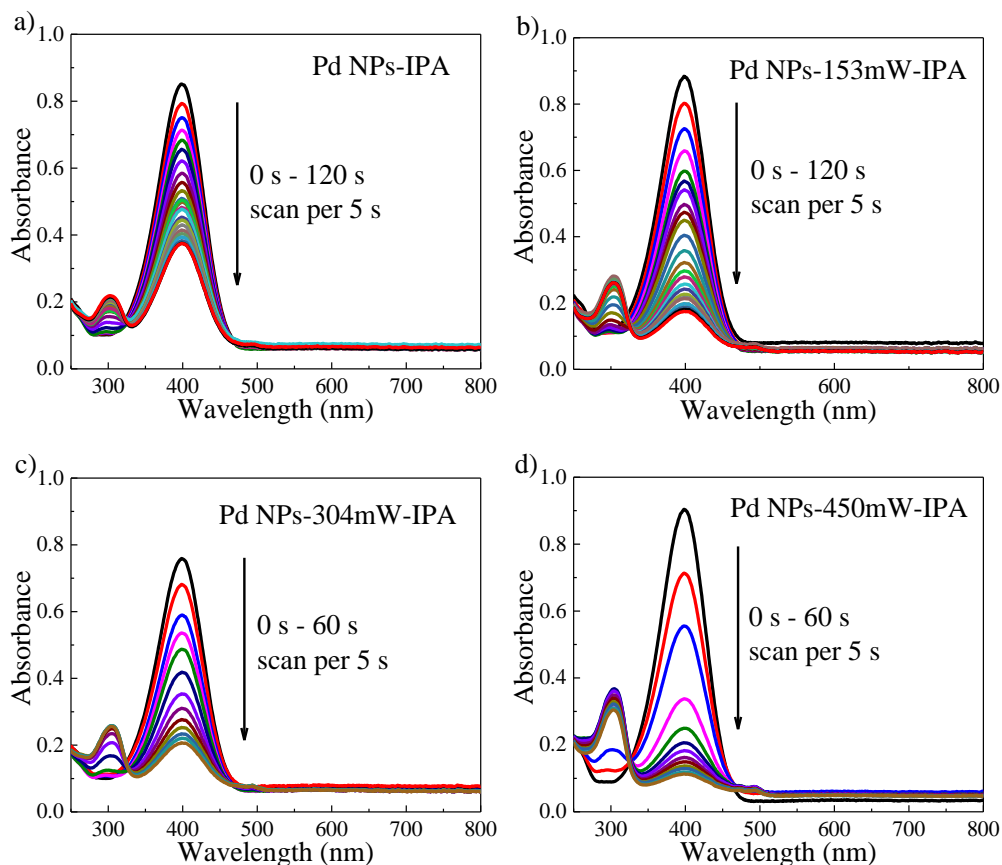


**Figure 3.4** UV-vis spectra of 4-nitrophenol reduction with  $\text{NaBH}_4$  catalyzed by Pd NPs without and with photocharging. Charging condition: isopropanol and 6-hour irradiation of 405 nm LED with different incident powers: (a) without photocharging, (b) charging



with 153 mW, (c) charging with 304 mW, and (d) charging with 450 mW. The extracted kinetic data were plotted in Figures 3.1c and 3.1d.

### 3.5 Quantification of accumulated electrons from photo-charging process

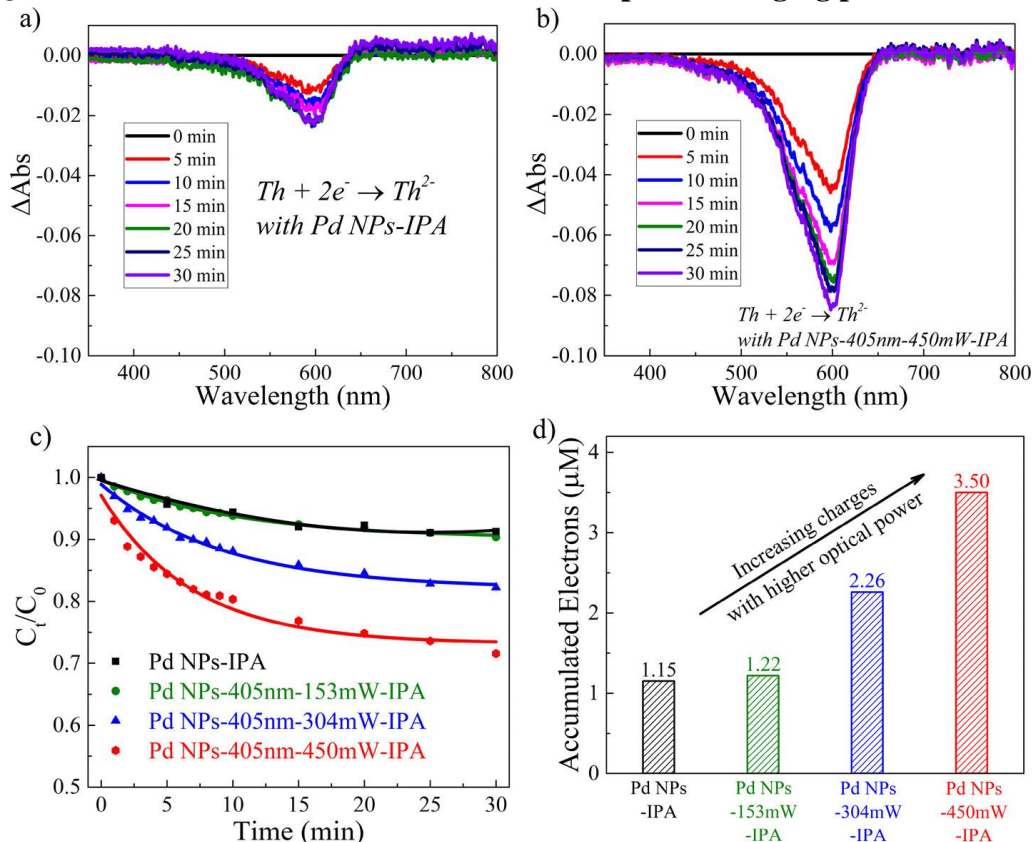


**Figure 3.5** Quantification of accumulated electrons from photo-charging process. (a, b) Absorbance change of thionine titrated with Pd NPs not undergoing and undergoing photo-charging (405 nm LED, 450 mW, 6 h, IPA). (c) Kinetic traces of titrated thionine retrieved from the absorbance at 600 nm. Solids lines are exponential fits. (d) Estimation of electrons accumulated under non-charging and charging conditions.

Redox titration with thionine (Th) was conducted on the photo-charged Pd NP solutions to estimate the accumulated electrons as thionine has a relatively low reduction potential.<sup>28</sup> In these aqueous titration solutions, despite that the standard reduction potential of  $\text{Th}/\text{Th}^{2-}$  is 0.064 V (vs NHE), the concentration of Th is 65 times higher than the proton concentration, thus the protons cannot quench significantly the accumulated electrons. Experimentally, right after photo-charging, 10  $\mu\text{L}$  of 1 mM thionine solution was injected into the solution of the catalysts, and the decay of  $\lambda_{\text{max}} = 600$  nm of thionine was monitored for estimating the number of electrons transferred from the nanoparticles (Figure 3.5). Noted that the uncharged Pd NPs also reacted with thionine (Figure 3.5a), probably because they already contained excess electrons from their reduction synthesis. The intrinsic charge of these Pd NPs were estimated and set as a reference for comparing to photo-charged Pd NPs.

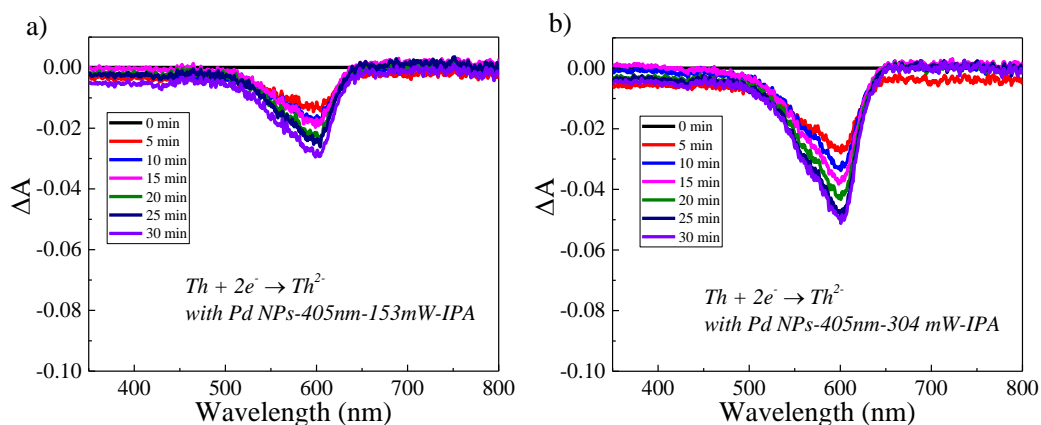


**Figure 3.6** Absorbance change of thionine (Th) when titrating with Pd NPs after photocharging with: (a) 405 nm LED, 153 mW, 6 h, IPA, and (b) 405 nm LED, 304 mW, 6 h, IPA.

Considering the 4-nitrophenol reduction happened relatively fast, about a half conversion within a minute, and the particles transferred electrons to thionine within a comparable time scale, a 30-minute titration with thionine was chosen as the endpoint to estimate the accumulated charge (Figures 3.5c and Figure 3.6). Figure 3.5d shows a strong correlation between the optical power and the accumulated charges. A similar trend was observed for the correlation between optical power and reaction rate constant as shown in Fig 3.1d. This set of data proved the higher activity of the Pd NP catalysts under charging condition. A possible explanation for this improvement is that the more electrons accumulated in the metallic nanoparticles the larger gap built between the Fermi level and d-band center.<sup>43</sup> Consequently, these electrons could fill the antibonding orbitals hybridized between metal and absorbates, which decreased and moved the adsorption energy of nitrophenol closely to the optimal point for catalysis.<sup>44</sup> This optimal point was proposed in a systematic study on the same reaction using dendrimer encapsulated metal nanoparticles.

### 3.6 Evaluation of photo-charging effect on catalytic performance of Pd NPs under different conditions

Some other factors impacting the photo-charging process and the consequent catalysis were investigated, such as charging time, wavelengths of the light source, and different kinds of hole scavengers (Figure 3.7). Firstly, the amount of charge should be affected by charging time. For a short period of charging (3 hours for example, Figure 3.7a), the number of accumulated electrons per nanoparticle was probably low and did not make a significant change to the reaction rate yet. After 6 hours of charging, the accumulation of electrons reached a certain number that signified the photo-charging effect on catalysis. For a longer charging time (9 and 12 hours, Figure 3.7a), the catalytic activity of the particles dropped. We speculate that the particles may still maintain a comparable amount of charge as in the 6-hour charged sample, but more oxidized products may form due to

hole quenching. They may adsorb on the nanoparticle surface and block the active sites for the further reduction reaction.

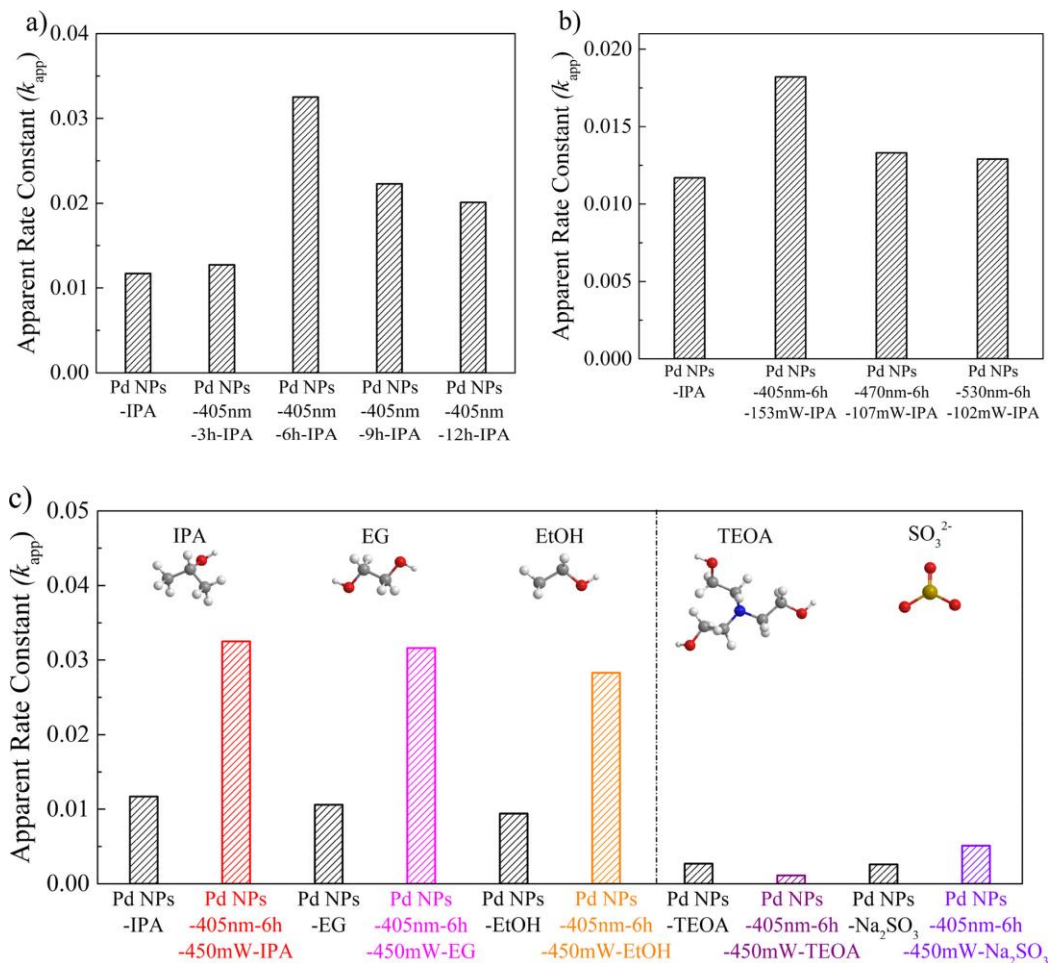


**Figure 3.7** Evaluation of photo-charging effect on catalytic performance of Pd NPs under different conditions: (a) charging time, (b) irradiation wavelength, and (c) hole scavenger.

Secondly, the wavelength dependence of the photocatalytic performance of Pd NPs was already thoroughly discussed in our previous work.<sup>23</sup> Under shorter wavelength excitation, interband transitions of Pd NPs generate deeper holes (below the Fermi level) with increasing oxidizing power. For photo-charging with 405 nm LED irradiation, the deeper hot holes could react easier with the hole scavengers, resulting in accumulating more electrons in the nanoparticles for the following reaction (Figure 3.7b). With longer wavelengths (470 or 530 nm), the photo-charging effect was not such strong because the hot holes were not deep enough to effectively oxidize IPA and build more charges. It should be noted that the absorbed photon fluxes were kept the same across the three studied wavelengths to make a fair comparison for these photo-charging processes (Table 3.2). Similar wavelength-dependent trend was also observed for gold nanoparticle photocatalysts under continuous irradiation.<sup>14, 19, 20</sup>

**Table 3.2** Calculation of absorbed photon fluxes under various excitation wavelengths.

Entry	Samples	Wavelength (nm)	Incident light (mW)	Absorbed light (mW)	Absorbed photon flux ( $10^{17}$ photons $\cdot$ s $^{-1}\cdot$ cm $^{-2}$ )
1	Pd NPs-IPA	N/A	N/A	N/A	N/A
2	Pd NPs-405nm-153mW-IPA	405	153	54	1.5
3	Pd NPs-470nm-107mW-IPA	470	107	46	1.5
4	Pd NPs-530nm-102mW-IPA	530	102	42	1.6

Notes: See charging conditions in the Experimental section. The charging time was 6 hours. These conditions were corresponded to data shown in Figure 3.7b. Due to the limited output power of the commercially available 470 and 530 nm LEDs, these experiments were conducted at low power to have the same number of absorbed photons across the three wavelengths.

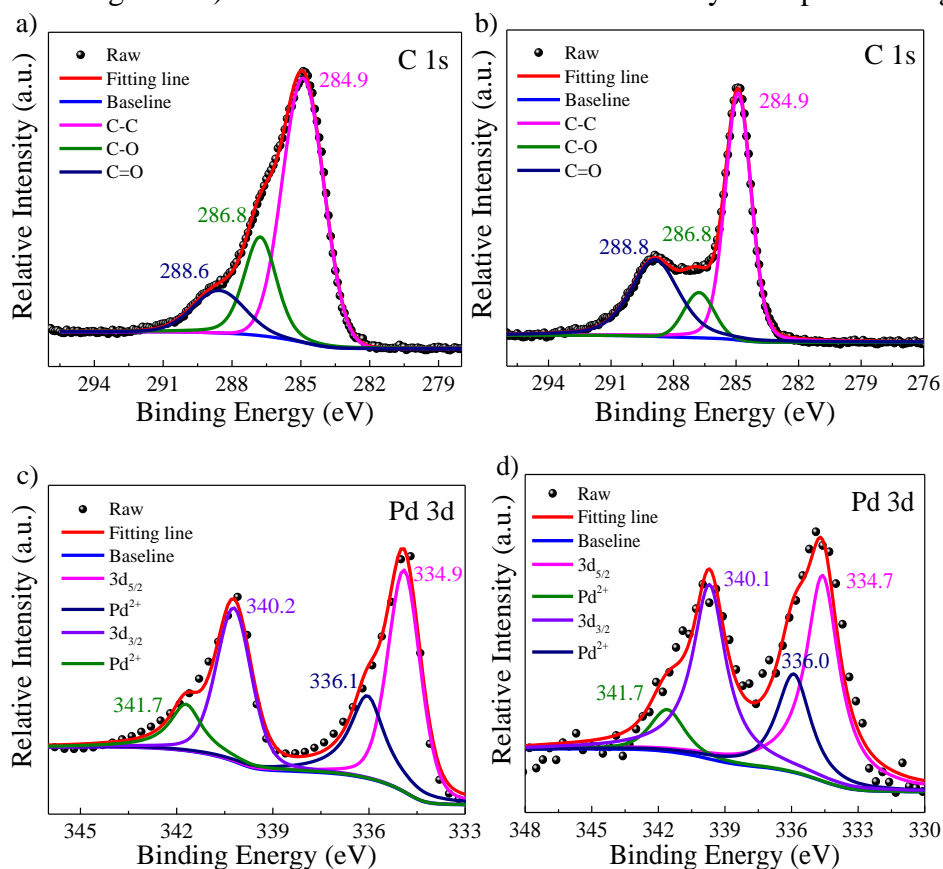
Thirdly, as the hole scavengers adsorbed on the particle surface and reacted with the photogenerated holes to accumulate electrons, the molecular interaction and reduction potential of those scavengers would also influence the photo-charging process. The commonly used hole scavengers, such as isopropyl alcohol (IPA), ethylene glycol (EG), and ethanol (EtOH), were all proved to be good candidates for sacrificial reagents in this study (Figure 3.7c). Compared to the non-charging counterparts, those charged Pd NPs showed a significant increase in the reaction rate constants. The increments were quite close to each other probably due to the comparable reduction potentials and similar functional groups of those scavengers.<sup>45</sup> Similarly, IPA and EtOH scavengers do not give a drastic difference in rate constants of ferricyanide reduction catalyzed by gold nanoparticle photocatalysts under continuous irradiation.<sup>19</sup> However, triethanolamine (TEOA) and sodium sulfite ( $\text{Na}_2\text{SO}_3$ ) almost quenched the 4-nitrophenol reduction reaction (Figure 3.7c). The reaction happened very slowly for the non-charging catalysts, which could be ascribed to the strong adsorption of amine and sulfite ions on the catalysts' surface and reducing the catalytic activity.<sup>46, 47</sup>

### 3.7 Conclusion and outlook

From all above evidence, photo-charging process is proved to be correlated to reduction kinetics. With more electrons built up after charging, a higher apparent reaction rate constant was achieved. The number of extra electrons accumulated per nanoparticle was estimated up to around  $2.3 \times 10^3$  from a typical photo-charging and the quantum yield of

this process was about 0.042 % (see details in note S1). A previous study showed that  $\text{NaBH}_4$  could adsorb on colloidal gold nanorods and charged these particles,<sup>48</sup> thus we cannot rule out this possibility from our system.

However, we emphasize that the additional charging by  $\text{NaBH}_4$  in the second step of our experiment does not overwhelm or erase the amount of charge in the first step. If this phenomenon has happened, we would not have seen any difference in reaction rate constants of the catalyzed reaction when we changed the charging conditions. Since  $\text{NaBH}_4$  will react to thionine, we cannot do redox titration on the reaction solution in the second step to determine any possible extra charge that  $\text{NaBH}_4$  may create on the catalysts. Finally, the oxidation state of surface Pd in our catalysts was examined carefully by X-ray photoelectron spectroscopy, and no significant change of Pd oxidation state was observed (see details in Figure 3.8). This result further validates the catalysis of photo-charging.



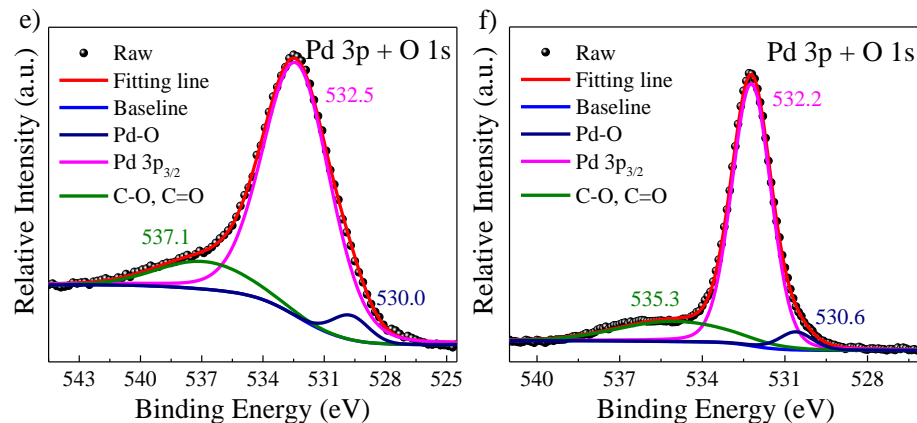


**Figure 3.8** XPS analysis of Pd NPs: (a, c, e) before, and (b, d, f) after a typical photocharging process (6-hour irradiation with 450 mW of 405 nm LED, and IPA was used as a hole scavenger). High-resolution XPS spectra and deconvoluted peak analysis of: (a, b) C 1s, (c, d) Pd 3d, and (e, f) Pd 3p + O 1s. The samples were prepared by drop-casting and drying the Pd NPs solution on a silicon wafer and sent for XPS immediately.

In principle, the oxidation states of surface Pd are not expected to change after the photocharging process. The assignment and deconvolution analysis of all peaks were based on the XPS handbook and literature.<sup>49-54</sup> Starting with the C 1s in Figures 3.8a and b, atmospheric carboxylic acids adsorbed on the catalyst surface<sup>55</sup> caused these C-O, C=O peaks, and the contamination carbon (C-C) around 284.9 eV was set as the reference to calibrate the binding energy of other elements. After the photocharging process, the C=O peaks seemed to increase possibly due to the absorbed acetone generated by hot-hole catalyzed oxidation of isopropyl.<sup>56</sup> As for the Pd 3d spectra in Figures 3.8c and 3.8d, there was always a certain amount of Pd<sup>2+</sup> that occurred on the Pd surface,<sup>51, 54</sup> which could be ascribed to the thin oxide layer formed on its surface.<sup>50</sup> The two main peaks of Pd 3d<sub>5/2</sub> and 3d<sub>3/2</sub> still stayed at around the same binding energy range and the deconvoluted peaks of Pd<sup>2+</sup> maintained almost the same intensities. These pieces of evidence demonstrated that the oxidation state of surface Pd did not change significantly after the photocharging process. Moreover, in the Pd 3p and O 1s region in Figures 3.8e and 3.8f, the corresponding C-O/C=O and Pd-O peaks were also deconvoluted for comparison.<sup>57</sup> Except for some differences in peak width that may come from the uneven distribution of sample measurement, there was no other significant change. Overall, the high-resolution XPS analysis confirmed that there is almost no changes of surface Pd oxidation state after the photocharging process.

In summary, the correlation between the number of accumulated electrons from photocharging and the catalytic activity of Pd NPs was built. For the best demonstration in this study, a three-time increase in accumulated charges results in a three-time increase in the catalytic activity of the photo-charged nanoparticles. This correlation brings a different perspective on understanding photocatalytic mechanisms of metallic nanoparticles, and helps to design high efficient photocatalysts. The photo-charged metallic nanoparticles may still catalyze chemical reactions after stopping irradiation, and this process should be considered in photocatalysis.

### 3.8 Supporting notes

#### 3.8.1 Note S1. Estimation of number of electrons per nanoparticle and quantum yield of photocharging

To rationalize photocharging effect on the nanoparticle catalysis, the number of electrons per nanoparticle was estimated from redox titration with thionine. The below calculation steps are demonstrated for Pd NPs-IPA and Pd NPs-IPA-450mW-IPA samples.

(1) Number of electrons transferred from reaction with thionine

$$\#(e^-) = AE \times N_A$$

Where:  $\#(e^-)$ : the number of electrons per liter of reaction solution,  $L^{-1}$ .

$N_A$ : Avogadro constant,  $6.0221 \times 10^{23} \text{ mol}^{-1}$ .

AE: accumulated electron concentration,  $\text{mol} \cdot L^{-1}$ .

As for the Pd NPs-IPA sample (AE= 1.15  $\mu\text{M}$ ), the number of electrons per particle is  $6.9254 \times 10^{17} L^{-1}$ .

As for the Pd NPs-IPA-450mW-IPA sample (AE= 3.50  $\mu\text{M}$ ), the number of electrons per particle is  $2.1077 \times 10^{18} L^{-1}$ .

(2) Number of nanoparticles used in titration with thionine

The general approach is calculating the total molar concentration of Pd element in Pd NPs used and estimating the moles of Pd element in one nanoparticle (accounting for the porosity of the particle). The average diameter (63 nm) and pore volume ( $0.30 \text{ cm}^3 \cdot \text{g}^{-1}$ ) are retrieved from our previous work.<sup>23</sup>

$$\#(NPs) = \frac{[Pd]}{n(Pd \text{ NP})}$$

Where:  $\#(NPs)$ : the number of nanoparticles,  $L^{-1}$ .

$[Pd]$ : molar concentration of Pd element in Pd NP catalysts used, 297  $\mu\text{M}$ .

$n(Pd \text{ NP})$ : moles of Pd element in one porous Pd nanoparticle, mol.

$$n(Pd \text{ NP}) = \frac{\rho(Pd) \times [V(Pd \text{ NP}) - V(\text{pore in Pd NP})]}{M(Pd)}$$

$\rho(Pd)$ : density of Pd,  $12.023 \text{ g} \cdot \text{cm}^{-3}$ .

$V(Pd \text{ NP})$ : volume of one Pd nanoparticle,  $\text{cm}^3$ .

$$V(Pd \text{ NP}) = \frac{4}{3} \pi r^3$$

r: radius of one Pd nanoparticle, 31.5 nm.

$V(\text{pore in Pd NP})$ : pore volume of one Pd nanoparticle,  $\text{cm}^3$ .

$$V(\text{pore in Pd NP}) = \frac{V(\text{pore})}{\#(NPs \text{ per g})}$$

$V(\text{pore})$ : pore volume,  $0.30 \text{ cm}^3 \cdot \text{g}^{-1}$ .

$$\#(NPs \text{ per g}) = \frac{1 \text{ g}}{M(Pd) \times n(Pd \text{ NP})}$$

$M(Pd)$ : molar mass of Pd,  $106.42 \text{ mol} \cdot \text{g}^{-1}$ .

Thus, the number of nanoparticles is  $9.2506 \times 10^{13} L^{-1}$ .

(3) Number of electrons per nanoparticle

$$\#(e^- \text{ per NP}) = \frac{\#(e^-)}{\#(NPs)}$$

As for the Pd NPs-IPA sample, the number of electrons per nanoparticle is 7486. Considering that our nanoparticles are large and porous, the particles can accumulate a large amount of charge due to the donation of electrons from ascorbic acid during the particle synthesis step. We also cannot rule out the possibility that thionine adsorbs on the particles and reduces their absorbance, thus the number of calculated electrons may be artificially larger than the actual number.

As for the Pd NPs-IPA-450mW-IPA sample, the estimated number of electrons per nanoparticle is 30131. Thus, photocharging adds an average of 22645 electrons to each particle. Considering the size of 63 nm of our nanoparticles, this amount of charge is acceptable as compared to the charge densities from other studies such as 66 electrons per photocharged Ag/TiO<sub>2</sub> core@shell particle (around 5 nm),<sup>58</sup> up to around 8800 electrons per photocharged gold nanoparticles (13 nm),<sup>16</sup> and around 1600 electrons per electrochemical-charged Ag particle (around 11 nm).<sup>59</sup> Further calculation on the efficiency of the photocharging shows a very low quantum yield. This quantum yield is lower than the quantum yield of other photocatalysis processes<sup>14, 23</sup> as our intention here is demonstrating photocharging effect rather than optimizing the catalytic efficiency.

#### (4) Quantum yield of photocharging process

With the above number of accumulated electrons and absorbed photon flux (Table 3.1), the quantum yield (QY) of the photocharging process was calculated for further reference. Here, we demonstrate the calculation for Pd NPs-IPA-450mW-IPA sample.

$$QY = \frac{\#(e^- \text{ from photocharging})}{\#(\text{absorbed photons})}$$

$\#(e^- \text{ from photocharging}) = 1.4152 \times 10^{18}$ , number of electrons accumulated from photocharging, which is equal to the difference of electrons in photocharged and control samples.

$\#(\text{absorbed photons}) = 3.3683 \times 10^{21}$ , number of absorbed photons in 6 hours.

Thus, the quantum yield for this photocharging process is 0.042 %.



### 3.9 References

- (1) Zhang, C.; Li, Y.; Li, M.; Shuai, D.; Zhou, X.; Xiong, X.; Wang, C.; Hu, Q. Continuous Photocatalysis via Photo-charging and Dark-discharging for Sustainable Environmental Remediation: Performance, Mechanism, and Influencing Factors. *J. Hazard. Mater.* **2021**, *420*, 126607.
- (2) Choi, Y.; Koo, M. S.; Bokare, A. D.; Kim, D.-h.; Bahnemann, D. W.; Choi, W. Sequential Process Combination of Photocatalytic Oxidation and Dark Reduction for the Removal of Organic Pollutants and Cr(VI) Using Ag/TiO<sub>2</sub>. *Environ. Sci. Technol.* **2017**, *51*, 3973-3981.
- (3) Boruah, B. D.; Mathieson, A.; Wen, B.; Feldmann, S.; Dose, W. M.; De Volder, M. Photo-rechargeable Zinc-ion Batteries. *Energ. Environ. Sci.* **2020**, *13*, 2414-2421.
- (4) Xu, J.; Chen, Y.; Dai, L. Efficiently Photo-charging Lithium-ion Battery by Perovskite Solar Cell. *Nat. Commun.* **2015**, *6*, 8103.
- (5) Tatsuma, T.; Saitoh, S.; Ohko, Y.; Fujishima, A. TiO<sub>2</sub>-WO<sub>3</sub> Photoelectrochemical Anticorrosion System with an Energy Storage Ability. *Chem. Mater.* **2001**, *13*, 2838-2842.
- (6) Trześniewski, B. J.; Smith, W. A. Photocharged BiVO<sub>4</sub> Photoanodes for Improved Solar Water Splitting. *J. Mater. Chem. A* **2016**, *4*, 2919-2926.
- (7) Brus, L. Noble Metal Nanocrystals: Plasmon Electron Transfer Photochemistry and Single-Molecule Raman Spectroscopy. *Acc. Chem. Res.* **2008**, *41*, 1742-1749.
- (8) Wilson, A. J.; Jain, P. K. Light-Induced Voltages in Catalysis by Plasmonic Nanostructures. *Acc. Chem. Res.* **2020**, *53*, 1773-1781.
- (9) Mao, Z.; Espinoza, R.; Garcia, A.; Enwright, A.; Vang, H.; Nguyen, S. C. Tuning Redox Potential of Gold Nanoparticle Photocatalysts by Light. *ACS Nano* **2020**, *14*, 7038-7045.
- (10) Choi, H.; Chen, W. T.; Kamat, P. V. Know Thy Nano Neighbor. Plasmonic versus Electron Charging Effects of Metal Nanoparticles in Dye-Sensitized Solar Cells. *ACS Nano* **2012**, *6*, 4418-4427.
- (11) Tatsuma, T.; Saitoh, S.; Ngaotrakanwivat, P.; Ohko, Y.; Fujishima, A. Energy Storage of TiO<sub>2</sub>-WO<sub>3</sub> Photocatalysis Systems in the Gas Phase. *Langmuir* **2002**, *18*, 7777-7779.
- (12) Zhang, Z.; Yates, J. T. Band Bending in Semiconductors: Chemical and Physical Consequences at Surfaces and Interfaces. *Chem. Rev.* **2012**, *112*, 5520-5551.
- (13) Yuan, W.; Zhu, B.; Fang, K.; Li, X.-Y.; Hansen, T. W.; Ou, Y.; Yang, H.; Wagner, J. B.; Gao, Y.; Wang, Y.; Zhang, Z. In situ Manipulation of the Active Au-TiO<sub>2</sub> Interface with Atomic Precision during CO Oxidation. *Science* **2021**, *371*, 517-521.
- (14) Zhao, J.; Nguyen, S. C.; Ye, R.; Ye, B.; Weller, H.; Somorjai, G. A.; Alivisatos, A. P.; Toste, F. D. A Comparison of Photocatalytic Activities of Gold Nanoparticles Following Plasmonic and Interband Excitation and a Strategy for Harnessing Interband Hot Carriers for Solution Phase Photocatalysis. *ACS Cent. Sci.* **2017**, *3*, 482-488.
- (15) Wu, X.; Redmond, P. L.; Liu, H.; Chen, Y.; Steigerwald, M.; Brus, L. Photovoltage Mechanism for Room Light Conversion of Citrate Stabilized Silver Nanocrystal Seeds to Large Nanoprisms. *J. Am. Chem. Soc.* **2008**, *130*, 9500-9506.
- (16) Kim, Y.; Dumett Torres, D.; Jain, P. K. Activation Energies of Plasmonic Catalysts. *Nano Lett.* **2016**, *16*, 3399-3407.
- (17) Zhai, Y.; DuChene, J. S.; Wang, Y.-C.; Qiu, J.; Johnston-Peck, A. C.; You, B.; Guo, W.; DiCiaccio, B.; Qian, K.; Zhao, E. W.; Ooi, F.; Hu, D.; Su, D.; Stach, E. A.; Zhu, Z.; Wei, W. D. Polyvinylpyrrolidone-induced Anisotropic Growth of Gold Nanoprisms in Plasmon-driven Synthesis. *Nat. Mater.* **2016**, *15*, 889-895.
- (18) Yu, S.; Wilson, A. J.; Heo, J.; Jain, P. K. Plasmonic Control of Multi-Electron Transfer and C-C Coupling in Visible-Light-Driven CO<sub>2</sub> Reduction on Au Nanoparticles. *Nano Lett.* **2018**, *18*, 2189-2194.

- (19) Kim, Y.; Smith, J. G.; Jain, P. K. Harvesting Multiple Electron–hole Pairs Generated through Plasmonic Excitation of Au Nanoparticles. *Nat. Chem.* **2018**, *10*, 763-769.
- (20) Wilson, A. J.; Mohan, V.; Jain, P. K. Mechanistic Understanding of Plasmon-Enhanced Electrochemistry. *J. Phys. Chem. C* **2019**, *123*, 29360-29369.
- (21) Yu, S.; Jain, P. K. The Chemical Potential of Plasmonic Excitations. *Angew. Chem. Int. Ed.* **2020**, *59*, 2085-2088.
- (22) Mao, Z.; Vang, H.; Garcia, A.; Tohti, A.; Stokes, B. J.; Nguyen, S. C. Carrier Diffusion—The Main Contribution to Size-Dependent Photocatalytic Activity of Colloidal Gold Nanoparticles. *ACS. Catal.* **2019**, *9*, 4211-4217.
- (23) Lyu, P.; Espinoza, R.; Khan, M. I.; Spaller, W. C.; Ghosh, S.; Nguyen, S. C. Mechanistic Insight into Deep Holes from Interband Transitions in Palladium Nanoparticle Photocatalysts. *ChemRxiv* **2021**, DOI: 10.26434/chemrxiv-2021-2qx43.
- (24) Corby, S.; Rao, R. R.; Steier, L.; Durrant, J. R. The Kinetics of Metal Oxide Photoanodes from Charge Generation to Catalysis. *Nat. Rev. Mater.* **2021**, *6*, 1136-1155.
- (25) Zhan, C.; Chen, X.-J.; Yi, J.; Li, J.-F.; Wu, D.-Y.; Tian, Z.-Q. From Plasmon-enhanced Molecular Spectroscopy to Plasmon-mediated Chemical Reactions. *Nat. Rev. Chem.* **2018**, *2*, 216-230.
- (26) Redmond, P. L.; Brus, L. E. “Hot Electron” Photo-Charging and Electrochemical Discharge Kinetics of Silver Nanocrystals. *J. Phys. Chem. C* **2007**, *111*, 14849-14854.
- (27) Akuto, K.; Sakurai, Y. A Photorechargeable Metal Hydride/Air Battery. *J. Electrochem. Soc.* **2001**, *148*, A121-A125.
- (28) Kongkanand, A.; Kamat, P. V. Electron Storage in Single Wall Carbon Nanotubes. Fermi Level Equilibration in Semiconductor–SWCNT Suspensions. *ACS Nano* **2007**, *1*, 13-21.
- (29) Takai, A.; Kamat, P. V. Capture, Store, and Discharge. Shuttling Photogenerated Electrons across TiO<sub>2</sub>–Silver Interface. *ACS Nano* **2011**, *5*, 7369-7376.
- (30) Erwin, W. R.; Zarick, H. F.; Talbert, E. M.; Bardhan, R. Light Trapping in Mesoporous Solar Cells with Plasmonic Nanostructures. *Energ. Environ. Sci.* **2016**, *9*, 1577-1601.
- (31) Wang, Q.; Butburee, T.; Wu, X.; Chen, H.; Liu, G.; Wang, L. Enhanced Performance of Dye-sensitized Solar Cells by Doping Au Nanoparticles into Photoanodes: A Size Effect Study. *J. Mater. Chem. A* **2013**, *1*, 13524-13531.
- (32) Novo, C.; Funston, A. M.; Gooding, A. K.; Mulvaney, P. Electrochemical Charging of Single Gold Nanorods. *J. Am. Chem. Soc.* **2009**, *131*, 14664-14666.
- (33) Li, C.; Iqbal, M.; Jiang, B.; Wang, Z.; Kim, J.; Nanjundan, A. K.; Whitten, A. E.; Wood, K.; Yamauchi, Y. Pore-Tuning to Boost the Electrocatalytic Activity of Polymeric Micelle-Templated Mesoporous Pd Nanoparticles. *Chem. Sci.* **2019**, *10*, 4054-4061.
- (34) Subramanian, V.; Wolf, E. E.; Kamat, P. V. Catalysis with TiO<sub>2</sub>/Gold Nanocomposites. Effect of Metal Particle Size on the Fermi Level Equilibration. *J. Am. Chem. Soc.* **2004**, *126*, 4943-4950.
- (35) Hervés, P.; Pérez-Lorenzo, M.; Liz-Marzán, L. M.; Dzubielia, J.; Lu, Y.; Ballauff, M. Catalysis by Metallic Nanoparticles in Aqueous Solution: Model Reactions. *Chem. Soc. Rev.* **2012**, *41*, 5577-5587.
- (36) Xiao, Q.; Sarina, S.; Waclawik, E. R.; Jia, J.; Chang, J.; Riches, J. D.; Wu, H.; Zheng, Z.; Zhu, H. Alloying Gold with Copper Makes for a Highly Selective Visible-Light Photocatalyst for the Reduction of Nitroaromatics to Anilines. *ACS. Catal.* **2016**, *6*, 1744-1753.
- (37) Jensen, S. C.; Bettis Homan, S.; Weiss, E. A. Photocatalytic Conversion of Nitrobenzene to Aniline through Sequential Proton-Coupled One-Electron Transfers from a Cadmium Sulfide Quantum Dot. *J. Am. Chem. Soc.* **2016**, *138*, 1591-1600.
- (38) Yao, L.; Li, X.; Peng, W.; Yao, Q.; Xia, J.; Lu, Z.-H. Co-CeO<sub>x</sub> Nanoparticles Anchored on a Nitrogen-doped Carbon Nanosheet: A Synergistic Effect for Highly Efficient Hydrolysis of Sodium Borohydride. *Inorg. Chem. Front.* **2021**, *8*, 1056-1065.

- (39) Yao, Q.; Ding, Y.; Lu, Z.-H. Noble-metal-free Nanocatalysts for Hydrogen Generation from Boron- and Nitrogen-based Hydrides. *Inorg. Chem. Front.* **2020**, *7*, 3837-3874.
- (40) Aditya, T.; Pal, A.; Pal, T. Nitroarene Reduction: A Trusted Model Reaction to Test Nanoparticle Catalysts. *Chem. Commun.* **2015**, *51*, 9410-9431.
- (41) Wunder, S.; Polzer, F.; Lu, Y.; Mei, Y.; Ballauff, M. Kinetic Analysis of Catalytic Reduction of 4-Nitrophenol by Metallic Nanoparticles Immobilized in Spherical Polyelectrolyte Brushes. *J. Phys. Chem. C* **2010**, *114*, 8814-8820.
- (42) Mendes, P. C. D.; Costa-Amaral, R.; Gomes, J. F.; Da Silva, J. L. F. The Influence of Hydroxy Groups on the Adsorption of Three-carbon Alcohols on Ni(111), Pd(111) and Pt(111) Surfaces: A Density Functional Theory Study within the D3 Dispersion Correction. *Phys. Chem. Chem. Phys.* **2019**, *21*, 8434-8444.
- (43) Hammer, B.; Nørskov, J. K. Theoretical Surface Science and Catalysis—Calculations and Concepts. *Advances in Catalysis* **2000**, *45*, 71-129.
- (44) Pozun, Z. D.; Rodenbusch, S. E.; Keller, E.; Tran, K.; Tang, W.; Stevenson, K. J.; Henkelman, G. A Systematic Investigation of p-Nitrophenol Reduction by Bimetallic Dendrimer Encapsulated Nanoparticles. *J. Phys. Chem. C* **2013**, *117*, 7598-7604.
- (45) Pan, H.; Heagy, M. D. Bicarbonate Reduction with Semiconductor Photocatalysts: Study of Effect of Positive Hole Scavengers. *MRS Commun.* **2018**, *8*, 1173-1177.
- (46) Cookson, J. The Preparation of Palladium Nanoparticles. *Platinum Met. Rev.* **2012**, *56*, 83-98.
- (47) Albers, P.; Pietsch, J.; Parker, S. F. Poisoning and Deactivation of Palladium Catalysts. *J. Mol. Catal. A: Chem.* **2001**, *173*, 275-286.
- (48) Mulvaney, P.; Pérez-Juste, J.; Giersig, M.; Liz-Marzán, L. M.; Pecharrómán, C. Drastic Surface Plasmon Mode Shifts in Gold Nanorods Due to Electron Charging. *Plasmonics* **2006**, *1*, 61-66.
- (49) Chastain, J.; King Jr, R. C. *Handbook of X-ray Photoelectron Spectroscopy*. Perkin-Elmer, USA: 1992; p 261.
- (50) Nguyen, L.; Tao, F. F.; Tang, Y.; Dou, J.; Bao, X.-J. Understanding Catalyst Surfaces during Catalysis through Near Ambient Pressure X-ray Photoelectron Spectroscopy. *Chem. Rev.* **2019**, *119*, 6822-6905.
- (51) Chen, D.; Li, C.; Liu, H.; Ye, F.; Yang, J. Core-shell Au@Pd Nanoparticles with Enhanced Catalytic Activity for Oxygen Reduction Reaction via Core-shell Au@Ag/Pd Constructions. *Sci. Rep.* **2015**, *5*, 11949.
- (52) Collins, G.; O'Dwyer, C.; Holmes, J. Colloidal Palladium Nanoparticles versus Commercial Palladium Catalysts for Suzuki Cross Coupling Reactions—The Influence of Surface Functionalization. *TechConnect Briefs* **2015**, *2*, 79-82.
- (53) Xing, X.-L.; Zhao, Y.-F.; Li, H.; Wang, C.-T.; Li, Q.-X.; Cai, W.-B. High Performance Ag Rich Pd-Ag Bimetallic Electrocatalyst for Ethylene Glycol Oxidation in Alkaline Media. *J. Electrochem. Soc.* **2018**, *165*, J3259-J3265.
- (54) Nazemi, M.; Soule, L.; Liu, M.; El-Sayed, M. A. Ambient Ammonia Electrosynthesis from Nitrogen and Water by Incorporating Palladium in Bimetallic Gold–Silver Nanocages. *J. Electrochem. Soc.* **2020**, *167*, 054511.
- (55) Balajka, J.; Hines, M. A.; DeBenedetti, W. J. I.; Komora, M.; Pavelec, J.; Schmid, M.; Diebold, U. High-affinity Adsorption Leads to Molecularly Ordered Interfaces on TiO<sub>2</sub> in Air and Solution. *Science* **2018**, *361*, 786-789.
- (56) Mohan, V.; Wu, E.; Heo, J.; Das, A.; Jain, P. K. Synergistic Photochemistry of Alcohols Catalyzed by Plasmonic Nanoparticles and a Metal Complex. *ACS Energy Lett.* **2021**, *6*, 1980-1989.
- (57) Zemlyanov, D.; Aszalos-Kiss, B.; Kleimenov, E.; Teschner, D.; Zafeiratos, S.; Hävecker, M.; Knop-Gericke, A.; Schlögl, R.; Gabasch, H.; Unterberger, W.; Hayek, K.; Klötzer, B. In situ XPS

Study of Pd(111) Oxidation. Part 1: 2D Oxide Formation in  $10^{-3}$  mbar  $O_2$ . *Surf. Sci.* **2006**, *600*, 983-994.

(58) Hirakawa, T.; Kamat, P. V. Charge Separation and Catalytic Activity of Ag@TiO<sub>2</sub> Core–Shell Composite Clusters under UV–Irradiation. *J. Am. Chem. Soc.* **2005**, *127*, 3928-3934.

(59) Ung, T.; Giersig, M.; Dunstan, D.; Mulvaney, P. Spectroelectrochemistry of Colloidal Silver. *Langmuir* **1997**, *13*, 1773-1782.

## Chapter 4 From Noble to Non-noble Metallic Nanoparticle Photocatalyst: What Can Interband Transition Bring?

(This chapter covers similar materials as in a submitted manuscript to *JACS Au* as a full article. Reproduced with permission, copyright © The Authors and 2023 American Chemical Society.)

### Abstract

Metallic nanoparticles have been developed as versatile photocatalysts, exemplified by those of noble metals with interesting plasmonic properties. The transitioning from precious to Earth abundant metals for sustainable photocatalysis requires the understanding and evaluation of catalytic performance. Photocatalysis induced by interband transitions of metallic nanoparticles has been explored for the unique properties of corresponding hot carriers and opportunities to expand from noble to low-cost non-noble metals. In this work, we presented an approach of how the electronic structure, *d*-band structure, and related interband transitions change across gold, palladium, and cobalt nanoparticles. We demonstrated that the better alignment of energy levels between metal-adsorbate states and interband-induced hot carriers in cobalt-based nanoparticles could benefit the better photocatalysis enhancement toward reduction reactions than gold and palladium. This proof-of-concept study leads us to expand the metallic nanoparticle photocatalysts into non-noble metals and our understanding of the role of interband transitions in related photocatalysis.

### 4.1 Introduction

Metallic nanocrystals have gained great interest in photocatalysis due to their strong and tunable light absorption, robust nature for multi-cycle operation, and versatile integration with other supporting materials.<sup>1-13</sup> Currently, most metallic nanocrystal photocatalysts are based on noble metals, such as Au<sup>11, 14, 15</sup>, Ag<sup>16-18</sup>, Pt<sup>19, 20</sup>, and Pd<sup>13, 21-23</sup>. However, the high cost hinders their large-scale application for photocatalysis. The low-cost alternatives are non-noble and less precious versions.<sup>24,25</sup> To explore and evaluate the transition to more affordable materials, Co-B alloy nanocrystals will be demonstrated in this study. Photocatalysis of the crystals will be studied for a model reduction reaction, and the photocatalytic activities will be directly compared to Au and Pd nanocrystal photocatalysts.

When moving from noble to non-noble metals (i.e. moving from the bottom right to the top left of the periodic table), the electronic structures and the associated catalytic properties of metallic nanocrystals change significantly. The trends of these changes can be predicted by building on our knowledge in solid state chemistry as long as the crystal sizes are large enough for possessing metallic states. The electronic interaction between the metals and chemical reactants can be roughly predicted by the energy levels of the metals' valence electrons. First, electron filling in the *d*-bands reduces gradually from full-filling to partially-filling states when moving from noble to non-noble metals. According to Newns–Anderson–Grimley model<sup>26, 27</sup> and *d*-band theory<sup>28-30</sup>, the broad nature of the

*sp*-bands in different transition metals results in similar bond strength between metals and adsorbates, while less electron filling in *d*-band states results in less filling of metal-adsorbate antibonding states and eventually strengthening metal-adsorbate bonds (see Scheme 1). Second, the Fermi levels of these metals gradually shift from *sp*- to *d*- bands and have more *d*-character. Third, less nuclear charge leads to less *d*-orbital contraction within individual atoms, but more *d*-orbital spatial overlap between of neighboring atoms in the nanocrystals, and eventually gives wider *d*-bands.<sup>31</sup> The wider *d*-bands also give more *d*-character to the antibonding states of metal-adsorbate states. All these factors, as illustrated in Scheme 1, contribute to stronger overlaps between *d*-orbitals of the metals and the molecular orbitals of the adsorbates. This condition facilitates the adsorption of reactants on the metal surface for catalysis and generally correlates to catalytic activities. For example, Co metal provides better catalysis for O<sub>2</sub> dissociation than Pd and Au.<sup>32</sup> In the production of methane from syngas, Co metal catalysts demonstrated a much higher turnover frequency than Pd and Au because Co has stronger CO dissociative chemisorption, a rate determining step of the methanation reaction.<sup>28</sup> In the context of this study, Co-B alloyed nanocrystals behave like Co metal (*vide infra*), and we expect that the reactants of the catalyzed reactions have a stronger adsorption on Co-B nanocrystals than on Au and Pd nanocrystals.

Following the adsorption of the reactants on the metal surfaces, the photocatalysis of metallic nanocrystals also concern various mechanisms evolving energy and charge transfers to the reactants, such as hot-carrier generation and transfer,<sup>33, 34</sup> field enhancement<sup>35</sup> and photothermal effect<sup>36</sup>. As for the photocatalyzed reduction reaction demonstrating in this study, the first mechanism is our focus, and the properties of the photogenerated hot carriers depend on the optical excitation regions and the metal elements. As moving from noble to non-noble metals, the localized surface plasmon resonances (LSPRs) of the nanocrystals are less distinctive, but their interband transitions are ubiquitous and strong in the visible region.<sup>37</sup> Unlike the LSPR with high optical tunability via varying the particle size, shape and assembly, the interband transitions are less affected by these geometry factors. Interband transitions have been recently explored for producing “deep” hot holes below the Fermi levels and improving catalytic activities of many suitable reactions.<sup>22, 38, 39</sup> As interband transitions in d-block metals generate hot electrons near the Fermi levels and hot holes in the d-bands below the Fermi levels,<sup>33, 40, 41</sup> one strategy to utilize these carriers for catalyzing reduction reactions is quenching the hot holes and accumulating ground-state electrons for catalysis. This photo-charging approach was proved to effectively raise the Fermi levels of the nanoparticles. The approach should work well for the reduction pathway where the catalysis needs to have electrons transferred from the nanoparticles to the reactants. This mechanism was demonstrated for noble metal nanoparticles in previous studies,<sup>39, 42</sup> and we hypothesize that it is suitable for utilizing interband transitions in non-noble metal nanoparticles and elevating Fermi levels for photocatalyzed reduction reactions.

## 4.2 Experimental section

### 4.2.1 Chemicals and characterizations

All chemicals and reagents were used without any purification. Absorbance and related time-dependent profiles were measured by a UV-vis spectrometer (USB4000 Ocean Optics

with UV-VIS-NIR light source). Morphology of Au, Pd and Co-B NPs were examined by transmission electron microscopy (TEM, Talos F200C G2, 200 kV, Thermo Fisher Scientific). The size distribution and zeta potential were measured by dynamic light scattering (DLS, Zetasizer Pro, Malvern Panalytical). Crystalline structure of Au, Pd and Co-B NPs was determined by powder x-ray diffraction pattern (PXRD, PANalytical X'Pert PRO Theta/Theta, Co tubes, 40 kV, 45 mA) and was processed with X'Pert HighScore data analysis software. Surface structure of Au, Pd and Co-B NPs was examined by Fourier-transform infrared spectroscopy (FTIR, Nicolet iS50R, Thermo Fisher Scientific) and surface oxidation state of Co-B NPs before and after reaction was determined by x-ray photoelectron spectroscopy (XPS, Nexsa, Al K $\alpha$  X-ray source, Thermo Fisher Scientific). The samples were prepared by drop-casting and drying the Co-B NPs solution on a silicon wafer and sent for XPS immediately, in which the contamination carbon (C-C) around 284.9 eV was set as the reference to calibrate the binding energy of other elements. The possible intermediates and products from nitrobenzene reduction were determined qualifiedly by proton nuclear magnetic resonance ( $^1\text{H-NMR}$ , Varian-INOVA 400 MHz, Agilent Technologies), in which deuterated chloroform ( $\text{CDCl}_3$ ) was used as the solvent and mesitylene as the internal standard.

#### **4.2.2 Synthesis of Au nanoparticles (denoted as Au NPs)**

The synthesis protocol was modified from seed-mediated growth method developed by Xia's group<sup>43</sup> and used in our previous publication.<sup>44</sup> Briefly, the Au clusters were firstly prepared by rapid-injection of fresh  $\text{NaBH}_4$  solution (0.6 mL, 10 mM) into the 10 mL mixture of gold precursors  $\text{HAuCl}_4$  (0.25 mM) and CTAB (100 mM). After incubating for 3 hours, the Au clusters (5 mL) were mixed with ascorbic acid (150 mL, 100 mM), CTAC (200 mL, 200 mM) before the rapid-injection of more precursors  $\text{HAuCl}_4$  (200 mL, 0.5 mM). Followed by incubation at 30 °C 15 min and centrifugation, the 10 nm Au seeds were achieved for growing 40 nm Au NPs by drop-wise more precursors  $\text{HAuCl}_4$  through a syringe pump.

#### **4.2.3 Synthesis of porous Pd nanoparticles (denoted as Pd NPs)**

The synthesis protocol was modified from the hard-template method developed by the Yamauchi's group<sup>45</sup> and used in our previous publication<sup>22, 42</sup>. Briefly,  $\text{PS}_{5000}\text{-b-PEO}_{2200}$  (polystyrene-block-polyethylene oxide, Polymer Source Co.) was used as the template (8 mg dissolved in 200  $\mu\text{L}$  THF),  $\text{H}_2\text{PdCl}_4$  as the Pd precursor (500  $\mu\text{L}$ , 76.8 mM), ascorbic acid (2 mL, 0.1 M) as the reducing agent and HCl for adjusting the pH (160  $\mu\text{L}$ , 2M), afterwards incubating at 50 °C for 10 hours. The final products were washed and calcinated to remove the excess polymers before acting as the catalysts.

#### **4.2.4 Synthesis of amorphous cobalt-boron nanoparticles (denoted as Co-B NPs)**

The synthesis protocol was modified from the chemical reduction method developed by the Li's group.<sup>46</sup> Briefly, tetrabutylphosphonium bromide ( $\text{Bu}_4\text{PBr}$ , 51 mL, 0.05 M), cobalt(II) chloride ( $\text{CoCl}_2$ , 5.1 mL, 0.1 M) and KCl (21 g to form a saturated solution) were mixed well and then put into an ice bath for maintaining the temperature at 273 K. Then freshly-made  $\text{KBH}_4$  (40 mL, 0.5 M) was injected into the mixture with a rate of 20 mL/h.

After the reaction was complete, the black precipitates were washed and storage in ethanol solution for further characterization and catalysis.

#### **4.2.5 Nitrobenzene reduction with Co-B NPs as a model reaction for catalytic performance**

In a typical reaction condition, nitrobenzene (50  $\mu\text{L}$ , 10 mM, isopropanol as solvent), isopropanol (950  $\mu\text{L}$ ), hydrazine hydrate (50  $\mu\text{L}$ , 50-60 % aqueous solution), Co-B NPs (100  $\mu\text{L}$ , 0.3 M, stored in ethanol solution) and  $\text{H}_2\text{O}$  (850  $\mu\text{L}$ ) were mixed in a 4-side quartz cuvette (1x1 cm, R-3010-T, Spectrocell) and immediately sent for time-dependent UV-vis spectra measurement with a time interval of 1 second for 5 minutes under 700 rpm magnetic stirring. The absorbance at 262 nm was assigned to the reactant nitrobenzene and the concentration of it was corrected by subtracting the absorbance at 800 nm due to the relatively flat absorbance of Co-B NPs across the visible range. The absorbance at 278 nm confirmed the formation of the product aniline. The concentration change of nitrobenzene was further used for the kinetic analysis and rate constant calculation. The linear fit applied of  $\ln(C_t/C_0)$  vs. time between 100 s and 180 s (after the induction time of the catalyst activation) was used to achieve the apparent rate constant ( $k_{app}$ ,  $\text{s}^{-1}$ ).

As for the photocatalyzed reactions, a series of LED with different wavelengths (405 nm, 415nm, 450 nm, 470 nm, 490 nm, 530 nm, 595 nm, Thorlabs) were used as the light source to photo-excite the nanoparticles in the 4-clear sided cuvette, a cooling fan was used to keep the reaction at room temperature, and the other conditions remained the same with typical reaction condition above, unless specified. The incident power was measured by a power meter (PM100D console with S170C sensor, Thorlabs) and was kept as 150 mW, except for those experiments when adjusting different incident power. Since the absorbance of the reactant nitrobenzene cut off completely at 380 nm and product aniline off at 320 nm (Figure 4.7), the relatively narrow bandwidth of the LED in which the 405 nm LED started from 380 nm (Figure 4.11), there would no spectra overlap of the reactants or products that would interfere the monitoring of chemical kinetics from the light source.

#### **4.2.6 Nitrobenzene reduction with photo-charged Co-B NPs for mechanistic study**

To prove the photo-charging mechanism, one approach is to separate the charging step and catalysis reaction and to evaluate the catalytic performance with different charging conditions such as time or types of hole scavengers.<sup>42</sup> The photo-charging step was followed by charging the stock Co-B NPs (0.3 M, stored in ethanol solution) with a 405 nm LED and the incident power was kept at 450 mW. After a certain amount of charging time (varying from 10 min to 9 h), 100  $\mu\text{L}$  of photo-charged Co-B NPs was used as the catalysts for the nitrobenzene reduction in the dark. The rest protocol and data analysis was exactly the same as mentioned above when dealing with the photocatalytic reactions.

#### **4.2.7 Nitrobenzene reduction with Au NPs and Pd NPs for catalytic performance**

For Au NPs, since high concentration of isopropanol in the reaction solution was reducing the electrostatic interaction between nanoparticles thus causing the nanoparticles to form large aggregates, the typical reaction condition was modified to maintain the colloidal form of the reaction solution and the total volume of reaction solution was still 2

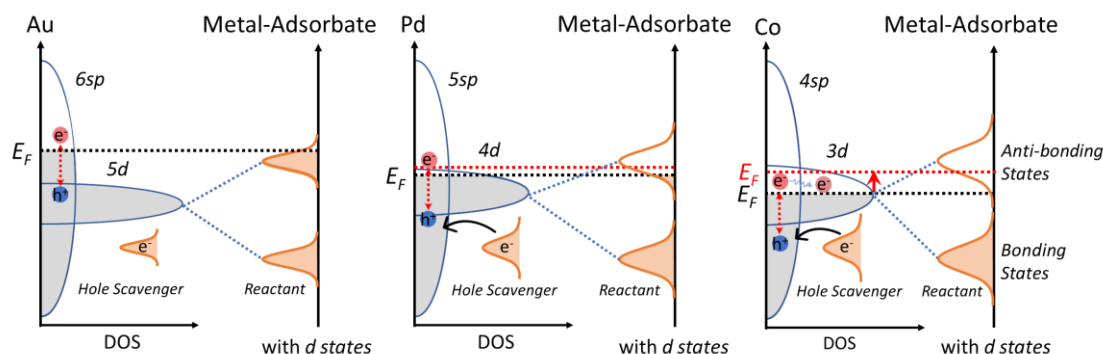


mL. Nitrobenzene (50  $\mu\text{L}$ , 10 mM, isopropanol as solvent), hydrazine hydrate (50  $\mu\text{L}$ , 50-60 % aqueous solution), Au NPs (500  $\mu\text{L}$ , 0.26 mM, stored in CTAC solution) and  $\text{H}_2\text{O}$  (1400  $\mu\text{L}$ ) were used as the reaction solution. The following conditions remained the same with typical condition and photocatalyzed reactions.

For Pd NPs, the only changes to the typical reaction condition were the amount of  $\text{H}_2\text{O}$  (700  $\mu\text{L}$ ) and Pd NPs (250  $\mu\text{L}$ , 2.26 mM, stored in water). Eventually the final amount of Co-B NPs in the reaction solutions was 27 times higher than Pd NPs, and the amount of Pd NPs was 8.7 times higher than Au NPs. Noting that even the absolute concentration of different NPs was not the same and the different optical responses to photo-excitation (especially interband transition was directly depending on the spectra absorbance), the optical adsorption of these nanoparticles at 400 nm (which was assigned to interband transitions) remained quite close to each other (in Figure 4.6a) and thus provided us a comparable analysis of its photocatalytic performance compared to its dark reaction.

### 4.3 Systematic comparison of Au, Pd and Co NPs

For the Co-B alloy nanoparticles used in this study, they must be stocked in an ethanol solution to prevent the oxidation of the particles. Thus, this alcohol type of hole quencher is conveniently used to demonstrate the photo-charging mechanism. In this work, we evaluate the photocatalysis based on photo-charging mechanism when moving from noble to non-noble metals. Within the photo-charging approach, we propose that when the hot holes generated from interband transition have an energetic alignment with the bonding states of hole scavengers, the photo-charging effect for raising the Fermi level and facilitating the electron transfer from metal to reactants will be enhanced. This hypothesis will be based on correlating the intrinsic  $d$ -band states, associated hot carriers and metal-adsorbate hybridized states across Au, Pd and Co nanoparticles, and will be evaluated by systematically comparing their photocatalytic performance accordingly.



**Scheme 4.1** Comparison of density of states (DOS), metal-adsorbate splitting states (bonding and antibonding), and interband transitions in three studied transition metals, (a) Au, (b) Pd, and (c) Co.  $E_F$  represents the Fermi level.

To be more specific, as shown in Scheme 1, in Au nanoparticles, fully filling of  $5d$  states and partially filling of  $6sp$  states makes the Fermi level far above the  $d$  band, and hot holes generated from  $d$ - $sp$  interband transitions have a large energy barrier to be quenched

by the electrons in bonding states of the hole scavengers. Noting that the interaction between the hole scavengers and metal surface are also treated similar to metal-reactant interaction as they are all adsorbates, and it should follow the same trend of metal-adsorbate splitting states as reactants across different metals, but in the scheme, it is simplified for clarification (or emphasizing) on catalysis by photo-charging effect. Since hole scavengers are more prone (or affinitive) to quench the hot holes, the relative potential of bonding states in hole scavengers should be higher than that in reactants but still below the *d*-band states of metals. Combined with the weak interaction between metal and reactants, photocatalysis by interband transition with almost no photo-charging effect cannot improve the catalysis significantly.

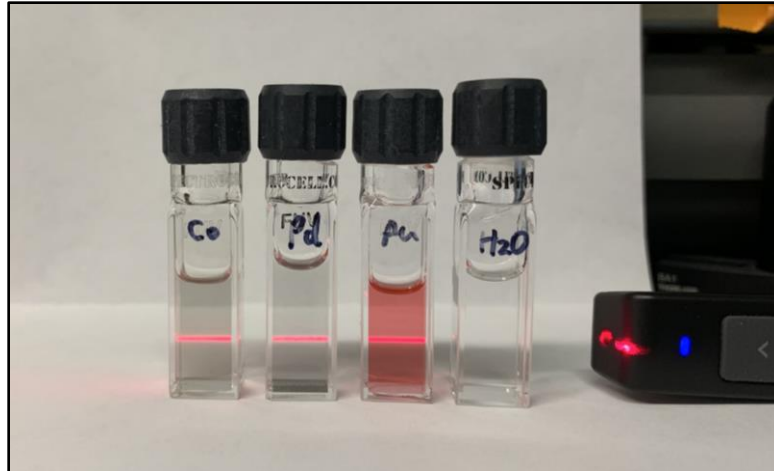
In Pd (known as platinum group metals and great catalysts), slightly partially filling of *4d* states makes the Fermi level across the *d* band, and hot holes from mostly *d-sp* interband transitions reside deeper in the *d* band. Also, there is a possibility that a small portion of interband transitions may occur as the *sp-d* transitions, which puts the hot holes even deeper down in the *sp* band. Then, those hot holes afford a chance to be quenched by the hole scavengers and offer a photo-charging effect to raise the Fermi level to a higher energy level. In such case, more electron filling in the antibonding states of metal-reactant states weakens metal-reactant bond and can promote the electron transfer reactions, eventually enhancing the photocatalytic activity.

In Co (known as non-noble and earth-abundant metal), partially filling of the *3d* states with more unoccupied states makes the Fermi level much lower in the *d*-band, and hot holes from *sp-d* interband transitions reside much deeper in the *sp* band. This provides an energetic alignment between hot holes and HOMO-like bonding states of the hole scavengers, thus promoting a stronger photo-charging effect and a significantly raising of Fermi level. Under such consideration, the weakening of metal-reactant bond and facilitating of electron transfer reactions should be more pronounced than Pd and Au, thus offering a better photocatalysis enhancement.

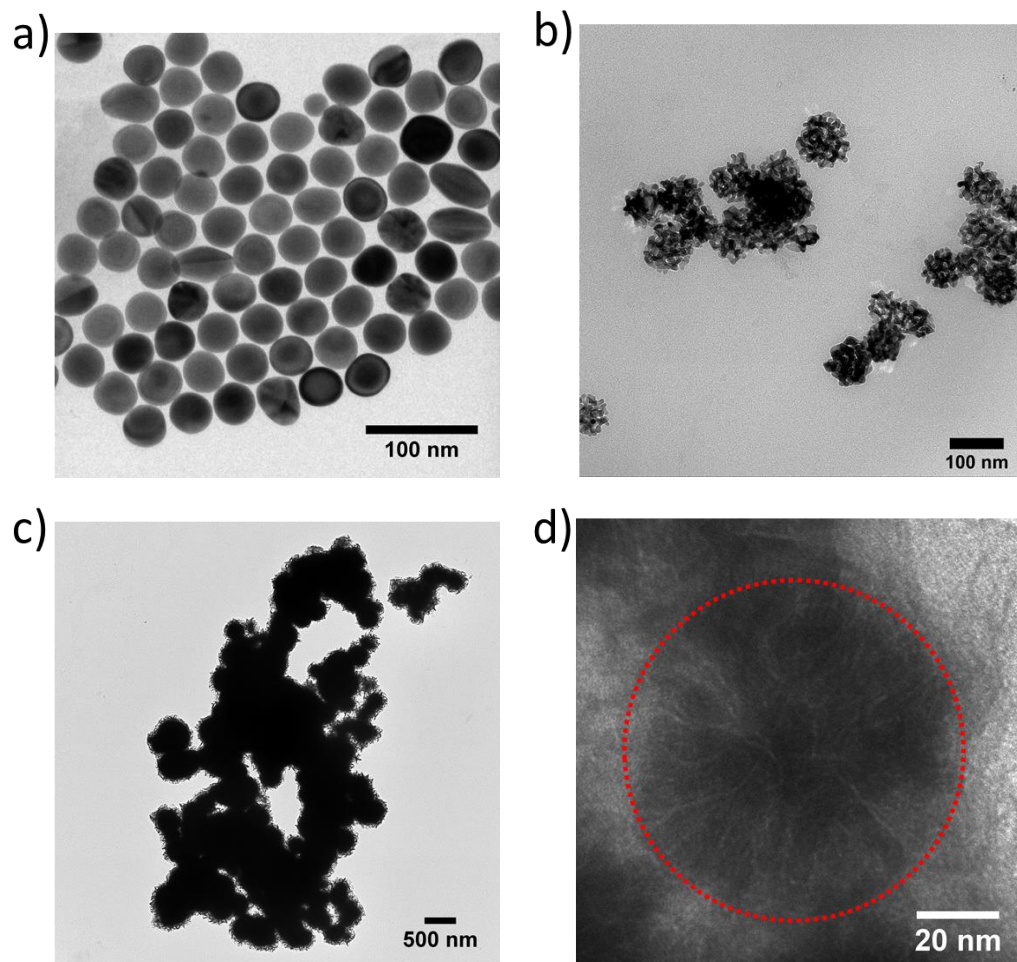
## **4.4 Experimental design and physicochemical properties of prepared NPs**

### **4.4.1 Size and shape distributions of colloidal Au, Pd and Co-B NPs**

Now, moving to the experimental design, considering the need for mechanistic interpretation, the colloidal metallic nanoparticles of Au, Pd, and Co were synthesized with similar physicochemical properties, especially the optical responses in the surveyed range supposed to be dominated by interband transitions (See more details in Experimental section above). Noting that the experimental challenge to maintain exactly the same size, shape, and surface status across the synthesis of different metallic nanoparticles is still in the wind and deserves more effort, but our goal here is to compare how the interband transitions affected by *d*-band structures and the interband transitions are independent of these parameters. Even with some deviations from the physicochemical properties, it should not compromise the validity of our comparison.

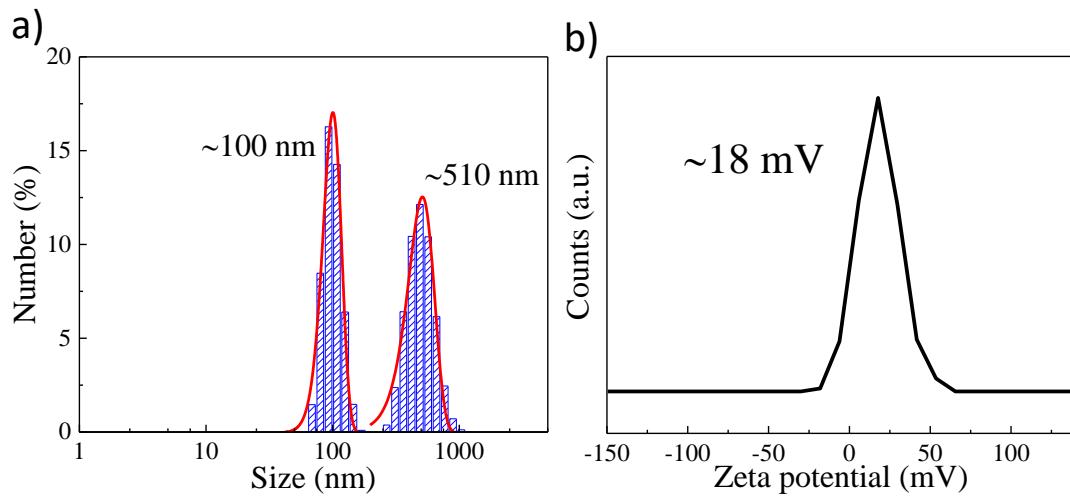


**Figure 4.1** Digital images of colloidal solutions of metallic nanoparticles in 4-side cuvettes. From left to right: Co-B NPs (in ethanol), Pd NPs (in H<sub>2</sub>O), Au NPs in (CTAC solution) and H<sub>2</sub>O as a reference.

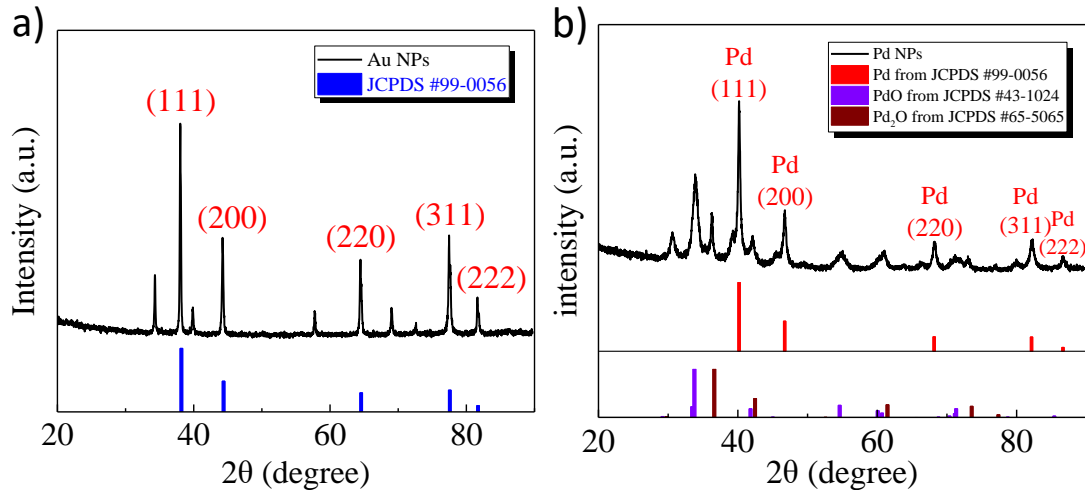


**Figure 4.2** TEM images of (a) Au, (b) Pd, (c) Co-B NPs and (d) one representative Co-B nanoparticle with crack structure inside. The average size of Au NPs is around  $38\pm 2$  nm, of Pd NPs around  $68\pm 12$  nm and of Co-B NPs around  $83\pm 22$  nm. Noting that the larger aggregates are not included in the size counting in Co-B NPs.

As then, the as-synthesized metallic nanoparticles were dispersed well and colloiddally in the solutions respectively (Figure 4.1), in the size range from around 40-80 nm (Figures 4.2 and 4.3), and in the metallic form with a relatively clean surface (Figures 4.4 and 4.5). For the record, the porous version of Pd NPs (denoted as Pd NPs) was used for separating the interband transitions from plasmon resonance (more details in later discussion)<sup>22</sup> and the cobalt-boron alloy version of Co NPs (denoted as Co-B NPs) was used for stabilizing the cobalt nanoparticles from intense and unavoidable surface oxidation.<sup>46</sup>



**Figure 4.3** Size distribution and zeta potential of Co-B NPs from DLS measurements.



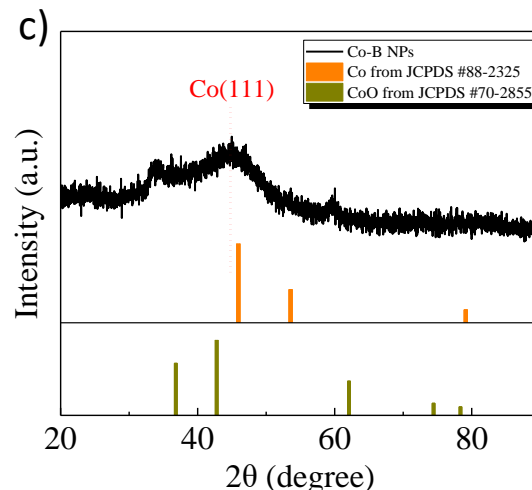


**Figure 4.4** PXRD patterns of (a) Au NPs, (b) Pd NPs, and (c) Co-B NPs. The JCPDF (Joint Committee on Powder Diffraction Standards) cards were retrieved from X’Pert HighScore data analysis software for comparing the crystal structure of those nanoparticles with standard database. The shift of Co(111) peak to a lower degree indicated the successful alloying of B into the lattice of Co nanoparticles.

As shown Figure 4.5, For Au NPs, C-H stretching mode of  $-\text{CH}_2$  group at  $2918$  and  $2849\text{ cm}^{-1}$ ,<sup>47</sup> C-H bending at around  $1464\text{ cm}^{-1}$ ,<sup>48</sup> C-N<sup>+</sup> stretching at  $960$  and  $908\text{ cm}^{-1}$ ,<sup>49</sup> and rocking mode<sup>49</sup> of  $-\text{CH}_2-$  chain at  $718\text{ cm}^{-1}$  indicated the existence of CTAC as a surfactant to stabilize the colloidal form of Au nanoparticles. For Pd NPs, there were few leftover polymers from the synthesis process and refer to more details in our previous publication.<sup>22</sup> For Co-B NPs, pulse vibrations from  $695$ - $1420\text{ cm}^{-1}$  were accounted for the borate<sup>50</sup> and the peaks around  $580\text{ cm}^{-1}$  for Co-O stretching mode<sup>51</sup>, which both formed on the particles’ surface.

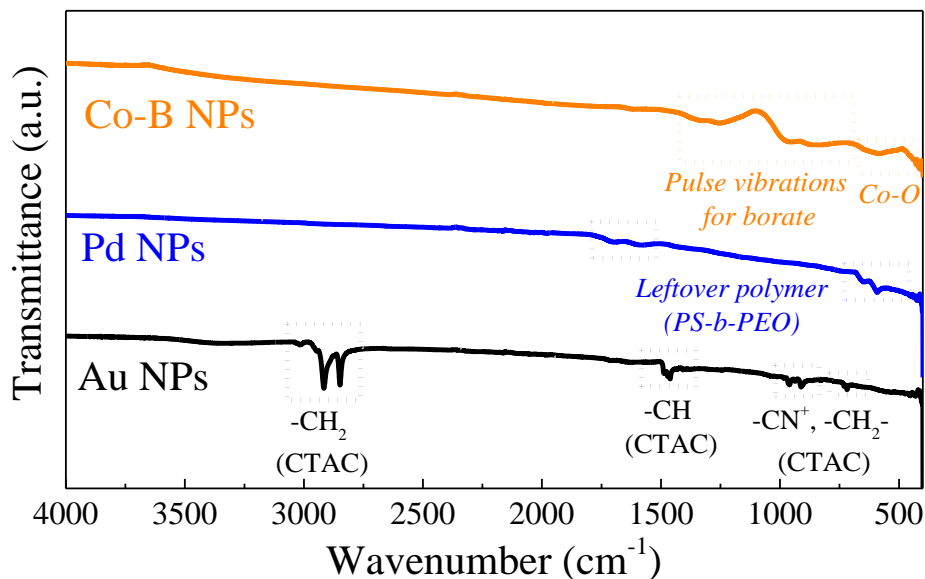


**Figure 4.5** FTIR spectra of Au NPs, Pd NPs, and Co-B NPs in ATR (attenuated total reflection) mode.

#### 4.4.2 Optical properties of colloidal Au, Pd and Co-B NPs

Furthermore, in the light of optical properties for these nanoparticles (Figure 4.6a), a comprehensive survey of Au NPs and Pd NPs was already conducted in our previous work.<sup>11, 22</sup>

In short, for Au NPs, the interband transitions rise from UV region up to visible range with a cut-off at around 600 nm and the plasmon resonance peaks at around 520 nm, in which with a light source at around 400 nm the interband transitions are responsible for the generation of hot carriers mostly.

As for Pd NPs, the common plasmon resonance is pretty broad across the ultraviolet-visible region and on top of the interband transitions in that region, in which this spectral overlap makes the mechanistic interpretation almost impossible.<sup>22</sup> Fortunately, the porous version of Pd NPs provided an alternative method to shift the plasmon resonance into a longer wavelength in the red-photon region, leaving the region around 400 nm dominated by interband transitions and featureless flat adsorption across the whole visible range.<sup>22</sup>

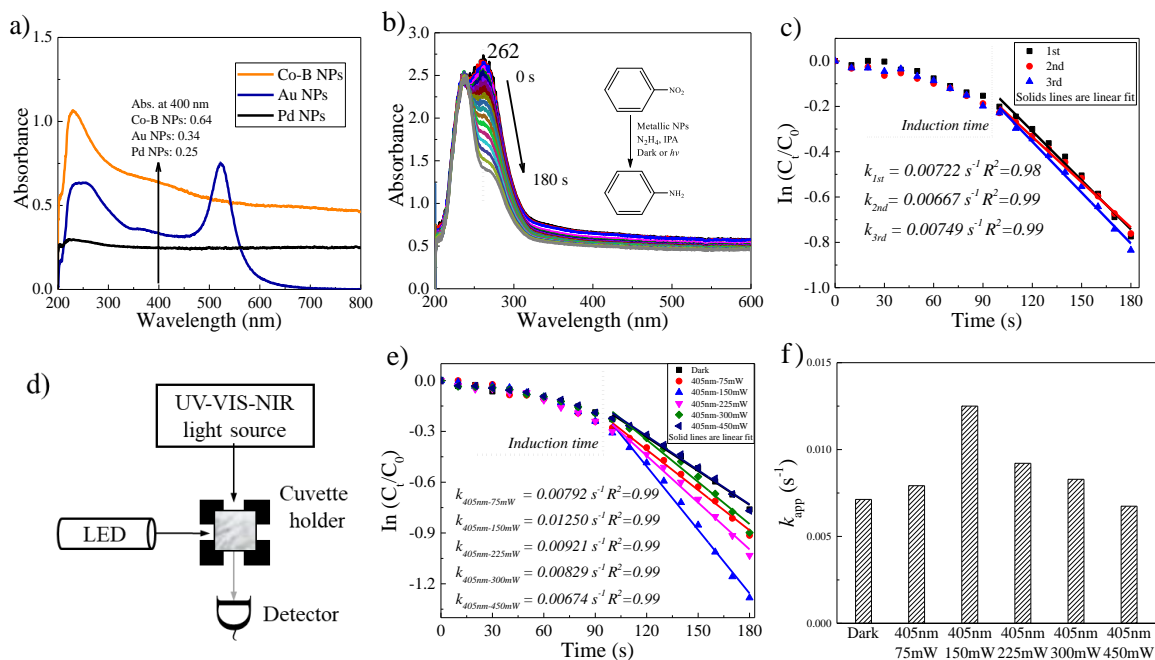
As for the Co-B NPs, to our best knowledge, very few and only recently reported the experimental measurement of optical properties,<sup>52-54</sup> however with different assignments of plasmon resonance and without any discussion on interband transitions. According to the theoretical prediction,<sup>37</sup> the plasmon resonance of cobalt should be in the deep-UV region and become pretty weak in the visible region, in which our adsorption spectrum of Co-B NPs did represent this trend (Figure 4.6a). However, the relatively flat adsorption across the whole visible range was still in the mystery and we suspected different types of electronic transitions may be responsible for that.

### 4.5 Evaluation of catalytic performance of Co-B NPs and mechanistic study

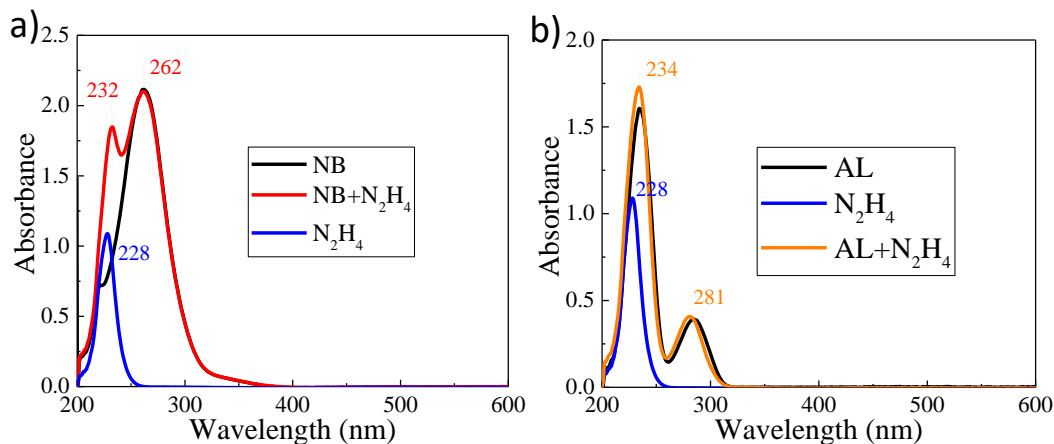
#### 4.5.1 Catalytic performance of Co-B NPs under dark and photo-excitations

Hence, a systematic investigation of the photocatalytic behavior of Co-B NPs across the visible range should be conducted before moving into the cross-over comparison among different metallic nanoparticles. On the other hand, the electron transfer reaction could be a good evaluating system for the comparison as shown in Scheme 4.1. With this regard, the model reaction of nitroaromatic reduction by metallic nanoparticles was employed in this work and proved to be a good indicator for kinetics analysis.<sup>42, 55</sup> The UV-vis adsorption of standard solutions for either reactant (nitrobenzene, at around 262 nm) or product (aniline, at around 281 nm) indicated the distinguishable difference between them (Figure 4.7), and a reliable kinetic analysis of the reduction process by Co-B NPs in the dark (see typical reaction conditions in the Experimental section above) could be monitored by the peak absorbance of nitrobenzene at 262 nm (Figure 4.6b). This dark reaction was repeated three times with a consistent apparent rate constant ( $k_{app}$ ) by performing a linear regression of  $\ln(C_t/C_0)$  vs. time after a certain period of induction time (Figure 4.6c). This induction time was also observed by many other metal catalysts possibly due to the reconstruction and activation of the metal surface for the adsorption of reactants,<sup>55</sup> in which Co-B NPs may take longer time than others due to the surface oxides occurred in the system.

However, with a relatively strong and sustainably green reducing agent hydrazine ( $N_2H_4$ ) used in the reaction condition, the actual active sites for either dark reaction or photocatalytic reactions should be the metallic form of cobalt metals.

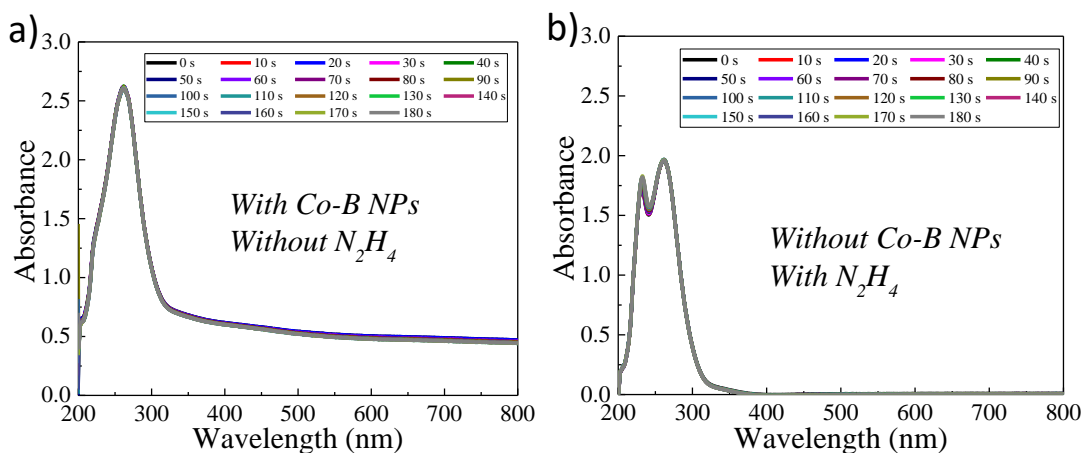


**Figure 4.6** Optical properties of different metallic nanoparticles and catalytic performance of Co-B NPs under dark and photo-excitations. (a) UV-Vis spectra of Co-B, Au, and Pd NPs. (b) UV-Vis time-dependent profiles of reaction solution for nitrobenzene reduction by  $N_2H_4$  with Co-B NPs in the dark. A reaction scheme is inserted. (c) Kinetic analysis for the reaction with Co-B NPs in the dark (repeated 3 times). After a certain induction time, the reaction follows a pseudo-first-order process for nitrobenzene. (d) Scheme for *in-situ* monitoring the reaction kinetics of photocatalyzed reactions by modified UV-Vis spectroscopy. (e) Reaction kinetics for nitrobenzene reduction with Co-B NPs in the dark or under photo-excitation by 405 nm LED (varied incident power). (f) Comparison of apparent rate constant ( $k_{app}$ ) extracted from panel e.



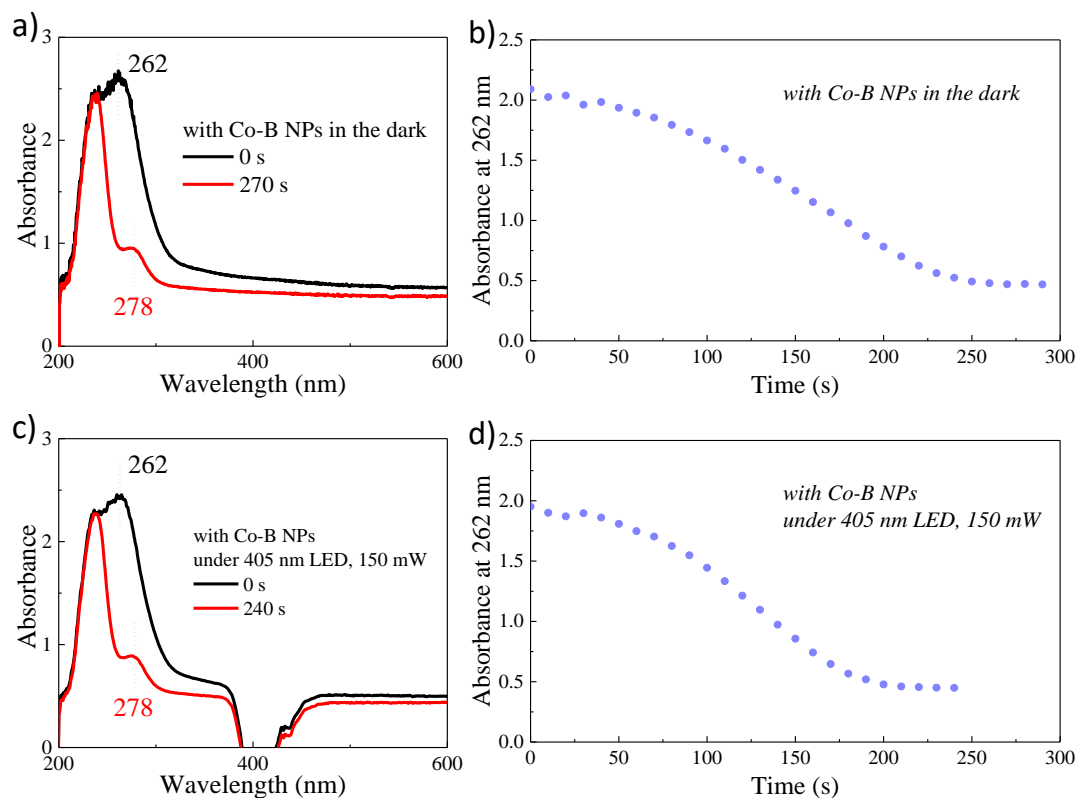
**Figure 4.7** UV-vis spectra of standard solutions with either reactants or products from the nitrobenzene reduction. (a) Nitrobenzene (NB), hydrazine ( $N_2H_4$ ) and their mixture. (b) Aniline (AL), hydrazine ( $N_2H_4$ ) and their mixture. The concentration of those substances is exactly the same as the typical reaction conditions.

Meanwhile, the dark reaction did not proceed either without hydrazine or without Co-B NPs (Figure 4.8), which excluded other possible reaction pathways but only the reduction reaction catalyzed by metallic nanoparticles. The photocatalytic setup was modified from a commercial UV-vis spectrometer and light-emitting diode (LED) with different wavelengths as the light sources (Figure 4.6d), in which the typical condition was 405 nm LED and 150 mW unless specified.



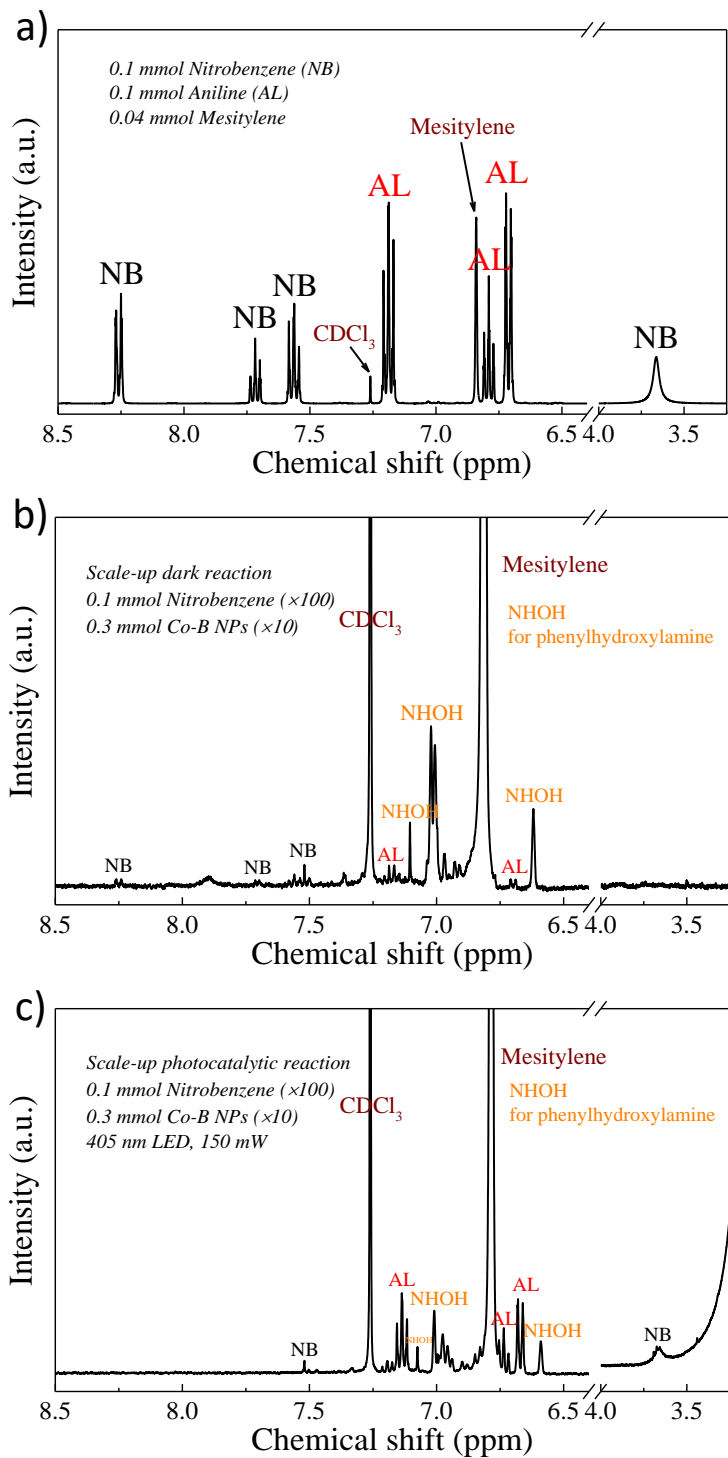
**Figure 4.8** UV-vis spectra of control reaction solutions in the dark (a) with Co-B NPs but without  $N_2H_4$  reducing agent, and (b) with  $N_2H_4$  but without Co-B NPs. Other conditions are the same as typical reaction conditions.





**Figure 4.9** UV-vis spectra of reaction solutions with Co-B NPs (a) in the dark of 0 s and 270 s, and (c) under typical photocatalyzed conditions with 405 nm LED, 150 mW of 0 s and 240 s. The peak at 278 nm indicates the formation of aniline products. Absorbance trace at 262 nm for comparison of reaction rate (b) in the dark and (d) under photocatalyzed reactions.

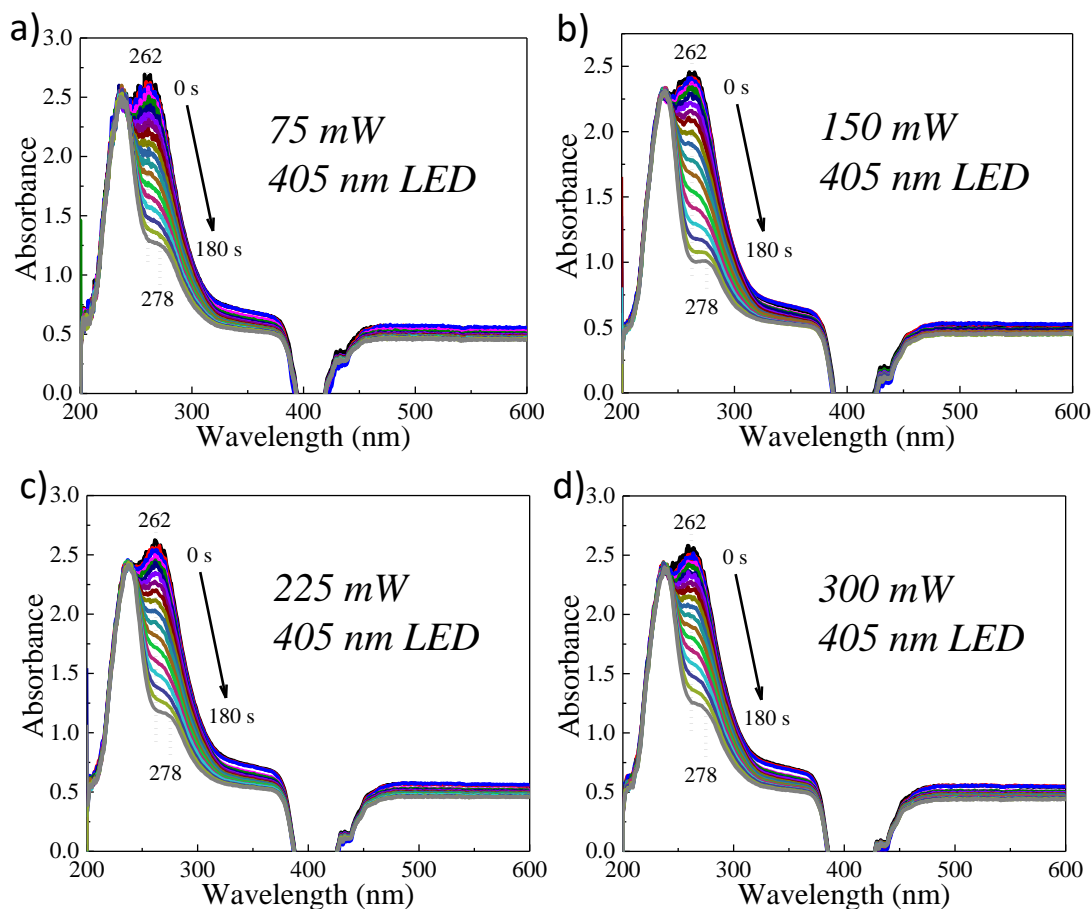
Comparing the UV-vis spectra of both typical dark and photocatalytic reactions (Figure 4.9), the absorbance at 262 nm for nitrobenzene followed an exponential decay of reactant after the induction time, thus indicating a pseudo-first-order process of nitrobenzene.<sup>56</sup> Also, the peak at 278 nm was assigned to the product aniline after the completion of nitrobenzene reduction in a few minutes (Figure 4.9). Noting that due to the rapid reduction process and the mixing alcohol-water system with Co-B NPs, up to this point, we cannot quantify the products generated by time, but we were still able to observe the reaction intermediates (phenylhydroxylamine) and final reduction product (aniline) by <sup>1</sup>H-NMR analysis of crude reaction solutions after reaction and separation (Figure 4.10). However, we believe it should not affect our kinetic analysis of the reactants since the electron and proton-transfer from the Co-B NPs and hydrazine to the nitrobenzene is the critical step for the reaction to start and this can be fairly used for the following comparison.



**Figure 4.10** NMR spectra of (a) standard solution including the reactants and products from nitrobenzene reduction, (b) scale-up dark reaction, and (c) scale-up photocatalyzed reaction. The mesitylene was used as an internal standard and deuterated chloroform ( $\text{CDCl}_3$ ) as the solvent. The scale-up amount of nitrobenzene was up to 100 times,  $\text{N}_2\text{H}_4$  to 20 times, and Co-B NP catalysts to 10 times compared to the typical reaction condition, in

which the reaction kinetics may change but the reaction mechanism was not supposed to change dramatically.

Furthermore, the photocatalytic behavior of Co-B NPs towards nitrobenzene reduction was screened before diving into the comparison across different metallic nanoparticles, including optimizing the incident power for balancing the hot carriers' dynamics and reaction kinetics, examining different wavelengths for distinguishing different types of electronic transitions and separating photo-charging and catalysis for confirming the photo-charging mechanism. First of all, different incident power was adjusted with the 405 nm LED from 75 mW to 450 mW, and the kinetic traces were measured for comparison (Figures 4.6e and 4.6f, and detailed spectra in Figure 4.11). Noting that the adsorbed photon flux should be a better description across all the photocatalytic tests for the quantification of quantum yield, however our setup with the 4-side cuvette cannot prevent strong scattering to all angles thus the adsorbed photon flux was hard to measure. Nevertheless, as long as we kept the concentration of Co-B NPs the same in our experiments and the adsorbed photon flux should also be proportional to the incident power.



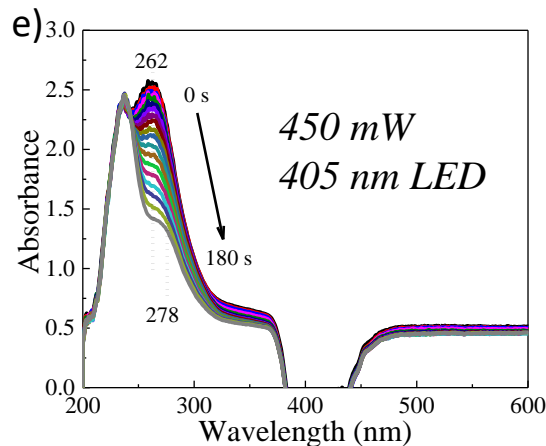


**Figure 4.11** UV-vis time-dependent profiles of reaction solutions with Co-B NPs under typical photocatalyzed condition when using 405 nm LED (FWHM=12 nm) as the light source but with different incident power (a) 75 mW, (b) 150 mW, (c) 225 mW, (d) 300 mW and (e) 450 mW. The kinetics data were retrieved to plot the Figure 4.6e above.

Back to the power-dependence, the apparent rate constant ( $k_{app}$ ) increased as the incident power increased and reached the maximum at 150 mW, in which more absorbed photons generated more hot holes to be quenched by the hole scavengers and then a higher level-up of Fermi level of the nanoparticles was achieved by photo-charging. As mentioned earlier, raising the Fermi level would also weaken the metal-reactant bond and facilitate the electron transfer, thus providing a higher reduction reaction rate. But when the adsorbed photons kept increasing and the Fermi level kept rising, the metal-reactant bond became weaker enough to override the photo-charging effect. Thus, phenomenally the rate constant started to decrease after its optimum. We believe the balance between metal-adsorbate interaction and photo-charging effect would play an important role in the photocatalytic reactions and how to distinguish and quantify them is worth for some further study in the future.

#### 4.5.2 Photocatalytic performance of Co-B NPs under different wavelengths

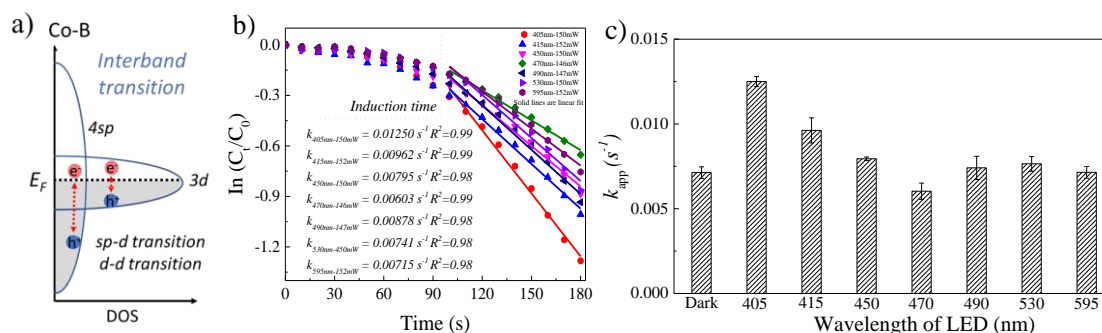
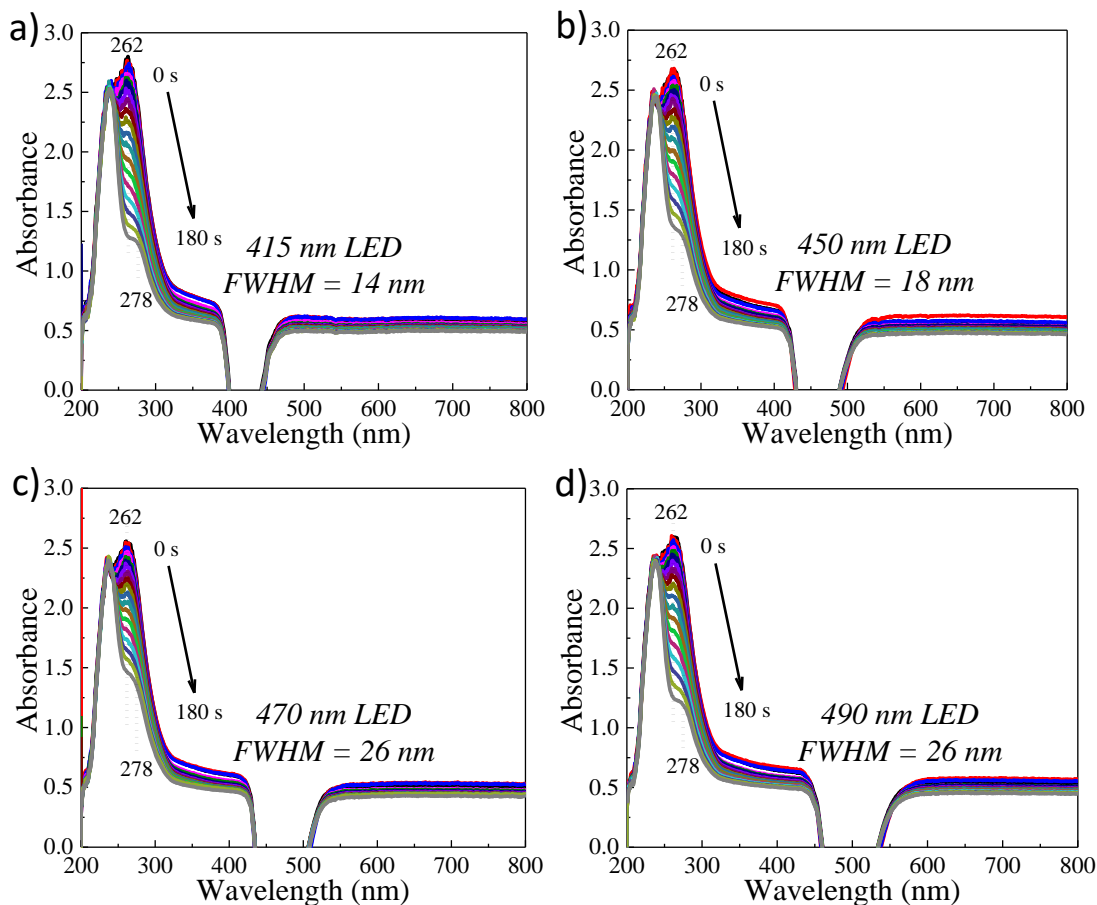


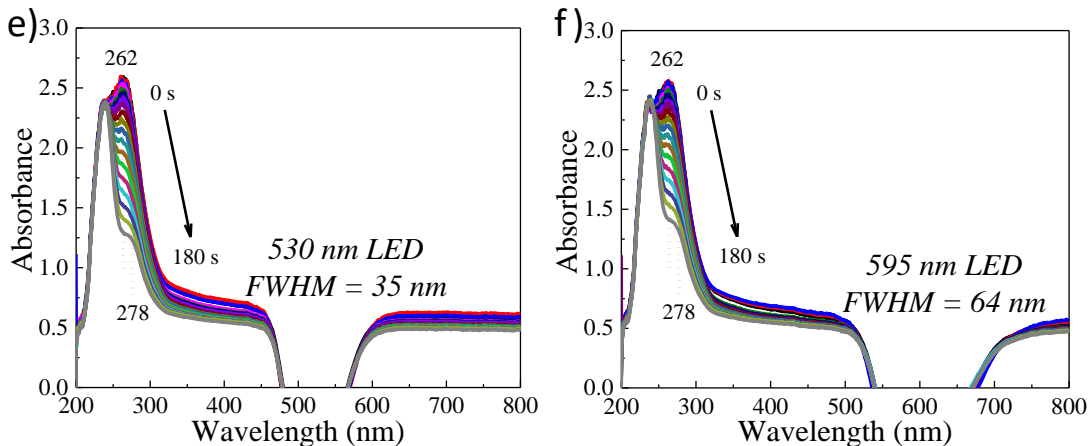
**Figure 4.12** Photocatalytic performance under different wavelength excitation and experimental evidence of photo-charging mechanism of Co-B NPs. (a) Scheme of hot carrier's relative energy diagram from  $sp-d$  interband transition and  $d-d$  intraband transition of Co-B NPs. (b) Reaction kinetics for nitrobenzene reduction with Co-B NPs under photo-

excitation by different wavelength LED with the same incident power. (c) Comparison of apparent rate constant ( $k_{app}$ ) extracted from panel b. Error bars represent one standard deviation of the mean.

As mentioned earlier, the 405 nm photo-excitation provided *sp-d* interband transitions in Co-B NPs, and promoted the hot electron near the Fermi level across the *d* band and the hot holes resided deep in the *sp* band (Figure 4.12a). During the photocatalytic reactions, the hot holes would be quenched by the hole scavengers (in this case the isopropyl alcohol as the solvent and with excess amount) to photo-charge the nanoparticles with extra accumulated electrons for a higher Fermi level, eventually facilitating the nitrobenzene reduction reactions. Due to the nature of interband transitions, the hot carriers' behavior should not be deviated from other metallic nanoparticles and follow the same trend when changing the wavelength.<sup>22, 57</sup>

Indeed, the apparent rate constant ( $k_{app}$ ) decreased when shifting from 405 nm to 470 nm of the incident power (Figures 4.12b and 4.12c, and Figure 4.13), in which at a longer wavelength with lower photon energy, the hot holes generated would become “shallower” close to the Fermi level and the photo-charging effect became weaker. This trend was also observed with the Pd NPs in our previous report.<sup>42</sup>

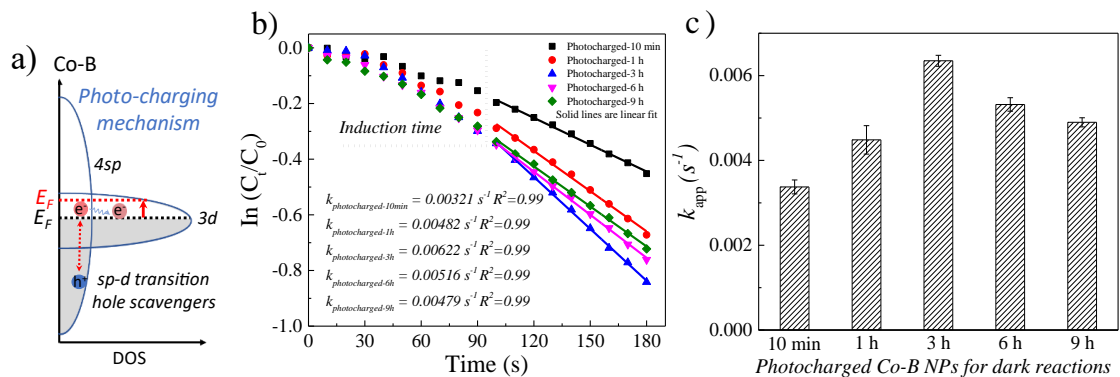




**Figure 4.13** UV-vis time-dependent profiles of reaction solutions with Co-B NPs under typical photocatalyzed condition when using different wavelengths of LED but with the same incident power (150 mW). (a) 415 nm LED, (b) 450 nm LED, (c) 470 nm LED, (d) 490 nm LED, (e) 530 nm, and (e) 595 nm LED. The kinetics data were retrieved to plot the Figure 4.12b.

In addition, when moving to a much longer wavelength after 490 nm with much lower photon energy, the photo-excitation had already fallen out of the interband transition region, and the *d-d* intraband transitions jumped in under these excitations (Figure 4.12a). Even though the hot carrier's dynamics in this region were not clear yet, we could still reasonably speculate its behavior based on our experimental results. The photocatalytic activity of Co-B NPs under the photo-excitation from 490 nm to 595 nm was close to the dark reaction, indicating that the hot carriers may not be involved in the reduction reaction in the timescale of our experiments, in which it may arise from the low energy gap between hot electron and hot hole making the separation and extraction of hot carriers much harder for the following catalysis.

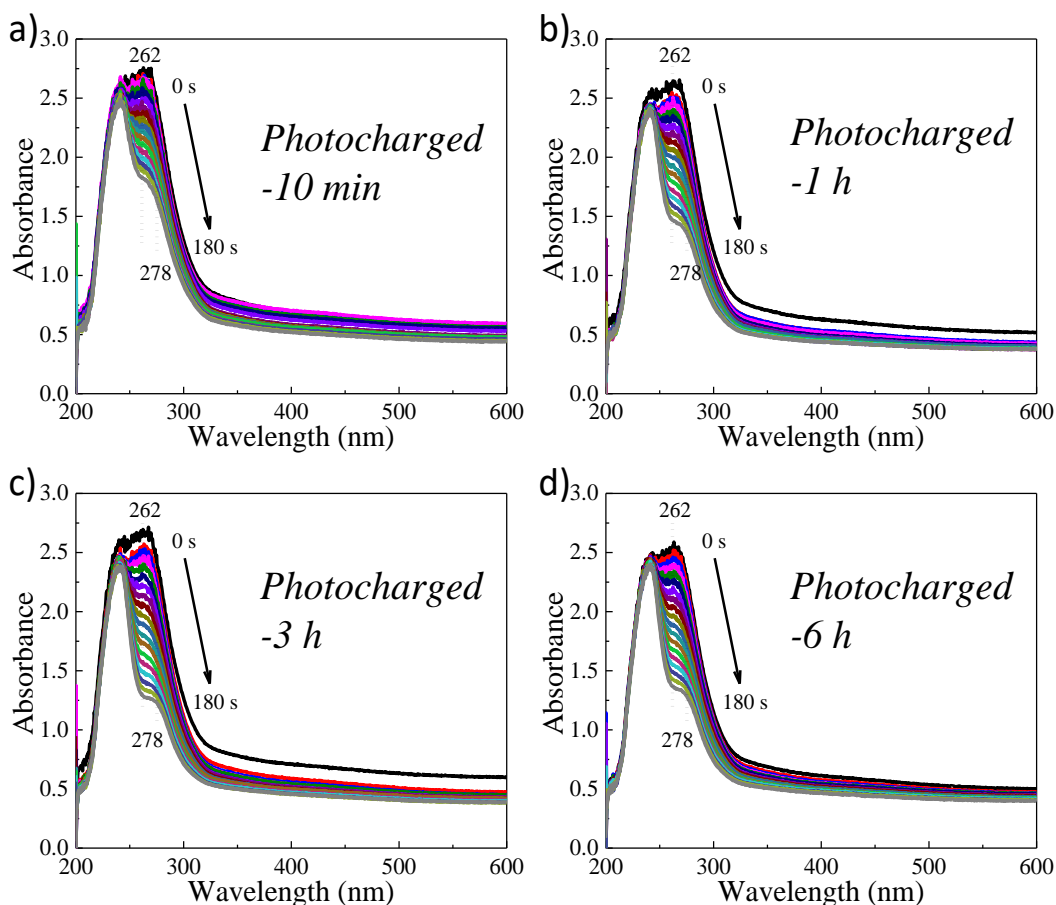
#### 4.5.3 Mechanistic study of photo-charging effect on Co-B NPs



**Figure 4.14** Experimental evidence of photo-charging mechanism for Co-B NPs. (a) Scheme for photo-charging mechanism of raising the Fermi level by quenching the hot holes from interband transitions in Co-B NPs. (b) Reaction kinetics for nitrobenzene reduction with photo-charged Co-B NPs. Charging time varies from 10 minutes to 9 hours

as labeled. (c) Comparison of apparent rate constant ( $k_{app}$ ) extracted from panel e. Error bars represent one standard deviation of the mean.

Thirdly, to confirm the photo-charging mechanism in the Co-B NPs, we separated the charging step and catalytic reactions, in which the same method was detailed in our previous work when using the same Pd NPs in this work. As expected (Figures 4.14 a-c and 4.15), the photo-charged Co-B NPs also demonstrated a similar trend of maximizing the charging effect with a peaked reaction rate constant at 3 h, as reported previously. We speculate that the photo-charging still happens after 3h but the excess oxidized products by hole scavengers may block the active sites for further reactions, which also explains the different kinetics trace in this set of experiments compared to the *in-situ* photo-charging during photocatalytic processes. Nonetheless, the photocatalysis survey did present the relationship between interband transition and reaction kinetics, and provided us the optimized photocatalytic conditions for the following comparison among different metallic nanoparticles.



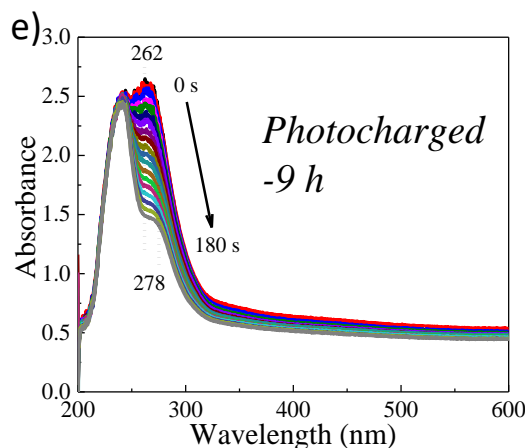


**Figure 4.15** UV-vis time-dependent profiles of reaction solutions with photo-charged Co-B NPs when using 405 nm LED (FWHM=12 nm) as the light source under different charging time (a) 10 min, (b) 1 h, (c) 3 h, (d) 6 h and (e) 9 h. The kinetics data were retrieved to plot the Figure 4.14b in the main text. See the charging conditions in the experimental section.

#### 4.6 Photocatalytic performance of Au, Pd and Co-B NPs

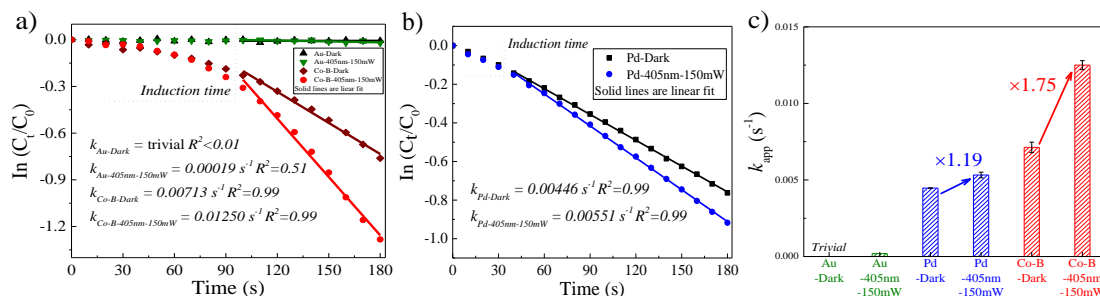
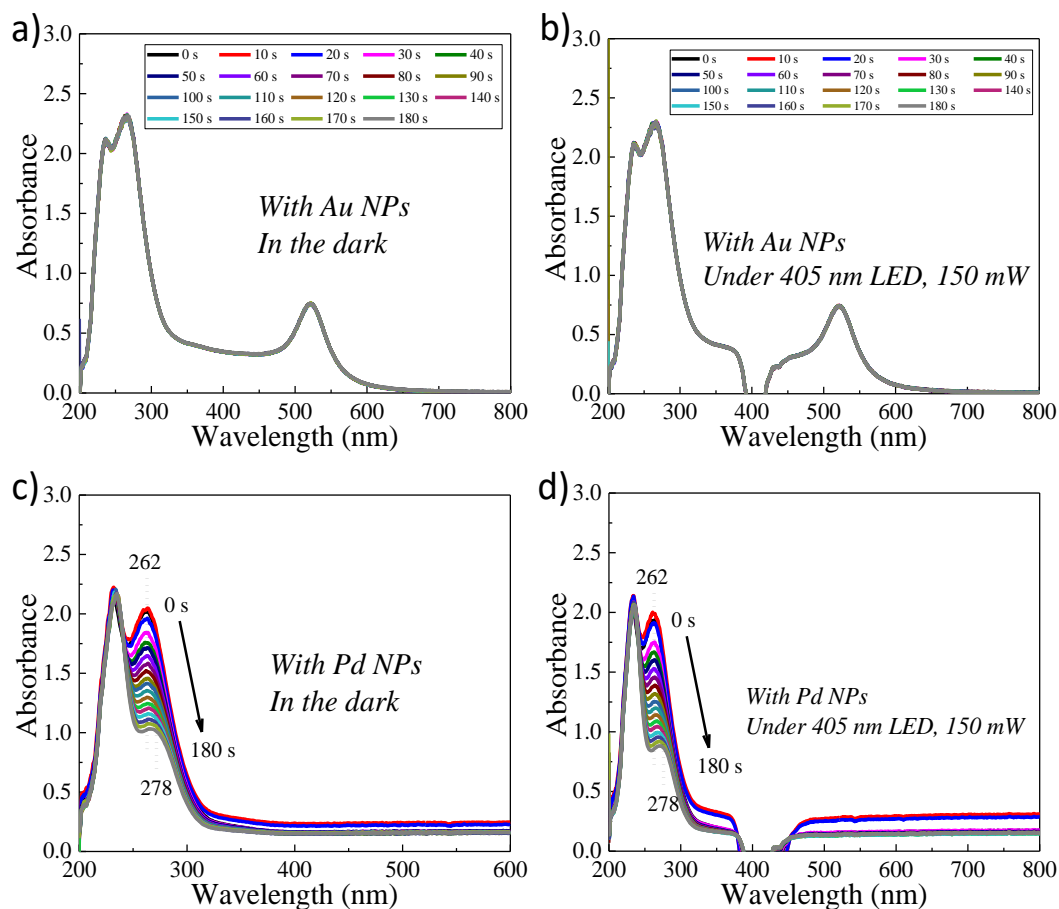


**Figure 4.16** Photocatalytic performance of different metallic NPs. Reaction kinetics for nitrobenzene reduction in the dark or under typical photo-excitation conditions (405 nm LED, 150 mW) with (a) Au NPs, Co-B NPs, and (b) Pd NPs. Noting that the induction time for different metallic NPs is different due to the difference of surface activity and related adsorption rate of reactants. (c) Comparison of apparent rate constant ( $k_{app}$ ) extracted from panel a and b. Error bars represent one standard deviation of the mean.

Ultimately, with the comprehensive understanding of the interband transitions in Au, Pd, and Co-B NPs, we now can dive into how the  $d$ -band structure impacts on the photocatalytic performance of these nanoparticles by interband transitions. Starting with Au NPs, there was no distinct activity either in the dark or in typical photocatalytic conditions (Figure 4.16a, Figures 4.17a and 4.17b) as compared to the Co-B NPs in the surveyed time range. It matched with the prediction of the inert nature of Au NPs, in which the full filling of  $d$ -band made the interaction of metal-adsorbate states weak and hot holes from interband transitions (mostly in  $d$ -band) would have a larger energy barrier to be quenched by the hole scavengers (Scheme 4.1). Such weak photo-charging effect could not contribute to improving the activity significantly. Still, in another separate experiment with a longer reaction time under the same photocatalytic conditions (not shown here), the Au



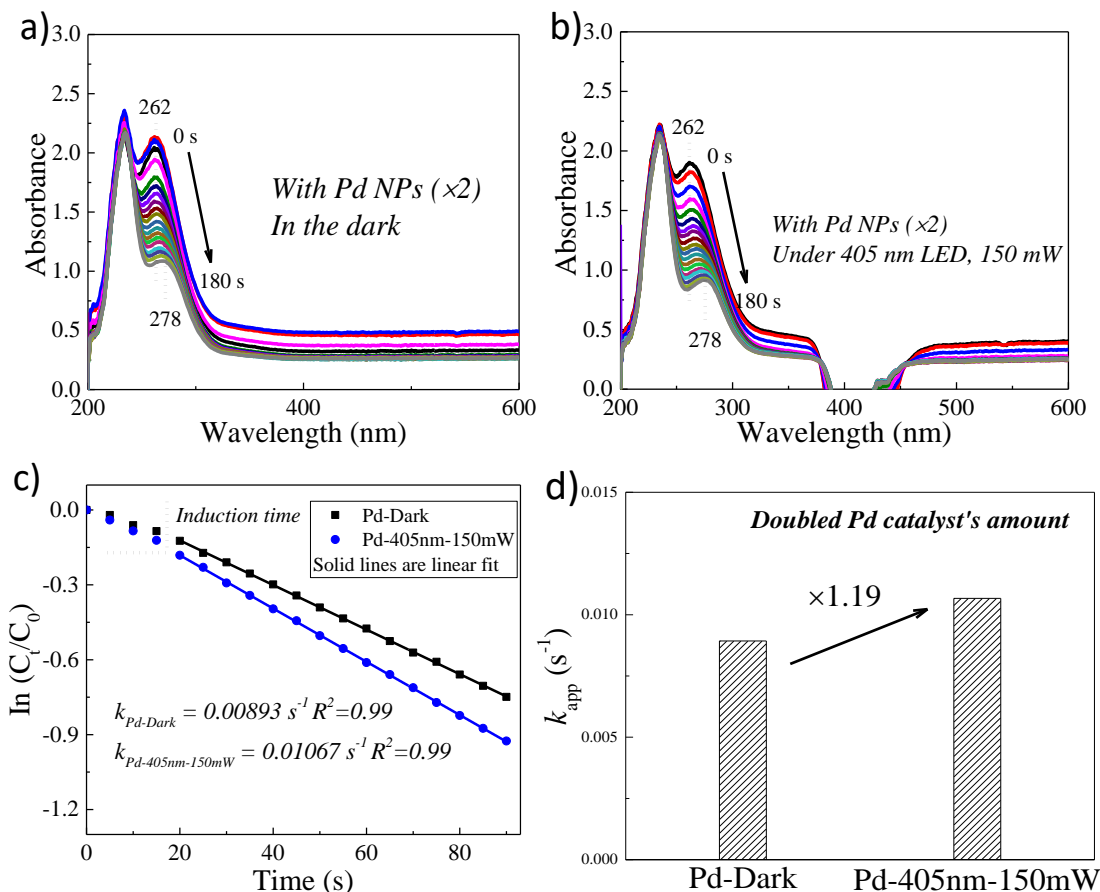
NPs could catalyze the reduction of nitrobenzene up to 20 % conversion in 5 hours, which proved that Au NPs could catalyze this reduction but just in a very slow kinetic process.



**Figure 4.17** UV-vis time-dependent profiles of reaction solutions with Au NPs and Pd NPs in the dark or typical photocatalyzed condition. (a) Au NPs in the dark, (b) Au NPs under 405 nm LED 150 mW, (c) Pd NPs in the dark, and (d) Pd NPs under 405 nm LED 150 mW. The kinetics data were retrieved to plot the Figures 4.16a and 4.16b.

Then, moving to Pd NPs, the reduction reaction happened much faster than the Au NPs, and even with a much shorter induction time than the other two nanoparticles (Figure 4.16b, Figures 4.17c and 4.17d). And the photocatalytic performance did show a distinguishable enhancement with a factor of 1.19, which also matched with the previous prediction of some unoccupied states occurring in the *d*-band benefiting both metal-adsorbates interaction and interband transitions (Scheme 1). One thing to mention here, since we wanted to compare the photocatalysis enhancement of different metallic nanoparticles rather than the absolute value of the catalytic activity, we had to maintain the similar optical response of these nanoparticles in reaction solutions around 400 nm, ideally for the same number of hot carriers generated for catalysis (Figure 4.6a). In that case, the atomic concentration of metals across different metallic nanoparticles may experience some discrepancy, for example, the concentration of Pd NPs was around 8.7 times higher than

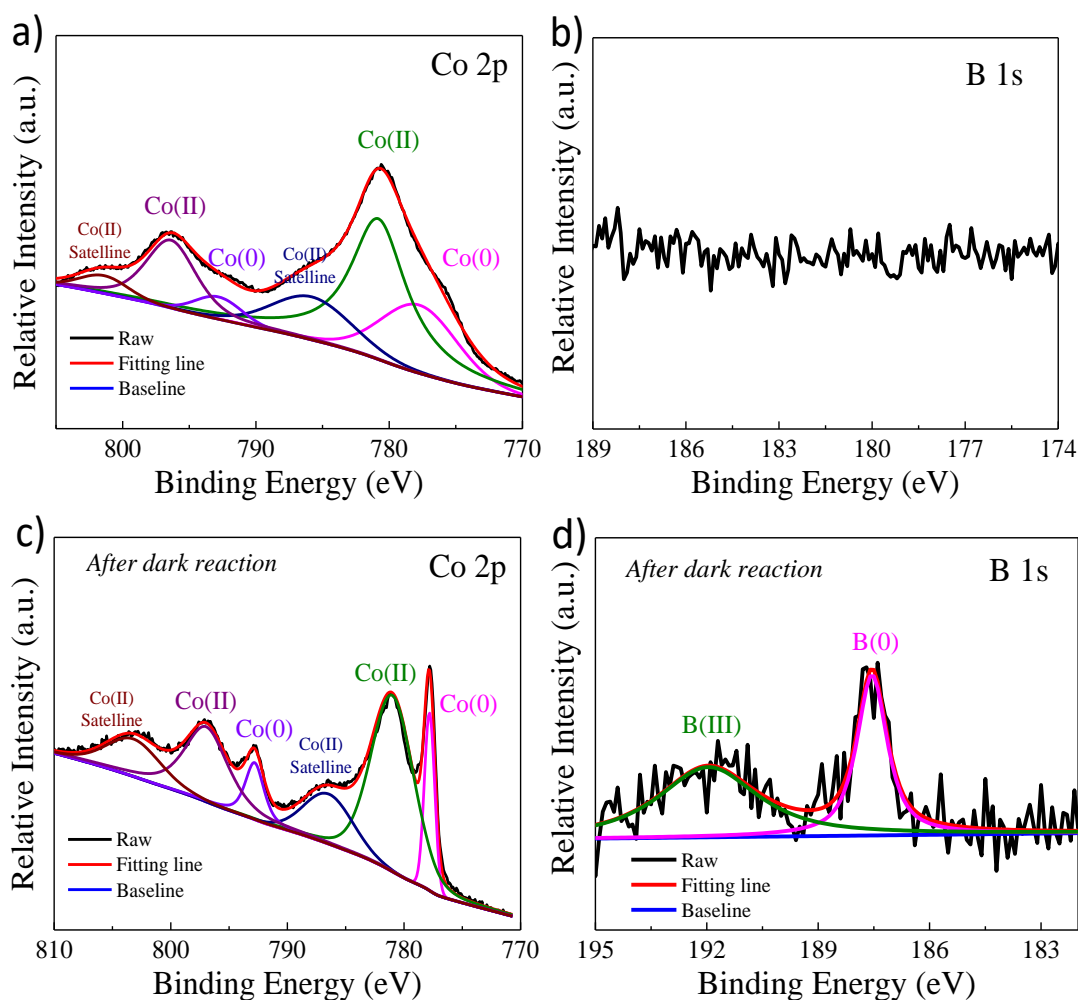
Au NPs and 27 times lower than Co-B NPs (see details in the Experimental section above), making the direct comparison of absolute catalytic activity not rigorous. But it should not affect the photocatalytic enhancement by interband transitions since the contribution of photo-charging effects would only build up based on the dark reaction kinetics, as proved by the control experiment with doubled concentration of Pd NPs also showing the same photocatalysis enhancement factor of 1.19 compared to its dark reaction (Figure 4.18).



**Figure 4.18** UV-vis time-dependent profiles of reaction solutions with Pd NPs (a) in the dark or (b) under 405 nm LED 150 mW. (c) Reaction kinetics retrieved from (a) and (b). (d) Comparison of apparent rate constant. Noting that in this condition, the concentration of Pd NPs was doubled compared to the typical photocatalyzed condition of Pd NPs (in Figure 4.16b), in order to examine the effect of catalyst's amount on enhancement factor of photocatalyzed reaction from interband transitions by dark reaction.

Last but not the least, the Co-B NPs demonstrated a much higher enhancement with a factor of 1.75 than both Pd NPs under typical photocatalytic reactions (Figure 4.16c). It was consistent with our previous prediction, in which hot holes generated in the *sp*-band would have an energetic alignment of HOMO-like bonding states of the hole scavengers, and the stronger photo-charging effect with a much higher Fermi level would weaken the metal-reactant bond more and facilitate the electron transfer better, eventually providing a higher photocatalysis enhancement. (Scheme 1).

Besides, there were no significant changes in the surface oxidation status after the dark and photocatalytic reactions for Co-B NPs (see XPS details in Figure 4.19, and for Pd NPs see details in our previous work<sup>22,42</sup>), indicating the integrity of the *d*-band structure during the reduction reaction and further confirming the contribution of interband transition from the *d*-band structure. Similarly, some recent reports also demonstrate the photocatalytic enhancements of cobalt nanoparticles but in the supported catalysts and lack of the insight of interband transitions,<sup>58-61</sup> and we hope our systematic comparison across different colloidal metallic nanoparticles could bring more attention to the non-noble metallic nanoparticle photocatalysts especially under interband transitions, and expand the photocatalysis into more practical applications.



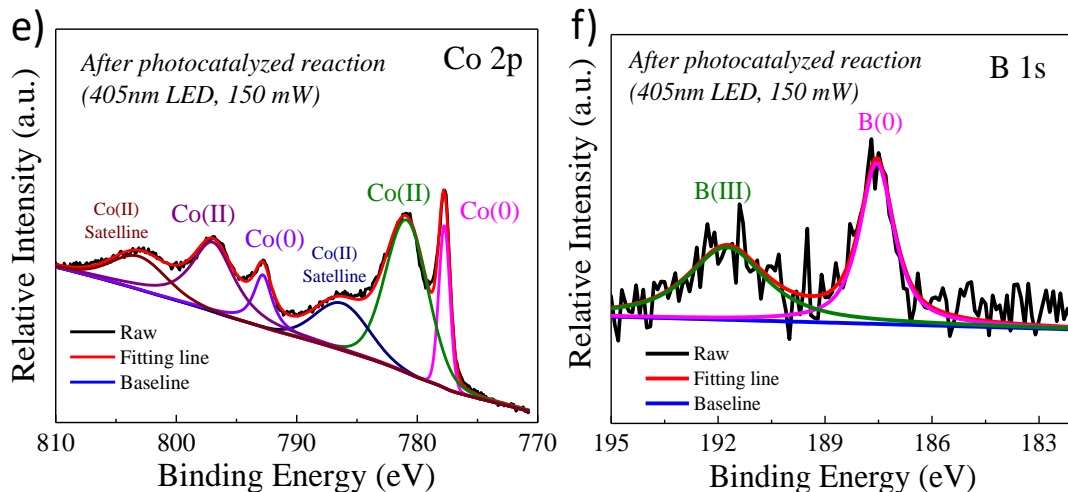


**Figure 4.19** XPS analysis of Co-B NPs (a, b) before reduction reaction, (c, d) after dark reaction, and (e, f) after a typical photocatalyzed reaction (405 nm LED, 150 mW). High-resolution spectra and deconvoluted peak analysis of (a, c, e) Co 2p and (b, d, f) B 1s.

Due to the active nature of metallic cobalt, there is always metal oxide formed on the surface as soon as the cobalt is exposed to air,<sup>62</sup> not mentioned to the fact that when it comes to nanoscales the cobalt oxides are expected in the XPS analysis. The assignment and deconvolution analysis were based on the XPS handbook and literature.<sup>63-68</sup> Starting with the Co-B NPs before reaction (Figures 4.19 and 4.19b), the peaks at 778.1 eV for Co 2p<sub>3/2</sub> and 792.9 eV for Co 2p<sub>1/2</sub> indicated the metallic cobalt in the nanoparticles, while the Co<sup>2+</sup> species (such as CoO or Co(OH)<sub>2</sub>) were also observed in a higher binding energy. This result confirmed the metallic form of the Co-B NPs with some oxides on their surfaces, which was consistent with other reports.<sup>64-66</sup> However, no obvious peak of metallic boron was observed in B 1s spectrum, which may be attributed to the oxide layers form on the surface that blocked the signal. Furthermore, when moving to the XPS spectra of Co-B NPs after the dark and photocatalyzed reaction (Figures 4.19 c-f), a sharp peak separated from the Co<sup>2+</sup> peaks at around 777.8 eV was observed in both samples, which was also shifted about 0.3 eV compared to the Co<sup>0</sup> peak before the reaction and indicated the electron transfer from the metallic Co to elemental B.<sup>64</sup> Considering the strong reducing agent N<sub>2</sub>H<sub>4</sub> was used in the reaction, a fast cleaning process may occur on the surface of Co-B NPs that would remove the oxidized species and expose the active metallic cobalt for further reaction.<sup>67</sup> In the meantime, the peaks at around 187.5 eV in B 1s spectra of both samples were corresponding to the metallic boron on the surface of Co-B NPs, and there were some boron oxide formed on the surface due to the sample preparation process under air exposure.<sup>68</sup> Lastly, the percentage of metallic Co<sup>0</sup> in both samples after reactions were estimated by peak area analysis to be 16 % after dark reaction and 18 % after photocatalyzed reaction, which were quite close and showed that the numeric change of active sites was not the major contribution to the difference of catalytic activity in those two conditions. Overall, these results demonstrated that the metallic form of Co-B alloy NPs and the active sites for the catalytic reduction reaction should be the metallic cobalt site whether in the dark reaction or photocatalyzed reactions.

## 4.7 Conclusion

In conclusion, we demonstrated that the *d*-band structure of metallic nanoparticles not only contributed to the interaction between metal surface and adsorbates, but also to the hot carriers' behavior in interband transitions, which were both critical for photocatalytic reactions. And the cobalt-based metallic nanoparticle photocatalysts were proved to be a good candidate for designing better energy alignment between the *d*-band structure and interband transition than Au and Pd nanoparticles, which leads us to shift from noble to non-noble metallic nanoparticle photocatalyst and a sustainable future.

## 4.8 References

- (1) Linic, S.; Chavez, S.; Elias, R. Flow and Extraction of Energy and Charge Carriers in Hybrid Plasmonic Nanostructures. *Nat. Mater.* **2021**, *20*, 916-924.
- (2) Lee, S. A.; Link, S. Chemical Interface Damping of Surface Plasmon Resonances. *Acc. Chem. Res.* **2021**, *54*, 1950-1960.
- (3) Cortés, E.; Govorov, A. O.; Misawa, H.; Willets, K. A. Special Topic on Emerging Directions in Plasmonics. *J. Chem. Phys.* **2020**, *153*, 010401.
- (4) Zhan, C.; Moskovits, M.; Tian, Z.-Q. Recent Progress and Prospects in Plasmon-Mediated Chemical Reaction. *Matter* **2020**, *3*, 42-56.
- (5) Narang, P.; Sundararaman, R.; Atwater, H. A. Plasmonic Hot Carrier Dynamics in Solid-State and Chemical Systems for Energy Conversion. *Nanophotonics* **2016**, *5*, 96-111.
- (6) Gellé, A.; Jin, T.; de la Garza, L.; Price, G. D.; Besteiro, L. V.; Moores, A. Applications of Plasmon-Enhanced Nanocatalysis to Organic Transformations. *Chem. Rev.* **2020**, *120*, 986-1041.
- (7) Kazuma, E.; Kim, Y. Mechanistic Studies of Plasmon Chemistry on Metal Catalysts. *Angew. Chem. Int. Ed.* **2019**, *58*, 4800-4808.
- (8) Devasia, D.; Das, A.; Mohan, V.; Jain, P. K. Control of Chemical Reaction Pathways by Light-Matter Coupling. *Annu. Rev. Phys. Chem.* **2021**, *72*, 423-443.
- (9) Robotjazi, H.; Bao, J. L.; Zhang, M.; Zhou, L.; Christopher, P.; Carter, E. A.; Nordlander, P.; Halas, N. J. Plasmon-Driven Carbon-Fluorine (C(sp<sup>3</sup>)-F) Bond Activation with Mechanistic Insights into Hot-Carrier-Mediated Pathways. *Nat. Catal.* **2020**, *3*, 564-573.
- (10) Schroeder, E.; Christopher, P. Chemical Production Using Light: Are Sustainable Photons Cheap Enough? *ACS Energy Lett.* **2022**, *7*, 880-884.
- (11) Zhao, J.; Nguyen, S. C.; Ye, R.; Ye, B.; Weller, H.; Somorjai, G. A.; Alivisatos, A. P.; Toste, F. D. A Comparison of Photocatalytic Activities of Gold Nanoparticles Following Plasmonic and Interband Excitation and a Strategy for Harnessing Interband Hot Carriers for Solution Phase Photocatalysis. *ACS Cent. Sci.* **2017**, *3*, 482-488.
- (12) Zhang, Y.; He, S.; Guo, W.; Hu, Y.; Huang, J.; Mulcahy, J. R.; Wei, W. D. Surface-Plasmon-Driven Hot Electron Photochemistry. *Chem. Rev.* **2018**, *118*, 2927-2954.
- (13) Sytwu, K.; Vadai, M.; Hayee, F.; Angell, D. K.; Dai, A.; Dixon, J.; Dionne, J. A. Driving Energetically Unfavorable Dehydrogenation Dynamics with Plasmonics. *Science* **2021**, *371*, 280-283.
- (14) Kim, Y.; Smith, J. G.; Jain, P. K. Harvesting Multiple Electron-Hole Pairs Generated through Plasmonic Excitation of Au Nanoparticles. *Nat. Chem.* **2018**, *10*, 763-769.
- (15) Mukherjee, S.; Libisch, F.; Large, N.; Neumann, O.; Brown, L. V.; Cheng, J.; Lassiter, J. B.; Carter, E. A.; Nordlander, P.; Halas, N. J. Hot Electrons Do the Impossible: Plasmon-Induced Dissociation of H<sub>2</sub> on Au. *Nano Lett.* **2013**, *13*, 240-247.
- (16) Christopher, P.; Xin, H.; Linic, S. Visible-Light-Enhanced Catalytic Oxidation Reactions on Plasmonic Silver Nanostructures. *Nat. Chem.* **2011**, *3*, 467-472.

- (17) Sarina, S.; Waclawik, E. R.; Zhu, H. Photocatalysis on Supported Gold and Silver Nanoparticles under Ultraviolet and Visible Light Irradiation. *Green Chem.* **2013**, *15*, 1814-1833.
- (18) Xie, W.; Schlücker, S. Hot Electron-Induced Reduction of Small Molecules on Photorecycling Metal Surfaces. *Nat. Commun.* **2015**, *6*, 7570.
- (19) Zhang, N.; Han, C.; Xu, Y.-J.; Foley Iv, J. J.; Zhang, D.; Codrington, J.; Gray, S. K.; Sun, Y. Near-Field Dielectric Scattering Promotes Optical Absorption by Platinum Nanoparticles. *Nat. Photon.* **2016**, *10*, 473-482.
- (20) Sytwu, K.; Vadai, M.; Dionne, J. A. Bimetallic Nanostructures: Combining Plasmonic and Catalytic Metals for Photocatalysis. *Adv. Phys.: X.* **2019**, *4*, 1619480.
- (21) Swearer, D. F.; Zhao, H.; Zhou, L.; Zhang, C.; Robotjazi, H.; Martirez, J. M. P.; Krauter, C. M.; Yazdi, S.; McClain, M. J.; Ringe, E.; Carter, E. A.; Nordlander, P.; Halas, N. J. Heterometallic Antenna-Reactor Complexes for Photocatalysis. *Proc. Natl. Acad. Sci.* **2016**, *113*, 8916-8920.
- (22) Lyu, P.; Espinoza, R.; Khan, M. I.; Spaller, W. C.; Ghosh, S.; Nguyen, S. C. Mechanistic Insight into Deep Holes from Interband Transitions in Palladium Nanoparticle Photocatalysts. *iScience* **2022**, *25*, 103737.
- (23) Vadai, M.; Angell, D. K.; Hayee, F.; Sytwu, K.; Dionne, J. A. In-Situ Observation of Plasmon-Controlled Photocatalytic Dehydrogenation of Individual Palladium Nanoparticles. *Nat. Commun.* **2018**, *9*, 4658.
- (24) Kim, S.; Kim, J.-M.; Park, J.-E.; Nam, J.-M. Nonnoble-Metal-Based Plasmonic Nanomaterials: Recent Advances and Future Perspectives. *Adv. Mater.* **2018**, *30*, 1704528.
- (25) Zhou, L.; Zhang, C.; McClain, M. J.; Manjavacas, A.; Krauter, C. M.; Tian, S.; Berg, F.; Everitt, H. O.; Carter, E. A.; Nordlander, P.; Halas, N. J. Aluminum Nanocrystals as a Plasmonic Photocatalyst for Hydrogen Dissociation. *Nano Lett.* **2016**, *16*, 1478-1484.
- (26) Anderson, P. W. Localized Magnetic States in Metals. *Phys. Rev.* **1961**, *124*, 41-53.
- (27) Newns, D. M. Self-Consistent Model of Hydrogen Chemisorption. *Phys. Rev.* **1969**, *178*, 1123-1135.
- (28) Nørskov, J. K.; Abild-Pedersen, F.; Studt, F.; Bligaard, T. Density Functional Theory in Surface Chemistry and Catalysis. *Proc. Natl. Acad. Sci.* **2011**, *108*, 937-943.
- (29) Jens K. Nørskov, F. S., Frank Abild-Pedersen, Thomas Bligaard. The Electronic Factor in Heterogeneous Catalysis. In *Fundamental Concepts in Heterogeneous Catalysis*, John Wiley & Sons, Inc.: 2014; pp 114-137.
- (30) Hammer, B.; Nørskov, J. K. Theoretical Surface Science and Catalysis—Calculations and Concepts. In *Advances in Catalysis*, Academic Press: 2000; Vol. 45, pp 71-129.
- (31) Xin, H.; Vojvodic, A.; Voss, J.; Nørskov, J. K.; Abild-Pedersen, F. Effects of d-band Shape on the Surface Reactivity of Transition-Metal Alloys. *Phys. Rev. B* **2014**, *89*, 115114.
- (32) Montemore, M. M.; van Spronsen, M. A.; Madix, R. J.; Friend, C. M. O<sub>2</sub> Activation by Metal Surfaces: Implications for Bonding and Reactivity on Heterogeneous Catalysts. *Chem. Rev.* **2018**, *118*, 2816-2862.
- (33) Khurgin, J. B. Fundamental Limits of Hot Carrier Injection from Metal in Nanoplasmonics. *Nanophotonics* **2020**, *9*, 453-471.
- (34) Aslam, U.; Rao, V. G.; Chavez, S.; Linic, S. Catalytic Conversion of Solar to Chemical Energy on Plasmonic Metal Nanostructures. *Nat. Catal.* **2018**, *1*, 656-665.
- (35) Ueno, K.; Misawa, H. Surface Plasmon-Enhanced Photochemical Reactions. *J. Photochem. Photobiol. C: Photochem. Rev.* **2013**, *15*, 31-52.
- (36) Un, I.-W.; Sivan, Y. The Role of Heat Generation and Fluid Flow in Plasmon-Enhanced Reduction–Oxidation Reactions. *ACS Photonics* **2021**, *8*, 1183-1190.
- (37) Creighton, J. A.; Eadon, D. G. Ultraviolet–Visible Absorption Spectra of the Colloidal Metallic Elements. *J. Chem. Soc., Faraday Trans.* **1991**, *87*, 3881-3891.

- (38) Brus, L. Noble Metal Nanocrystals: Plasmon Electron Transfer Photochemistry and Single-Molecule Raman Spectroscopy. *Acc. Chem. Res.* **2008**, *41*, 1742-1749.
- (39) Wilson, A. J.; Jain, P. K. Light-Induced Voltages in Catalysis by Plasmonic Nanostructures. *Acc. Chem. Res.* **2020**, *53*, 1773-1781.
- (40) Christopher, P.; Moskovits, M. Hot Charge Carrier Transmission from Plasmonic Nanostructures. *Annu. Rev. Phys. Chem.* **2017**, *68*, 379-398.
- (41) Weaver, J. H.; Benbow, R. L. Low-energy interband absorption in Pd. *Phys. Rev. B* **1975**, *12*, 3509-3510.
- (42) Lyu, P.; Nguyen, S. C. Effect of Photocharging on Catalysis of Metallic Nanoparticles. *J. Phys. Chem. Lett.* **2021**, *12*, 12173-12179.
- (43) Zheng, Y.; Zhong, X.; Li, Z.; Xia, Y. Successive, Seed-Mediated Growth for the Synthesis of Single-Crystal Gold Nanospheres with Uniform Diameters Controlled in the Range of 5–150 nm. *Part. Part. Syst. Char.* **2014**, *31*, 266-273.
- (44) Mao, Z.; Vang, H.; Garcia, A.; Tohti, A.; Stokes, B. J.; Nguyen, S. C. Carrier Diffusion—The Main Contribution to Size-Dependent Photocatalytic Activity of Colloidal Gold Nanoparticles. *ACS. Catal.* **2019**, *9*, 4211-4217.
- (45) Li, C.; Iqbal, M.; Jiang, B.; Wang, Z.; Kim, J.; Nanjundan, A. K.; Whitten, A. E.; Wood, K.; Yamauchi, Y. Pore-Tuning to Boost the Electrocatalytic Activity of Polymeric Micelle-Templated Mesoporous Pd Nanoparticles. *Chem. Sci.* **2019**, *10*, 4054-4061.
- (46) Zhu, Z.; Ma, J.; Xu, L.; Xu, L.; Li, H.; Li, H. Facile Synthesis of Co–B Amorphous Alloy in Uniform Spherical Nanoparticles with Enhanced Catalytic Properties. *ACS. Catal.* **2012**, *2*, 2119-2125.
- (47) Zhou, S.; Huo, D.; Goines, S.; Yang, T.-H.; Lyu, Z.; Zhao, M.; Gilroy, K. D.; Wu, Y.; Hood, Z. D.; Xie, M.; Xia, Y. Enabling Complete Ligand Exchange on the Surface of Gold Nanocrystals through the Deposition and Then Etching of Silver. *J. Am. Chem. Soc.* **2018**, *140*, 11898-11901.
- (48) Su, G.; Yang, C.; Zhu, J.-J. Fabrication of Gold Nanorods with Tunable Longitudinal Surface Plasmon Resonance Peaks by Reductive Dopamine. *Langmuir* **2015**, *31*, 817-823.
- (49) de Barros, H. R.; Piovan, L.; Sasaki, G. L.; de Araujo Sabry, D.; Mattoso, N.; Nunes, Á. M.; Meneghetti, M. R.; Riegel-Vidotti, I. C. Surface Interactions of Gold Nanorods and Polysaccharides: From Clusters to Individual Nanoparticles. *Carbohydr. Polym.* **2016**, *152*, 479-486.
- (50) Bu, Y.; Liu, J.; Chu, H.; Wei, S.; Yin, Q.; Kang, L.; Luo, X.; Sun, L.; Xu, F.; Huang, P.; Rosei, F.; Pimerzin, A. A.; Seifert, H. J.; Du, Y.; Wang, J. Catalytic Hydrogen Evolution of NaBH<sub>4</sub> Hydrolysis by Cobalt Nanoparticles Supported on Bagasse-Derived Porous Carbon. *Nanomaterials* **2021**, *11*, 3259.
- (51) Mussa, Y.; Ahmed, F.; Abuhimad, H.; Arsalan, M.; Alsharaeh, E. Enhanced Electrochemical Performance at High Temperature of Cobalt Oxide/Reduced Graphene Oxide Nanocomposites and its Application in Lithium-Ion Batteries. *Sci. Rep.* **2019**, *9*, 44.
- (52) Braik, M.; Sow, I.; Nelayah, J.; Belkhir, A.; Faustini, M.; Mercone, S.; Nowak, S.; Decorse, P.; Piquemal, J.-Y.; Félidj, N. Introducing Cobalt as a Potential Plasmonic Candidate Combining Optical and Magnetic Functionalities within the Same Nanostructure. *Nanoscale* **2021**, *13*, 2639-2647.
- (53) Bhatta, H. L.; Aliev, A. E.; Drachev, V. P. New Mechanism of Plasmons Specific for Spin-Polarized Nanoparticles. *Sci. Rep.* **2019**, *9*, 2019.
- (54) Kaminskiene, Z.; Prosycevas, I.; Stonkute, J.; Guobiene, A. Evaluation of Optical Properties of Ag, Cu, and Co Nanoparticles Synthesized in Organic Medium. *Acta Phys. Pol., A* **2013**, *123*, 111-114.

- (55) Hervés, P.; Pérez-Lorenzo, M.; Liz-Marzán, L. M.; Dzubielia, J.; Lu, Y.; Ballauff, M. Catalysis by Metallic Nanoparticles in Aqueous Solution: Model Reactions. *Chem. Soc. Rev.* **2012**, *41*, 5577-5587.
- (56) Aditya, T.; Pal, A.; Pal, T. Nitroarene Reduction: A Trusted Model Reaction to Test Nanoparticle Catalysts. *Chem. Commun.* **2015**, *51*, 9410-9431.
- (57) Mao, Z.; Espinoza, R.; Garcia, A.; Enwright, A.; Vang, H.; Nguyen, S. C. Tuning Redox Potential of Gold Nanoparticle Photocatalysts by Light. *ACS Nano* **2020**, *14*, 7038-7045.
- (58) Chu, C.; Zhu, Q.; Pan, Z.; Gupta, S.; Huang, D.; Du, Y.; Weon, S.; Wu, Y.; Muhich, C.; Stavitski, E.; Domen, K.; Kim, J.-H. Spatially Separating Redox Centers on 2D Carbon Nitride with Cobalt Single Atom for Photocatalytic H<sub>2</sub>O<sub>2</sub> production. *Proc. Natl. Acad. Sci.* **2020**, *117*, 6376-6382.
- (59) Feng, K.; Wang, S.; Zhang, D.; Wang, L.; Yu, Y.; Feng, K.; Li, Z.; Zhu, Z.; Li, C.; Cai, M.; Wu, Z.; Kong, N.; Yan, B.; Zhong, J.; Zhang, X.; Ozin, G. A.; He, L. Cobalt Plasmonic Superstructures Enable Almost 100% Broadband Photon Efficient CO<sub>2</sub> Photocatalysis. *Adv. Mater.* **2020**, *32*, 2000014.
- (60) Jiang, D.; Chen, X.; Zhang, Z.; Zhang, L.; Wang, Y.; Sun, Z.; Irfan, R. M.; Du, P. Highly Efficient Simultaneous Hydrogen Evolution and Benzaldehyde Production Using Cadmium Sulfide Nanorods Decorated with Small Cobalt Nanoparticles under Visible Light. *J. Catal.* **2018**, *357*, 147-153.
- (61) Kotal, M.; Sharma, A.; Jakhar, S.; Mishra, V.; Roy, S.; Sahoo, S. C.; Sharma, H. K.; Mehta, S. K. Graphene-Templated Cobalt Nanoparticle Embedded Nitrogen-Doped Carbon Nanotubes for Efficient Visible-Light Photocatalysis. *Cryst. Growth Des.* **2020**, *20*, 4627-4639.
- (62) Tompkins, H. G.; Augis, J. A. The Oxidation of Cobalt in Air from Room Temperature to 467°C. *Oxid. Met.* **1981**, *16*, 355-369.
- (63) Chastain, J.; King Jr, R. C. *Handbook of X-ray Photoelectron Spectroscopy*. Perkin-Elmer, USA: 1992; p 261.
- (64) Jiang, B.; Song, H.; Kang, Y.; Wang, S.; Wang, Q.; Zhou, X.; Kani, K.; Guo, Y.; Ye, J.; Li, H.; Sakka, Y.; Henzie, J.; Yusuke, Y. A Mesoporous Non-Precious Metal Boride System: Synthesis of Mesoporous Cobalt Boride by Strictly Controlled Chemical Reduction. *Chem. Sci.* **2020**, *11*, 791-796.
- (65) Masa, J.; Weide, P.; Peeters, D.; Sinev, I.; Xia, W.; Sun, Z.; Somsen, C.; Muhler, M.; Schuhmann, W. Amorphous Cobalt Boride (Co<sub>2</sub>B) as a Highly Efficient Nonprecious Catalyst for Electrochemical Water Splitting: Oxygen and Hydrogen Evolution. *Adv. Energy Mater.* **2016**, *6*, 1502313.
- (66) Fernandes, R.; Patel, N.; Kothari, D. C.; Miotello, A. Harvesting Clean Energy Through H<sub>2</sub> Production Using Cobalt-Boride-Based Nanocatalyst. In *Advanced Nanomaterials in Biomedical, Sensor and Energy Applications*, Chattopadhyay, J.; Srivastava, R., Eds. Springer Singapore: Singapore, 2017; pp 35-56.
- (67) Popat, Y.; Orlandi, M.; Gupta, S.; Bazzanella, N.; Pillai, S.; Patel, M. K.; Miotello, A.; Patel, N. Morphological and Elemental Investigations on Co-Fe-B-O Thin Films Deposited by Pulsed Laser Deposition for Alkaline Water Oxidation: Charge Exchange Efficiency as the Prevailing Factor in Comparison with the Adsorption Process. *Catal. Lett.* **2022**, *152*, 438-451.
- (68) Kang, Y.; Jiang, B.; Yang, J.; Wan, Z.; Na, J.; Li, Q.; Li, H.; Henzie, J.; Sakka, Y.; Yamauchi, Y.; Asahi, T. Amorphous Alloy Architectures in Pore Walls: Mesoporous Amorphous NiCoB Alloy Spheres with Controlled Compositions via a Chemical Reduction. *ACS Nano* **2020**, *14*, 17224-17232.



## Chapter 5 Summary and Future Perspectives

### 5.1 Summary

Metal nanoparticles have certain advantages for photocatalysis, such as their robust nature for multicycle operation, strong light absorption, and new catalytic mechanisms (e.g., hot-carrier transfer or optical-field enhancement) that are not accessed by other conventional catalysts such as thermally-driven heterogeneous catalysts or molecular photocatalysts.<sup>1-8</sup> Nanoparticle photocatalysts made of noble metals have demonstrated these advantages beautifully, especially via the popular Au and Pd nanocrystals.

In this dissertation, we have summarized the two key photo-excitation mechanisms involved in these noble metal nanoparticles, Plasmon Resonance, and Interband Transitions, in terms of solid-state physical picture, hot carriers' generation, charge transfer, and related photocatalyzed reactions in **Chapter 1**. As followed, we took a deep look at the roles of the hot carriers, both hot electrons and hot holes, that participate in the photocatalytic Suzuki–Miyaura C-C coupling reactions in **Chapter 2**. Furthermore, we have built a comprehensive criterion for evaluating the accurate and reliable efficiency of the photocatalysts, based on the quantum yield which relied on the photon flux and reaction kinetics. On top of that, we proposed a possible mechanism, elucidating the decisive roles of hot holes and the wavelength-dependent quantum yield, which contributed to a new insight into the photocatalytic Suzuki–Miyaura reaction.

In addition, in **Chapter 3**, we have examined an overlooked mechanism that is involved in photocatalysis of metal nanoparticles, named photo-charging. As we have observed in our group's previous publication,<sup>9, 10</sup> the photo-stationary state of the nanoparticles was proved to be critical for tuning the redox potential or impacting the catalysis efficiency. As so, we proposed a new method to separate the charging step and catalysis step and evaluate the effect of photo-charging on the catalysis of Pd nanoparticles. It was the first time, to our best knowledge, that the a concrete proportional correlation between reduction reaction rate constants and accumulated charges from photo-excitation. This work has advanced our fundamental understanding of the roles of the hot carriers, which are not only responsible for direct transferring for further reactions, but also may provide extra charging photo-stationary state for improving the catalytic performance.

However, noble metals like Au and Pd are precious and expensive. It is of necessity to develop nanocrystal photocatalysts from more affordable metals. As so, in **Chapter 4**, we have demonstrated the feasibility of interband transitions in Co-B nanoparticles for the model nitrobenzene reduction and proved the photo-charging mechanism was also responsible for the observed catalysis. Furthermore, inspired by *d*-band theory which focused on the interaction between metal and adsorbate states, we have established the systematic comparison of electronic structures and associated photocatalytic pathways across different metallic nanoparticles, Au, Pd, and Co-B. And through delicate experiment design, we have proved that hypothesis and confirmed that the energetic alignment of the interband transition and metal-adsorbate hybrid states facilitated the photo-charging process and electron transfer-dominant reduction process. We believe this work contributes to a new strategy of interband transitions when designing non-noble metallic nanoparticles for photocatalysis.

## 5.2 Future Perspectives

Moving from precious to earth-abundant metal elements for a cost-effective and sustainable alternative is well aware in homogeneous catalysis research as shown in Figure 5.1.<sup>11, 12</sup> This approach also has attracted attention in heterogeneous photocatalysis, but understanding the catalytic mechanism is still one of the main challenges.<sup>13-15</sup> Another reason for moving from noble to non-noble metal nanoparticle photocatalysts is the availability of exploring the catalytic mechanism induced by interband transitions. Cu and Al are earth-abundant and considered to be alternative non-noble metals to Au and Ag, however, their surface oxidation hampers their practical applications. Mn, Ti, Fe, and Ga nanoparticles exhibit strong LSPRs in the UV region while Co, Ni, and In nanoparticles have weak LSPRs in the visible.<sup>15</sup> In all of these metals, interband transitions are pronounced, and many of them are available in the visible region for photocatalysis. Surface oxidation of these metals is a big obstacle to utilizing them as photocatalysts in metal nanocrystal form. Co and Bi nanoparticles are our best choices for the reason mentioned above.<sup>13-15</sup>

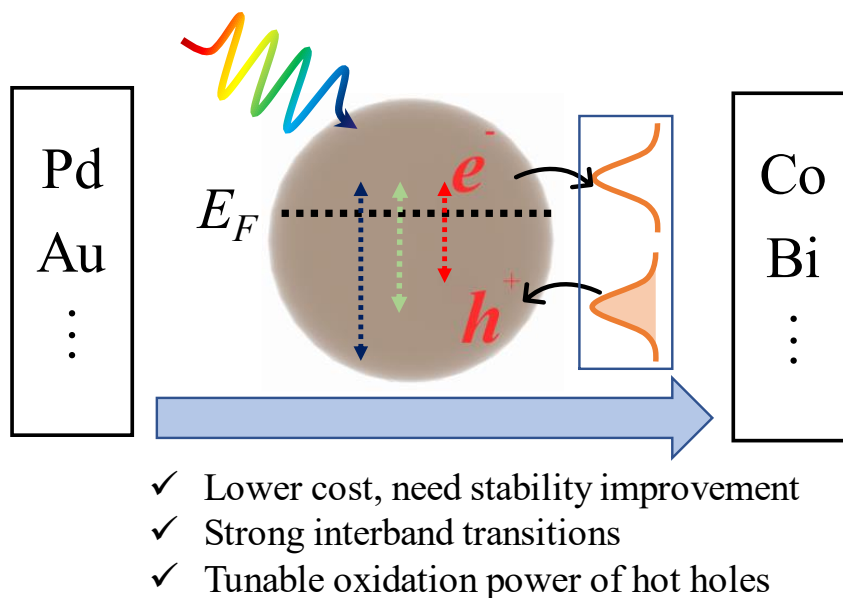


**Figure 5.1** Some benefits of moving from noble to affordable metal nanoparticles and utilizing their interband transitions for photocatalysis.

When moving from noble to non-noble metals, the localized surface plasmon resonances (LSPRs) of their nano-scaled structures become less distinctive, but the photo-induced interband transitions are strong and accessible by photoexcitation in the visible region.<sup>15, 16</sup> Interband transitions in metallic nanoparticles have recently gained more attention for photocatalysis due to the unique properties of the corresponding hot carriers.<sup>5, 17-20</sup> It is then logical to explore interband transitions in non-noble metal nanoparticles for photocatalysis.

As for Bismuth, bulk monocrystalline Bi is a low-cost semi-metal with very interesting electronic properties, such as small carrier effective masses, long carrier mean free path and high carrier mobility.<sup>21, 22</sup> Bi metal is twice more abundant than Au in the earth's crust,

but its price is about a haft of Ni and comparable to Cu metal. Strictly speaking, Bi is not an earth-abundant element, but its cost is very affordable. At the nanometer scale, Bi nanocrystals have broad and tunable LSPR covering the entire UV-vis-NIR region depending on the particle size, shape, and surrounding environment.<sup>15, 22, 23</sup> Bi nanocrystals have gained an increased interest for photocatalysis, such as photocatalyzed oxidation of NO and molecular dyes, or water splitting reactions<sup>14, 15, 23-25</sup>. In all these studies, the photocatalytic mechanism was proposed for the LSPR pathway, in which hot electrons play the decisive role. However, a careful optical study showed that the LSPR of Bi nanocrystals has strong interband damping.<sup>22</sup> An initial survey on the UV-vis spectrum of colloidal 10 nm Bi nanoparticles does not show a clear LSPR peak in the visible region. Although, we now cannot rule out the possibility that the broad LSPR of our nanoparticles could extend the absorbance tail to the vision region, we hypothesize that interband transitions in photoexcited Bi nanocrystals are strong in the visible region. Therefore, we want to utilize the deep hot holes below the Fermi level, rather than the hot electrons above the Fermi level with a well-known catalytic mechanism, for catalysis. So far, this hot-hole mediated mechanism has not been explored for Bi nanocrystals yet.

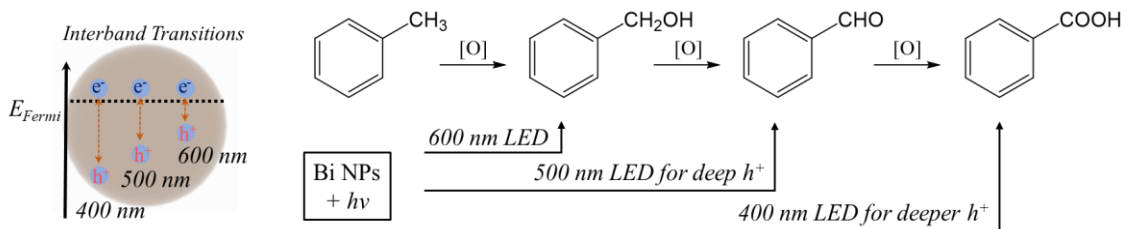


**Figure 5.2** Using different oxidation power of hot holes for selective oxidation of toluene.

Sequential oxidation catalyzed by nanoparticle photocatalysts can be used to tune catalytic activities.<sup>26, 27</sup> As in Bi nanoparticles, the oxidation power of the hot holes can be tuned by the energy of the photons triggering interband transitions. The tunable oxidation power will be used to drive the oxidation of toluene to different products (see Figure 5.2). The primary oxidizing agents will be the dissolved oxygen in the reaction solutions, and Bi nanoparticles can promote the activation of oxygen into reactive oxygen species to facilitate the oxidation process. XPS will be performed to get more insight. Experimentally, colloidal Bi nanocrystals will be used as the photocatalysts, and narrow-bandwidth LEDs with adjustable wavelengths ranging from 400 to 600 nm will be used as the light sources. Reactant conversion, product yield, and selectivity will be determined by gas chromatography. Kinetic analysis on optimized reaction conditions will also be executed for mechanism interpretation. The involvement of oxygen will be investigated by varying the reaction atmosphere and measuring the oxidation states of the particle surface elements by XPS. Different radicals and hole scavengers will be used to examine the roles of hot holes or radicals in catalysis steps. Finally, recycling tests of the photocatalysts will be performed to demonstrate the advantage of heterogeneous catalysts.

We envision that further understanding the photocatalytic properties of these alternative metal nanoparticles can push photocatalysis to more practical applications.

### 5.3 References

- (1) Narang, P.; Sundararaman, R.; Atwater, H. A. Plasmonic Hot Carrier Dynamics in Solid-State and Chemical Systems for Energy Conversion. *Nanophotonics* **2016**, *5*, 96-111.
- (2) Christopher, P.; Moskovits, M. Hot Charge Carrier Transmission from Plasmonic Nanostructures. *Annu. Rev. Phys. Chem.* **2017**, *68*, 379-398.
- (3) Aslam, U.; Rao, V. G.; Chavez, S.; Linic, S. Catalytic Conversion of Solar to Chemical Energy on Plasmonic Metal Nanostructures. *Nat. Catal.* **2018**, *1*, 656-665.
- (4) Zhang, Y.; He, S.; Guo, W.; Hu, Y.; Huang, J.; Mulcahy, J. R.; Wei, W. D. Surface-Plasmon-Driven Hot Electron Photochemistry. *Chem. Rev.* **2018**, *118*, 2927-2954.
- (5) Al-Zubeidi, A.; Hoener, B. S.; Collins, S. S. E.; Wang, W.; Kirchner, S. R.; Hosseini Jebeli, S. A.; Joplin, A.; Chang, W.-S.; Link, S.; Landes, C. F. Hot Holes Assist Plasmonic Nanoelectrode Dissolution. *Nano Lett.* **2019**, *19*, 1301-1306.
- (6) Zhang, Z.; Zhang, C.; Zheng, H.; Xu, H. Plasmon-Driven Catalysis on Molecules and Nanomaterials. *Acc. Chem. Res.* **2019**, *52*, 2506-2515.
- (7) Gelle, A.; Jin, T.; de la Garza, L.; Price, G. D.; Besteiro, L. V.; Moores, A. Applications of Plasmon-Enhanced Nanocatalysis to Organic Transformations. *Chem Rev* **2020**, *120*, 986-1041.
- (8) Wilson, A. J.; Jain, P. K. Light-Induced Voltages in Catalysis by Plasmonic Nanostructures. *Acc. Chem. Res.* **2020**, *53*, 1773-1781.
- (9) Mao, Z.; Vang, H.; Garcia, A.; Tohti, A.; Stokes, B. J.; Nguyen, S. C. Carrier Diffusion—The Main Contribution to Size-Dependent Photocatalytic Activity of Colloidal Gold Nanoparticles. *ACS. Catal.* **2019**, *9*, 4211-4217.
- (10) Mao, Z.; Espinoza, R.; Garcia, A.; Enwright, A.; Vang, H.; Nguyen, S. C. Tuning Redox Potential of Gold Nanoparticle Photocatalysts by Light. *ACS Nano* **2020**, *14*, 7038-7045.
- (11) Arevalo, R.; Chirik, P. J. Enabling Two-Electron Pathways with Iron and Cobalt: From Ligand Design to Catalytic Applications. *J. Am. Chem. Soc.* **2019**, *141*, 9106-9123.
- (12) Bullock, R. M.; Chen, J. G.; Gagliardi, L.; Chirik, P. J.; Farha, O. K.; Hendon, C. H.; Jones, C. W.; Keith, J. A.; Klosin, J.; Minter, S. D.; Morris, R. H.; Radosevich, A. T.; Rauchfuss, T. B.; Strotman, N. A.; Vojvodic, A.; Ward, T. R.; Yang, J. Y.; Surendranath, Y. Using nature's blueprint to expand catalysis with Earth-abundant metals. *Science* **2020**, *369*, eabc3183.
- (13) Kim, S.; Kim, J.-M.; Park, J.-E.; Nam, J.-M. Nonnoble-Metal-Based Plasmonic Nanomaterials: Recent Advances and Future Perspectives. *Adv. Mater.* **2018**, *30*, 1704528.
- (14) Yi, S.-S.; Zhang, X.-B.; Wulan, B.-R.; Yan, J.-M.; Jiang, Q. Non-noble metals applied to solar water splitting. *Energ. Environ. Sci.* **2018**, *11*, 3128-3156.
- (15) Sayed, M.; Yu, J.; Liu, G.; Jaroniec, M. Non-Noble Plasmonic Metal-Based Photocatalysts. *Chem. Rev.* **2022**, *122*, 10484-10537.
- (16) Creighton, J. A.; Eadon, D. G. Ultraviolet–Visible Absorption Spectra of the Colloidal Metallic Elements. *J. Chem. Soc., Faraday Trans.* **1991**, *87*, 3881-3891.
- (17) Hou, W.; Hung, W. H.; Pavaskar, P.; Goepfert, A.; Aykol, M.; Cronin, S. B. Photocatalytic Conversion of CO<sub>2</sub> to Hydrocarbon Fuels via Plasmon-Enhanced Absorption and Metallic Interband Transitions. *ACS. Catal.* **2011**, *1*, 929-936.
- (18) Liu, L.; Li, P.; Adisak, B.; Ouyang, S.; Umezawa, N.; Ye, J.; Kodiyath, R.; Tanabe, T.; Ramesh, G. V.; Ueda, S.; Abe, H. Gold Photosensitized SrTiO<sub>3</sub> for Visible-Light Water Oxidation Induced by Au Interband Transitions. *J. Mater. Chem. A* **2014**, *2*, 9875-9882.
- (19) Zhao, J.; Nguyen, S. C.; Ye, R.; Ye, B.; Weller, H.; Somorjai, G. A.; Alivisatos, A. P.; Toste, F. D. A Comparison of Photocatalytic Activities of Gold Nanoparticles Following Plasmonic and Interband Excitation and a Strategy for Harnessing Interband Hot Carriers for Solution Phase Photocatalysis. *ACS Cent. Sci.* **2017**, *3*, 482-488.
- (20) Kim, Y.; Dumett Torres, D.; Jain, P. K. Activation Energies of Plasmonic Catalysts. *Nano Lett.* **2016**, *16*, 3399-3407.

- (21) Yang, F. Y.; Liu, K.; Chien, C. L.; Searson, P. C. Large Magnetoresistance and Finite-Size Effects in Electrodeposited Single-Crystal Bi Thin Films. *Phys. Rev. Lett.* **1999**, *82*, 3328-3331.
- (22) Toudert, J.; Serna, R.; Jiménez de Castro, M. Exploring the Optical Potential of Nano-Bismuth: Tunable Surface Plasmon Resonances in the Near Ultraviolet-to-Near Infrared Range. *J. Phys. Chem. C* **2012**, *116*, 20530-20539.
- (23) Dong, F.; Xiong, T.; Sun, Y.; Zhao, Z.; Zhou, Y.; Feng, X.; Wu, Z. A semimetal bismuth element as a direct plasmonic photocatalyst. *Chem. Commun.* **2014**, *50*, 10386-10389.
- (24) Fan, W.; Li, C.; Bai, H.; Zhao, Y.; Luo, B.; Li, Y.; Ge, Y.; Shi, W.; Li, H. An in situ photoelectroreduction approach to fabricate Bi/BiOCl heterostructure photocathodes: understanding the role of Bi metal for solar water splitting. *J. Mater. Chem. A* **2017**, *5*, 4894-4903.
- (25) Li, A.; Zhang, P.; Chang, X.; Cai, W.; Wang, T.; Gong, J. Gold nanorod@TiO<sub>2</sub> yolk-shell nanostructures for visible-light-driven photocatalytic oxidation of benzyl alcohol. *Small* **2015**, *11*, 1892-1899.
- (26) Jensen, S. C.; Bettis Homan, S.; Weiss, E. A. Photocatalytic Conversion of Nitrobenzene to Aniline through Sequential Proton-Coupled One-Electron Transfers from a Cadmium Sulfide Quantum Dot. *J. Am. Chem. Soc.* **2016**, *138*, 1591-1600.
- (27) Yu, S.; Wilson, A. J.; Heo, J.; Jain, P. K. Plasmonic Control of Multi-Electron Transfer and C–C Coupling in Visible-Light-Driven CO<sub>2</sub> Reduction on Au Nanoparticles. *Nano Lett.* **2018**, *18*, 2189-2194.